

***The Effects of Additives on the Nucleation and
Growth Kinetics of Electrodeposited Copper
Nanostructures and Thin Films***

by

Yun Yu (Joseph) Han

M.A. (Physical Chemistry), Shandong Normal University, 1986
B.Sc. (Chemistry), Shandong Normal University, 1983

THESIS SUBMITTED IN PARTIAL FULFILLMENT
OF THE REQUIREMENTS FOR THE DEGREE OF
DOCTOR OF PHILOSOPHY

in the
Department of Chemistry
Faculty of Science

© Yun Yu (Joseph) Han 2012

SIMON FRASER UNIVERSITY

Fall 2012

All rights reserved.

However, in accordance with the *Copyright Act of Canada*, this work may be reproduced, without authorization, under the conditions for "Fair Dealing." Therefore, limited reproduction of this work for the purposes of private study, research, criticism, review and news reporting is likely to be in accordance with the law, particularly if cited appropriately.

Approval

Name: Yun Yu (Joseph) Han

Degree: Doctor of Philosophy

Title of Thesis: *The Effects of Additives on the Nucleation and Growth Kinetics of Electrodeposited Copper Nanostructures and Thin Films*

Examining Committee:

Chair: Dr. Robert A. Britton, Associate Professor, Graduate Chair

Dr. Gary W. Leach

Associate Professor
Senior Supervisor

Dr. Michael H. Eikerling

Professor
Committee member

Dr. Zuo-Guang Ye

Professor
Committee member

Dr. Steven Holdcroft

Department of Chemistry, Professor
Internal Examiner

Alexandre Brolo

Associate Professor, Department of Chemistry
University of Victoria
External Examiner

Date Defended/Approved: December 6, 2012

Partial Copyright Licence



The author, whose copyright is declared on the title page of this work, has granted to Simon Fraser University the right to lend this thesis, project or extended essay to users of the Simon Fraser University Library, and to make partial or single copies only for such users or in response to a request from the library of any other university, or other educational institution, on its own behalf or for one of its users.

The author has further granted permission to Simon Fraser University to keep or make a digital copy for use in its circulating collection (currently available to the public at the "Institutional Repository" link of the SFU Library website (www.lib.sfu.ca) at <http://summit/sfu.ca> and, without changing the content, to translate the thesis/project or extended essays, if technically possible, to any medium or format for the purpose of preservation of the digital work.

The author has further agreed that permission for multiple copying of this work for scholarly purposes may be granted by either the author or the Dean of Graduate Studies.

It is understood that copying or publication of this work for financial gain shall not be allowed without the author's written permission.

Permission for public performance, or limited permission for private scholarly use, of any multimedia materials forming part of this work, may have been granted by the author. This information may be found on the separately catalogued multimedia material and in the signed Partial Copyright Licence.

While licensing SFU to permit the above uses, the author retains copyright in the thesis, project or extended essays, including the right to change the work for subsequent purposes, including editing and publishing the work in whole or in part, and licensing other parties, as the author may desire.

The original Partial Copyright Licence attesting to these terms, and signed by this author, may be found in the original bound copy of this work, retained in the Simon Fraser University Archive.

Simon Fraser University Library
Burnaby, British Columbia, Canada

Abstract

The effects of additives on copper electrodeposition processes have been investigated with electrochemical methods, atomic scale imaging techniques, surface nonlinear optical spectroscopy, and by molecular dynamics simulations.

Linear potential sweep voltammograms (LPSV) and cyclic voltammograms (CV) of additive-free CuSO_4 solutions, and with addition of 1-propanol or malachite green (MG) to the electrolyte were measured on Au electrodes. Addition of 1.0 M 1-propanol to the electrolyte resulted in a pronounced decrease of the cathodic peak current. In contrast, much smaller concentrations of the additive malachite green displayed dramatic effects on the electrochemistry. Addition of 0.0050 M MG to the electrolyte drove cathodic peak potential more negative by 200 mV. In both cases, blocking effects of the additives were identified, but complexes between the additive molecules and copper ions were not detected.

The morphologies of electrodeposited Cu films on Au thin film electrodes (TFE) were investigated by means of atomic force microscopy (AFM) and scanning electron microscopy (SEM). The copper grain sizes and film roughness were decreased by 1-propanol and MG; the shapes of the electrodeposited particles were altered from non-regular grains formed in additive-free solution to trigonal pyramids formed in solutions containing 1-propanol, and square pyramids from solutions containing MG. X-ray diffraction (XRD) analysis indicated that the formation of preferential shaped Cu grains may be due to the “selective” adsorption of additive molecules onto specific crystalline facets.

In situ electrochemical scanning tunneling microscopy (EC-STM) was employed to monitor copper nucleation and initial growth on Au (111) and on highly oriented pyrolytic graphite (HOPG) electrodes from CuSO_4 solutions with and without additives. The *in situ* EC-STM images provided visual information of

nucleation and initial growth of Cu electrodeposition. It was revealed that additives (particularly MG) significantly altered the nucleation and growth characteristics of Cu, resulting in nucleation and growth along terrace edges. The initial growth was changed from 3-dimensional in additive-free electrolyte to 2-dimensional in electrolytes containing MG.

The effects of MG on copper electrodeposition have also been investigated by the surface sensitive nonlinear optical spectroscopy, second harmonic generation (SHG). The rotational anisotropy of Cu(111) and Cu(100) was detected; SHG response to incident light polarization on interfaces of Cu(111)/MG(aq) and Cu(100)/MG(aq) were also obtained and indicated sensitivity to the organic additive. Fitting the polarization-resolved SHG data provided information regarding the averaged orientation of the additive MG on the Cu surfaces. Further understanding of the effects of MG on copper electrodeposition was provided by molecular dynamics simulations. The adsorption of MG on crystal facets were simulated using Materials Studio software. The results indicate that both neutral MG molecules and their positive ions prefer the (111) plane to (100) facets of Cu. Both the SHG experiments and computational simulation results suggest that MG interacts preferentially with the Cu(111) surface, resulting in faster Cu growth kinetics on the Cu(100) facet.

Keywords: copper; electrodeposition; malachite green; second harmonic generation; atomic force microscopy; scanning tunneling microscopy.

Dedication

This thesis is dedicated to my wife who has always given me support and encouraged me throughout my studies.

Acknowledgements

My heartily thankfulness goes to my senior supervisor, Dr. Gary W. Leach, for his help and advice throughout the project. I have always appreciated his teaching, advice and valuable guidance during my graduate program. I would also like to thank my supervisory committee members, Dr. Michael H. Eikerling and Dr. Zuo-Guang Ye, for all of their assistance and helpful discussions. I wish to acknowledge Dr. Steven Holdcroft for generous help. I would like to give thanks to Dr. Hogan Yu and his group members for allowing equipment and their assistance. I want to thank Dr. Jean Claude Brodovitch for valuable suggestions and encouragements. I also want to thank Li Yang for SEM assistance and Swati Vartak for assistance computation.

I would like to express my gratitude to my friends and my colleagues who have supported me during my studies at SFU. My sincere thanks go to the members of our group, Dr. Tom Johansson, Dr. Greg Cetnarowski, Dr. Jusroop Mattu, Dr. Claire McCague, and Dr. Tianhong Xu, Dr. Tarak Burai and Anna Katharina Schiffer, from whom I have had helpful discussions during my experiments.

I would also like to thank Simon Fraser University, 4D Labs and the Natural Sciences and Engineering Research Council for their financial support.

Table of Contents

Approval.....	ii
Abstract.....	iii
Dedication.....	v
Acknowledgements.....	vi
Table of Contents.....	vii
List of Tables.....	x
List of Figures.....	xi
Glossary.....	xvii

Chapter 1. Introduction	1
1.1. History of Copper.....	1
1.2. Copper Electrodeposition	2

Chapter 2. Effects of Additives on Electrochemical Processes.....	9
2.1. Fundamentals of Electrochemistry.....	9
2.1.1. Metal and Electrolyte Solution Interface	9
2.1.2. Electrodeposition.....	14
2.2. Additives for Electrodeposition.....	15
2.2.1. Functions of Additives for Electrodeposition	16
2.2.2. Additives for Copper Electrodeposition.....	17
2.3. Experimental	19
2.3.1. Electrochemical Cell.....	19
2.3.2. Electrochemical Techniques.....	21
2.4. Effect of Additives on the Electrochemical Process of Cu Deposition	22
2.4.1. Cyclic Voltammetry of CuSO_4 Solutions	22
2.4.2. Voltammograms of Blank Solutions.....	26
2.4.2.1. LPSV of 1-Propanol.....	26
2.4.2.2. LPSV of Malachite Green	28
2.4.2.3. CV of Malachite Green	31
2.4.3. Voltammograms of CuSO_4 Solutions.....	34
2.4.3.1. Effect of Alcohols on the CV of CuSO_4	34
2.4.3.2. Effect of 1-Propanol on the LPSV and CV of CuSO_4	36
2.4.3.3. The Effect of Malachite Green on the LPSV and CV of CuSO_4	42
2.5. Conclusions.....	49

Chapter 3. The Effect of Additives on the Morphologies of Electrodeposited Copper Films	52
3.1. Techniques for Probing Thin Films	52
3.1.1. Atomic Force Microscopy	52
3.1.1.1. AFM Tips and Cantilevers.....	53
3.1.1.2. AFM Instrumentation	54
3.1.1.3. Forces and Imaging Methods	56
3.1.2. Scanning Electron Microscopy	59
3.1.3. X-ray Diffraction (XRD).....	61

3.1.3.1.	X-ray Diffractometer.....	61
3.1.3.2.	Bragg's Law.....	63
3.2.	Experimental	65
3.2.1.	Preparation of Sample.....	65
3.2.2.	Measurement of Sample	67
3.3.	The Effects of Additives on the Properties of Cu Films	68
3.3.1.	Morphologies of Copper Thin Films.....	68
3.3.1.1.	AFM Images	68
3.3.1.1.1.	Crystallite Dependence on MG Concentration	71
3.3.1.1.2.	Crystallite Dependence on Electrodeposition Potential	73
3.3.1.1.3.	Crystallite Dependence on Copper Film Thickness	74
3.3.1.2.	Scanning Electron Microscopy Images	76
3.3.2.	Roughness.....	78
3.3.3.	Grain Analysis	83
3.3.4.	Film Crystallinity	85
3.4.	Conclusion.....	89

Chapter 4.	Electrochemical-Scanning Tunneling Microscopy (EC-STM) of Cu	
	Electrodeposition	92
4.1.	Scanning Tunneling Microscopy (STM)	92
4.1.1.	Electron Tunneling in STM	93
4.1.2.	Instrumentation	95
4.1.3.	Modes of STM.....	97
4.2.	<i>In situ</i> EC-STM	100
4.3.	Experiment.....	101
4.3.1.	Sample Treatment.....	102
4.3.2.	Tip Preparation.....	103
4.3.3.	Cell Construction.....	106
4.3.4.	In Situ EC-STM Measurements.....	107
4.4.	Initial Stages of Cu Electrodeposition Imaged by <i>in Situ</i> EC-STM.....	109
4.4.1.	Cu Electrodeposition On Au(111)	109
4.4.1.1.	Effect of Additives	117
4.4.2.	Cu Electrodeposition on HOPG.....	121
4.4.2.1.	STM of HOPG	122
4.4.2.2.	Effect of Additives on Cu Electrodeposition on HOPG	123
4.5.	Characteristics of (111) and (100) Surfaces and Effect of Additives on Cu Electrodeposition	128
4.5.1.	Packing of (111) and (100) Surface of Au and Cu	128
4.5.2.	Electronic and Energetic Properties of (111) and (100) Surfaces of Cu and Au.....	129
4.6.	Cu Nanoparticle Arrays.....	133
4.6.1.	Making Cu Nanoparticle Arrays.....	134
4.6.2.	AFM images of Cu Nanoparticle Arrays.....	136
4.6.3.	Applications of nanoscale electrode arrays	138
4.7.	Conclusions.....	139

Chapter 5. Second Harmonic Generation Investigation of MG adsorption at Cu(111)/H₂O and Cu(100)/H₂O Interfaces	141
5.1. Optical Second Harmonic Generation.....	141
5.2. SHG Experiment.....	145
5.3. Results and Discussion	146
5.3.1. SHG Rotational Anisotropy of Cu(111) and Cu(100)	146
5.3.2. SHG of Cu(100) and Cu(111) in MG Solution.....	152
5.3.3. Potential Effect on SHG of Cu/MG(aq) Interface	159
5.4. Orientation of MG on Cu.....	160
5.4.1.1. SHG Data Fitting	160
5.5. Conclusion.....	164
Chapter 6. Computational Analysis of Effect of Additives on Cu Electrodeposition	167
6.1. Molecular Dynamic Simulations.....	167
6.2. Optimal Geometry of Additives	169
6.3. Adsorption of Additives on Au, Cu and HOPG	171
6.3.1. Adsorption of MG on Au	173
6.3.2. Adsorption Energies of MG on Cu.....	176
6.3.3. Adsorption of MG on HOPG	179
6.3.4. Adsorption of 1-Propanol on Substrates	182
6.4. MG Molecular Orientation Simulation	184
6.5. Conclusion.....	187
Chapter 7. Summary, Conclusions and Future Work.....	189
7.1. Summary and Conclusions.....	189
7.2. Future Work.....	194
References.....	196
Appendices.....	208
Appendix A. Refining SPM Images.....	209
Appendix B. Laser System for SHG Experiment.....	211
Appendix C. Adsorption Locator, Material Studio.....	212

List of Tables

Table 1. The Impact of Scan Rate on CV Peak Potentials and Currents of 0.050 M CuSO ₄ on Au Electrode.	24
Table 2. Changes of Peak Potentials and Currents from Cyclic Voltammograms Scanned at 20 mV/s on Au Electrode with various Concentrations of CuSO ₄	24
Table 3. Effect of MG on copper ions' reduction parameters from CV curves	48
Table 4. Electrodeposition potentials $E_p^{c_{1/2}}$ and currents $j_p^{c_{1/2}}$ for different electrolyte solutions	66
Table 5. The area standard roughness parameters of Cu films of 200 nm. AFM Image is 5x5 μm with resolution of 200 pixels.....	80
Table 6. The line standard roughness parameters of Cu films of 210 nm. AFM Image is 10 x 10 μm with resolution of 200 pixels.....	83
Table 7. Grain parameter of 5 x 5 μm AFM images of 200 nm thick Cu film on Au-TFE electrodeposited from different solutions.....	85
Table 8. Relative intensities (%) of preferred XRD orientation in Cu films from additive-free CuSO ₄ , with 1-propanol or MG solutions.	88
Table 9. Work function and surface energy values for Au(111), Au(100), Cu(111) and Cu(100).....	130
Table 10. SHG data fitting results of copper in 10 ⁻⁴ M MG solution. Susceptibility components unit: 10 ⁻⁸ a.u.....	163
Table 11. A typical energy output: adsorption of MG ⁺ on two-layer Au(111) with surface charge density of -0.03 electron/atom. Energy unit is kJ/mol.	172
Table 12. Adsorption energies of MG and MG ⁺ on Au(111) and Au(100) surfaces. Energy unit is kJ/mol and surface charge density electron/atom.	173
Table 13. Adsorption energies of MG and MG ⁺ on Cu(111) and Cu(100) surfaces. Energy unit is kJ/mol and surface charge density electron/atom.....	177
Table 14. Adsorption energies of MG and MG ⁺ on HOPG(111) and HOPG(100) surfaces. Energy unit is kJ/mol and surface charge density electron/atom.....	180
Table 15. Adsorption energies of 1-propanol on Au(111) and Au(100) surfaces. Energy unit is kJ/mol and surface charge density electron/atom.	182
Table 16. Molecular dynamic simulation of MG orientation on copper substrate. "- " stands for negatively charged substrate.	185

List of Figures

Figure 1. An ankh, the Egyptian copper symbol.	2
Figure 2. IBM CMOS with six levels of copper interconnections.	4
Figure 3. Schematic model of the electrical double layer at the interface between uncharged metal and solution. IHP refers to inner Helmholtz plane; OHP outer Helmholtz plane; Charge transfer process 1 represents an ion diffusing to the surface and accepting an electron; 2 represents an electron transfer to an oxidized species in the diffuse layer. Please note the difference in orientation of water molecules around anions compared to the cations.....	11
Figure 4. Cyclic Voltammograms of 0.050 M CuSO ₄ on Au and Pt electrodes at scan rate of 20 mV/s. Peak parameters are marked for Au.....	23
Figure 5. Effect of 1-propanol on the linear potential sweep voltammograms for the hydrogen evolution reduction on Au electrode from water solution. Scan rate: 20mV/s; Concentration of 1-propanol: 0~1.70M.....	27
Figure 6. Effect of malachite green on the linear potential sweep voltammograms for the hydrogen evolution on Au from water solution. Scan rate: 20 mV/s; Concentration of malachite green: 0 M to 0.0050 M. Inset: the equivalent experiment with the same concentration range of NaCl.	29
Figure 7. Influence of malachite green on the hydrogen evolution potentials. Reference cathodic current density is 1.0 mA•cm ⁻² at which the potentials are taken from LPSV. A trend line is added to guide the eye.	31
Figure 8. Cyclic Voltammogram of 0.0050 M Malachite Green on Au electrode at 20 mV/s.	33
Figure 9. Change of cathodic peak potentials and currents of CV on Au with increasing concentration of MG. Scan rate is 20 mV/s.....	33
Figure 10. Transformation between malachite green and leuco-malachite green at the surface of the cathodic Au electrode.	34
Figure 11. Effect of carbon numbers in alcohol molecules on peak currents and potentials of CV of 0.050 M CuSO ₄ on Au electrode. Alcohols' concentrations are all 0.20 M. Scan rate is 20 mV/s. Data series color matches the colors of the axes' titles. Dashed trend lines are shown to guide the eye.	35
Figure 12. Linear potential sweep voltammograms of 0.050 M CuSO ₄ on Au electrode with various amount of 1-propanol at a potential scan rate of 20 mV/s.	37
Figure 13. Effect of 1-propanol on cyclic voltammograms of 0.050 M CuSO ₄ on Au electrode. Scan rate is 20 mV/s.....	38
Figure 14. The changes of peak characteristics of LPSV and CV of 0.050 M CuSO ₄ measured at the Au surface with a potential scan rate of 20	

mV/s. With increasing 1-propanol concentrations: (a) Cathodic and anodic peak currents decrease. (b) Peak potentials move to high energy. (c) The differences between anodic current and cathodic current become smaller. and (d) The separations of redox peak potentials increases.	39
Figure 15. A schematic diagram of hydrogen bonding between 1-propanol and aqueous copper ion.	42
Figure 16. Effect of MG on LPSV of 0.050 M CuSO ₄ on Au surface at a scan rate of 50 mV/s. The arrow lines indicate the slopes of cathodic sweep.	43
Figure 17. Cyclic voltammetry of 0.050 M CuSO ₄ with different concentration of malachite green on the Au electrode. Scan rate: 50 mV/s. E _x : crossover potential; E _n : nucleation potential. Blue arrowed lines indicate the anodic sweep slopes.	45
Figure 18. CV of 0.050 M CuSO ₄ with different concentration of MG on the Au electrode. Supporting electrolyte is 0.50 M Na ₂ SO ₄ . Scan rate: 50 mV/s.	46
Figure 19. SEM image of triangular/V-shaped SPM cantilever with zoom-in probe.	54
Figure 20. Schematic of AFM instrument showing “beam bounce” method of detection using a laser and position sensitive photodiode detector.	55
Figure 21. Plot of potential/force as a function of probe-sample separation. The insets represent the tip deflections at different working modes. Contact mode operates in the repulsive force regime; and non-contact mode operates in the attractive force regime.	57
Figure 22. SEM diagram with major parts' geometry	60
Figure 23. Schematic of X-Ray Diffractometer.....	62
Figure 24. The diagram of X-ray diffraction and geometry for deriving Bragg's Law.....	64
Figure 25. Current-time characteristic of copper electrodeposition from 0.050 M CuSO ₄ and 0.0050 M MG solution at -500 mV.....	67
Figure 26. AFM topographic images with 3D view of electrodeposited copper films on Au-TFE electrodes from 0.050 M CuSO ₄ solution. Electrodeposition time: 5 minutes; film thickness: 220 ± 20 nm.....	69
Figure 27. AFM topographic images with 3D view of electrodeposited copper films on Au-TFE electrodes from 0.050 M CuSO ₄ + 1.0 M 1-propanol solution. Electrodeposition time: 5 minutes; film thickness: 220 ± 20 nm.	70
Figure 28. AFM topographic images with 3D view of electrodeposited copper films on Au-TFE electrodes from 0.050 M CuSO ₄ + 0.0050 M MG solution. Electrodeposition time: 5 minutes; film thickness: 220 ± 20 nm.	70

Figure 29. Topographic images of Cu films from 0.050 M CuSO ₄ with different concentrations of MG. [MG] and depositing potentials are: a. 0.00010 M and -310 mV; b. 0.00050 M and -380 mV; c. 0.0010 M and -440 mV; d. 0.0050 M and -500 mV. Electrodeposition times are all 5 minutes.	72
Figure 30. Topographic images of Cu thin films from 0.050 M CuSO ₄ + 0.0050 M MG solution for 5 minutes at different electrodeposition potentials: a. -300 mV; b. -400 mV, c. -500 mV and d. -600 mV.	73
Figure 31. AFM topographic images of different thickness of Cu films from 0.050 M CuSO ₄ + 0.0050 M MG solution. Thickness of Cu films are: a. 200 nm ; b. 1600 nm; c. 6400 nm; and d. 12800 nm.	75
Figure 32. SEM images of electrodeposited Cu films from different electrolyte solutions. a. 0.050 M CuSO ₄ , b. 0.050 M CuSO ₄ + 1.0 M 1-propanol, and c. 0.050 M CuSO ₄ + 0.0050 M MG. The Cu films are 1.3 ± 0.1 μm. Tilt angles for a. b. and c are 0°. d. a zoom-in view for c at a tilt angle of 45°	77
Figure 33. Area roughness changes with electrodeposition time of Cu film on Au-TFE from 0.050 M CuSO ₄ + 0.0050 M MG.	80
Figure 34. Linear profile of AFM images of Cu films from different solutions. a. 0.050 M CuSO ₄ ; b. 0.050 M CuSO ₄ + 1.0 M 1-propanol; c. 0.050 M CuSO ₄ + 0.0050 M MG.	81
Figure 35. X-ray diffraction patterns of electrodeposited 200 nm thick Cu films on Au-TFE from 0.050 M CuSO ₄ . Cu films from solutions with 1-propanol and MG have similar diffraction patterns but the relative and absolute intensities are modified by the additives.	86
Figure 36. X-ray diffraction of 200 nm thick Cu films electrodeposited from 0.050 M CuSO ₄ with additives and additive-free solutions. Cu films from solutions containing 1-propanol or MG have lower intensities.	87
Figure 37. Schematic diagram of Cu square pyramid from CuSO ₄ with MG solution. A comparison of AFM image (left) with growing model (right).	90
Figure 38. Schematic of electron tunneling in STM. E _f is the Fermi energy, φ _s the work function of sample, and E _v the electron energy under application of a bias voltage V.	93
Figure 39. Schematic of a scanning tunneling microscopy	96
Figure 40. Comparison of constant-height (a) and constant-current (b) modes of STM operation.	97
Figure 41. Schematic of an in situ scanning tunneling microscopy.	99
Figure 42. Schematic for EC-STM tip coating.	104
Figure 43. Diagram of components and construction of the EC-STM cell.	106
Figure 44. STM of flaming annealed Au(111) surface with terraces and linear analysis. The step height 0.21 nm indicates mono atomic layer.	110

- Figure 45. *In situ* EC-STM images of Cu electrodeposition at -200 mV (vs. Pt) on Au(111) surface from 0.050 M CuSO₄ solution. Scan setting: PID = (2.0, 1.0, 1.0); scan rate 10 Hz, I_t = 1 nA and E_t = 100 mV. a. before electrodeposition, z = 0.87 nm. b. t_d = 11 min, z = 0.85 nm. c. t_d = 34 min, z = 1.02 nm. d. t_d = 100 min, z = 1.17 nm. 111
- Figure 46. *In situ* EC-STM images of Cu dissolving at 0 mV (vs. Pt) on Au(111) surface in 0.050 M CuSO₄ solution. Scan settings: PID = (2.0, 1.0, 1.0); scan rate 10 Hz, I_t = 1 nA and E_t = 100 mV. a. newly deposited Cu grains. b. t_s = 2 min. c. t_s = 4 min. d. t_s = 6 min. 112
- Figure 47. A 3-dimensional view of *in situ* EC-STM images of Cu electrodeposition at -300 mV (vs. Pt) on Au(111) surface from 0.050 M CuSO₄ solution. Scan settings: PID = (2.0, 1.0, 1.0); scan rate 10 Hz, I_t = 1 nA and E_t = 100 mV, t_d = 3 min. The linear analysis shows the deposited Cu islands are up to 2.0 nm high and 3.0 nm wide. 114
- Figure 48. *In situ* EC-STM images of Cu deposition at 100 mV (vs. Ag|AgCl) and dissolution at 500 mV, on the Au(111) surface in 0.050 M CuSO₄ solution. Scan settings: PID = (2.0, 1.0, 0.0); scan rate 7 Hz, I_t = 1 nA and E_t = 100 mV. a. Initial image before deposition. b. t_d = 4 min. c. t_d = 8 min. d. E_s = 500 mV, t_s = 1 min. 115
- Figure 49. *In situ* EC-STM images of Cu deposition at 100 mV (vs. Ag|AgCl) on the Au(111) surface in 0.050 M CuSO₄ solution. Scan settings: PID = (2.0, 1.0, 0.0); scan rate 7 Hz, I_t = 1 nA and E_t = 100 mV. a. t_d = 10 min. b. a close look at the selected area. 116
- Figure 50. *In situ* EC-STM images of Cu depositing on Au(111) surface in 0.050 M CuSO₄ + 1.0 M 1-propanol solution, by potential step. Scan settings: PID = (2.0, 1.0, 0.0); scan rate 6 Hz, I_t = 2 nA and E_t = 100 mV. a. E_i = 300 mV (vs. Ag|AgCl, the same for following), no deposition. b. E_d = 150 mV, t_d = 4 min. c. E_d = 140 mV, t_d = 4 min. d. E_d = 130 mV, t_d = 4 min. 118
- Figure 51. *In situ* EC-STM images of Cu deposition on the Au(111) surface in 0.050 M CuSO₄ + 0.0050 M MG solution, by potential step. Scan settings: PID = (1.0, 1.0, 0.0); scan rate 8 Hz, I_t = 1 nA and E_t = 200 mV. a. E_i = 200 mV (vs. Ag|AgCl), no deposition. b. E_d = 90 mV, t_d = 4 min. c. E_d = 70 mV, t_d = 4 min. d. E_d = 50 mV, t_d = 4 min. 120
- Figure 52. STM images of HOPG obtained in 0.050 M CuSO₄ solution. The bottom line profile shows that the step height is 0.35 nm. 122
- Figure 53. *In situ* EC-STM topographic images of Cu electrodeposition on HOPG at -100 mV from 0.050 M CuSO₄ solution. Scan settings: PID = (2.0, 1.0, 0.0), E_t = 200 mV, and scan rate is 6 Hz. a. I_t = 6 nA, t_d = 0 min. b. I_t = 6 nA, t_d = 2 min. c. I_t = 9 nA, t_d = 4 min. d. I_t = 9 nA, t_d = 6 min. 124
- Figure 54. *In situ* EC-STM topographic images of Cu electrodeposition on HOPG from 0.050 M CuSO₄ + 1.0 M 1-propanol solution by potential step. Scan settings: PID = (2.0, 1.0, 0.0), I_t = 2 nA, E_t = 100 mV, scan rate is 6 Hz, and area is 1000 x 1000 nm. a. E_i = 300 mV. b. E_d = 200 mV, t_d = 2 min. c. E_d = 100 mV, t_d = 2 min. d. E_d = 0 mV, t_d = 2 min. 125

Figure 55. <i>In situ</i> EC-STM topographic images of Cu electrodeposition on HOPG from 0.050 M CuSO ₄ + 0.0050 M MG solution by potential step. Scan settings: PID = (2.0, 1.0, 0.0), and scan rate is 10 Hz. a. I _t = 1 nA, E _t = 100 mV, E _d = 100 mV. b. I _t = 6 nA, E _t = 500 mV, E _d = -240 mV, t _d = 2 min. c and d: I _t = 6 nA, E _t = 600 mV, E _d = -250 mV. c. t _d = 2 min. d. t _d = 4 min.	127
Figure 56. Schematic diagram of Cu(111) and Cu(100) surfaces with unit cell, lattice size, coordination and adsorption sites.	129
Figure 57. Designed experiment of Cu nanometer square pyramidal array formed by electrodeposition on Au microelectrode from CuSO ₄ electrolyte solution with MG.	134
Figure 58. AFM image of electrodeposition produced copper nanoparticle arrays. 5x5 μm.....	135
Figure 59. AFM images showing formation of copper nanoparticle arrays. a. before electrodeposition, b. electrodeposition 280 s at -500 mV and c. 420 s.....	137
Figure 60. Schematic diagram of surface SHG from Cu/air interface.....	143
Figure 61. Schematic setup for SHG measurement with potential control system.	145
Figure 62. SHG rotational anisotropy of copper single crystal. a. Cu(111)/air interface, PS (P _{in} -S _{out}) polarization. b. Cu(100)/air interface, SP (S _{in} -P _{out}) polarization. The points indicate the experimental data and the solid lines the fitted data.	149
Figure 63. Comparison of SHG polarization spectroscopy of copper single crystal. a. Cu(111)/air interface, P _{out} polarization to incident HWP. b. Cu(100)/air interface, S _{out} polarization to incident HWP. The points indicate the experimental data and the solid lines are for eye guide.	150
Figure 64. Comparison of SHG polarization spectroscopy of Cu(111) and Cu(100) in water and in 10 ⁻⁴ M MG solution. a. Cu(111), P _{out} polarization to incident HWP. b. Cu(100), P _{out} polarization to incident HWP angle. The points indicate the experimental data and the solid lines the fitted data.....	153
Figure 65. Comparison of SHG polarization spectroscopy of Cu(111) and Cu(100) in 10 ⁻⁴ M MG solution. a. P _{out} polarization to incident HWP angle. b. S _{out} polarization to incident HWP. The points indicate the experimental data and the solid lines the fitted data.....	154
Figure 66. Isotherms of Pin-Pout polarized square root SHG of (a) Cu(111)/MG(aq) and (b) Cu(100)/MG(aq) versus MG concentration. Insets present the enormous increase with 10 ⁻³ M MG.	158
Figure 67. Potential effect on SHG response from Cu in 10 ⁻⁴ M MG solution. a. Cu(111)/MG(aq). b. Cu(100)/MG(aq).	160
Figure 68. Schematic of the definitions of the orientation angles θ, δ and φ, defining the molecular orientation with respect to the surface. The	

molecular coordinate system X'Y'Z' describing MG ⁺ orientation was also shown.....	162
Figure 69. Geometric structure of ionized malachite green.....	170
Figure 70. Geometric structure of 1-propanol.	170
Figure 71. The most suitable configuration for adsorption of MG ⁺ on two-layer negatively charged Au (111) substrate obtained by Adsorption Locator module.....	174
Figure 72. The most suitable configuration for adsorption of MG ⁺ on two-layer negatively charged Cu (111) substrate obtained using Adsorption Locator module.	177
Figure 73. Model of Cu nucleation along existing terraces in the presence of additive MG in electrolyte solution.	178
Figure 74. Model of the formation of a Cu square pyramid from the electrolyte with additive MG.	179
Figure 75. The most suitable configuration for adsorption of MG ⁺ on negatively charged one-layer HOPG (111) substrate obtained using Adsorption Locator module. A and B refer to different types of carbon atoms on the surface.....	180
Figure 76. The most suitable configuration for adsorption of 1-propanol on two-layer Au (111) with surface charge density -0.03 electron/atom, obtained by Adsorption Locator of Materials Studio.	183
Figure 77. Simulating result of MG ⁺ orientation on cathodic Cu(100) substrate.	185

Glossary

2D	2 dimension
2θ	Polarization angle
3D	3 dimension
<i>a.u.</i>	Arbitrary unit
A_0	Total area of electrode;
AC	Alternating current
<i>ads</i>	Adsorbed species
A_{eff}	Effective area of electrode
AFM	Atomic force microscopy
<i>aq</i>	Aquated species
Au-mica	Gold thin films on mica
Au-TFE	Gold thin film electrode
BTA	Benzotriazole
CdA	Cadmium arachidate
CE	Counter electrode
CFM	Chemical force microscopy
COMPASS	Condensed-phase optimized molecular potentials for atomistic simulation studies
C_{Ox}	Concentrations of the oxidized species
C_{Red}	Concentrations of the reduced species
CV	Cyclic voltammograms
CVFF	Consistent valence forcefield
<i>D</i>	Debye, dipole moment unit
<i>d</i>	Interlayer spacing of the layers
D_0	Diffusion constant
DFT	Density functional theory
D_g	Density of grains.
D_{max}	Maximum diagonal
<i>E</i>	Potential; energy

e^-	Negative electron
$\vec{E}^{(2)}$	Electric field component
E^0	Standard electrode potential
E_{ad}	Adsorption energy
E_b	Potential energy barrier
E_{ba}	Energy of deformation
E_{cell}	Cell voltage
EC-STM	Electrochemical scanning tunneling microscopy
E_d	Depositing potential
EDL	Electrical double layer
E^{eq}	Equilibrium potential
E_f	Fermi energy
E_i	Initial potential
E_n	Nucleation potential; electron energy
E_{nop}	Nucleation over potential
E_p	Peak potential
E_p^a	Anodic peak potential
E_p^c	Cathodic peak potential
$E_p^c \frac{1}{2}$	Cathodic half-wave potentials
E_q	Energy of electrostatic interactions
E_s	Dissolving potential
E_t	Tip bias
E_V	Electron energy under bias of V
eV	Electron volt
E_{vdW}	Energy of van der Waals
E_{vib}	Energy of couplings
E_x	Crossover potential
F	Faraday constant; force
FSI	Fluid-solid interface
GGA	Generalized gradient approximation
\hbar	Reduced Planck's constant

H_{avg}	Average height of grains.
H_{max}	Maximum height of grains.
HOPG	Highly oriented pyrolytic graphite
HO-R	Alcohols
<i>HWP</i>	Half wave plate
$I_{2\omega}$	SHG signal intensity
IHP	Inner Helmholtz plane
I_p	Peak current
I_p^a	Anodic peak current
I_p^c	Cathodic peak current
I_t	Tunneling current
I_ω	Intensity of incident light
j_{Cat}	Cathodic current density
JGB	Janus green b
j_p^a	Anodic peak current density
j_p^c	Cathodic peak current density
$j_p^c \frac{1}{2}$	Reduction half-wave current
k	Constant
\vec{k}_1	Wave vector
k_{Red}	Reduction constant
LMG	Leuco-malachite green
LPSV	Linear potential sweep voltammograms
<i>MFM</i>	Magnetic force microscopy
MG	Malachite green
MG ⁺	Malachite green cation
MPSA	Mercapto-1-propanesulfonate
<i>MS</i>	Materials Studio
n	An integer
OHP	Outer Helmholtz plane
Ox	Oxidized species
$\vec{p}^{(2)}$	Polarization

\vec{P}_0	Constant polarization
PCFF	Polymer consistent forcefield
PEG	Polyethylene glycols
PID	Proportional gain, integral gain, and derivative gain
PPG	Polypropylene glycols
\vec{P}_ω	Polarization at ω
R	Gas constant
r	Distance
\bar{r}	Average distance
R_a	Average roughness
RE	Reference electrode
<i>Red</i>	Reduced species
RMS	Root-mean-square roughness
R_p	Highest peak
R_p	Mean peak profile height
R_t	Maximum peak-to-valley height
R_{tm}	Mean peak-to-valley roughness
SEM	Scanning electron microscopy
SFG	Sum frequency generation
SHE	Standard hydrogen electrode
SHG	Second harmonic generation
SPM	Scanning probe microscope
SPS	Bis(sodiumsulfopropyl) disulfide
STM	Scanning tunneling microscopy
T	Absolute temperature
t_d	Electrodepositing time
TFE	Thin film electrode
t_s	Dissolving time
UPD	Under potential deposition
UV	Ultra violet

VASP	Vienna ab initio simulation package
V_{avg}	Average volume of grains.
VdW	Van der Waals
V_{is}	Visible
$W(Z)$	Probability of finding an electron
WE	Working electrodes
WSxM	Name of a free SPM software
x	Cantilever deflection
X	X axis
$x^{(2)}$	Bulk susceptibility
$x_{\text{eff}}^{(2)}$	Effective nonlinear susceptibility
XRD	X-ray diffraction
$x_s^{(2)}$	Second-order susceptibility
Y	Y axis
Z	Z axis
z'	Molecular axis
\bar{z}	Average height
z''	Normal of bare benzene ring
Z_{max}	Maximum height
α	Charge transfer coefficient; angle of Z'' to Z
γ	Half wave plate angle
δ	Angle rotating around Z'
ΔE_p	Difference of peak potentials
ΔG	Change of Gibbs free energy
Δj_p	Difference of peak currents
η	Overpotential
θ	X-ray incident angle; angle of Z' to Z
λ	Wavelength
ν	Scan rates
ξ	Angle of x' to surface normal

π	Surface pressure
ρ	Surface tension
ρ_0	Surface tension of the clean surface
φ	Azimuthal angle
$X_{xzx}, X_{zxx}, X_{zzz}$	Components of susceptibility tensor
ψ	Polarization detection angle
$\psi(Z)$	Energy levels of electrons

Chapter 1. Introduction

Copper electrodeposition and the effects of electrolyte additives on the electrodeposition of copper are subjects of fundamental scientific interest as well as practical importance. It is expected that, while our research is focused on copper, the insights that are obtained from this work can be extended to other metals and electrodeposited films more generally. Nevertheless, why is copper special?

1.1. History of Copper

Among the most important metals, copper was the first used over 10 thousand years ago. It is estimated that copper was discovered as early as 8700 B. C. in the Middle East. The earliest copper smelting was dated back to about 4500 B.C.. Actually, copper is the oldest mined metal used by humans. And for nearly 5,000 years, copper was the only metal known to man.

Copper is named after the Island of Cyprus which was the principal supply source in the Roman area. The Egyptians used the ankh symbol (Figure 1) to denote copper in their system of hieroglyphs to express the importance of copper to life, because the symbol also represented eternal life to them[1]. Now we know

copper is an essential metal our body needs, and one of the most important in the human body.



Figure 1. An ankh, the Egyptian copper symbol.

Copper and its alloys, brass and bronze, were historically used in casting and piping, which illustrated its staying power because the very malleable copper is not as susceptible to corrosion as other metals. Unlike plastic, copper does not give off fumes, melt, or burn. In addition, copper has antibacterial properties that help to ward off microorganisms that may cause diseases. So today copper is not only still used for pipes, but also in many other fields, such as architecture, automotive, electrical, and marine and telecommunication applications.

1.2. Copper Electrodeposition

Copper is a chemical element with atomic number 29. On the modern periodic table, it is in Period 4 and Family IIB with a $3d^{10}4s^1$ electronic configuration. It is a transition metal with a melting point of $1083\text{ }^{\circ}\text{C}$ and a boiling point of $2567\text{ }^{\circ}\text{C}$, but found in nature mostly in impure mineral forms. To obtain pure copper,

smelting, leaching and electrolysis are required. Pure copper has a very high conductivity which leads to its wide use in modern industry and electronics.

Copper electrodeposition is the process of copper electroplating, in which Cu cations in a solution are moved by an electric field to coat an electrode. Copper electrodeposition is primarily used for depositing a layer of copper to bestow a desired property like corrosion protection and high conductivity to a surface that otherwise lacks these properties.

It is believed that Italian chemist, Luigi Brugnatelli, was the first person to apply the electrodeposition process to electroplate gold in 1800. By 1839, scientists had built up devices for copper electrodeposition. By 1840, electrodeposition was adapted and refined by Henry and George Elkington of Birmingham, England; later on, after more than a hundred years of development, electrodeposition technologies have been improved significantly. Recently, there has been renewed interest in electrodeposition of metals for the fabrication of integrated circuits, deposition of magnetic recording devices, deposition of multilayer structures, as well as the deposition of nanowires and other nanostructures. Electrodeposition of copper for integrated circuit fabrication has been successfully used since 1997 for the production of interconnection lines down to less than 20 nm width. Electrodeposition methods represent a very attractive alternative to conventional fabrication methods. Figure 2 shows an example of copper-based CMOS technology from IBM Corp. which has six levels of interconnections and has effective transistor channel-length of only 0.12 μm [2].

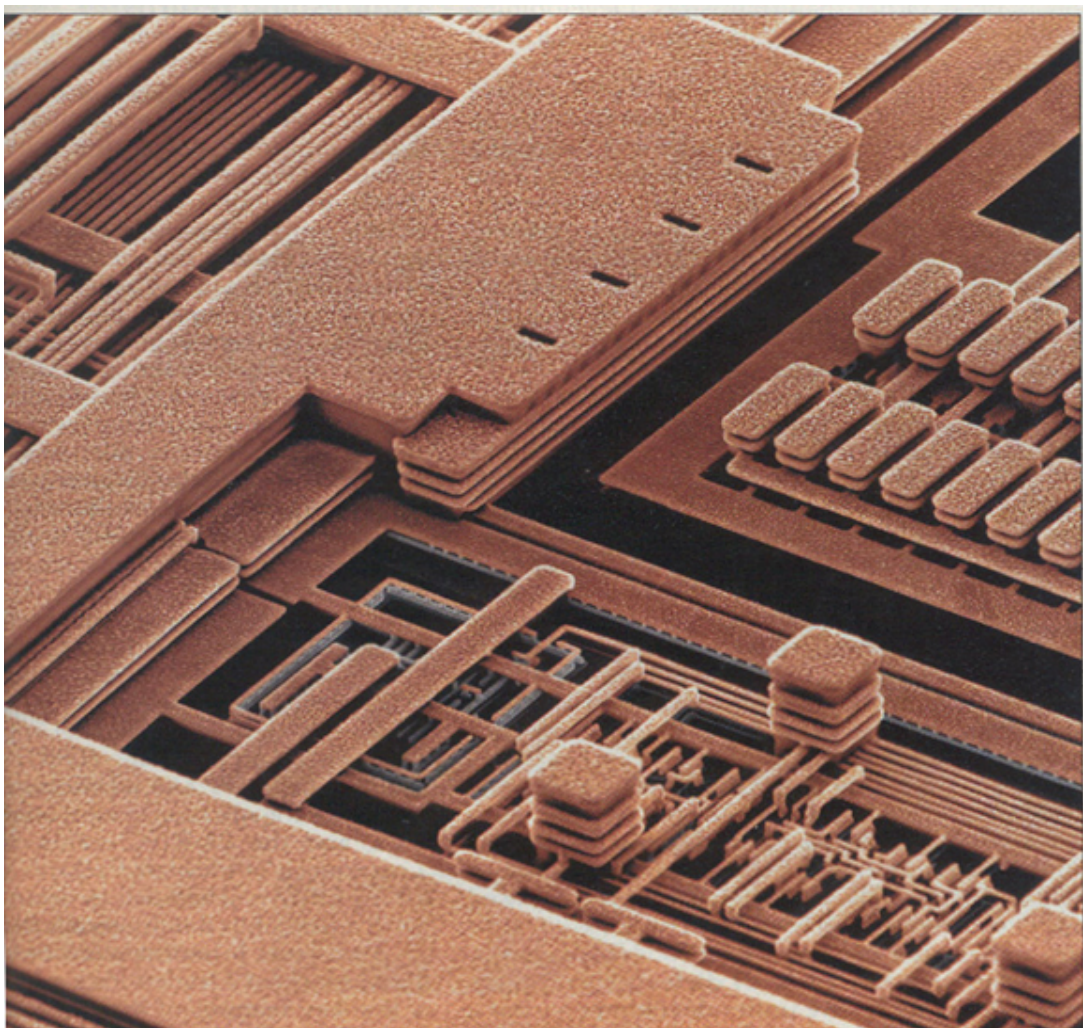


Figure 2. IBM CMOS with six levels of copper interconnections.

In 2000, new PowerPC chips with copper interconnect came into use, which made copper electrodeposition a crucial area of study. For deposited copper to be used as chip interconnects, it must be void free and trench free. Product quality is determined by the role of electrolyte additives at the molecular scale where they act to impart remarkable shape control and deposition properties.

The introduction of copper electrodeposition into chip interconnection technology as a replacement for aluminum has renewed the interests of scientists

in the mechanism of copper electrodeposition and the role of additives [3, 4]. Numerous research groups have studied the nucleation and growth of Cu deposits during electroplating with additives. By using suitable additives in the electrolyte solution, the rate of metal ion deposition onto selected gold film electrodes can be controlled and a variety of different sizes and shapes of nanostructured particles can be obtained, which have significant industrial potential in the areas of catalysis, chemical sensors and magnetic recording [5]. In order to get further insight into the correlations of nucleation, growth, changes of morphologies with simultaneous electrochemical phenomena, *in situ* scanning probe microscopy (SPM) has been widely used in the study of Cu electrodeposition [6-12]. Traditionally copper electrodeposits are gained from acid baths containing CuSO_4 and a certain concentration of organic or inorganic additives which enhances the quality of the deposit by forming smoother and shinier deposits than without additives. Many additives like polyethylene glycols (PEG), polypropylene glycols (PPG), and halogenide ions used alone or in a mixture have been studied to elucidate their effects on the nucleation, growth and properties of metal deposits. The additive molecules moderate the nucleation rate by sitting on the active sites of the substrate. This “blocking mechanism” has been widely discussed [13-18]. Not only experimental but also theoretical studies on the effect of additives on copper electrodeposition have been progressing. A suitable model system for the study of electrochemical nucleation and nuclei growth of Cu electro-crystallization on foreign substrates has been developed [19]. The studies indicate that the deposit quality of copper is determined by the role of additives at the molecular scale

where they bestow shape and morphology control of the deposit, but current knowledge of additive behavior is insufficient for future microelectronic process requirements. Rapid innovation of additive systems for copper electrodeposition is required for modern microelectronics [16, 20-23].

The goal of this thesis research is to investigate the role of additives in the electrochemical deposition process generally, and copper electrodeposition specifically. While many studies looking at the role of additives in electrodeposition describe the macroscopic results of additives, we seek a molecular level understanding of this process and try to make a connection between the characteristics of the additive molecules and the resulting electrodeposited films. We have employed a variety of chemically different additives and a wide range of characterization tools to investigate the resulting electrodeposited films. These methods include the use of modern *in situ* and *ex situ* microscopy techniques, x-ray diffraction methods, and surface sensitive nonlinear optical spectroscopies.

In the thesis, a variety of additives have been investigated in order to understand their effects on the electrochemical process of Cu reduction. The tested additives include alcohols (one to six carbons in the alkane group), citrate, rhodamine and malachite green (MG). The process of copper electrodeposition has been investigated by linear sweep and cyclic voltammetry techniques. Gold thin films on mica (Au-mica) are used as substrates for electrodeposition. 1-propanol is a very common medium size alcohol with excellent solubility in water. It is selected as a representative of alcohol additives. MG is an organic probe

molecule which provides a significant second harmonic generation (SHG) nonlinear optical response. Our research group has previously employed MG as an organic probe molecule for surface second harmonic generation (SHG) studies, where we have demonstrated the ability to measure with sub-monolayer sensitivity, the averaged orientations of MG molecules at the fused silica/air interface [24, 25]. The effects of 1-propanol and MG on morphologies, surface roughness, and grain size and the micro-crystallinity of electrodeposited Cu films are investigated. Atomic force microscopy (AFM), scanning electron microscopy (SEM) and X-ray diffraction (XRD) methods are employed to study the properties of the electrodeposited copper thin films. These measurements indicate that 1-propanol and MG have pronounced effects on the properties of Cu electrodeposition. Cu films with improved smoothness and regular texture were obtained with use of additives in electrolyte solutions. *In situ* electrochemical scanning tunneling microscopy (EC-STM) was used to monitor the initial stages of copper nucleation and electrodeposition on Au-mica and highly oriented pyrolytic graphite (HOPG) electrodes. The second harmonic generation (SHG) response from single crystals Cu(111), Cu(100) in air and in solution with different concentrations of MG were also measured. These experimental methods have allowed the development of a plausible model to explain the interactions between the organic additives and the single crystal and polycrystalline metal electrodes employed in these studies. The experimental measurements are supported with electronic structure calculations and molecular dynamics simulations. Taken together, the work provides a detailed understanding of the interactions between the organic additives and electrode

surfaces, the observed nucleation and growth kinetics of copper on single crystal surfaces, as well as the growth of preferentially shaped copper nanostructures, and offers a potential route to inexpensive, shape-controlled metal nanostructure fabrication.

Chapter 2. Effects of Additives on Electrochemical Processes

2.1. Fundamentals of Electrochemistry

Electrochemistry is regarded as a mature scientific discipline that examines chemical reactions which take place in a solution at the interface of an electron conductor (a metal or a semiconductor) and an ionic conductor (the electrolyte). The reactions always involve electron transfer between the electrode and the electrolyte or species in solution. The most common applied devices based on electrochemical technology are batteries which have been in widespread use by the general public throughout the twentieth century. With the development of fuel cells, rechargeable batteries and electrodeposition, products made by electrochemical techniques, such as computers and portable electronics, play a more important role in industry and daily life.

2.1.1. *Metal and Electrolyte Solution Interface*

Water is the most widely used solvent in chemistry. Because its molecules are polar, when an electrolyte is dissolved in water, the dipole strongly interacts with the ions, which helps in the dissolution process. When a metal electrode is inserted into the electrolyte solution, water molecules and ions move toward the

surface of the metal. The boundary between water molecules and solvated ions and the electrode surface forms the metal-solution interface [26].

Because water can react with some metals even at standard conditions, noble metals like gold and platinum are often used for electrochemical research. Although multi-crystalline metals are used, most structural investigations are performed at their single crystal surfaces. Under certain conditions, at the metal-solution interface, the famous electrical double layer (EDL) forms. Different models of EDL were developed by Helmholtz, Gouy-Chapman, Stern, or Grahame. Figure 3 is a diagram of the commonly-invoked EDL model at the metal-solution interface. This schematic shows the uncharged metal and solution interface. If the metal is negatively or positively charged by applying a potential, the EDL will be altered [27, 28]. This static and continuum model has been widely used for over one hundred years and forms the basis for our current understanding of the electrochemical interface. As our ability to characterize the metal electrolyte interface improves, so too will our understanding of complex interfacial electrochemical phenomena.

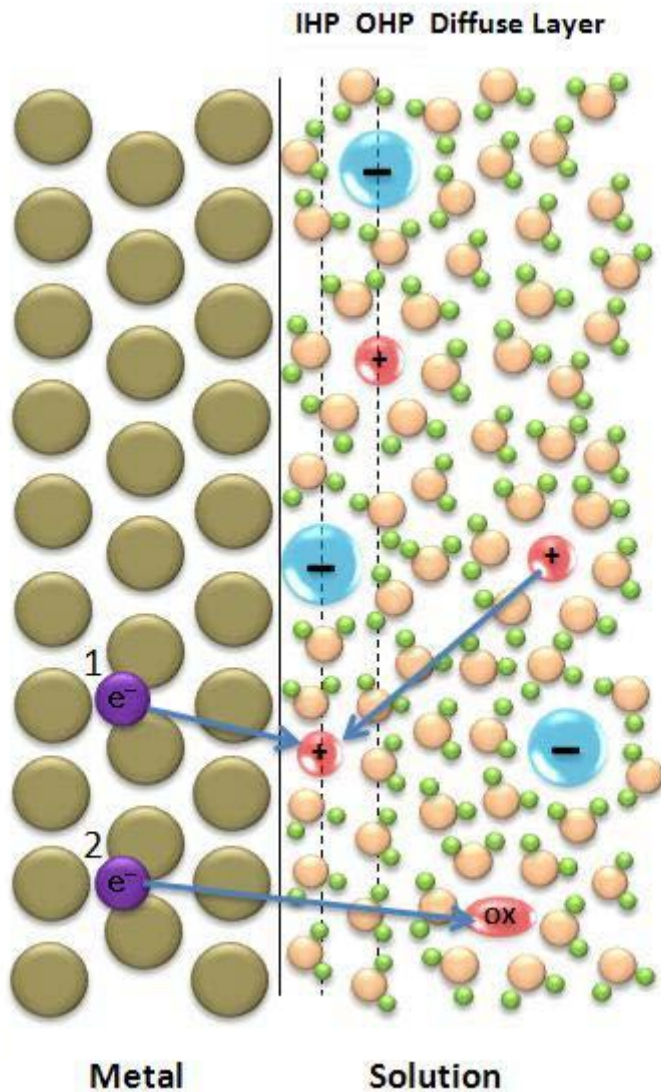


Figure 3. Schematic model of the electrical double layer at the interface between uncharged metal and solution. IHP refers to inner Helmholtz plane; OHP outer Helmholtz plane; Charge transfer process 1 represents an ion diffusing to the surface and accepting an electron; 2 represents an electron transfer to an oxidized species in the diffuse layer. Please note the difference in orientation of water molecules around anions compared to the cations.

Electrical double layers exist at all metal-solution interfaces, including those at which charge transfer is taking place. When charge transfer is allowed across a metal-solution interface and the system comes to equilibrium, the potential of the metal assumes a value characteristic of the system. A more reactive metal such as zinc imparts a more negative potential than a less reactive metal such as copper. In an electrochemical system, the reducing species loses electrons, which are obtained by the oxidizing species. Although the absolute potential of a metal is not experimentally measurable, the standard electrode potentials are available, which are relative potentials of metal-solution interfaces against the standard hydrogen electrode (SHE) whose standard reduction potential is taken to be zero by definition. The SHE is an ideal electrode in which hydrogen ions and hydrogen gas are in equilibrium in their standard states. The half reaction for Cu^{2+} reduction in non-complex aqueous media is:



where (aq) denotes the aqueous species, while (s) indicate a solid. The standard electrode reduction potential $E^{\circ}_{\text{Cu}^{2+}/\text{Cu}}$ is +0.3394 V, but the equilibrium potentials of an electrode under specific experimental conditions should be calculated according to Nernst equation. Consider the general electrode reaction:



in which *Ox* denotes the oxidized species and *Red* the reduced species, *p* and *q* indicate their stoichiometric coefficients, and *n* gives the number of electrons transferred. For this equilibrium, the Nernst equation, accounting for non-standard state concentrations is

$$E^{eq} = E^0 - \frac{RT}{nF} \ln \left(\frac{C_{Red}^q}{C_{Ox}^p} \right) \quad (3)$$

where E^0 is the standard reduction potential of the electrode, R is the gas constant, T is the absolute temperature, F is the Faraday constant ($96\,487\text{ C}\cdot\text{mol}^{-1}$), and C_{Ox} and C_{Red} are the activities of the oxidized and reduced species, respectively. Equation (3) shows that the equilibrium potential E^{eq} can be calculated by the activities of oxidized and reduced species. If the concentration is not very high, the activities can be approximated by concentrations.

Applying equation (3) to (1), we can obtain the equilibrium potential of the $\text{Cu}|\text{Cu}^{2+}$ electrode:

$$E_{\text{Cu}^{2+}|\text{Cu}}^{eq} = E_{\text{Cu}^{2+}|\text{Cu}}^0 + \frac{RT}{2F} \ln(C_{\text{Cu}^{2+}}) \quad (4)$$

and use it to obtain the equilibrium potential of the copper electrode if the concentration of Cu^{2+} is known.

2.1.2. Electrodeposition

Since the cell voltage E_{cell} determines if the reaction in a cell is spontaneous or not, it must be related to the ΔG , the change in the Gibbs free energy. The relationship is

$$\Delta G = -nFE_{\text{cell}} \quad (5)$$

where n is the number of electrons that are exchanged during the balanced redox reaction. The electrode current is not determined by equilibrium thermodynamics, but it is controlled by resistances, diffusion properties and activation barriers, all of which determine the kinetics of the electrode reaction. When equation (1) proceeds forward, a reduction reaction occurs and copper electrodeposition occurs. The electrodeposition is a heterogeneous cathodic reaction. The electrochemical kinetics consists of diffusion of solvated copper ions from the bulk solution, ion migration in the region close to electrode surface and adsorption of copper ions onto the surface of the electrode. Finally, charge transfer at the metal-solution interface occurs where the Cu^{2+} ions accept electrons to deposit onto the electrode surface. The charge transfer reaction must overcome the potential-controlled activation energy, from one phase to another, across the electrical double layer. The reaction rate depends on the surface concentration of Cu^{2+} , temperature and electrode potential. This dependence in the charge transfer rate leads to the Butler-Volmer equation for the reduction process described in reaction (2):

$$j_{Cat} = -nFk_{Red}C_{Ox}exp\left(\frac{-n\alpha_c F\eta}{RT}\right) \quad (6)$$

This equation illustrates that cathodic current density j_{Cat} depends on the reduction rate constant k_{Red} , charge transfer coefficient α_c , concentration of oxidized species C_{Ox} , absolute temperature T and overpotential,

$$\eta = E - E^{eq} \quad (7)$$

where E is the potential at which the redox event is experimentally observed and η negative for a cathodic process. For the reverse reaction of (2), there is a similar equation to (6). At equilibrium, the forward and back reactions have equal rates and, the current flowing in the forward and back reactions at equilibrium is known as the exchange current.

From equation (6) and (7), the current density, or electrochemical reaction rate can be controlled by applied potential, concentration of electroactive species, and the composition of bulk solution through the addition of additive molecules to the electrolyte by modifying the overpotential.

2.2. Additives for Electrodeposition

Numerous additives have been used for the electrodeposition of different metals such as chromium, nickel, zinc, and copper [23, 29-31]. The particular

choice of additive is based on the metal being electroplated and the desired function during the electrodeposition process [32-35].

2.2.1. *Functions of Additives for Electrodeposition*

Additives play an important role in improving the smoothness, brightness, hardness, reflectivity and levelling in various electrodeposition processes [33, 36]. They not only affect the charge transfer process which modifies the crystallization of the metal, but also influence the rates of the other steps like ion solvation, diffusion, migration and adsorption. The functions of additives on electrodeposition processes can be categorized into several types [16].

The most common mechanism is the “dirt mechanism”, in which additive molecules are treated as a piece of dirt which may block ion diffusion and migration or may be adsorbed on the surface of the electrode, causing a decrease in the rate of electrode reaction. Depending on the size of the additive molecules, they may be adsorbed on the active site (a location available for nucleation), geometrical protrusions or specific crystallographic faces of the electrode surface. The adsorption ability is determined by the electronic and chemical structure of the additives molecules. The interactions between additives and the electrode result in effects known as levelling and brightening [16].

A second mechanism of additive effects occur when additive molecules can alter the charge transfer reaction in the Helmholtz layer, so changes in Helmholtz potential by additives account for any increases in reaction rate.

Another possible function of additives is complex formation with metal ions by replacing partial or all the solvated water molecules. The additive molecules or ions may act as ligands for the metal ion, displacing the solvent molecules in the solution sphere. This conformational change alters the transport and adsorption properties of the ion complex. It could, thereby accelerate the transfer of electrons from electrode to metal ions. However, if the ligands are too strongly bound to the metal ions, the complexes are too stable to discharge. Some common ligands used in electrodeposition are CN^- , NH_3 , Cl^- , Br^- , I^- , SCN^- , succinate and oxalate.

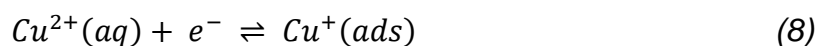
Finally, the changes in interfacial tension and filming of the electrode by the additives are one of the frequently observed functions [37-39]. Surfactants such as long-chain sulfonates and alcohols adsorbed on the electrode can cause changes in interfacial tension and act as an inhibitor [40, 41]. Additives also have many other ways to alter the rate of electrode reactions, such as ion pairing and by affecting the formation of intermediates.

2.2.2. Additives for Copper Electrodeposition

In the last two decades, numerous additives, including those of superfilling agents in the damascene copper electroplating process for on-chip metallization, have been investigated and their roles and mechanisms have been explained. Only few inorganic additives like NaCl are in use [4, 42]. Most additives are organic substances including polyethylene glycol (PEG), polypropylene glycol (PPG), bis(sodiumsulfopropyl) disulfide (SPS), thiourea, benzotriazole (BTA), Janus Green B (JGB), mercapto-1-propanesulfonate (MPSA), formaldehyde and acetone, etc. [3,

22, 43-48]. The common application of additives is to level and brighten copper electrodeposits. The literature on the various effects of additives for improving the quality of deposits is abundant, however, little information regarding the detailed, molecular level mechanisms of additives is known. It is this lack of information which has motivated the research described in this thesis.

Equation (1) shows the net cathodic reaction for copper deposition, but in an additive-free CuSO_4 solution. The mechanism consists of the following two steps [22].



where $\text{Cu}^{+}(\text{ads})$ is the intermediate formed after solvated $\text{Cu}^{2+}(\text{aq})$ ions migrate to the Helmholtz compact layer. Once adsorbed on the electrode, the adsorbed ions can accept electrons from the cathode and become part of the electrodeposited film. The first reaction is relatively slow, but the second is expected to be very fast, leading to concentrations of $\text{Cu}^{+}(\text{ads})$ maintained at very low values. An estimate of their concentrations can be obtained by subtracting equation (9) from (8) to form a new equilibrium expression:



The corresponding equilibrium constant under standard conditions, k ($[Cu^+(ads)]^2/[Cu^{2+}(aq)]$), is 6.0×10^{-7} M [3]. If the concentration of $Cu^{2+}(aq)$ is 0.050 M, the surface concentration of $Cu^+(ads)$ is very low at equilibrium. The important implications of this are that the adsorbed intermediates present in very low concentration affect the overpotential and the kinetics of electrodeposition. Additives can change the mechanism by inhibiting the formation of the intermediate; examples include levellers and suppressors such as PEG and PPG, whereas brighteners accelerate the formation of the adsorbed intermediate. Additive molecules can also regulate the presence of cuprous species on the surface by way of forming complexes with the Cu(I) ion [4, 7]. It is often seen that multiple additives are used in one electrolyte solution to provide different functions. This project aimed at exploring the effect of individual additive substances on copper electrodeposits, only one additive was added into an electrolyte solution at a time.

2.3. Experimental

2.3.1. *Electrochemical Cell*

A typical three-electrode cell is used for electrochemical process measurements and Cu electrodeposition. To study the effect of additives on copper electrodeposition, two commonly used noble metals, polycrystalline gold and platinum are used as working electrodes (WE). These metals are inert; and they should not undergo surface reconstruction as a result of interactions with the

additive and electrolyte solutions. In addition, they have a reasonably large potential window, i.e. a potential range in which the metals do not undergo either oxidation or reduction reactions with the water. The standard reduction potentials relevant for Au and Pt are $E_{Au^{3+}|Au}^0$ 1.50 V and $E_{Pt^{2+}|Pt}^0$ 1.2 V, but in practice, they are considered simply as a source of electrons. Also, the electrode surfaces have a reproducible composition and structure. Before experiment, the electrodes are cleaned with 6 M nitric acid for 30 minutes and rinsed with distilled water and ethanol to remove contaminants, then dried in air. The surfaces are refreshed by polishing and cleaning before each run.

The counter electrode (CE) is a platinum plate, which is cleaned with water and ethanol. The reference electrode (RE) is Ag|AgCl (3.5 M NaCl), which is easily prepared, cheap, electrochemically stable, and robust. Its standard reduction potential is 0.205 V with respect to the standard hydrogen electrode. The reference electrode is maintained in 3.5 M NaCl solution and is rinsed with distilled water before and after use.

The electrolyte solution consists of 0.050M CuSO₄ (99.995% metal basis, Aldrich). The additives tested are alcohols (HO-R, 99.5%, carbon number from 1 to 10 in alkyls chain length, Caledon Laboratories Ltd. or Anachemia Canada Inc.), malachite green hydrochloride (basic green 4, C₂₃H₂₆N₂O•HCl, FW = 382.9, Sigma Chemical Co.), sodium citrate (C₆H₅Na₃O₇•2H₂O, biotechnology grade, BioShop), thiourea (CH₄N₂S, 99.0%, BDH Inc.), meristic acid (C₁₄H₂₈O₂), polyoxyethylene 8 stearate [H(OCH₂CH₂)₈OCH₂(CH₂)₁₆CH₃], formaldehyde (H₂CO, Anachemia), and

rhodamine B ($C_{28}H_{31}ClN_2O_3$, Sigma). The solvent water used is deionized ($18.2 \text{ M}\Omega\cdot\text{cm}^{-1}$) by a Millipore system. To simplify experimental procedure, the water is not deaired and no acid or other source of ions is added into the electrolyte solutions unless noted. The pH value for 0.050 M CuSO_4 with or without additives, alcohols and malachite green or other additives, is 4.0 ± 0.5 , which shows little change during experiments although the solution is not buffered.

The electrochemical instrument is EGG potentiostat system, *VersaStat II*, computer controlled via *Power Suite* software.

2.3.2. Electrochemical Techniques

In this section, two of the most common electrochemical techniques are introduced, which are used to study the effect of additives on copper electrodeposition. The first technique used is linear potential sweep voltammetry (LPSV). In this research, the potential of the working electrode is swept to negative direction at a constant rate, such as 20 mV/s, while the current is measured through the *VersaStat II*. The sweep commences at an initial potential sufficiently high at which no reaction occurs (such as 800 mV for CuSO_4 solutions), and processes to negative potentials through values at which the reactions of interest occur (such as copper deposition or hydrogen evolution). Cyclic voltammetry (CV) is often used to obtain additional information by reversing the direction of the potential sweep, and continually cycling the potential at constant rate between upper and lower potential limits. For example the potential scans from 800 mV, is swept negatively to -800 mV and then returned to 800 mV to finish a cycle sweep.

The output from a typical LPSV or CV consists of a series of current peaks. A negative current peak corresponds to the reduction of some electroactive species in solution or on the surface like copper deposition. Conversely, a positive current peak corresponds to an oxidation reaction such as copper dissolution.

2.4. Effect of Additives on the Electrochemical Process of Cu Deposition

2.4.1. *Cyclic Voltammetry of CuSO₄ Solutions*

The cyclic voltammograms of CuSO₄ solutions were measured on gold and platinum electrodes respectively before any additives were added. Figure 4 shows typical CV curves on Au and Pt electrode. The CV curves on these electrodes are similar, but Au has higher peak current densities and smaller separations between the peak potentials,

$$\Delta E_p = E_p^a - E_p^c \quad (11)$$

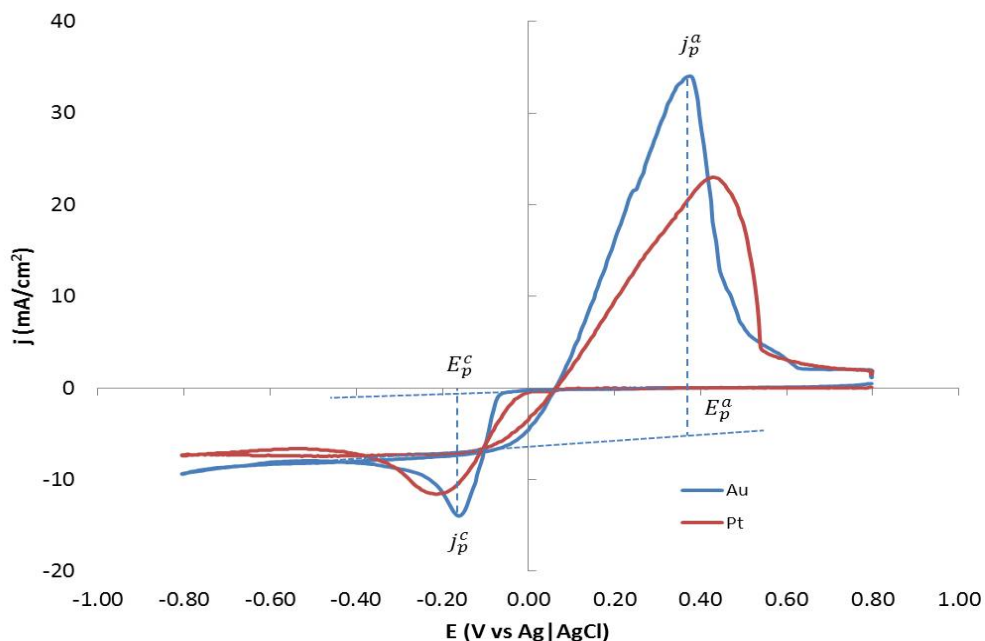


Figure 4. Cyclic Voltammograms of 0.050 M CuSO₄ on Au and Pt electrodes at scan rate of 20 mV/s. Peak parameters are marked for Au.

E_p^a is the anodic peak potential at oxidation peak current density j_p^a , and E_p^c is the cathodic peak potential at reduction peak current density j_p^c . The CV curves indicate that the kinetics of charge transfer on Au is faster than on Pt. Table 1 and Table 2 list the characteristics of the peak potentials and currents of the CV curves obtained from the Au-CuSO₄ solution interface. From this data, we can examine the properties of the reaction (1) on the Au electrode.

Table 1. The Impact of Scan Rate on CV Peak Potentials and Currents of 0.050 M CuSO₄ on Au Electrode.

v(V/s)	0.002	0.005	0.01	0.02	0.05	0.1	0.2	0.5
v ^{1/2}	0.0447	0.0707	0.1049	0.1414	0.2236	0.3162	0.4472	0.7071
ln(v)	-6.2146	-5.2983	-4.5099	-3.9120	-2.9957	-2.3026	-1.6094	-0.6931
I _p ^c (A)	-0.0010	-0.0013	-0.0016	-0.0020	-0.0030	-0.0036	-0.0046	-0.0061
I _p ^a (A)	0.0042	0.0054	0.0063	0.0058	0.0071	0.0074	0.0078	0.0098
E _p ^c (V)	-0.0833	-0.1179	-0.1305	-0.1808	-0.2153	-0.2625	-0.3316	-0.4291
E _p ^a (V)	0.2688	0.2908	0.3474	0.3285	0.3474	0.3977	0.4385	0.5768
ΔE _p (V)	0.3521	0.4087	0.4778	0.5092	0.5627	0.6601	0.7701	1.0059
I _p ^a /I _p ^c	4.2852	4.3431	4.0429	2.8754	2.3246	2.0330	1.7055	1.6046
(E _p ^a +E _p ^c)/2(V)	0.0927	0.0865	0.1085	0.0739	0.0660	0.0676	0.0534	0.0739

Table 2. Changes of Peak Potentials and Currents from Cyclic Voltammograms Scanned at 20 mV/s on Au Electrode with various Concentrations of CuSO₄

[Cu ²⁺](M)	I _p ^a (A)	I _p ^c (A)	E _p ^a (V)	E _p ^c (V)	ΔE _p (V)
0.010	0.0012	-0.0003	0.2688	-0.1588	0.4275
0.030	0.0045	-0.0011	0.3254	-0.1430	0.4684
0.050	0.0058	-0.0020	0.3285	-0.1776	0.5061
0.070	0.0088	-0.0023	0.3631	-0.1682	0.5313
0.090	0.0106	-0.0030	0.3662	-0.1242	0.4904

It is apparent from Figure 4 and the nature of the electrodeposition process that the Cu deposition is electrochemically irreversible. The CV data contained in Table 1 and 2 indicate that the peak potentials, E_p^a and E_p^c , and peak currents, I_p^a and I_p^c , depend on the potential scan rate and the concentrations of the CuSO₄. Plots of I_p^c and E_p^c vs. square root of the scan rate are almost linear ($R^2=0.98$, not shown). For example, when concentration changes from 0.010 M to 0.090 M, the

E_p^c value decreases from -0.1588 V to -0.1242 V. While this is sometimes taken as an indicator of reversibility, other characteristics of the CV curve illustrate the irreversibility of the system. The potential separation between the current peaks is expected to be

$$\Delta E_p = E_p^a - E_p^c = \frac{59}{n} \text{ mV} \quad (12)$$

for a reversible process at room temperature, where n is number of electrons transferred in the reaction. This requires that ΔE_p is 30 mV for a reversible reaction with n=2, while the measured values range from 350 to 1000 mV.

Similarly, the ratio of the peak currents is expected to be equal to one for a reversible reaction:

$$\left| \frac{I_p^a}{I_p^c} \right| = 1 \quad (13)$$

while the measured ratio ranges from 1.6 to 4.3. Finally, for a reversible reaction, half the sum of the two peak potentials is expected to be equal to E^0 for a reversible reaction:

$$\frac{E_p^a + E_p^c}{2} = E^0 \quad (14)$$

For this system, the equilibrium potential of Cu^{2+}/Cu is 0.134 V vs. Ag|AgCl (3.5 M NaCl). The measured values range from 0.0927 V to 0.0739 V.

Taking together the information from Figure 4 and Tables 1 and 2 enables us to understand the electrochemical properties of copper reduction. For other CV data presented in this thesis, unless otherwise specified, the potential scan rate was chosen to be 20 mV/s, to avoid convection effects and the concentration of CuSO_4 was selected to be 0.050 M to minimize the effects of uncompensated solution resistance.

2.4.2. Voltammograms of Blank Solutions

To learn how the adsorption of additives on the gold electrode surface influences the interfacial hydrogen evolution reaction, the linear potential sweep voltammograms and cyclic voltammograms of additive solutions without CuSO_4 electrolyte were performed first.

2.4.2.1. LPSV of 1-Propanol

Figure 5 shows the linear potential sweep voltammograms of pure water and with different concentration of 1-propanol, carried out on the Au surface at 20 mV/s, from 340 mV to -1400 mV vs. Ag|AgCl (3.5 M NaCl) electrode. For pure water, there is no significant current until the potential reaches -1130 mV, where the current increases quickly due to the hydrogen evolution reaction.

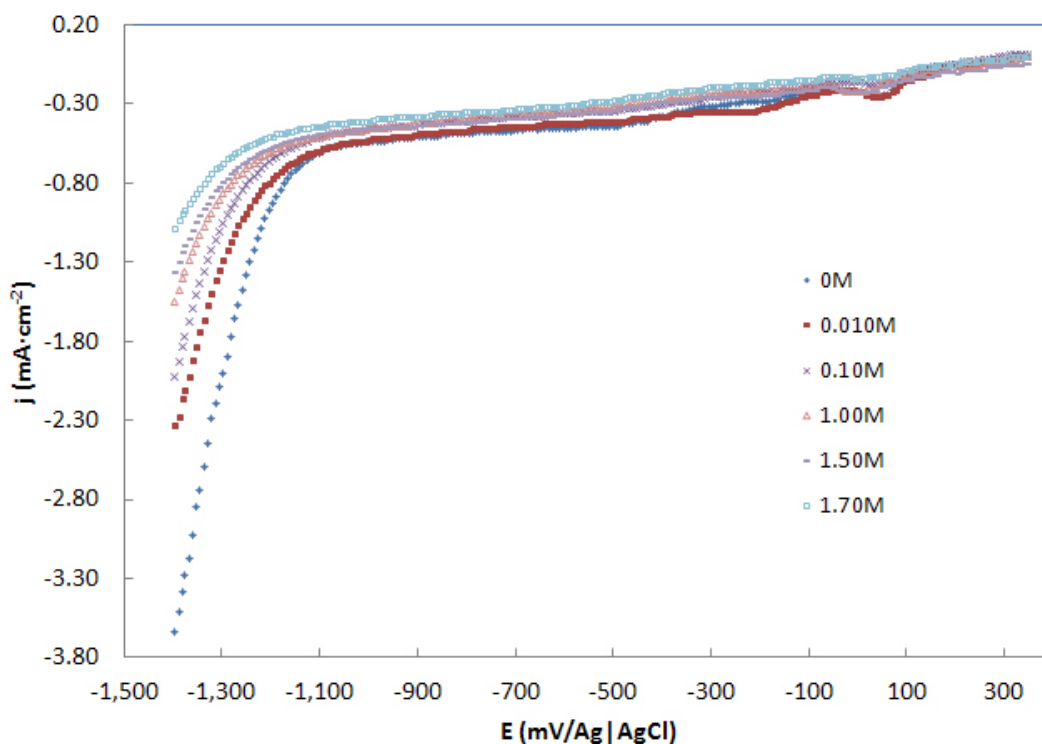


Figure 5. Effect of 1-propanol on the linear potential sweep voltammograms for the hydrogen evolution reduction on Au electrode from water solution. Scan rate: 20mV/s; Concentration of 1-propanol: 0~1.70M.

The theoretical hydrogen evolution potential in pure water vs. Ag|AgCl is calculated as -613 mV. Hence, the over potential η for proton reduction on the gold surface is significant, at -520 mV. For the solutions containing 1-propanol, the hydrogen evolution potentials are shifted to larger negative potentials and the higher the concentration 1-propanol, the higher the potential for hydrogen evolution becomes. Because there is no pH change after addition of 1-propanol into the water and no reactions expected between 1-propanol and proton, the change in potential of

hydrogen evolution reaction should be due to the adsorption of a 1-propanol layer on the gold surface.

There is no supplementary current observed until hydrogen evolution, so 1-propanol is not electroactive. It appears that the adsorbed layer effectively “blocks” the electrode active sites to slow down electrode reactions- the so-called “blocking effect” [16]. This accounts for the high over-potential upon 1-propanol addition to the solutions.

2.4.2.2. LPSV of Malachite Green

The linear potential sweep voltammograms of blank solution with malachite green are different from 1-propanol. After the addition of malachite green (MG) into water, even at low MG concentrations, the hydrogen evolution potential changes dramatically. Lower concentrations decrease the potential value, but higher concentrations increase the potential value (Figure 6), which indicates two effects that act oppositely. Because the malachite green reagent is actually its chloride salt, when it dissolves in water, malachite green cations and chloride anions are produced. Chloride is known to have a bridging effect that increases current or decreases overpotential of cathodic reactions [13, 16, 44, 46]. LPSV control experiments from electrolytes containing NaCl demonstrate the effects of Cl⁻ ions and their effects on overpotential (Figure 6 inset).

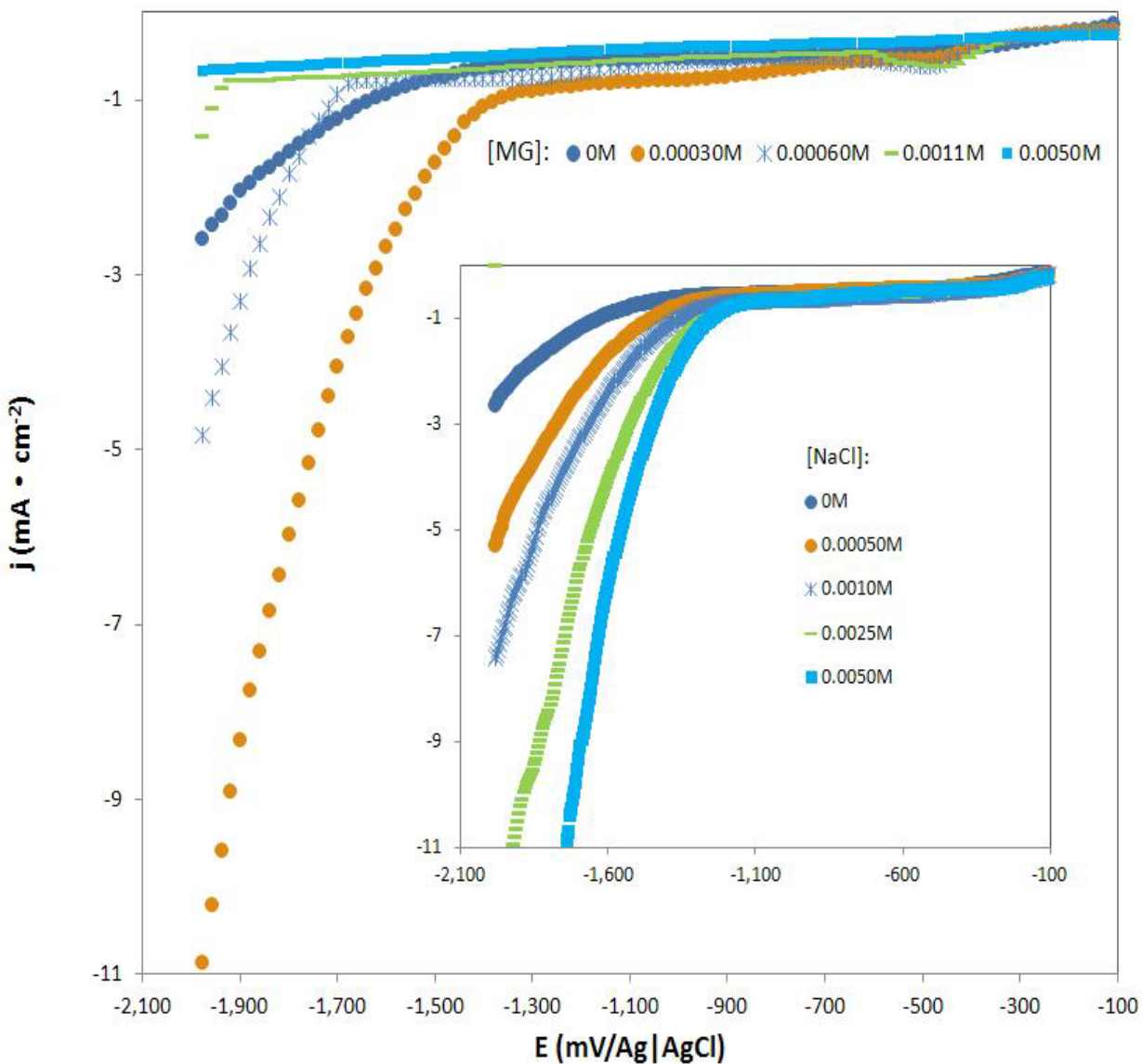


Figure 6. Effect of malachite green on the linear potential sweep voltammograms for the hydrogen evolution on Au from water solution. Scan rate: 20 mV/s; Concentration of malachite green: 0 M to 0.0050 M. Inset: the equivalent experiment with the same concentration range of NaCl.

These results indicate that at lower MG concentration, the chloride's bridging effects dominate. However at higher concentrations, the presence of malachite green completely dominates the additive effects on the electrode process, resulting in an increase in overpotential, consistent with a blocking mechanism.

As the additive MG dissociates to positive ions and chloride anions which potentially affects the pH of the solution, the effect of malachite green on the hydrogen evolution reaction seems to be more complex than for the addition of alcohols. Figure 6 shows LPSV at different concentration of MG in H₂O. At concentrations below 0.00030 M, the addition of MG decreases the hydrogen evolution potential whereas for higher malachite green concentrations, the potential values are increased. When the concentration of MG is higher than 0.0011 M, the evolution potential value is beyond the experimental range of -2.0 V. This is the reason only the flat part of LPSV for 0.0050 M MG is seen. In addition to the effect of MG cation and Cl⁻ anion, there is a third effect, the decrease of pH value after addition of MG. Practically, addition of MG increases the concentration of protons, which is expected, on the basis of the Nernst equation, to shift the hydrogen evolution potential value by approximately 100 mV at a MG concentration of 0.005 M. Figure 7 shows the trend of hydrogen evolution potentials with increasing concentration of MG and that this effect is a minor one.

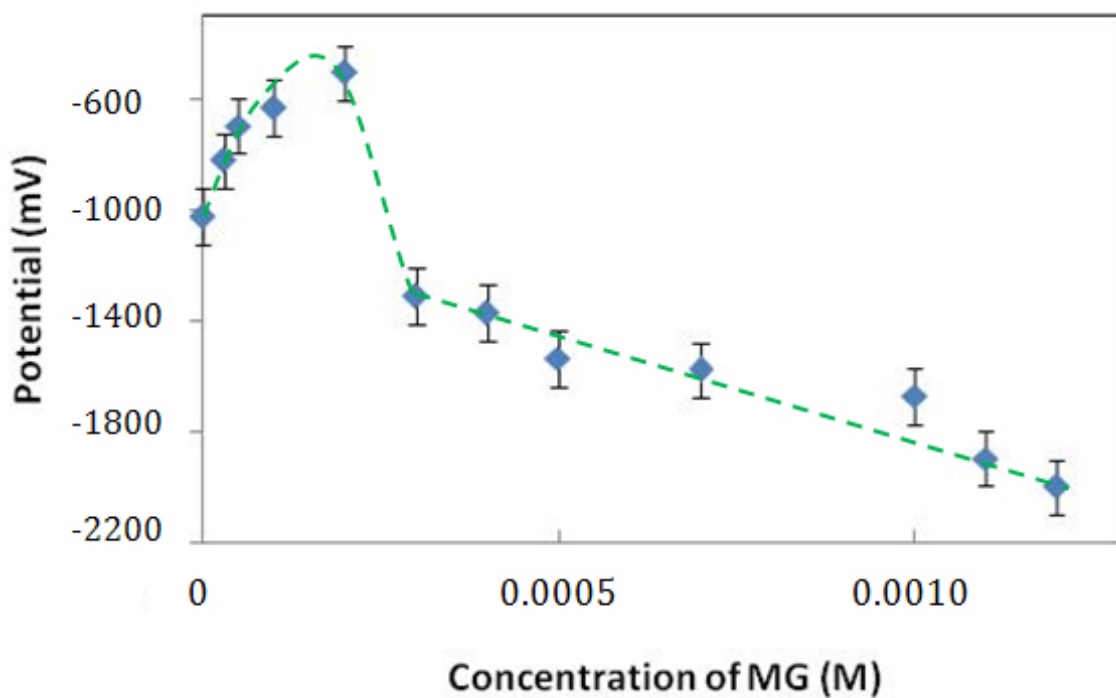


Figure 7. Influence of malachite green on the hydrogen evolution potentials. Reference cathodic current density is $1.0 \text{ mA}\cdot\text{cm}^{-2}$ at which the potentials are taken from LPSV. A trend line is added to guide the eye.

Comparing the effects of 1-propanol with malachite green on the overpotential for hydrogen evolution, one can easily see that MG has an enormous effect at very low concentrations, but 1-propanol only has significant effects at high concentrations.

2.4.2.3. CV of Malachite Green

From Figure 7, we know that there is no hydrogen evolution at potential of -2.0 V or greater when the concentration of MG is larger than 0.0012 M. To

investigate the reactivity of MG cations, the CV curves of malachite green solutions for concentrations up to 0.010 M are measured. Figure 8 shows a typical CV curve obtained on the Au surface in 0.0050 M MG. The MG ions are electroactive. The reduction peak potential of MG ions appears at -530 mV; and the oxidation peak potentials at -50 mV and 1016 mV. The 1016 mV anodic feature is attributed to the oxidation of Au and the formation of surface Au oxides [49, 50]. A series of CV curves with various concentrations of MG shows that the MG reduction peak potentials change from -400 mV to -540 mV, and at the same time the peak currents also increase with concentrations of MG (Figure 9). However, the anodic peak is not affected as significantly as the cathodic peak. The higher the concentration of MG is, the more negative the reduction peak potential and peak current are. The cathodic process is caused by the transformation of malachite green to leuco-malachite green (LMG) (Figure 10) [51, 52]. Its CV characteristics illustrate that this process is not reversible. This transformation changes the occupation of the electrode by the additive molecules.

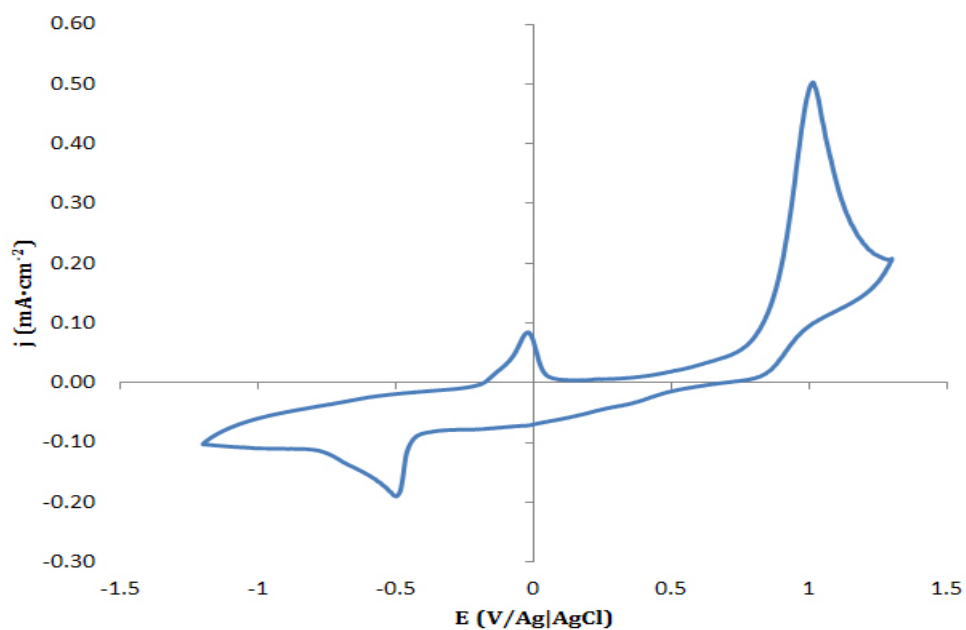


Figure 8. Cyclic Voltammogram of 0.0050 M Malachite Green on Au electrode at 20 mV/s.

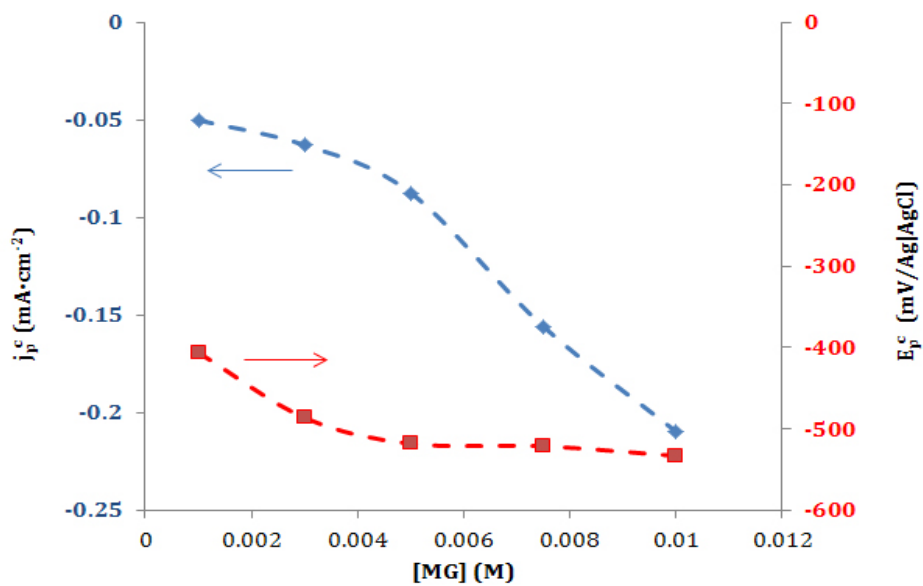


Figure 9. Change of cathodic peak potentials and currents of CV on Au with increasing concentration of MG. Scan rate is 20 mV/s.

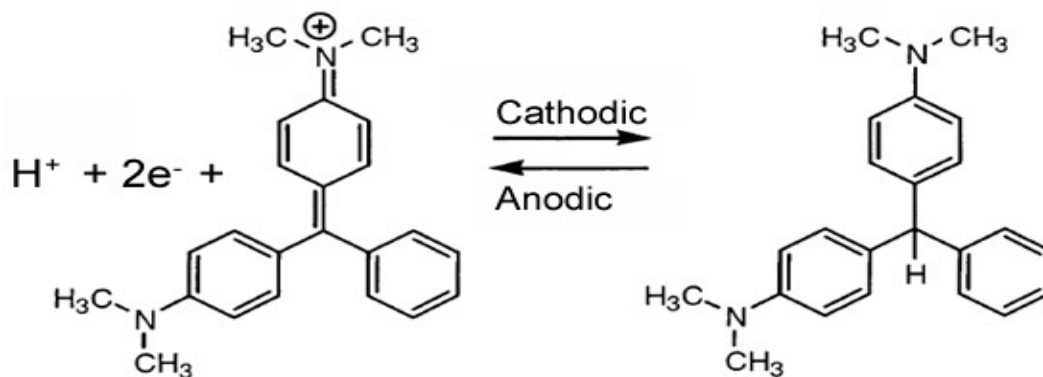


Figure 10. Transformation between malachite green and leuco-malachite green at the surface of the cathodic Au electrode.

Positively charged MG ion is expected to be strongly attracted to the negatively charged Au electrode and therefore to affect reactions occurring on the Au electrode surface.

2.4.3. Voltammograms of CuSO_4 Solutions

2.4.3.1. Effect of Alcohols on the CV of CuSO_4

The effects of the alcohols, methanol, ethanol, 1-propanol, 1-butanol and 1-pentanol, on the cyclic voltammograms of CuSO_4 have been investigated. The results show that low concentration of alcohols has insignificant effects on the electrochemical process of CuSO_4 ; and with similar concentrations, the longer alkyl alcohols have more significant effects on the redox process of copper ions. Figure 11 depicts the decrease of peak currents and increase of peak potentials caused by the increasing carbon numbers in the alcohols. Alcohol molecules are not

electroactive under these experimental conditions, so their blocking effects to copper redox processes are expected to increase with their size, as longer molecules are expected to be more surface active and to occupy more surface area of the electrode per molecule, increasing the over-potentials of electron transfer reactions.

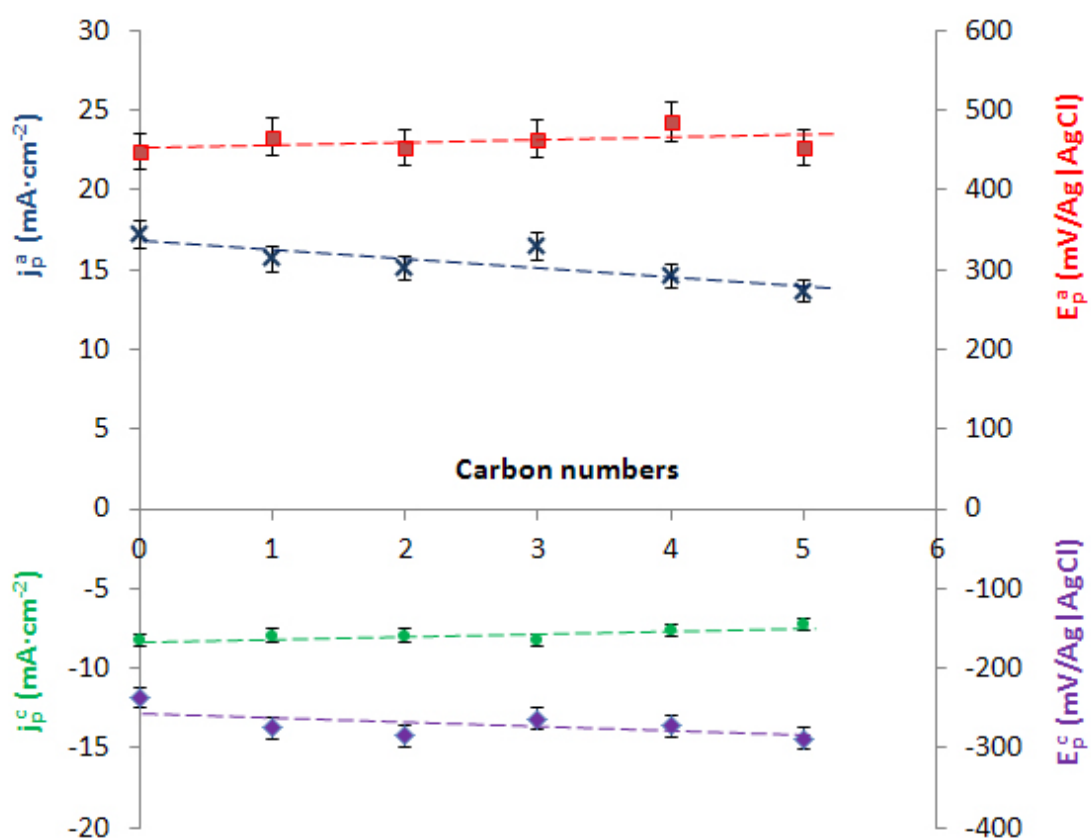


Figure 11. Effect of carbon numbers in alcohol molecules on peak currents and potentials of CV of 0.050 M CuSO₄ on Au electrode. Alcohols' concentrations are all 0.20 M. Scan rate is 20 mV/s. Data series color matches the colors of the axes' titles. Dashed trend lines are shown to guide the eye.

Consistent with these comments, the observed decrease of peak currents and increase of peak potentials are roughly proportional to the number of carbons in their molecules. Longer alkyl alcohols have also been tested, but due to their limited solubility in water, their effects are not presented in Figure 11. On the basis of this information, the medium chain length molecule 1-propanol was selected for further study on copper electro-reaction.

2.4.3.2. Effect of 1-Propanol on the LPSV and CV of CuSO_4

Similar to the case of hydrogen evolution, 1-propanol is also expected to demonstrate blocking effects on the copper deposition process. The effects of 1-propanol at different concentrations on linear potential sweep voltammograms and cyclic voltammograms of CuSO_4 solutions are presented in Figure 12 and Figure 13. From the LPSV and CV curves, one can see that copper deposition and dissolution peak currents decrease with increase of the 1-propanol concentration. Furthermore, the reduction peak potential shifts negatively but oxidation peak potential shifts positively, which increases the separation of peak potentials as the concentration of 1-propanol increases. Figure 14 shows the decreasing trends of peak currents (*a*) and increasing peak potentials (*b*); and also the narrowed difference between cathodic and anodic peak currents, $\Delta j_p = j_p^a - j_p^c$ (*c*) expanded separations between peak potentials, $\Delta E_p = E_p^a - E_p^c$ (*d*) with increasing concentrations of 1-propanol.

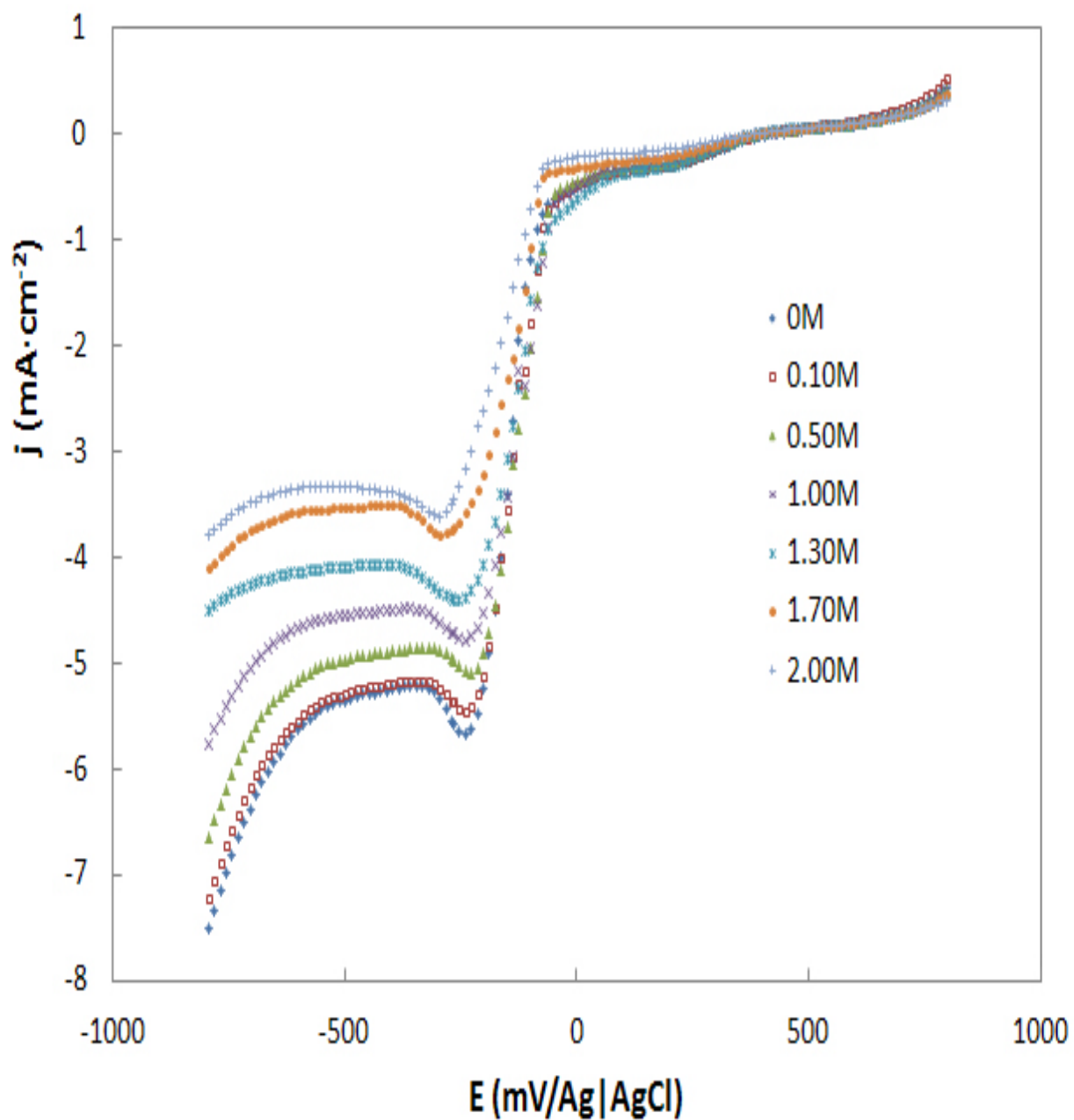


Figure 12. Linear potential sweep voltammograms of 0.050 M CuSO₄ on Au electrode with various amount of 1-propanol at a potential scan rate of 20 mV/s.

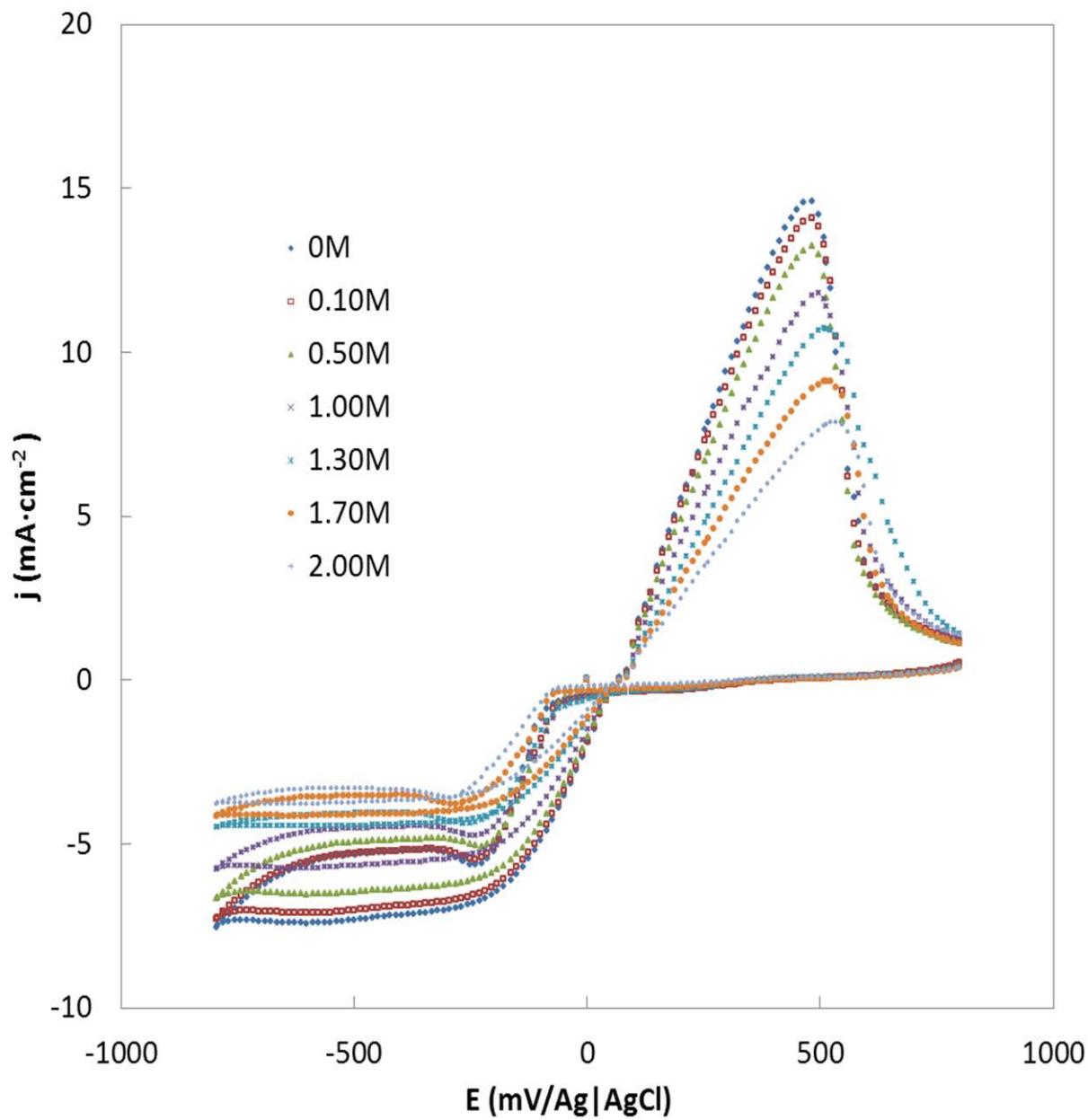


Figure 13. Effect of 1-propanol on cyclic voltammograms of 0.050 M CuSO₄ on Au electrode. Scan rate is 20 mV/s.

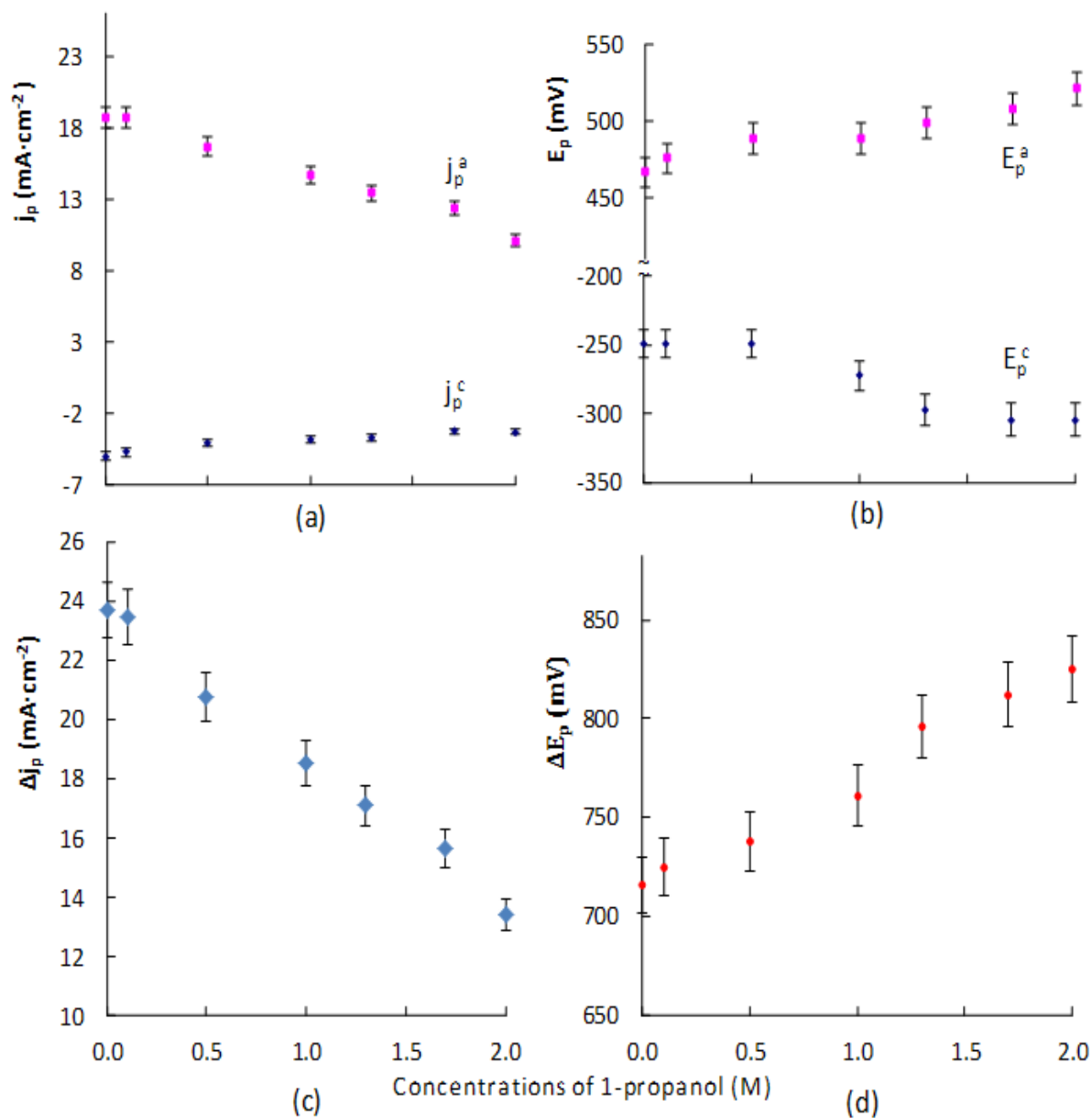


Figure 14. The changes of peak characteristics of LPSV and CV of 0.050 M CuSO₄ measured at the Au surface with a potential scan rate of 20 mV/s. With increasing 1-propanol concentrations: (a) Cathodic and anodic peak currents decrease. (b) Peak potentials move to high energy. (c) The differences between anodic current and cathodic current become smaller. and (d) The separations of redox peak potentials increases.

These results are consistent with a model in which molecules of 1-propanol are adsorbed at the surface of gold to increase the resistance to charge transfer reactions. The larger the number of molecules of 1-propanol in solution, the larger the fraction of electroactive sites of the gold surface are occupied, increasing the barrier to charge transfer and reducing the peak currents (*a*). As the resistance to redox reactions increases, larger driving forces (higher potentials) (*b*) are required to reach peak currents, raising the overpotential for copper deposition and dissolution processes, and increasing the separation between peak potentials (*b*, *d*). Increasing the carbon chain length of alcohols increases the size of the molecules, providing greater coverage of the electrode surface for equivalent alcohol concentration. On the basis of these observations, we conclude that the additive 1-propanol acts as a blocking agent to copper electrodeposition.

In addition to the observed blocking effects, 1-propanol also appears to change the mechanism of copper redox processes at the Au surface. Both the negatively and positively polarized slopes of the LPSV and CV curves are decreased (Figure 12 and Figure 13) by addition of 1-propanol to the electrolyte solution, which indicates a slower charge transfer constant. A plateau appears after the cathodic peak, which shows a limiting current due to the limiting diffusion of electrode active species. These limiting currents are obviously decreased by increasing 1-propanol concentration. This result may suggest the formation of copper-propanol complexes such as $[\text{Cu}(\text{C}_3\text{H}_7\text{O})_n(\text{H}_2\text{O})_{6-n}]^{2+}$. Some of the water molecules of hydrated copper ions could be replaced by 1-propanol molecules to

form a larger hydrated complex, which has a smaller diffusion coefficient and produces a smaller limiting current.

Copper ions may form two different complexes with water molecules, $[\text{Cu}(\text{H}_2\text{O})_4]^{2+}$ (tetraaquacopper(II) ion) and $[\text{Cu}(\text{H}_2\text{O})_6]^{2+}$ [53, 54]. The absorbance spectra of 0.050 M aqueous CuSO_4 with different concentrations of 1-propanol have been measured by a UV-Vis spectrometer. All the solutions have a wide absorbance band from 620 nm to 900 nm with a peak value at 810 nm, responsible for the blue color of CuSO_4 solutions and hydrated crystals [55, 56]. The absorption spectra showed no dependence on 1-propanol concentration, indicating that 1-propanol is not capable of displacing the solvating water molecules bound directly to the Cu^{2+} ion. This is consistent with the observed dipole moments of the water monomer (1.85 D) and 1-propanol monomer (1.68 D) in the gas phase, as well as their observed condensed phase dipole moments of 2.9 D and 2.36 D, respectively [57, 58]. A molecular dynamics study of aggregation phenomena in aqueous 1-propanol has shown that, through hydroxyl groups, 1-propanol molecules can form intense hydrogen bonds with water molecules [58]. The coordination number of water and 1-propanol may differ from 0 to 3. A diagram in Figure 15 shows the possible hydrogen bonds. Such a 1-propanol modified hexaaquacopper (II) with increased size would be expected to move more slowly and have more difficulty approaching the electrode and may account for the decreased slope and limiting current of the voltammograms in Figure 12 and Figure 13.

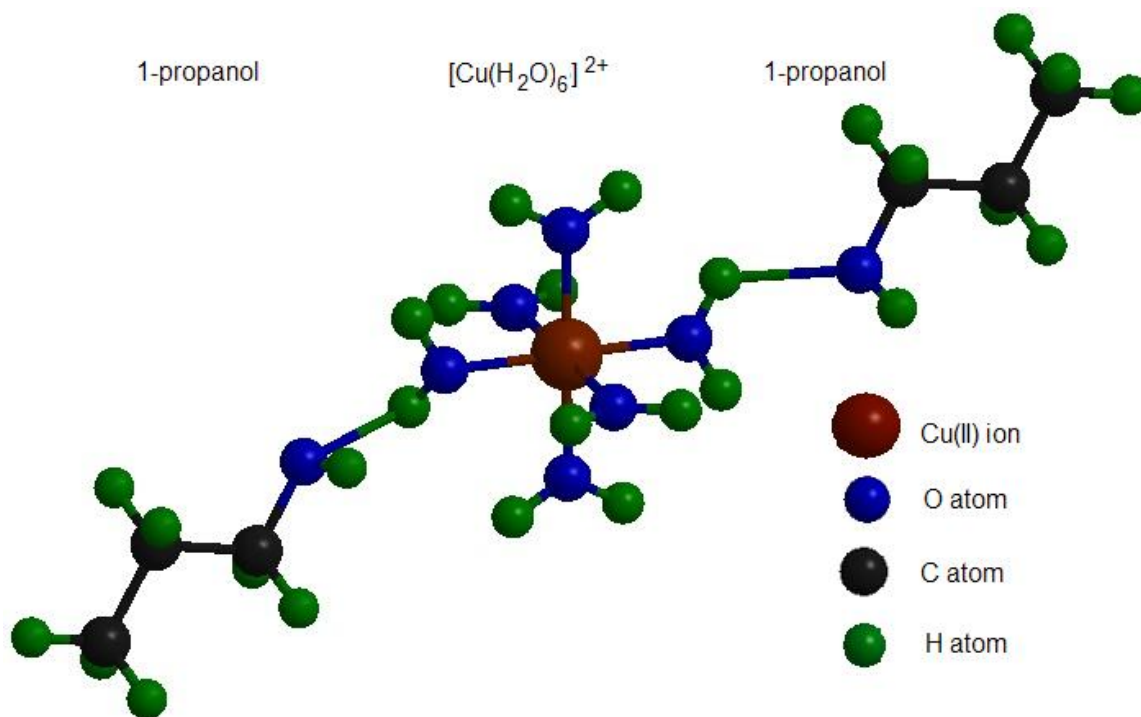


Figure 15. A schematic diagram of hydrogen bonding between 1-propanol and aqueous copper ion.

2.4.3.3. The Effect of Malachite Green on the LPSV and CV of CuSO_4

Figure 16 shows the linear potential sweep voltammograms obtained from 0.050 M CuSO_4 with concentration of MG from 0 to 0.0050 M. Comparison of the effects of 1-propanol on the voltammetry of CuSO_4 on the Au surface (Figure 12 and Figure 16) shows that MG has pronounced effects even at much lower concentrations than 1-propanol. MG presents a bigger effect on Cu reduction processes by shifting the cathodic peak potentials negatively dramatically with increase in MG concentration, and reaching its limiting value of -660 mV at a MG concentration of approximately 0.0030 M.

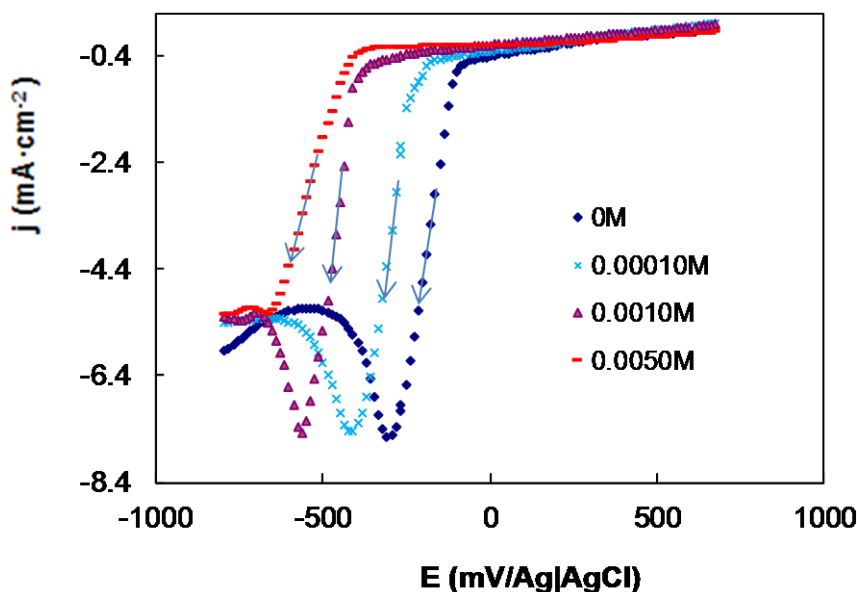


Figure 16. Effect of MG on LPSV of 0.050 M CuSO_4 on Au surface at a scan rate of 50 mV/s. The arrow lines indicate the slopes of cathodic sweep.

This result represents a significant increase in overpotential for Cu electrodeposition. The arrows appearing in Figure 16 represent the slopes of the cathodic currents on LPSV of CuSO_4 , which do not change at concentrations of MG lower than 0.0010 M, but become slightly smaller as the concentration of MG is increased, indicating the kinetics become somewhat slower with further addition of MG.

Figure 17 shows the effect of MG on the cyclic voltammograms of 0.050 M CuSO_4 on a gold electrode without any supporting electrolyte. To investigate the effect of supporting electrolyte to the effect of MG, an equivalent experiment with

addition of 0.50 M Na₂SO₄ in solution is undertaken. Figure 18 shows the CV curves with the supporting electrolyte. Comparing the CV curves in Figure 17 and Figure 18, one can see that MG presents the same effect on copper reduction potentials. Although the supporting electrolyte causes some increase to the peak currents because of the increase of solution conductivity, it does not change the ability of MG to shift the cathodic potential negatively significantly as indicated with an arrow in both figures. To make things as simple as possible, further experiments on additives are performed without the presence of supporting electrolyte. The curves in Figure 17 show that in additive-free solution, there is no obvious cathodic current until the potential reaches -114 mV versus Ag|AgCl (3.5 M), which is the potential corresponding to copper nucleation (defined as the nucleation potential E_n). As the potential is swept more negatively, the reduction current increases quickly due to the reduction of Cu, followed by a reduction peak and a plateau. The current peak indicates the potential where the activation current is equal to the diffusion current; but the plateau current indicates the limiting current controlled by mass transfer. When the potential is swept in the reverse (positive) direction, a crossover of the forward and backward current occurs due to the difference in deposition and dissolution potentials. The presence of the crossover is diagnostic of nuclei formation on the electrode.

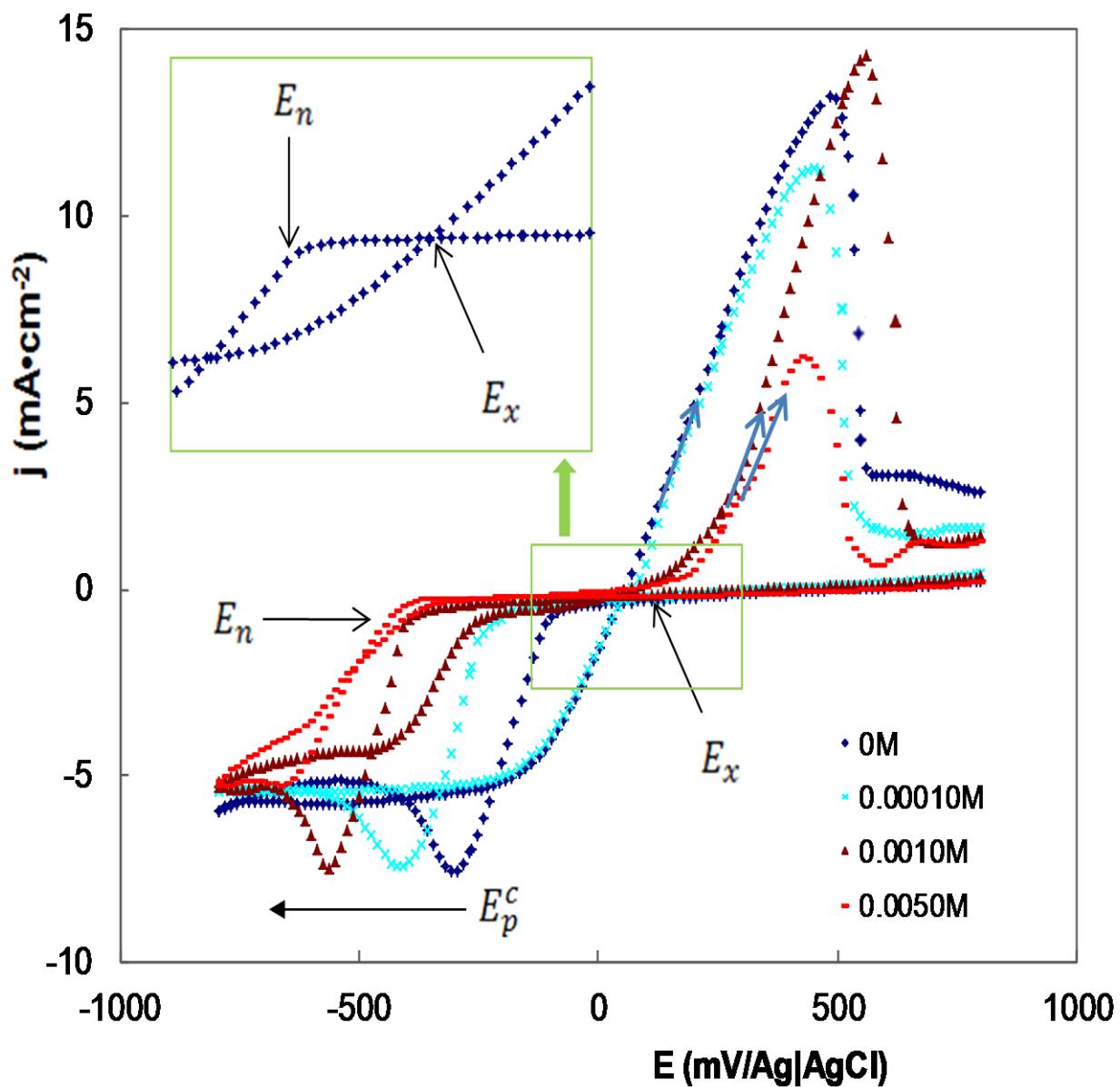


Figure 17. Cyclic voltammetry of 0.050 M CuSO₄ with different concentration of malachite green on the Au electrode. Scan rate: 50 mV/s. E_x : crossover potential; E_n : nucleation potential. Blue arrowed lines indicate the anodic sweep slopes.

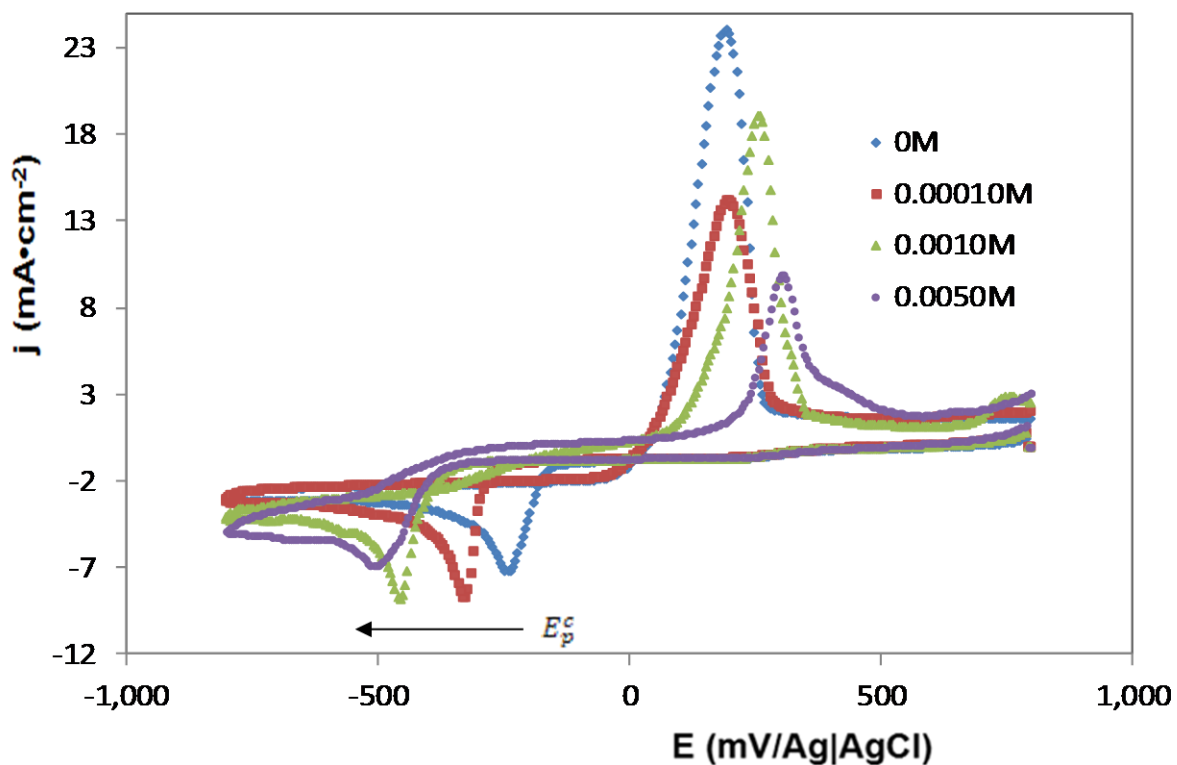


Figure 18. CV of 0.050 M CuSO₄ with different concentration of MG on the Au electrode. Supporting electrolyte is 0.50 M Na₂SO₄. Scan rate: 50 mV/s.

The crossover potential is 48 mV for additive-free CuSO₄ solution and denoted as E_x , which represents the point of zero current during the reverse scan. Similar shaped cyclic voltammograms from copper sulfate solution on a glassy carbon substrate have previously been observed [59]. From the CV curve, the nucleation over potential (E_{nop}) is defined as the difference between the nucleation potential and the crossover potential [30].

$$E_{nop} = E_n - E_x \quad (15)$$

In CuSO_4 solutions with the additive MG, the voltammograms are modified. Table 3 displays the defined potentials and copper nucleation peak parameters from the CV curves and how they change with MG concentrations. A strong blocking effect of MG on copper deposition can be observed through the significant shift of cathodic peak potential. As expected for the blocking mechanism, the nucleation potential E_n and cathodic peak potential E_p^c are shifted to more negative values; and the nucleation over potential E_{nop} increases with increasing concentration of MG until 0.0030 M. This concentration appears to be a critical concentration of MG because all the potentials, E_n , E_{nop} , and E_p^c , reach a stable value at this concentration. Furthermore, the peak current, j_p^c , drops dramatically at this concentration, which may indicate that the MG coverage on the electrode surface reaches a critical value. The limiting current at the plateau is $-5.2 \text{ mA}\cdot\text{cm}^{-2}$ and does not change with increasing MG concentration in solution. There is no apparent indication of complex formation between MG and the Cu^{2+} species in solution, since the diffusion coefficient of Cu^{2+} in solution would have been expected to be modified by complex formation, resulting in an MG concentration dependence of the limiting current.

Table 3. Effect of MG on copper ions' reduction parameters from CV curves

Concentration of MG (M)	E_n (mV)	E_{nop} (mV)	E_p^c (mV)	j_p^c (mA·cm ⁻²)	Limiting current (mA·cm ⁻²)
0	-114	547	-300	-7.5	-5.1
0.00010	-226	435	-415	-7.5	-5.3
0.0010	-408	253	-566	-7.5	-5.2
0.0030	-463	198	-665	-5.3	-5.2
0.0050	-453	208	-661	-5.2	-5.1
0.0070	-450	211	-652	-5.5	-5.2

This result is consistent with the analysis of the MG molecular structure. As MG is a cationic dye, it is not expected to readily form a copper salt or complex [60].

As discussed in section 2.4.1, the peak current is approximately proportional to the square root of the scan rate:

$$j_p^c = kv^{1/2} \quad (16)$$

where k encompasses the geometric and kinetic details of the electrode/electrolyte interface, including an exchange current coefficient, the number of electrons involved in the cathodic reaction, the effective and total electrode areas, the bulk concentration of oxidizing species, and the diffusion constant of the oxidizing species. Based on the data listed in Table 3, at low concentrations, MG does not show significant effects on peak currents. However, when the concentration exceeds 0.0030 M, j_p^c shows an approximate 30 % decrease, from -7.5 to -5.2 mA·cm⁻². This significant decrease in peak current density is a reflection of the

degree to which the additive MG affects the electrode. Reduction of the peak current density reflects significant modification of the electrode characteristics, including the effective electrode area as well as additional activation barriers presented by adsorbed additive molecules.

At low concentrations such as 0.0010 M, the effect of MG on anodic peak currents was not as remarkable as at high concentrations such as 0.0050 M, which indicated that at high concentrations, MG may prohibit the deposited copper from dissolving. The anodic peak potentials were not changed as much as the cathodic potentials by the addition of MG.

2.5. Conclusions

In this chapter, the effects of alcohol and malachite green on the additives electrochemical processes at the Au-CuSO₄ interface have been presented. In addition, other additives such as rhodamine B, Thiourea, sodium citrate and formaldehyde have also been investigated as they are common additives for electrodeposition[30, 47, 61]. Although they have shown some effect on the voltammograms of CuSO₄, the effects are not as notable as MG and 1-propanol.

Comparing the effects of all tested additives, 1-propanol shows significant effects on the electrochemical processes of CuSO₄ on the gold electrode, but requires relatively large concentrations before they are demonstrated. In contrast,

the additive Malachite Green demonstrates significant additive effects even at relatively low concentrations.

The results of linear and cyclic voltammetry indicate that both 1-propanol and malachite green (MG) show significant blocking effects on electrochemical reactions occurring on the Au-mica electrode surface. The over-potential for Cu nucleation increases with the addition of additives into the electrolyte solution; cathodic peak potentials were increased but peak current decreased with increased concentrations of additives. As 1-propanol reduces the plateau limiting current of the CV's, and evidence for formation of a complex of the type $[\text{Cu}(\text{C}_3\text{H}_7\text{O})_n(\text{H}_2\text{O})_{6-n}]^{2+}$ is not found, a model of hydrogen bonding between 1-propanol and $[\text{Cu}(\text{H}_2\text{O})_6]^{2+}$ has been suggested. Addition of MG to CuSO_4 electrolytes did not change the cathodic plateau currents, consistent with the absence of complex formation between MG^+ and hydrated Cu^{2+} ions in the electrolyte solution, but did shift the cathodic reduction potentials, indicating that MG does demonstrate significant additive blocking effects even at very low additive concentrations. The choice of MG as an organic additive was made based on the previous experimental history of this research group. The goal of this research was to employ this surface active molecule in nonlinear optical spectroscopy [24, 25, 62, 63] to help understand its behaviour as an additive and its effect on electrodeposition processes at the molecular level. The remarkable effects of MG on the electrochemical process of Cu reduction indicate that this choice of additive

was a fortunate one and that MG may have significant influence on the nucleation and growth characteristics of the resulting electrodeposited Cu films.

Chapter 3. The Effect of Additives on the Morphologies of Electrodeposited Copper Films

In this chapter we report the *ex situ* techniques to investigate morphologies of electrodeposited metal films. The deposited copper film and particles are studied with atomic force microscopy (AFM) and scanning electron microscopy (SEM). The crystalline properties are measured with X-ray diffraction (XRD). The effects of the additives MG and 1-propanol on the morphologies of the electrodeposited films are illustrated.

3.1. Techniques for Probing Thin Films

3.1.1. Atomic Force Microscopy

Atomic force microscopy (AFM) is one type of scanning probe microscopy (SPM). SPMs are designed to measure local properties, such as height, friction, magnetism, etc. with a small probe. To acquire an image, the SPM instrumental system scans the probe over a small area, measuring the local property. AFM has been used to solve processing and materials problems in a wide range of technologies including electronics, telecommunication, as well as biological, chemical, automotive, and energy industries [64-69]. The materials being investigating include thin and thick film coatings, ceramics, composites, glasses,

synthetic and biological membranes, metals, polymers, and semiconductors [70, 71].

3.1.1.1. AFM Tips and Cantilevers

In 1985, Gerd Binnig and his colleagues invented the AFM techniques. The first AFM tip, or probe, was made by meticulously gluing a tiny shard of diamond onto one end of a tiny strip of gold foil. Since then, advanced tips and their supports, cantilevers, have been developed by scientists and technologists. The commercial cantilevers are made with flexible materials, usually metals like gold and silicon. Cantilevers' backside sometimes may be coated with reflective aluminum. The length of the cantilevers may vary from 120 μm to 450 μm . The shape of cantilevers may be a bar or V-shaped. Figure 19 shows a V-shaped cantilever [72]. The tip is mounted right at the end of the cantilever. Normally, the probe is a sharp tip, which is a 3-6 μm tall pyramid with 10-30 nm end radius. Tips are typically made from Si_3N_4 , or Si that may be coated with other materials such as gold and diamond like carbon. For additional SPM applications such as chemical force microscopy (CFM) and magnetic force microscopy (MFM), the tips can be coated with molecules containing specific functionality or with materials showing a magnetic response.

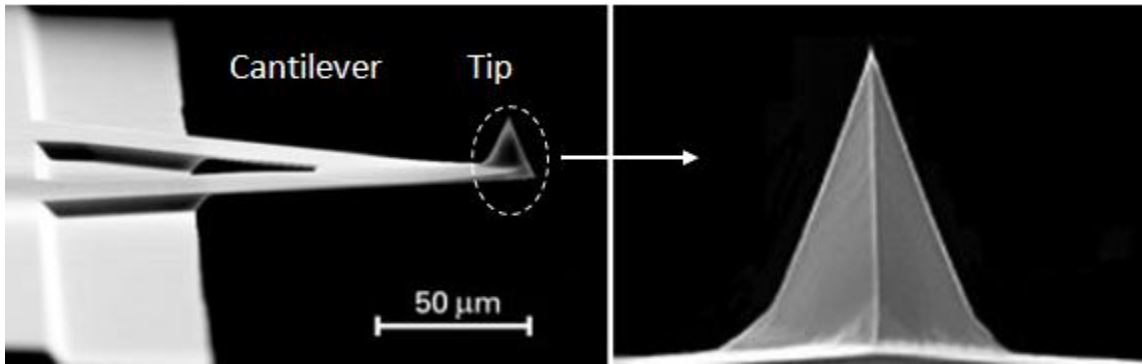


Figure 19. SEM image of triangular/V-shaped SPM cantilever with zoom-in probe.

A cantilever can be thought of as a spring. The typical value of the spring constant of a cantilever is $\sim 0.1\text{-}1$ N/m. According to Hooke's Law, the amount of force exerted on the tip is determined by the *spring constant* of the cantilever and the distance between the probe and the sample surface at which a deflection of the cantilever is to be monitored. The force is described as,

$$F = kx \quad (17)$$

where k is the spring constant, x the cantilever deflection and F is force felt by the tip. This typically results in forces in the range from nN to mN in open air.

3.1.1.2. AFM Instrumentation

An AFM schematic is given in Figure 20. The motion of the probe across the surface is controlled using a feedback loop and piezoelectronic scanners.

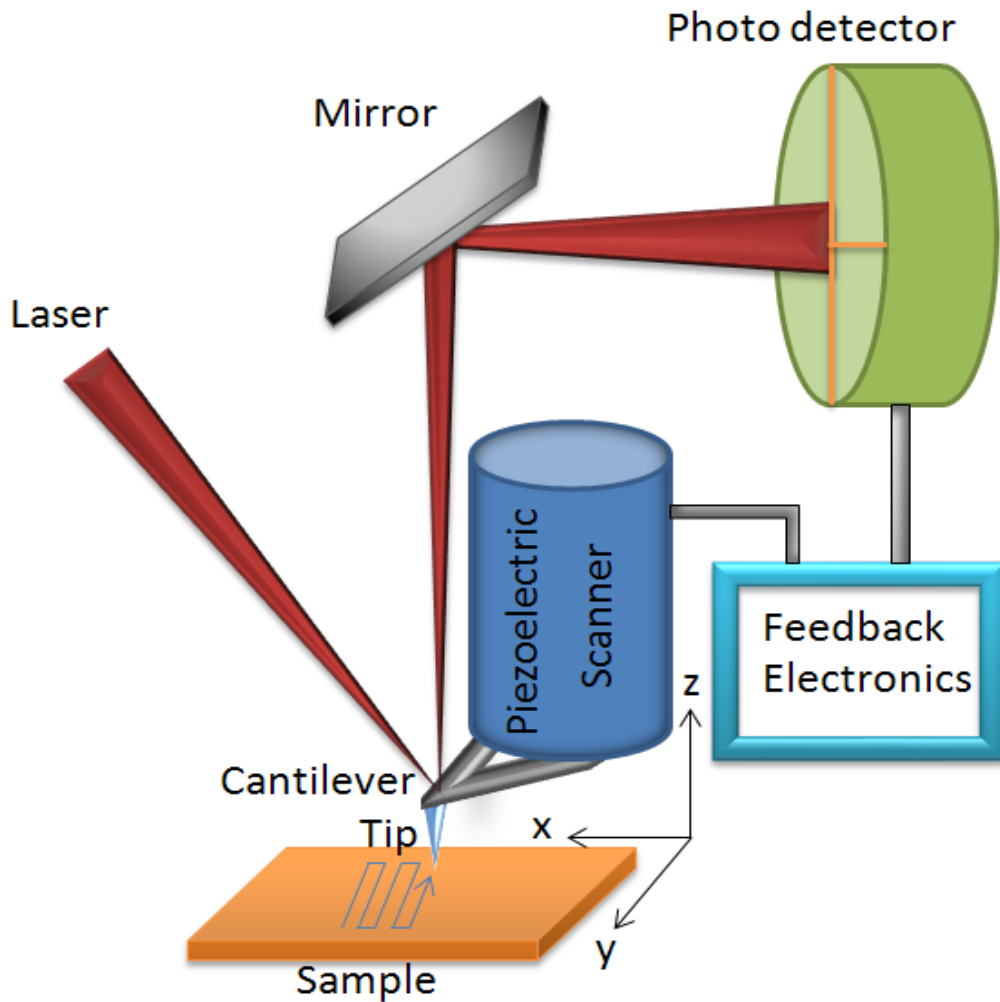


Figure 20. Schematic of AFM instrument showing “beam bounce” method of detection using a laser and position sensitive photodiode detector.

To monitor the forces between the tip and sample, the deflection of the probe is typically measured by a “beam bounce” method. A semiconductor diode laser is reflected off the back of the cantilever onto a position sensitive photodiode detector. This detector measures the bending of the cantilever as the tip is scanned over the sample. The motion of the probe over the surface is generated

by piezoelectric ceramics that move the probe and force sensor across the surface in the X and Y directions. Piezoelectric ceramics are a class of materials that expand or contract when in the presence of a voltage gradient, which measures the change of height in z direction. Piezo-ceramics make it possible to create three-dimensional positioning devices of arbitrarily high precision. The measured cantilever deflections are used to generate a map of the surface topography [70, 73].

3.1.1.3. Forces and Imaging Methods

The dominant interactions at short probe-sample distances in the AFM are Van der Waals (VdW) interactions. The force-distance curve between the tip and sample surface can be obtained by the Lennard-Jones interaction potential,

$$V = 4\varepsilon \left[\left(\frac{\sigma}{r} \right)^{12} - \left(\frac{\sigma}{r} \right)^6 \right] = \varepsilon \left[\left(\frac{r_m}{r} \right)^{12} - 2 \left(\frac{r_m}{r} \right)^6 \right] \quad (18)$$

where ε is the depth of the potential well, σ is the finite distance at which the inter-particle potential is zero, r is the distance between the particles, and r_m is the distance at which the potential reaches its minimum [74].

Based on the above equation, Figure 21 depicts the interaction potential between the atoms of the tip, and the surface atoms and molecules.

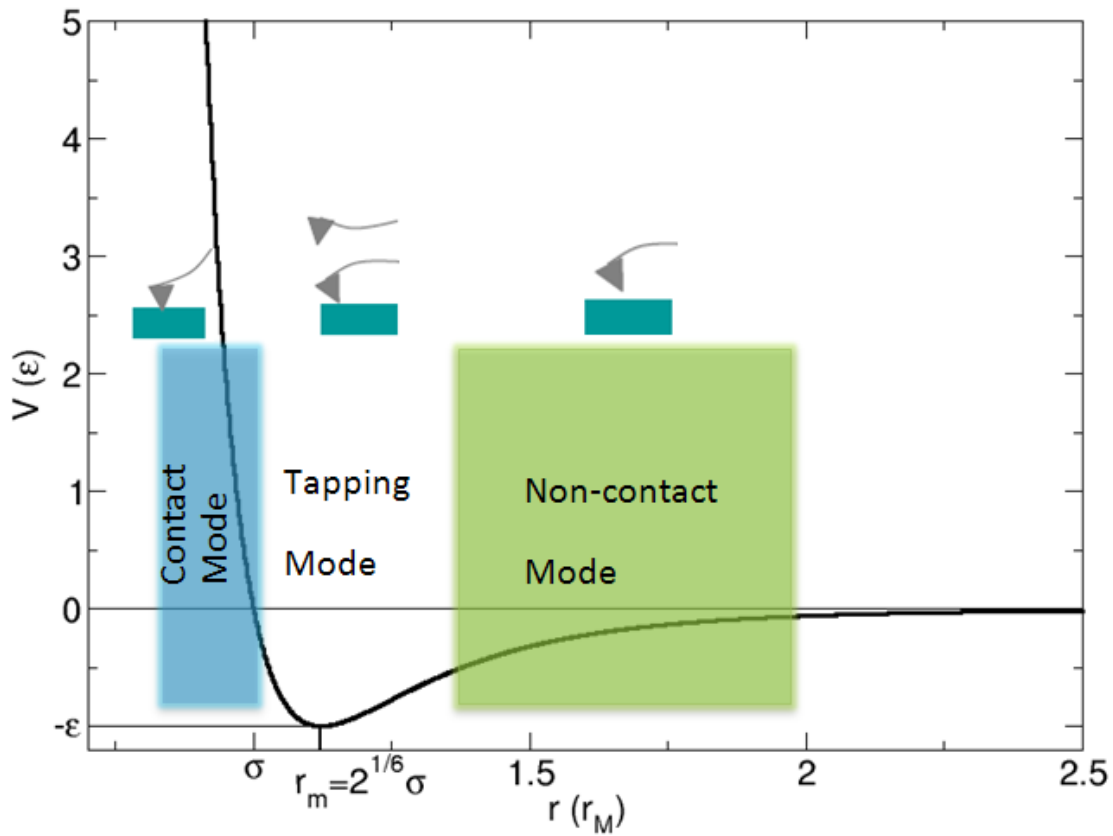


Figure 21. Plot of potential/force as a function of probe-sample separation. The insets represent the tip deflections at different working modes. Contact mode operates in the repulsive force regime; and non-contact mode operates in the attractive force regime.

During contact with the sample, the probe predominately experiences repulsive forces. AFM operation in this regime is called “contact mode”. This leads to tip deflection illustrated in the inset. As the tip moves further away from the surface attractive Van der Waals forces are dominant, and the tip can interact with the surface in “non-contact mode”. The tip may also work in intermittent contact with the sample, where the operation is sometimes characterized as “tapping

mode” [75]. Some important characteristics of operation in these three primary modes of operation are described below.

There are three primary imaging modes.

i. Contact Mode AFM

In contact mode, the tip-surface separation is typically smaller than 5 Å. If the spring constant of the cantilever is less than the compliance of the surface, the cantilever bends as depicted in the left most inset of Figure 21. The force on the tip is repulsive. By maintaining a constant cantilever deflection using the feedback loops, the force between the probe and the sample remains constant and an image of the surface is obtained. This operating mode scans fast, and is good for rough and hard samples.

ii. Tapping Mode AFM

The tip-surface separation in tapping mode operation is typically in the range 5 to 20 Å. In this mode the cantilever is driven to oscillate at its resonant frequency, as depicted in the central inset in Figure 21. The probe lightly “taps” on the sample surface during scanning, contacting the surface at the bottom of its swing. By maintaining constant oscillation amplitude, (typically 20-100 nm), or frequency, a constant tip-sample interaction is maintained and an image of the surface is obtained.

iii. Non-contact AFM

The tip-surface separation is from 10 to 100 Å. The probe does not contact the sample surface, but oscillates above the surface during scanning. Using a feedback loop to monitor changes in the amplitude due to attractive VdW forces the surface topography can be measured. This mode is useful for soft and fluid sample.

Electrodeposited copper films on Au-mica are relatively smooth, hard and dry, so that contact mode AFM is employed to study the resulting film morphologies in the project.

3.1.2. Scanning Electron Microscopy

A schematic diagram of a typical SEM showing major parts and geometry is given in Figure 22 [76]. The scanning electron microscopy (SEM) uses a focused beam of high-energy electrons to generate a variety of signals at the surface of solid samples. The signals that derive from electron-sample interactions reveal the information about the sample. Following the first scanning electron microscopy demonstration in 1942, the instruments and techniques have been improved significantly. Nowadays, the SEM has proven to be a valuable and indispensable tool in the development of scientific theory and it has contributed greatly to the development of chemistry, biology and material sciences.

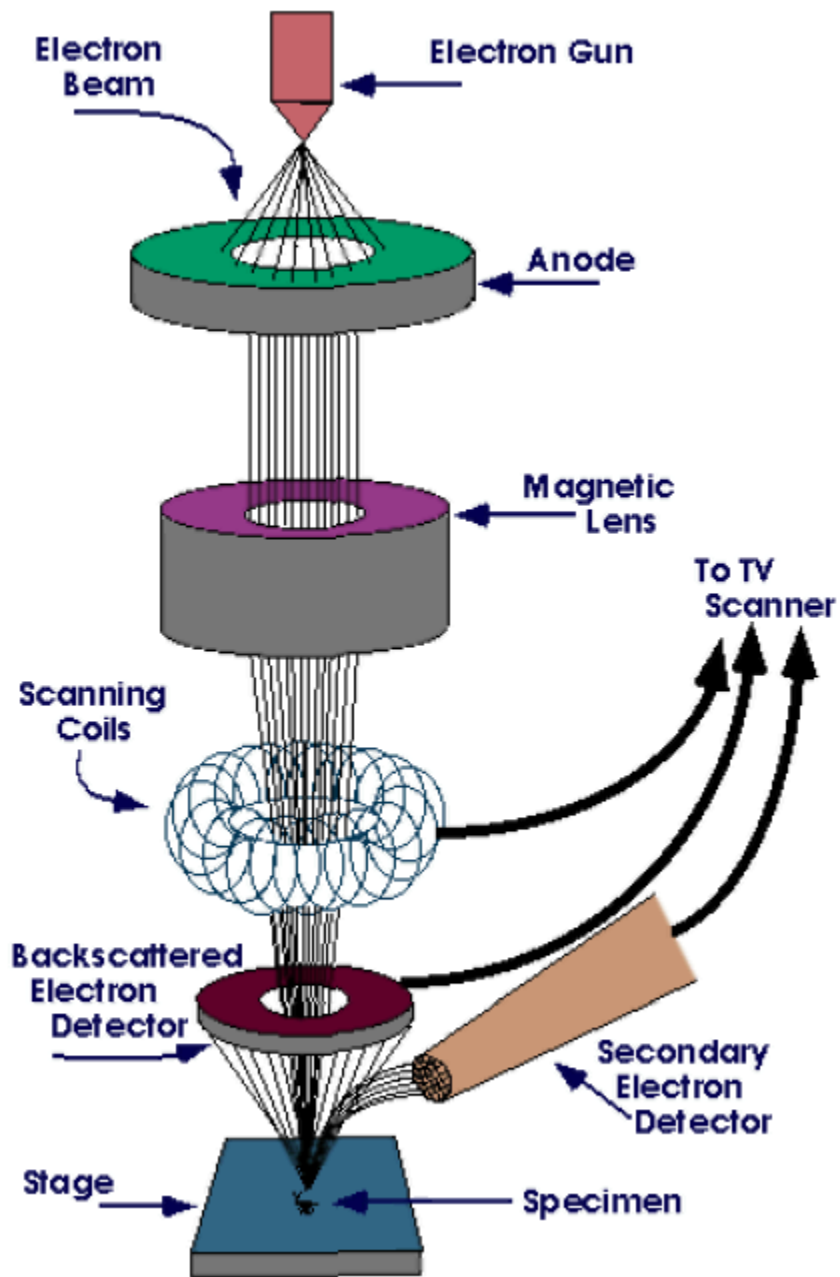


Figure 22. SEM diagram with major parts' geometry

This wide spread use of SEM is based on the fact that it permits the observation and characterization of materials on a nanometer to micrometer scale. With SEM

examination one can obtain information about the topography (surface features of a sample/specimen), morphology (shape and size of the particles making up the sample), and composition [77].

In SEM, a source of electrons is focused in vacuum into a fine probe that is rastered over the surface of the specimen. The electron beam passes through scan coils and an objective lens that deflects horizontally and vertically so that the beam scans the surface of the sample. The accelerated electrons carry significant amounts of kinetic energy, and this energy is dissipated as a variety of signals produced by electron-sample interactions when the incident electrons are decelerated in the solid sample. These signals include secondary electrons, backscattered electrons, diffracted back scattered electrons, photons, visible light, and heat. Secondary electrons and backscattered electrons are commonly used for imaging samples: secondary electrons are most valuable for showing morphology and topography on samples, which produce SEM images.

3.1.3. *X-ray Diffraction (XRD)*

3.1.3.1. X-ray Diffractometer

Figure 23 gives the schematic of a basic X-ray diffractometer [78]. X-rays are electromagnetic radiation similar to visible light, but with a much shorter wavelength. They are produced when electrically charged particles of sufficient energy are decelerated. In an X-ray tube, the high voltage maintained across the electrodes

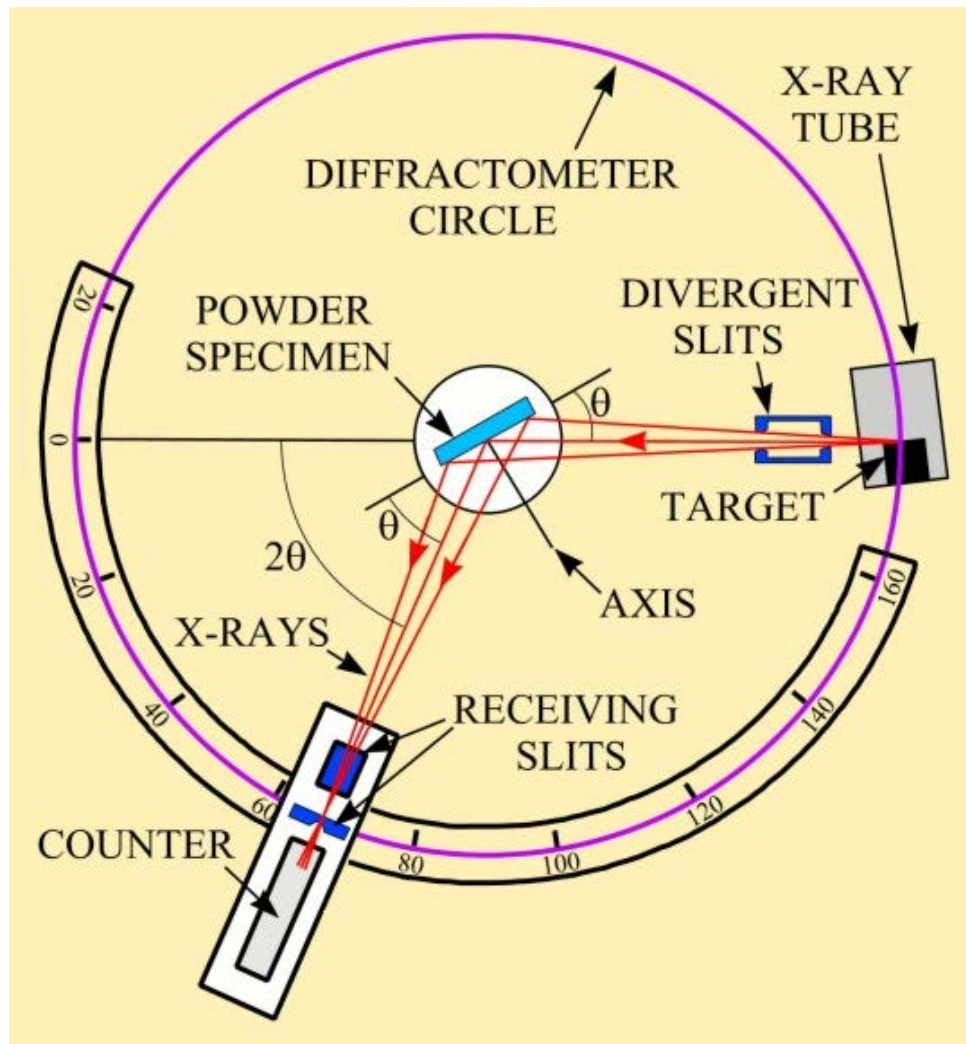


Figure 23. Schematic of X-Ray Diffractometer.

draws electrons toward a metal target or anode. X-rays are produced at the point of impact, and radiate in all directions. Tubes with copper targets produce their strongest characteristic radiation at a wavelength of 1.5418 \AA . An X-ray detector is usually situated on the circumference of a graduated circle centered on the specimen. Two divergent slits, located between specimen and the X-ray source, and the specimen and the detector, limit scattered radiation, reduce background

noise, and collimate the radiation. The detector and specimen holder are mechanically coupled with a goniometer so that the angle of the detector to the main beam is maintained at twice the incident angle θ between the X-ray beam and the surface of specimen [79-82].

3.1.3.2. Bragg's Law

XRD is a nondestructive technique to identify crystalline phases and orientation, to determine structural properties like lattice parameters, strain, grain size, and to characterize the crystalline structure of thin films and nano materials. When X-ray radiation passes through a crystalline sample, the X-rays interact with the electrons in the atoms and general scattering occurs. Although most scattering interferes destructively with itself and is eliminated, diffraction occurs when scattering in a certain direction is in phase with scattered rays from other atomic planes. These conditional reflections constructively interfere to form enhanced wavefronts where X-rays are scattered at characteristic angles based on the spaces between the atomic planes defining their crystalline structure. Most crystals can have many sets of planes passing through their atoms. Each set of planes has a specific interplanar distance and will give rise to a characteristic angle of diffracted X-rays. Bragg's Law describes the relationship between the specific distances and angles.

$$2d\sin\theta = n\lambda \quad (19)$$

where d is the interlayer spacing of the layers, θ is the incident angle of the X-rays in degrees, n is an integer, and λ is the wavelength of the X-rays (1.5418 \AA). The geometry used to derive Bragg's Law is shown in Figure 24. This observation is also an example of X-ray diffraction (XRD) that provides direct evidence for the periodically atomic structure of crystals [81].

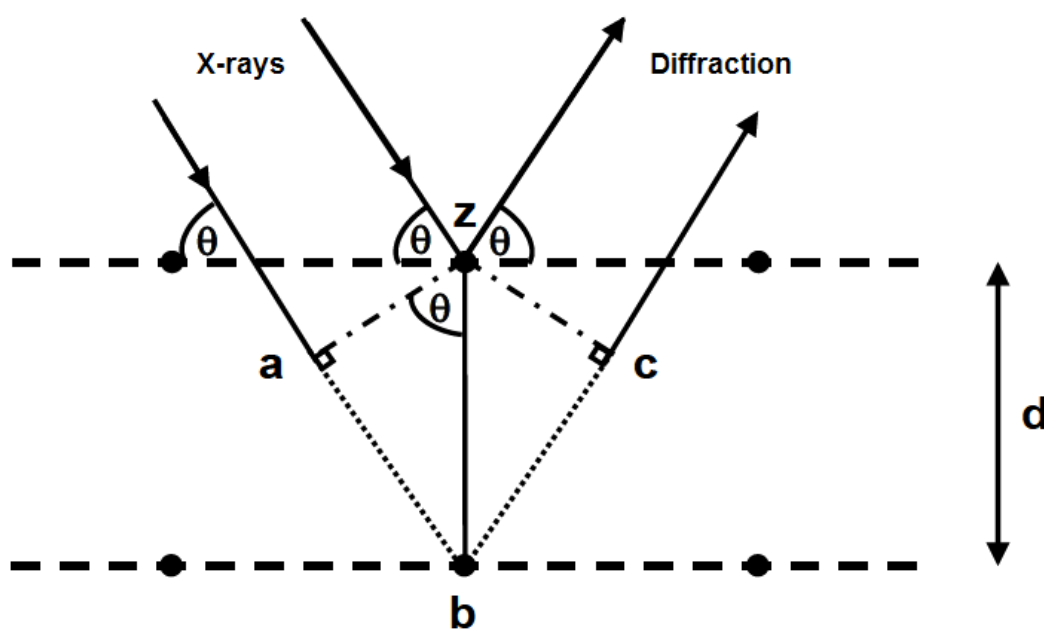


Figure 24. The diagram of X-ray diffraction and geometry for deriving Bragg's Law.

3.2. Experimental

3.2.1. Preparation of Sample

The gold thin film electrode (Au-TFE) is prepared by vacuum evaporating gold onto mica with an area of $1 \times 1 \text{ cm}^2$. A thickness of 100 nm gold thin films is deposited at 10^{-6} Torr, 370°C and 1.2~1.4 nm/s rate. To guarantee a good adhesion of gold to mica, the mica surface should be refreshed just before evaporation by cleaving a thin layer of it. The working electrodes (WE), Au-TFE, are kept in a closed container and washed with alcohol and acetone before experiment. The reference electrode (RE) is Ag|AgCl (3.5 M NaCl) and the counter electrode (CE) is a platinum plate.

The study of the effects of additives on the electrochemical process is carried out using linear sweep voltammetry and cyclic voltammetry for the additive-free electrolyte solutions or with different concentrations of additives with TopoMetrix bipotentiostat-galvanostat. Based on the results, three electrolyte solutions, 0.050 M CuSO_4 , 0.050 M CuSO_4 + 1.0 M 1-propanol and 0.050 M CuSO_4 + 0.0050 M MGCl (denoted as MG later), are selected to study the effect of additives on morphology, roughness and crystallinity of copper electrodeposits prepared under potentiostatic conditions.

According to the electrochemical studies, the cathodic half-wave potentials ($E_p^{c \frac{1}{2}}$), at which copper reduction current equals to half of the cathodic peak current density (j_p^c), are selected as copper electrodepositing potentials. All samples are prepared by electrodepositing copper films on $1 \times 1 \text{ cm}^2$ Au-TFE

substrate using potentiostatic method. The electrodeposition potentials for different electrolyte solutions are listed in Table 4. These potentials can control the copper film growth at a moderate rate, neither too fast nor too slow, to obtain a high quality film in a short time. Figure 25 shows the j-t characteristic while copper is deposited on a Au thin film electrode with potentiostatic method. The electrodeposition currents reach a stable value shortly after the potential is applied to the working electrode. In 0.050 M CuSO₄, the stable current densities are 2.2 mA·cm⁻² for additive-free and 1.0 M 1-propanol electrolyte solutions, and 1.8 mA·cm⁻² for 0.0050 M MG solution. With these current densities, the copper film growth rates are 0.74 ± 0.03 nm/s. Samples of different thickness of copper film on Au-TFE can be obtained for different electrodeposition times. Newly deposited copper thin film samples are rinsed with pure water, alcohol and acetone; air dried and kept in a closed container before use.

Table 4. Electrodeposition potentials E_p^c and currents j_p^c for different electrolyte solutions

Electrolyte solutions	E_p^c (mV)	j_p^c (mA·cm ⁻²)
0.050 M CuSO ₄	-200	2.2
0.050 M CuSO ₄ + 1.0 M 1-propanol	-200	2.2
0.050 M CuSO ₄ + 0.0050 M MG	-500	1.8

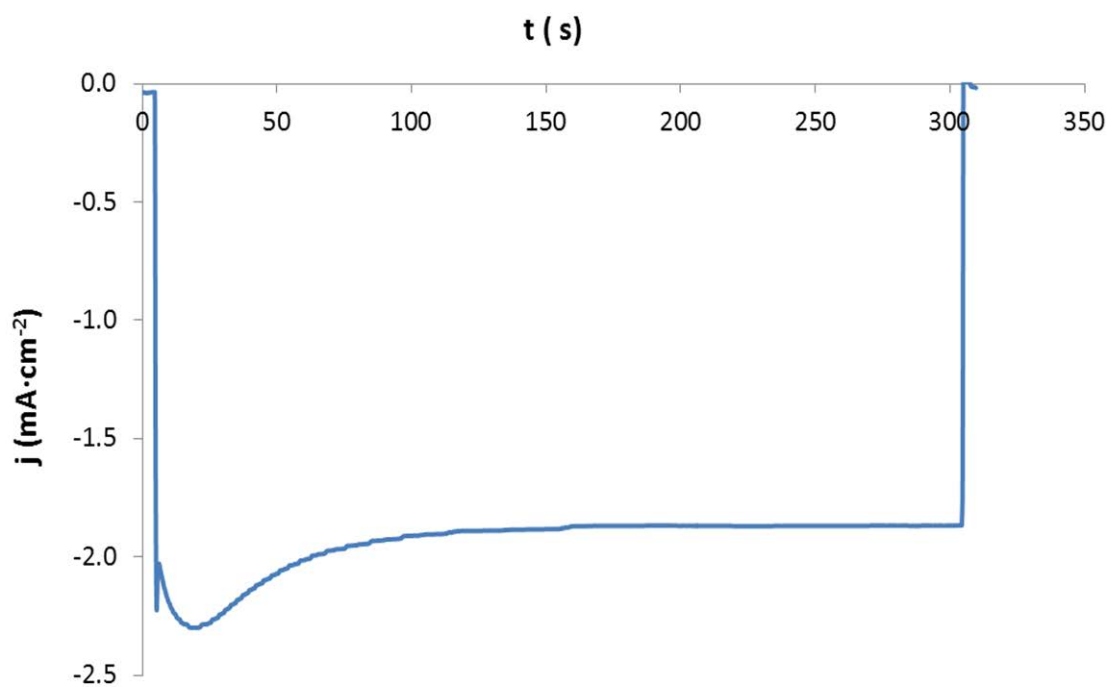


Figure 25. Current-time characteristic of copper electrodeposition from 0.050 M CuSO₄ and 0.0050 M MG solution at -500 mV.

3.2.2. Measurement of Sample

AFM experiments are performed in contact mode in air using a commercial instrument (ThermoMicroscopes Explorer), equipped with an 8 μm in z and 100 μm in x-y axes dry scanning head. A Si₃N₄ tip mounted on a V-shaped cantilever was used. AFM images are measured over different areas such as 2 \times 2 μm , 5 \times 5 μm , 10 \times 10 μm , 20 \times 20 μm , 40 \times 40 μm with a resolution of 200 \times 200 data points. The topographic and internal sensor images are obtained simultaneously through the scanning probe software supplied with the instrument (ThermoMicroscopes SPMLAB NT Version 5.01). Processing of the resulting AFM images was carried

out with the same software using the built in functionality to level the images and measure grain sizes and surface roughness.

SEM was performed using an FEI DualBeam Strata 235 electron microscope. The morphologies and grain shape and size of copper thin films were characterized at different resolutions and tilt angles.

XRD was performed on the RAPID (Rigaku) X-ray diffractometer with a copper target ($\lambda_{\text{Cu}} = 1.542 \text{ \AA}$) and an image plate detector. A source voltage and current of 46 kV and 42 mA are used during the operation, respectively.

3.3. The Effects of Additives on the Properties of Cu Films

3.3.1. *Morphologies of Copper Thin Films*

3.3.1.1. AFM Images

In this section, the topographic, internal sensor images showing the morphologies of the electrodeposited copper films are described and analyzed. Images shown in this thesis are raw data, processed only with simple leveling (for more processing, see Appendix A). As the thickness of the copper films is increased, the properties of the films from additive-free electrolyte solution and from electrolyte solutions with additives are compared at different stages of electrodeposition. Figure 26, Figure 27 and Figure 28 represent AFM topographic images of copper films from additive-free 0.050 M CuSO_4 , with 1.0 M 1-propanol, and with 0.0050 M malachite green electrolyte solutions respectively. It can be

seen that both the shape and size of the deposited Cu grains have been altered significantly by the presence of the additives. The Cu grains from the 0.050 M CuSO_4 electrolyte without additives are coarse and chunky with random shape orientation. Grains from 0.050 M CuSO_4 with 1.0 M 1-propanol are finer and have the shape of trigonal pyramids. The grains resulting from the electrodeposition from 0.050 M CuSO_4 with 0.0050 M MG are the finest and have the shape of square pyramids. Figure 28 shows grains that are truncated and have not yet attained their full square pyramidal structure and thus appear with square tops.

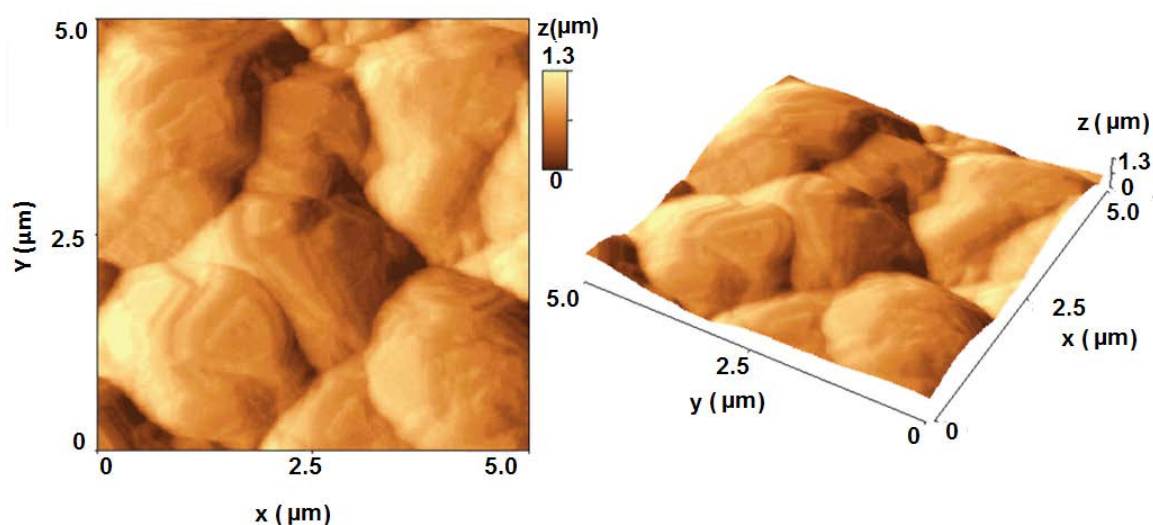


Figure 26. AFM topographic images with 3D view of electrodeposited copper films on Au-TFE electrodes from 0.050 M CuSO_4 solution. Electrodeposition time: 5 minutes; film thickness: 220 ± 20 nm.

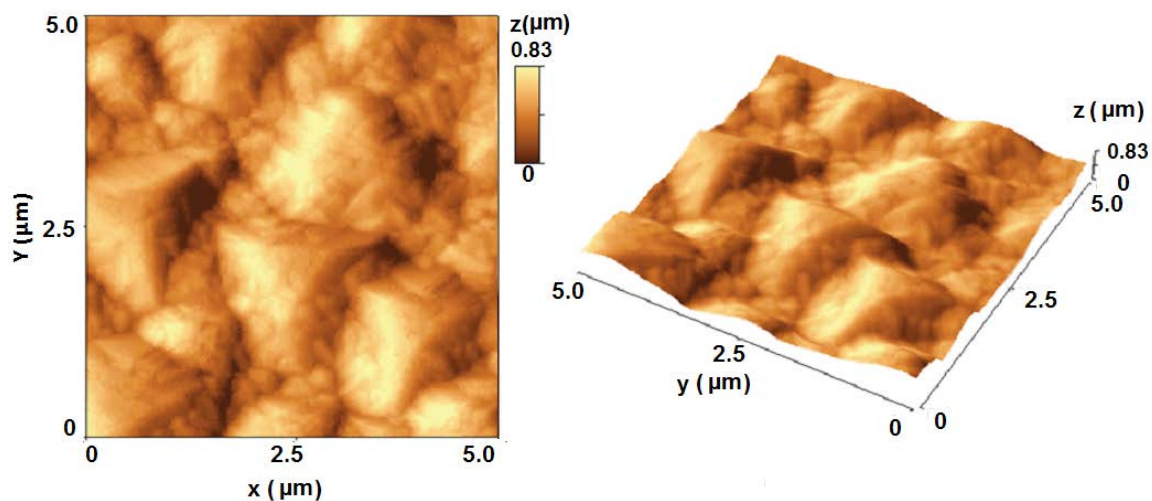


Figure 27. AFM topographic images with 3D view of electrodeposited copper films on Au-TFE electrodes from 0.050 M CuSO_4 + 1.0 M 1-propanol solution. Electrodeposition time: 5 minutes; film thickness: 220 ± 20 nm.

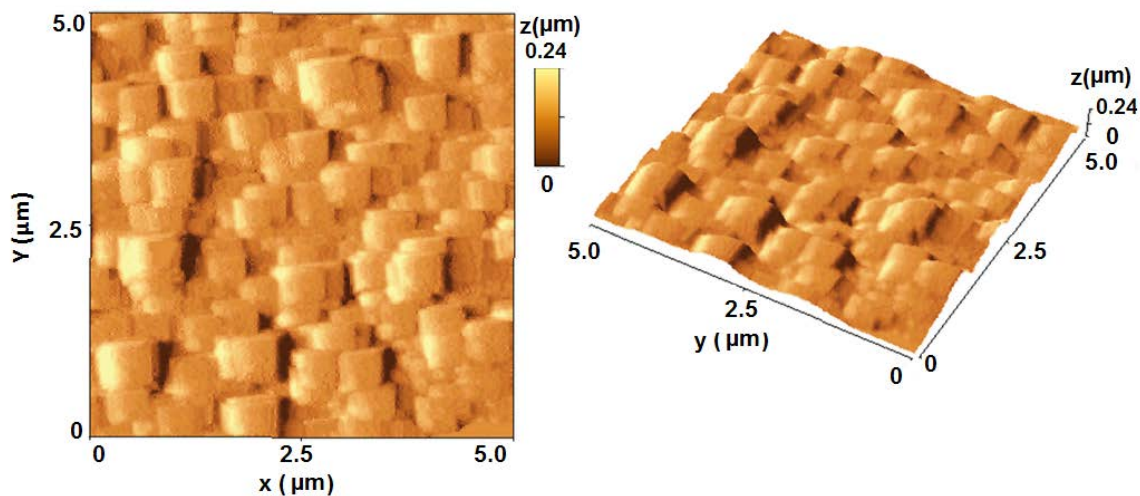


Figure 28. AFM topographic images with 3D view of electrodeposited copper films on Au-TFE electrodes from 0.050 M CuSO_4 + 0.0050 M MG solution. Electrodeposition time: 5 minutes; film thickness: 220 ± 20 nm.

The results of Figure 26-28 indicate that the size of the electrodeposited copper micro-crystallites is reduced in the sequence of additive-free (largest), with 1-propanol, and with MG (smallest) electrolyte solutions.

3.3.1.1.1. Crystallite Dependence on MG Concentration

It is interesting that copper grains take the shape of square pyramids when growing from the electrolyte with 0.0050 M MG. To find out if the concentration of MG in solution has an effect on the shapes of the electrodeposited grains, we have performed the same experiment with different concentrations of MG in the 0.050 M CuSO_4 electrolyte. For each electrolyte solution, the cyclic voltammograms were taken to determine the half-wave potentials for electrodeposition at each concentration. As a result, the electrodeposition potential was maintained at -310 mV, -380 mV, -440 mV and -500 mV for 0.00010 M, 0.00050 M, 0.0010 M and 0.0050 M MG respectively. Figure 29 presents the topographic images of copper films from different concentrations of MG deposited under their half-wave potentials. While all conditions investigated appear to give rise to the formation of square pyramidal copper grains, the optimal conditions giving rise to these structures appears to be for a MG additive concentration of 0.0050 M.

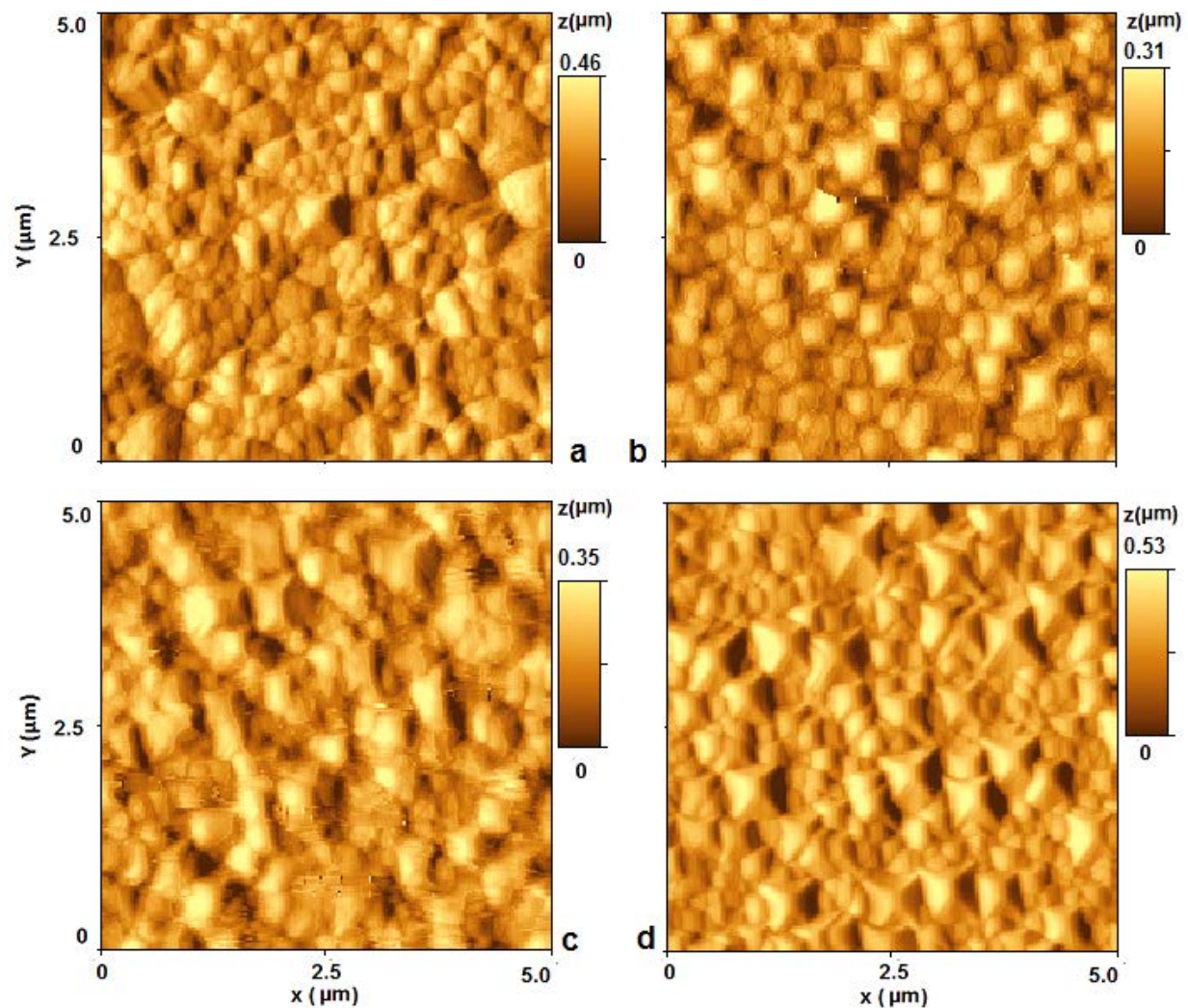


Figure 29. Topographic images of Cu films from 0.050 M CuSO_4 with different concentrations of MG. [MG] and depositing potentials are: a. 0.00010 M and -310 mV; b. 0.00050 M and -380 mV; c. 0.0010 M and -440 mV; d. 0.0050 M and -500 mV. Electrodeposition times are all 5 minutes.

3.3.1.1.2. Crystallite Dependence on Electrodeposition Potential

The effects of electrodeposition potential on the morphologies of the Cu films from 0.050 M CuSO₄ with 0.0050 M MG solution have also been investigated. The AFM topographic images are presented in Figure 30.

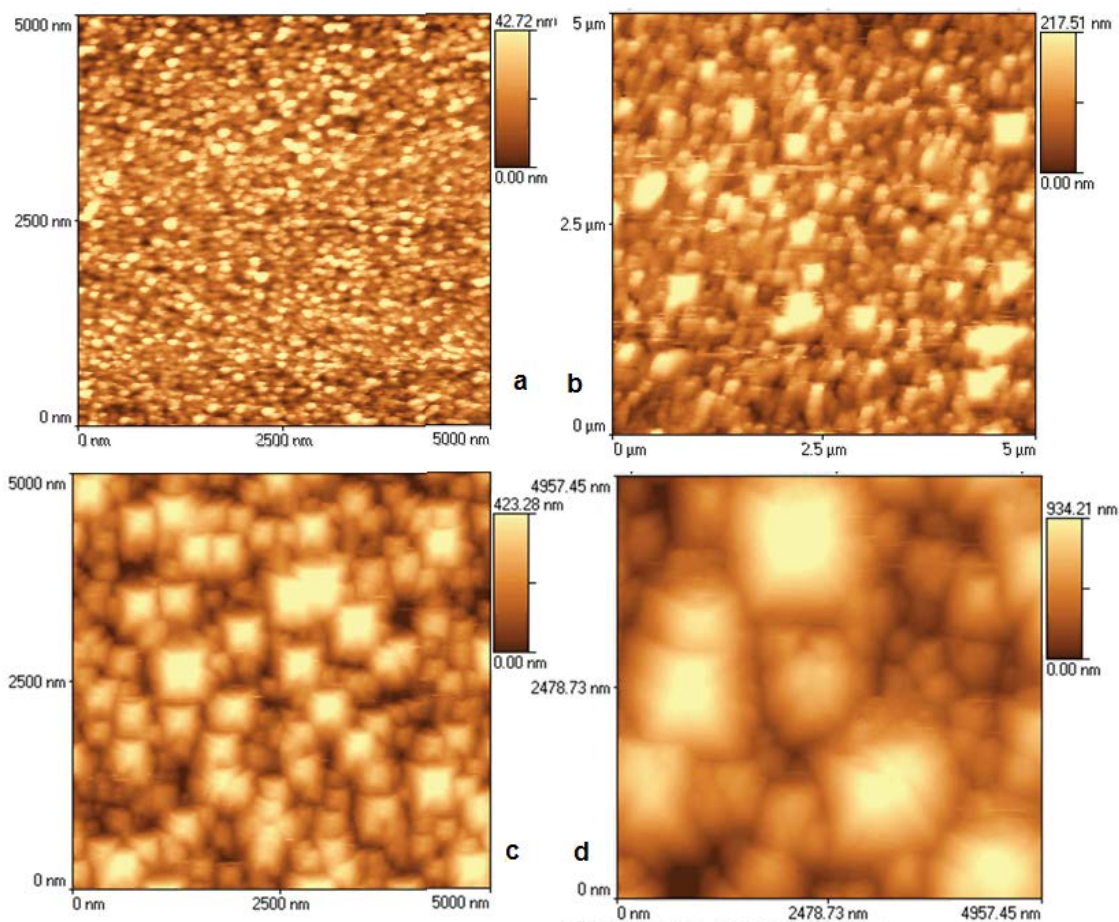


Figure 30. Topographic images of Cu thin films from 0.050 M CuSO₄ + 0.0050 M MG solution for 5 minutes at different electrodeposition potentials: a. -300 mV; b. -400 mV, c. -500 mV and d. -600 mV.

When the cathodic potential is more positive than -400 mV, electrodeposition occurs quite slowly and the resulting copper crystallites are not well developed. When the potential is more negative than -400 mV, the square pyramidal structures begin to form (Figure 30b). At electrodeposition potentials of -500 mV, the square pyramidal structures are fully developed. However, when the electrodeposition proceeds at potentials of -600 mV, the film structure becomes less well defined, and the roughness of the film increases dramatically. It appears that -500 mV is the most suitable potential for the deposition of the square pyramidal copper deposits from 0.050 M CuSO₄ + 0.0050 M MG solution.

3.3.1.1.3. Crystallite Dependence on Copper Film Thickness

The dependence of crystallite size and structure has been investigated as a function of electrodeposition time and film thickness. AFM images of Cu films deposited up to 320 minutes have been analyzed over length scales ranging from 1×1 μm up to 80×80 μm. The roughness and grain size appear to change and are dependent on electrodeposition time or thickness of the Cu films. Copper films from additive-free electrolytes and from electrolytes with the additives 1-propanol and malachite green have been measured. Not surprisingly, as electrodeposition time is lengthened, the thickness of the resulting Cu films on Au-TFE is increased. The total thickness of the Cu deposits can accumulate up to 14 μm. As expected based on our earlier findings, the resulting film morphologies depend on the presence and nature of the additive. Figure 31 shows 5×5 μm three-dimensional topographic images of copper films from 0.050 M CuSO₄ + 0.0050 M MG solution

at different electrodeposition times. The image shows that not only does the shape and morphology of the square pyramidal features become clearer with increasing thickness, but also the grain sizes get larger as the film thickness grows. As a consequence, one can also observe from the z-scale of the image, that as the film grows thicker, the film also gets rougher.

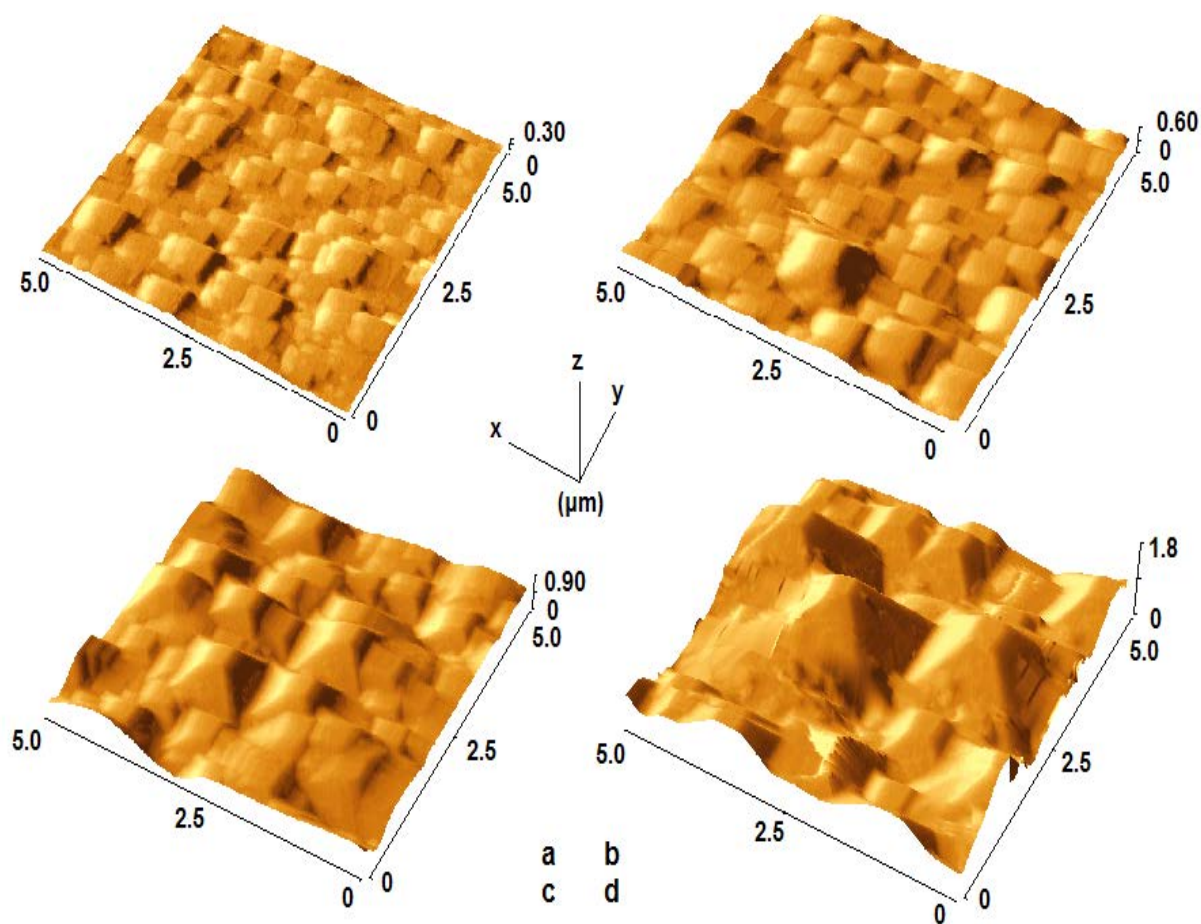


Figure 31. AFM topographic images of different thickness of Cu films from 0.050 M CuSO_4 + 0.0050 M MG solution. Thickness of Cu films are: a. 200 nm ; b. 1600 nm; c. 6400 nm; and d. 12800 nm.

3.3.1.2. Scanning Electron Microscopy Images

Further morphological investigation of the resulting electrodeposited films was carried out using scanning electron microscopy. And the results have been compared with those from AFM. Figure 32 shows SEM images of the electrodeposited copper films from electrolyte with and without additives after 30 min of deposition and resulting film thickness of $1.3 \pm 0.1 \mu\text{m}$. The SEM images reveal copper film morphologies consistent with those observed from AFM images and demonstrate the pronounced effect of additives on the property of deposited copper films. The SEM micrographs presented here show that Cu films deposited from additive-free, 0.050 M CuSO_4 , solution, do not have a regular texture, but the Cu films formed from solutions with additives exhibit regular crystallites, with trigonal pyramidal crystallites from the electrolyte with 1-propanol and square pyramidal crystallites with malachite green. The grain size and film roughness reduce with addition of additives and furthermore, at the thickness of $1.3 \pm 0.1 \mu\text{m}$, even the naked eye can tell that Cu films electrodeposited from solutions with additives become smoother and brighter. It is believed that the change in microstructure could be caused by a change in nucleation processes due to the effects of additives. Although some regular microstructures such as pyramidal features, columnar structures and flake-like crystallites have been reported [46, 83], shape controlled electrodeposits by additives as obtained in this work have not been reported previously. To show the orientation of the Cu crystallites, a zoom-in view of the copper film is presented in Figure 32d.

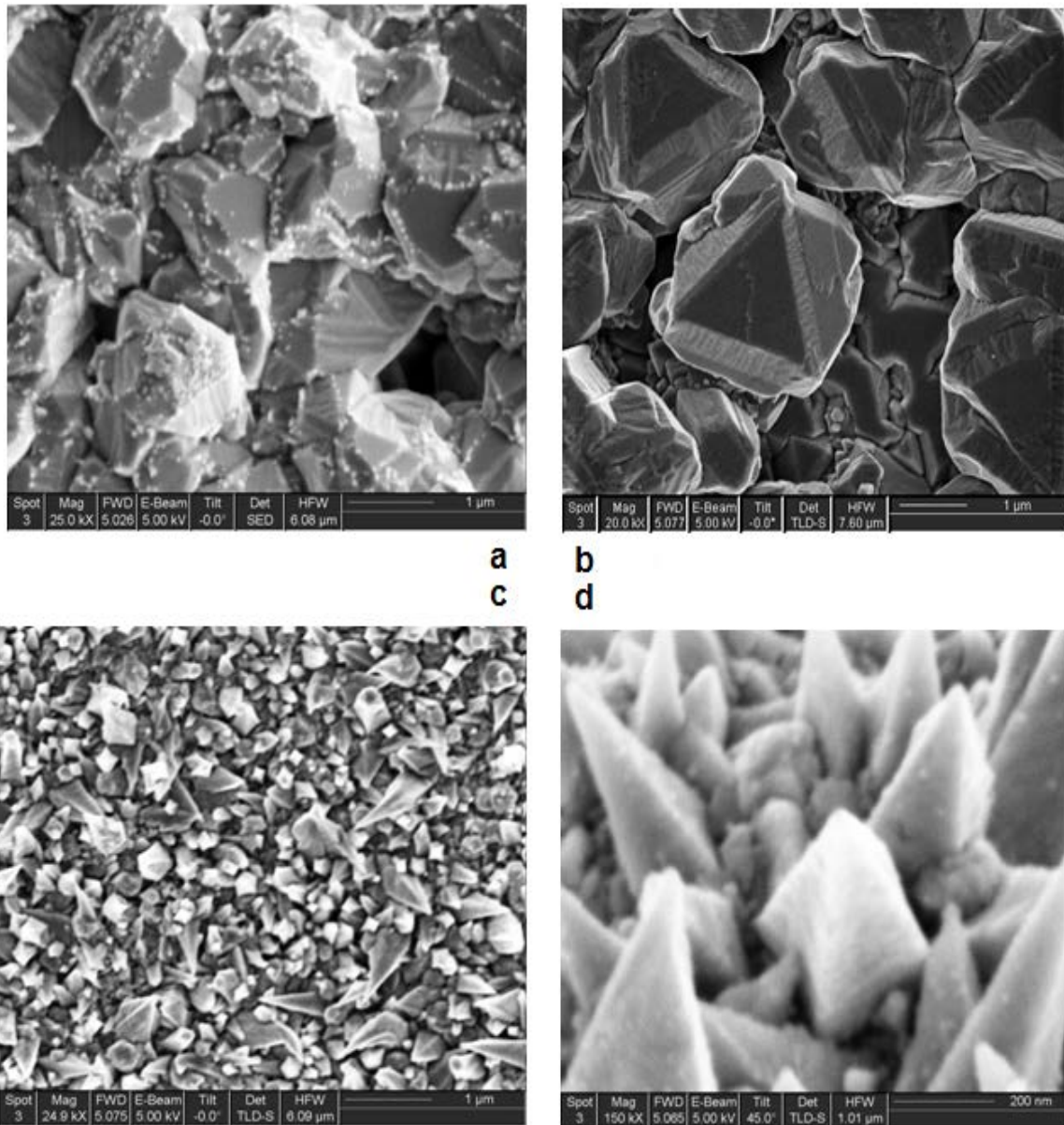


Figure 32. SEM images of electrodeposited Cu films from different electrolyte solutions. a. 0.050 M CuSO₄, b. 0.050 M CuSO₄ + 1.0 M 1-propanol, and c. 0.050 M CuSO₄ + 0.0050 M MG. The Cu films are 1.3 ± 0.1 μm. Tilt angles for a. b. and c are 0°. d. a zoom-in view for c at a tilt angle of 45°.

When the SEM tilt angle is 0° , the surface features are viewed from the top and their projection does not always provide detailed information regarding their shape. When the tilt angle is 45° , the image shows a side view of crystallites. Comparing Figure 32d with c, it appears that most of the pyramidal crystallites of Cu grow normal to the surface of the electrode, with a few crystallites oriented at some other angles from the surface normal.

From the AFM and SEM morphology studies of the Cu deposits, it is clear that additives have a significant effect on the shape of the resulting copper grains. These results indicate the possibility of making tailored metal nanostructure surface by electrodeposition with additives.

3.3.2. *Roughness*

The effect of additives on the morphologies of Cu films deposited on Au-TFE electrodes has been demonstrated qualitatively through AFM and SEM images. The quantitative analyses of the AFM images of Cu films were also performed with the ThermoMicroscopes SPMLab software to illustrate the effect of additives on the roughness of copper films in detail.

i. Area roughness

The area standard roughness of Cu films is usually expressed with the following four parameters,

$$Z_{max} \quad (20)$$

$$\bar{Z} = \frac{1}{N} \sum_1^N Z_i \quad (21)$$

$$R_a = \frac{1}{N} \sum_1^N |Z_i - \bar{Z}| \quad (22)$$

$$RMS = \sqrt{\frac{1}{N} \sum_1^N (Z_i - \bar{Z})^2} \quad (23)$$

where Z_{max} is the maximum height, defined as maximum peak-to-valley range; \bar{Z} is the average height, defined as an arithmetic mean of all height values averaged over the total number of pyramids on the evaluated area; R_a is the average roughness, defined as the arithmetic mean of the deviations in height from the mean value; RMS is the root-mean-square roughness. These grain parameters have been calculated for all copper film samples. Table 5 lists the results from 200 nm thick Cu films on Au-TFE from additive-free 0.050 M CuSO_4 solution and with additives. The Cu films electrodeposited on the Au-mica substrate electrode become less rough after addition of 1.0 M 1-propanol to the electrolyte solutions, and the least rough for the sample formed from the solution with 0.0050 M MG. For reference, roughness of the blank substrate Au-mica is also given in the table. Another way to analyze area roughness is using histograms of AFM image data. The results are consistent with those from the following table. The roughness of deposited Cu films increases with their thicknesses. Figure 33 shows how the

Table 5. The area standard roughness parameters of Cu films of 200 nm. AFM Image is 5×5 μm with resolution of 200 pixels.

Samples	Z_{\max} (nm)	\bar{Z} (nm)	R_a (nm)	RMS (nm)
Au-mica	179	59	3	8
Cu film from 0.050 M CuSO ₄	1104	504	120	160
Cu film from 0.050 M CuSO ₄ + 1.0 M 1-propanol	664	319	96	121
Cu film from 0.050 M CuSO ₄ + 0.0050 M MG	220	106	26	33

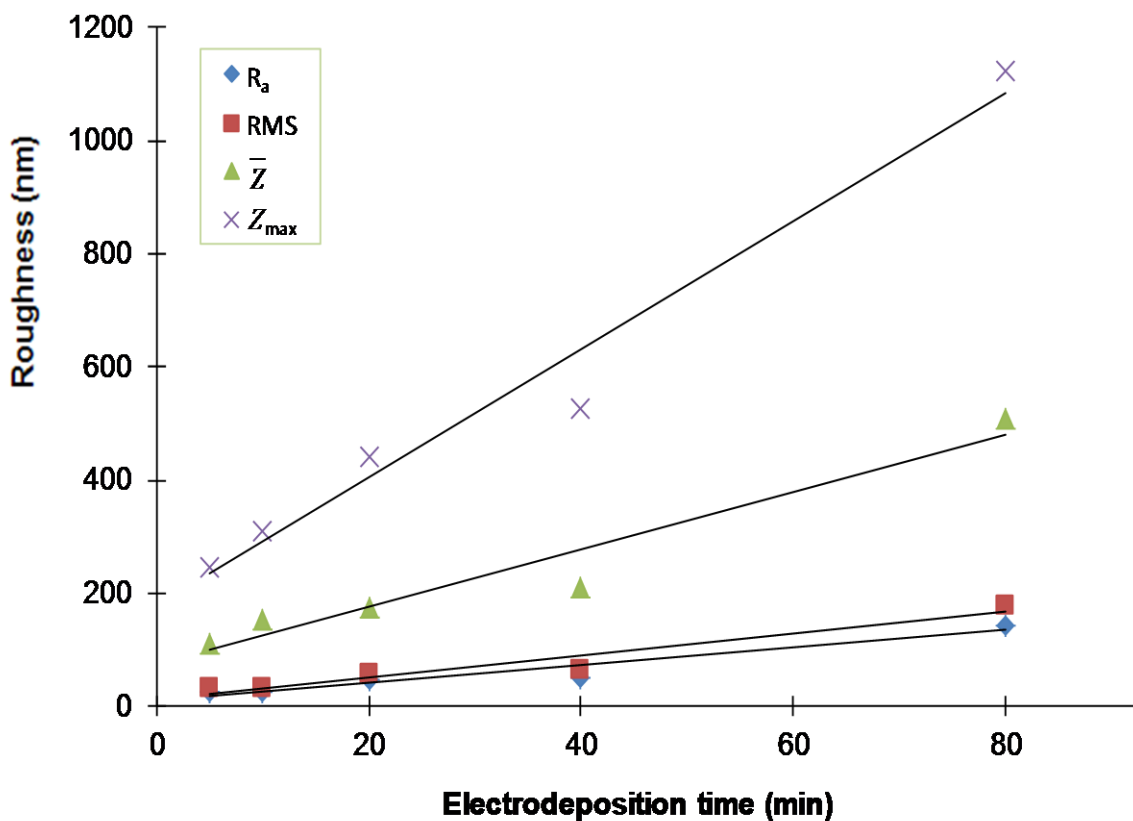


Figure 33. Area roughness changes with electrodeposition time of Cu film on Au-TFE from 0.050 M CuSO₄ + 0.0050 M MG.

roughness parameters depend on the electrodeposition time from the electrolyte solution 0.050 M CuSO_4 + 0.0050 M MG. The analyzed area is $20 \times 20 \mu\text{m}$.

ii. Line roughness

Line profiles of AFM topographic images of electrodeposited copper films were analyzed with ThermoMicroscopes software. The profiles in Figure 34 were obtained from $5 \times 5 \mu\text{m}$ topographic images. A decrease of roughness of deposited Cu films caused by the additives in solution is visible. One can relate observed line features to the shape of copper crystallites.

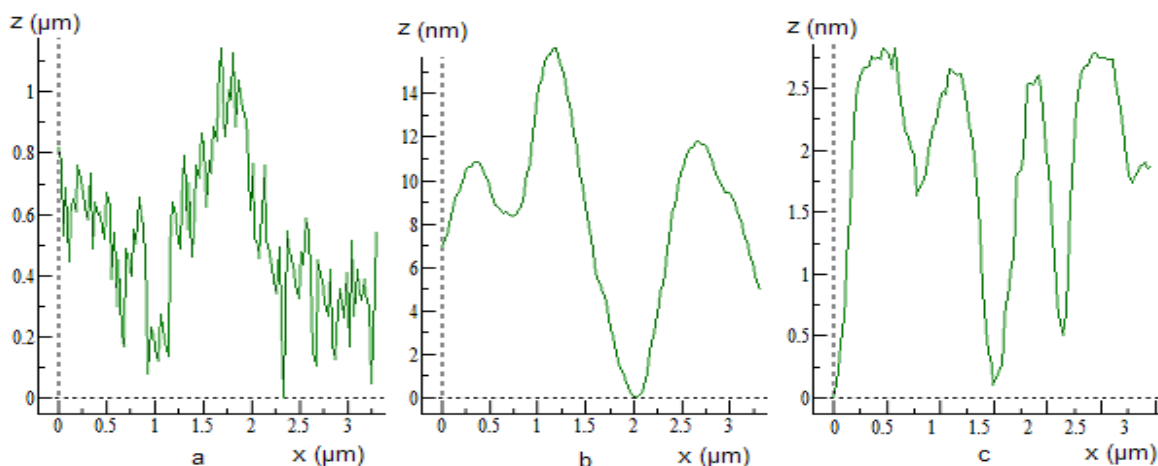


Figure 34. Linear profile of AFM images of Cu films from different solutions. a. 0.050 M CuSO_4 ; b. 0.050 M CuSO_4 + 1.0 M 1-propanol; c. 0.050 M CuSO_4 + 0.0050 M MG.

There is no regular shape for the Cu film formed from additive-free solution, triangle peaks for Cu film from with 1-propanol, and square peak tops (square

pyramids' cross sections) for Cu film formed from solution with malachite green. Similar to area roughness, line profiles can be analyzed using the following parameters.

- R_p : Highest peak. The maximum distance between the mean line and the highest point within the sample.
- R_{pm} : Mean peak profile height. The single highest peak is identified in five line profiles and then averaged.
- R_t : Maximum peak-to-valley height. The absolute value between the highest and lowest peaks.
- R_{tm} : Mean peak-to-valley roughness. It is determined by the difference between the highest peak and the lowest valley within multiple samples in the evaluation area. For profile data it is based on five sample lengths.

The line standard roughness parameters of $10 \times 10 \mu\text{m}$ AFM images of Cu films electrodeposited for 5 minutes from different solutions were analyzed. Results are presented in Table 6. The parameters listed in Table 6 demonstrate that the line roughness of Cu film decreases upon addition of 1-propanol and decreased further by malachite green.

Table 6. The line standard roughness parameters of Cu films of 210 nm. AFM Image is $10 \times 10 \mu\text{m}$ with resolution of 200 pixels.

Sample	R_p	R_{pm}	R_t	R_{tm}
Au-mica	20	5	41	9
Cu film from 0.050 M CuSO_4	595	331	1365	770
Cu film from 0.050 M CuSO_4 + 1.0 M 1-propanol	510	240	960	517
Cu film from 0.050 M CuSO_4 + 0.0050 M MG	402	102	744	177

3.3.3. Grain Analysis

One very important characteristic in thin films is the grain size, which can affect a variety of properties of the film including their electrical, optical and mechanical properties. The grain size distribution in polycrystalline thin films determines the performance of thin film devices [84-86]. The grain properties of Cu thin films are analyzed with the ThermoMicroscopes software through AFM topographic images. The grain size distribution is characterized by the following five parameters:

- D_g : the density of grains.
- V_{avg} : the average volume of grains.
- H_{avg} : the average height of grains.

- H_{max} : the maximum height of grains.
- D_{max} : maximum diagonal of the biggest grain in the whole analyzed area.

The first parameter provides information regarding grain distribution and the others describe the grain size. Table 7 presents the grain parameters of copper for 200 nm thick films and image areas of size $5 \times 5 \mu\text{m}$ obtained from electrodeposited films with and without additives. Table 7 shows that the density of grains is increased upon addition of additives, but that the grain size is decreased. The tendency of the grain parameters indicates that grain size and roughness of Cu films become smaller with the presence of additives in the electrodeposition solutions, which is consistent with the analyses of area and line roughness. All of the parameters from both area roughness and grain size analysis indicate that the roughness of Cu films from electrolyte solutions containing MG is ~5 times smaller than that of Cu films from additive-free solutions. Since it is generally accepted that hardness and strength increase as the grain size is reduced [86], we can infer that the Cu film deposited from solution with MG additives is stronger and has improved hardness. Similar levelling and brightening effects of additives on Cu electrodeposits have also been observed for polyethylene glycol (PEG) + Cl^- , and 4,5-dithiaoctane-1,8-disulfonic acid (SPS) + PEG additive systems [13, 46, 83]. However, the smoothing effects of MG demonstrated in this work are more pronounced than those of PEG + Cl^- , and MG appears to produce square pyramidal features of greater quality and density than SPS + PEG [83]. The

trigonal pyramidal features obtained from electrodeposited Cu in the presence of 1-propanol in electrolyte solution obtained from this work, have not yet been seen from the literature.

Table 7. Grain parameter of $5 \times 5 \mu\text{m}$ AFM images of 200 nm thick Cu film on Au-TFE electrodeposited from different solutions.

Samples	D_g (/100 μm^2)	V_{avg} (10^6 nm^3)	H_{avg} (nm)	H_{max} (nm)	D_{max} (nm)
Cu film from 0.050 M CuSO_4	36	10.4	86.8	549.9	3300
Cu film from 0.050 M CuSO_4 + 1.0 M 1-propanol	40	10.3	56.2	332.1	2100
Cu film from 0.050 M CuSO_4 + 0.0050 M MG	76	1.5	19.1	110.1	867

3.3.4. Film Crystallinity

X-ray diffraction (XRD) of the electrodeposited Cu films on Au-mica thin film electrodes was also performed to investigate the effect of additives on the orientation and crystallinity of the Cu crystallites. Figure 35 shows the XRD pattern of Cu films grown on Au-mica thin film electrodes from CuSO_4 solution in the absence of additives. In addition to the XRD signals from copper, the film shows diffraction intensity from the underlying layer of Au and from copper oxide produced in air on the surface of the copper film after electrodeposition. The Cu films deposited from the solutions containing 1-propanol or MG have similar XRD patterns with small changes in their intensities. Figure 36 shows the X-ray diffraction data of the Cu films from different electrolyte solutions in modified form

for clarity of presentation. All of the Cu films exhibit X-ray reflections from Cu (111), (200), (220), (311), and (222) planes, which illustrates the polycrystalline properties of the Cu films. It should also be noted that for all of the electrodeposited Cu films, the strongest X-ray reflections are visible from the Cu (111) planes; the intensity of reflections from Cu (200) are the second highest, which indicates that Cu crystallization from these electrolyte solutions occurs preferentially in the (111) and (200) directions. The intensity from the other

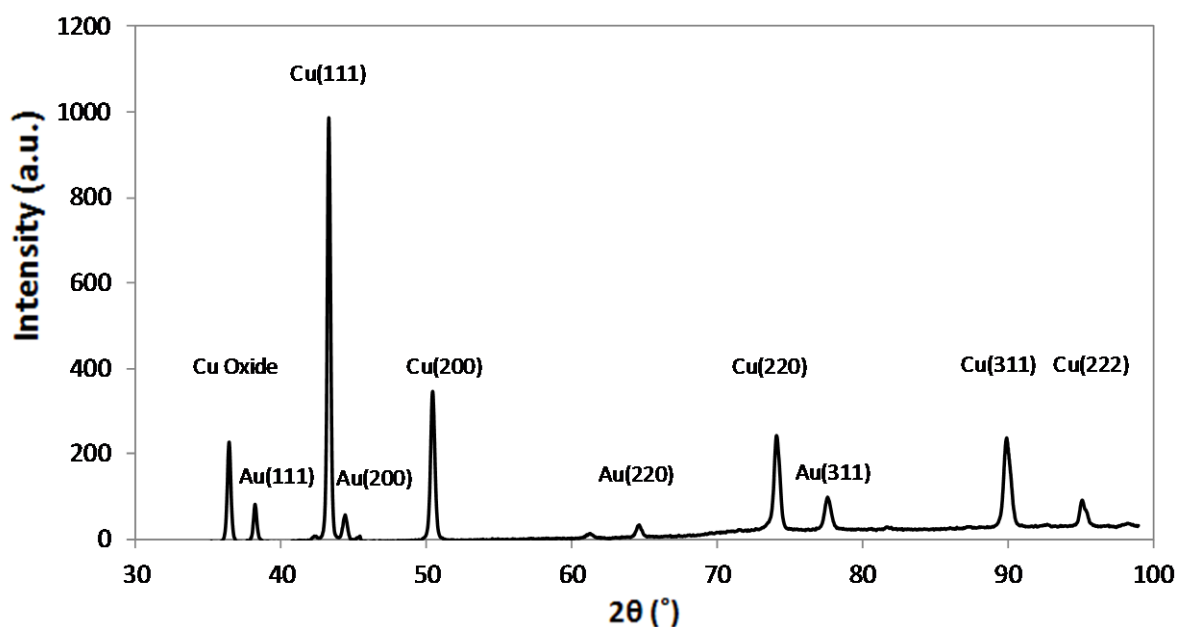


Figure 35. X-ray diffraction patterns of electrodeposited 200 nm thick Cu films on Au-TFE from 0.050 M CuSO_4 . Cu films from solutions with 1-propanol and MG have similar diffraction patterns but the relative and absolute intensities are modified by the additives.

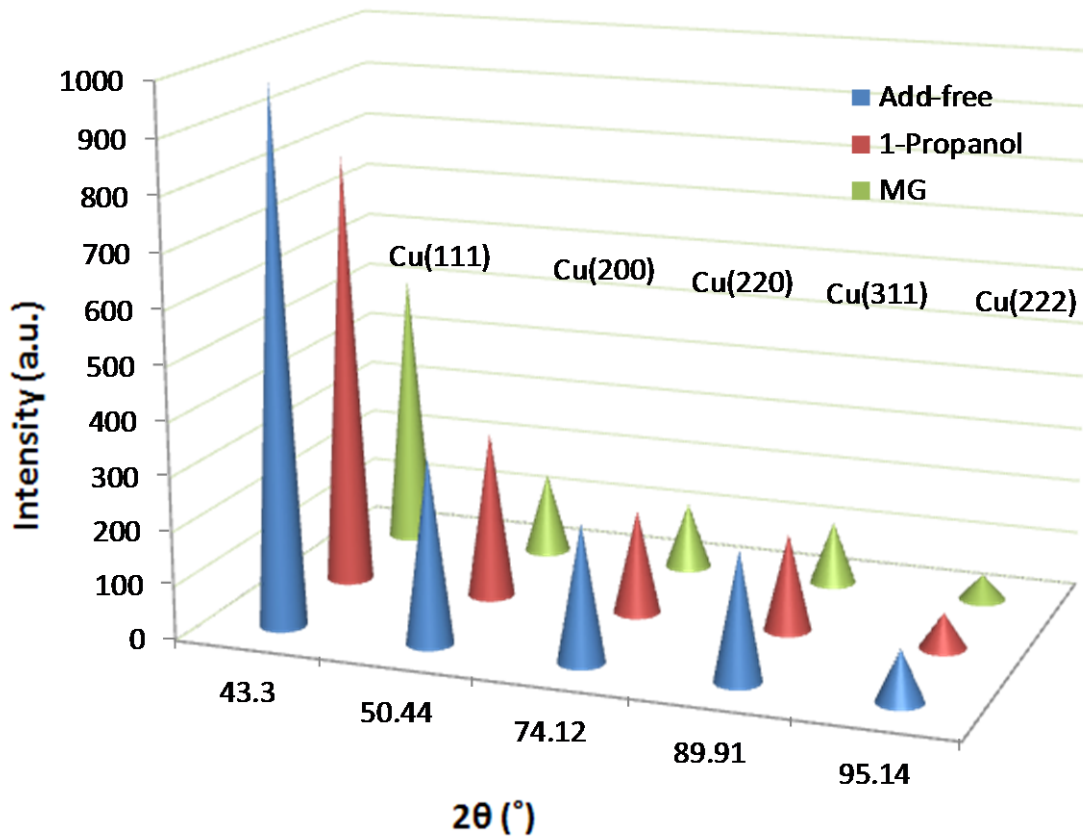


Figure 36. X-ray diffraction of 200 nm thick Cu films electrodeposited from 0.050 M CuSO₄ with additives and additive-free solutions. Cu films from solutions containing 1-propanol or MG have lower intensities.

planes is much weaker. In the case of the Cu film from solutions containing MG, the intensity of all reflections is significantly reduced relative to the other two. Relating these XRD results with the AFM area standard roughness analysis, we find that the Cu films with higher intensity of the (111)-oriented crystallites have rougher surfaces. This result is consistent with that reported by A.K. Sikder et al who have found that the electroplated Cu polycrystalline film that consists of more

(111)-oriented crystallites is rougher than the surface that consists of (110)- and (100)-oriented crystallites [87].

To assess the effect of additives on the preferred orientation of the electrodeposited Cu films, the intensities of X-ray reflections from Cu(*hkl*) were normalized with respect to the intensity of the Cu(111) reflection in the same sample. The relative intensities are tabulated in Table 8 along with the X-ray data of standard Cu powder sample [88]. Comparing to a standard sample expected to have a completely random orientation, shows that electrodeposited Cu films have lower (200) orientation intensities and that both additives films show the effect of a reduced (200) intensity, with the effect being more pronounced for MG. As the (220), (311) and (222) planes show no significant changes relative to the standard sample, it appears that the (111) orientation has dominated the copper crystallization, especially from the solution containing MG.

Table 8. Relative intensities (%) of preferred XRD orientation in Cu films from additive-free CuSO₄, with 1-propanol or MG solutions.

Plane (<i>hkl</i>)	2θ (°)	Add-free	1-propanol	MG	Data
Cu(111)	43.3	100	100	100	100
Cu(200)	50.44	34	37	27	46
Cu(220)	74.12	24	22	21	20
Cu(311)	89.91	22	20	20	17
Cu(222)	95.14	8	6	6	5

3.4. Conclusion

Changes in Cu electrodeposition through the use of additives lead to different characteristics of the resulting Cu films. These characteristics have been analyzed with AFM, SEM and XRD techniques. Analysis of the effects of additives on the morphology and grain properties of electrodeposited Cu films from AFM and SEM investigations are consistent. They reveal that the area roughness and grain size of Cu are decreased by the addition of 1-propanol and MG. The texture of Cu grains changes from non-regular shapes to trigonal pyramids with use of 1-propanol as an additive, and square pyramids with the additive MG. The XRD patterns illustrate that the electrodeposited Cu films are polycrystalline, but that the Cu(111) orientation is preferred over other planes. The additives can increase this preference, especially MG which decreases the intensity of the Cu(200) reflection relative to the intensity of the Cu(111) reflection. The XRD results are in accord with the observed growth of preferential grain shapes in the presence of the additives, as observed in the AFM and SEM studies.

The preferred shapes of Cu grain deposition observed in the presence of additives may result from the selective or preferential adsorption of additive molecules onto particular crystal faces of the growing crystallites. For example, electrodeposition in the presence of the additive MG leads to the preferential growth of square pyramidal copper crystallites. One possible mechanism for this

film growth is that MG molecules may preferentially occupy the surface sites on the (111) surface over those of the (200) surface. Stronger interaction of additive molecules with (111) facet could effectively “block” the deposition of Cu onto this facet, leaving Cu grow faster in other directions (such as the [200]/[100] direction). Figure 37 is a plausible model illustrating the growth of square pyramids while MG is present in electrolyte solution [89].

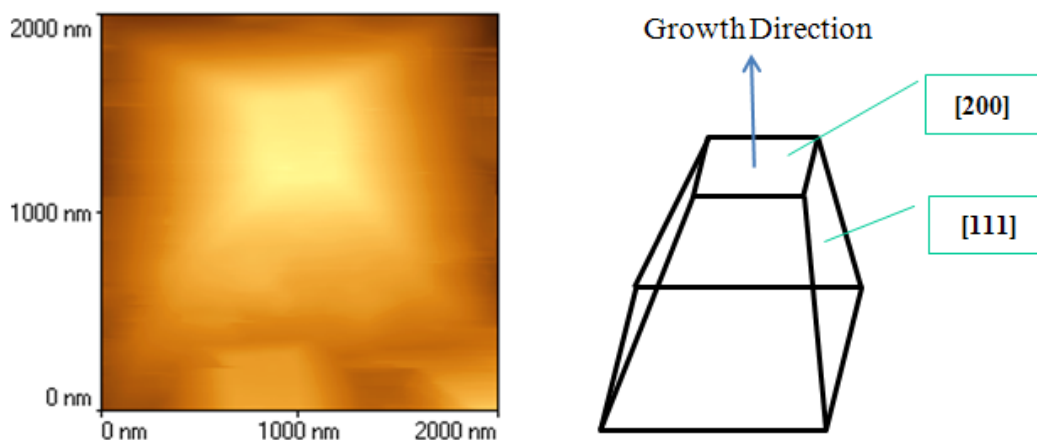


Figure 37. Schematic diagram of Cu square pyramid from CuSO_4 with MG solution. A comparison of AFM image (left) with growing model (right).

The “magical” effects of additives on the morphology of copper deposition stimulated us to investigate the mechanism of these preferential crystallite growth effects in greater detail and to test the model encompassed by Figure 37. The experimental studies described in Chapters 2 and 3 have motivated further study

with *in situ* electrochemical scanning tunneling microscopy (EC-STM), *in situ* second harmonic generation (SHG), and modeling studies to help provide insight into the detailed, molecular level mechanisms of this preferential crystallite growth. The results may help to provide methods to produce customized nanostructured metal surfaces via electrodeposition, a topic of escalating practical importance.

Chapter 4. Electrochemical-Scanning Tunneling Microscopy (EC-STM) of Cu Electrodeposition

4.1. Scanning Tunneling Microscopy (STM)

The scanning tunneling microscopy (STM) is a powerful technique that shows three-dimensional images of a sample. It was invented by Gerd Binnig and Heinrich Rohrer in 1981. The basic idea is to bring a fine metallic tip in close proximity (a few Å) to a conductive sample. By applying a voltage ($E_t \leq 4V$) between the tip and the sample, a small electric current (0.01 nA to 50 nA) can flow from the sample to the tip or reverse. Because the tip is not physically in contact with the sample, the current is produced by electron tunneling. The exponential dependence of the tunneling current on the distance between the tip and sample results in a high resolution imaging capability. A vertical resolution up to 0.01 Å can be achieved. By scanning the tip across the surface and detecting the current and vertical positioning signal, a map of the surface can be generated with atomic resolution. In addition to vertical variation, the lateral electronic state density at the sample surface also influences the tunneling current. The lateral resolution is approximately 1 Å, much lower than vertical. The STM can be used in ultra-high vacuum, air or liquids [90, 91].

4.1.1. *Electron Tunneling in STM*

Quantum mechanics tells us that electrons have both wave and particle like properties. Tunneling is an effect of the wavelike nature. These waves do not end abruptly when meeting a barrier, but taper off quite quickly in the classically forbidden regions. If the barrier is thin enough, the probability function may extend into the next region, through the barrier. A tunneling current occurs when electrons move through a barrier (Figure 38).

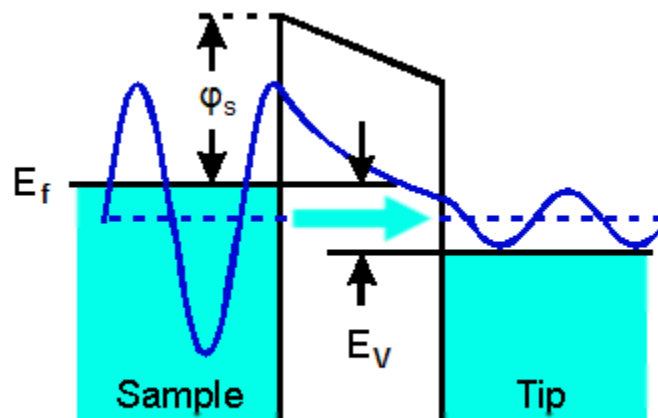


Figure 38. Schematic of electron tunneling in STM. E_f is the Fermi energy, ϕ_s the work function of sample, and E_v the electron energy under application of a bias voltage V .

To find out the probability that electrons with energy E can penetrate the potential energy barrier E_b , a quantum mechanical treatment of the problem is needed. The Schrödinger equation,

$$-\frac{\hbar^2}{2m} \frac{\partial^2 \psi(Z)}{\partial Z^2} + E_b \psi(Z) = E \psi(Z) \quad (24)$$

can be solved to obtain the wave function in the barrier region, where \hbar is the reduced Planck's constant, Z is the position, and m is the mass of an electron. $\psi(Z)$ is energy levels of electrons. In the barrier region, the solution to the equation is,

$$\psi(Z) = \psi(0)e^{-\kappa Z} \quad (25)$$

where

$$\kappa = \frac{\sqrt{2m|E - E_b|}}{\hbar} = \frac{\sqrt{2m\Phi}}{\hbar} \quad (26)$$

Φ is the work function of the metal from which the tunneling current is drawn. The probability of finding an electron that has tunneled through the barrier of the width Z is,

$$W(Z) = |\psi(Z)|^2 = |\psi(0)|^2 e^{-2\kappa Z} \quad (27)$$

The tunneling current is proportional to the probability that electrons can tunnel through the barrier,

$$I \propto \sum_{E_n=E_f-E_V}^{E_f} |\psi_n(0)|^2 e^{-2\kappa Z} \quad (28)$$

In scanning tunnelling microscopy a small bias voltage V is applied so that due to the electric field the tunneling of electrons results in a tunneling current I , which is exponentially dependent on the distance between the tip and sample. With 5 eV as a typical example for a work function value, a change of 1 Å in distance causes a change of nearly one order of magnitude in current. This facilitates the high vertical imaging resolution.

4.1.2. Instrumentation

The components of an STM include scanning tip, piezoelectric controlled height and x-y scanner, coarse sample-to-tip control, vibration isolation, and computer system to control the tip position and acquire tunneling current data. Figure 39 presents a schematic of a typical STM [91]. The resolution of an STM image is limited by the radius of curvature of the scanning tip. Additionally, image artifacts can occur if the tip is not sharp enough, leading to double-tip or multi-tip imaging effects. Therefore, it is essential to develop techniques for making consistently sharp and usable tips. There have been many groups studying STM tips [92-101]. Tip materials span a wide range, but the most often used are tungsten or platinum-iridium, gold, silver and cobalt are used vary frequently [93,

98]. Tungsten tips are usually made by electrochemical etching, and platinum-iridium tips by mechanical shearing [94, 96].

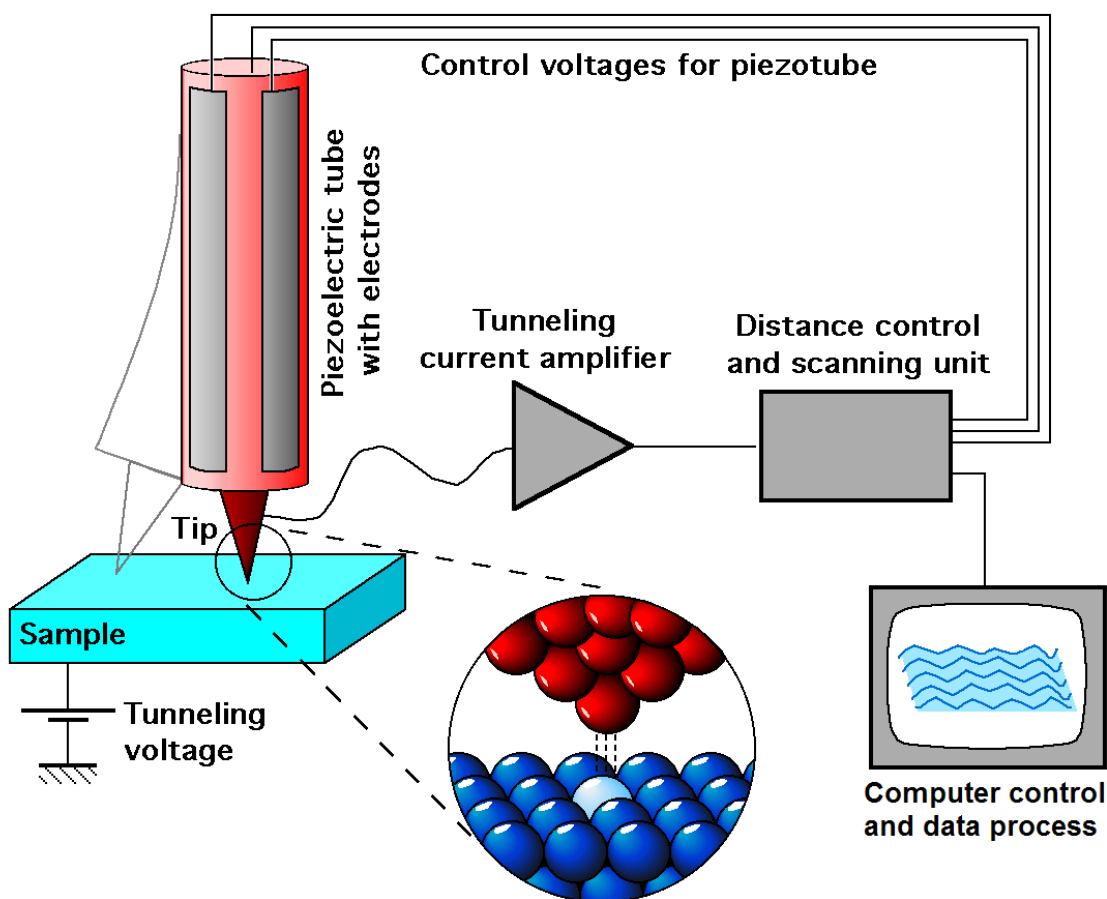


Figure 39. Schematic of a scanning tunneling microscopy

Due to the extreme sensitivity of tunnel current to distance, proper vibration isolation or an extremely rigid STM body is imperative for obtaining usable results. To keep the STM free from vibrations, magnetic levitation, mechanical spring or gas spring systems are often used. A computer is used to maintain and scan the

tip over the samples, acquire and process data, and enhance and measure the obtained images.

4.1.3. Modes of STM

STM is designed to scan a sample in either of two modes: constant-height or constant-current mode, as shown in Figure 40.

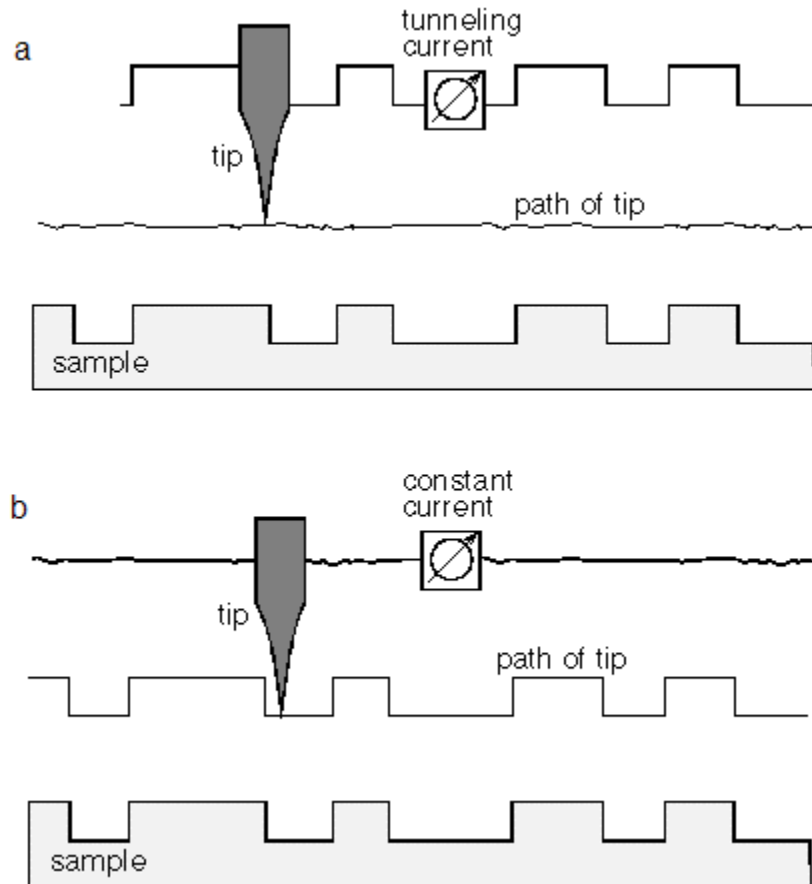


Figure 40. Comparison of constant-height (a) and constant-current (b) modes of STM operation.

In constant-height mode, the tip travels in a horizontal plane above the sample and the tunneling current varies depending on the topography and the local surface electronic properties of the sample. The tunneling current measured at each location on the sample surface constitutes the data set, the topographic image.

In constant-current mode, STM uses feedback to keep the tunneling current constant by adjusting the height of the scanner at each measurement point. For example, when the system detects an increase in tunneling current, it adjusts the voltage applied to the piezoelectric scanner to increase the distance between the tip and the sample. The motion of the scanner constitutes the data set, topographic image. If the system keeps the tunneling current constant to within a few percent, the tip-to-sample distance will be constant to within a few hundredths of an angstrom.

Each mode has advantages and disadvantages. Constant-height mode is faster because the system doesn't have to move the scanner up and down, but it provides useful information only for relatively smooth surfaces. Constant-current mode can measure irregular surfaces with high precision, but the measurement takes more time.

AFM and STM are both techniques of scanning probe microscope (SPM). They can produce high resolution images of samples. However STM is better in acquiring high resolution images because of the exponential dependence of the

tunneling current on distance, whereas in AFM, the image resolution is limited by the distance dependence of the interaction forces between tip and sample, and usually fall off more slowly with distance. AFM is generally more flexible because it can be applied to a larger variety of samples, either conductors or insulators, while STM is typically limited to imaging conductive substrates.

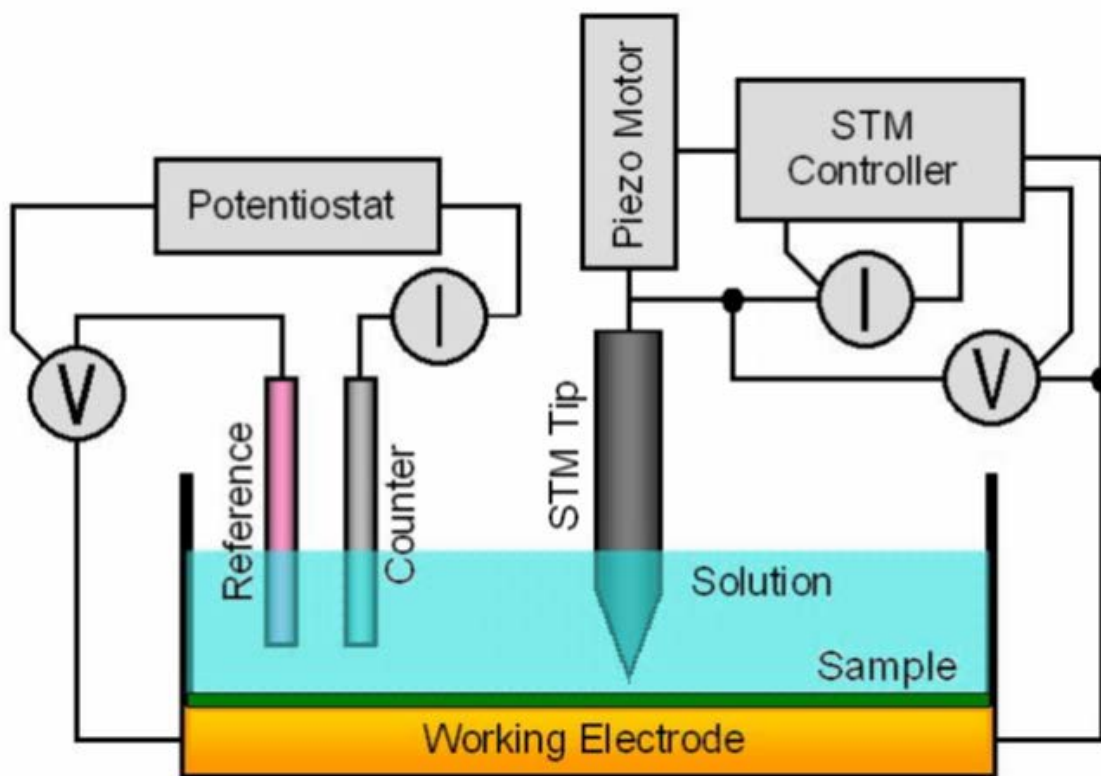


Figure 41. Schematic of an in situ scanning tunneling microscopy.

4.2. *In situ* EC-STM

Soon after the imaging potential of STM was realized in air and in high vacuum, STM operation and imaging was established in liquids and water for imaging electrodes in an electrochemical cell [102]. Figure 41 shows the schematic of an *in situ* electrochemical scanning tunneling microscope (EC-STM).

This configuration is similar to a regular three-electrode electrochemical cell equipped with a potentiostat, but incorporates a liquid-compatible STM to image the working electrode. The potential of the working electrode can be controlled with respect to a reference electrode, and the current is allowed to flow between the working and counter electrodes. The tip and its bias and tunneling current are controlled in separate circuitry. During the electrochemical and imaging processes, the tip (a metal in close proximity to the electrode) must be maintained such that it is not an active electrode in the cell, but is only used to scan the surface of the electrode to monitor the change in morphology while electrodeposition is in progress [103]. This so-called *in situ* EC-STM can provide real-space information with high spatial lateral resolution. As the tip must function in solution, a major technical challenge of this method is to collect the generally small tunneling current signals, while maintaining other currents, such as Faradaic current at the tip, negligible, so that the tip does not affect the electrochemistry [6, 10].

In situ EC-STM has revolutionized electrochemical surface science. It can provide atomic resolution of surfaces in real time while electrode processes are in progress. Compared with STM in air, vacuum and nonelectrolyte liquids, the *in situ*

EC-STM technique is more difficult to operate, because it requires independent and simultaneous control of the tip potential and the potential of the working electrode with respect to a common reference electrode. However, the advantages of *in situ* EC-STM have been established by its powerful application in a variety of electrochemical research studies. *In situ* EC-STM methods can be used to examine the interaction of organic molecules with a metal electrode [104]. The interest in EC-STM studies ranges from the adsorption of anions on metal surfaces to the initial stages of metal electrodeposition and surface reconstruction of electrodes under different potentials [8, 11, 105-107]. While the method has been employed very successfully in many ways, one important point that must be taken into consideration in EC-STM experiments is that, while the influence of the tip is minimized by maintaining its potential such that it does not participate in the electrodeposition process, to some extent, the tip can impede the diffusion of ions through the electrolyte and also shield the area which is being investigated. Care must be taken to operate in a regime where these factors are not limiting, and in the interpretation the resulting STM images.

4.3. Experiment

The configuration of the *in situ* EC-STM for copper electrodeposition on Au (111) and highly oriented pyrolytic graphite (HOPG) electrode surfaces from CuSO_4 solution is based on the diagram in Figure 41. The bipotentiostat (TopoMetrix), piezo motor/scanner and STM controller are from

ThermoMicroscopes. The resulting STM images were treated and analyzed with SPMLab NT 5.01.

4.3.1. Sample Treatment

The samples or working electrodes used for *in situ* EC-STM were single crystal Au(111), Au thin film on mica (Au-TFE) and highly oriented pyrolytic graphite.

A Au(111) single crystal disk is 10 mm in diameter and 1 mm in thickness was provided by MaTeck. Prior to each electrochemical measurement, the gold electrode was cleaned in boiling 6 M HNO₃ for 5 min, washed with copious amounts of Millipore water, hydrogen flame annealed to red hot for 1 min, and cooled in air.

The Au-TFE electrodes were prepared by vacuum evaporation Au on freshly cleaved mica to a thickness of 200 nm (see Section 3.2). The sample was washed with water, ethanol and acetone and dried, then hydrogen flame annealed for 1 min.

Hydrogen flaming annealing was carried out with an anti-backflash arrester, Teflon tubing, quartz plates and a quartz torch narrowing to a fine tip with inner diameter less than 0.25 mm. Everything involved in the annealing, including the fume hood in which the process is carried out should be very clean. The flow of the hydrogen is regulated to be just audible. The torch is lit in darkness, and the flame adjusted to be approximately 4 cm long. The substrate is placed onto the quartz

plate and the quartz plate is gently heated around the substrate (Au single crystal or Au film on mica) to assure even heating and reduced thermal gradients, before bringing the flame tip onto the substrate at a ~30 degree angle. The flame tip is moved back and forth on the substrate until it begins to glow dim orange and is continued to be moved to maintain the orange color for 60 seconds. The substrate is left to cool down, and then transferred to and kept in a closed container before use.

STM images show that both the Au(111) single crystal and Au-mica present Au(111) terraces up to 200 nm wide. So these substrates are generally called Au(111) electrodes for *in situ* EC-STM experiment.

HOPG substrates are freshly cleaved with transparent sticky tape just before it is used. The fresh surface was detected to be atomically smooth with large micron scale terraces.

4.3.2. Tip Preparation

Tips need to be atomically sharp in order to image a surface with molecular or atomic resolution. The preferred materials for tips for STM and EC-STM are platinum-iridium ($\text{Pt}_{0.8}\text{Ir}_{0.2}$). To make a sharp tip, Pt-Ir wire was mechanically cleaved with a cutting tool at approximately 30 degree to the wire. The tip was then sharpened with fine sand paper and observed under a microscope. If the tip was observed to be sharp, it was tested for regular STM operation in air. However, in order to reduce the electro-active area of the tip in contact with the electrolyte, the

tips were coated with Apiezon-wax. An apparatus shown schematically in Figure 42 was developed to insulate the STM tips in a systematic and reproducible way.

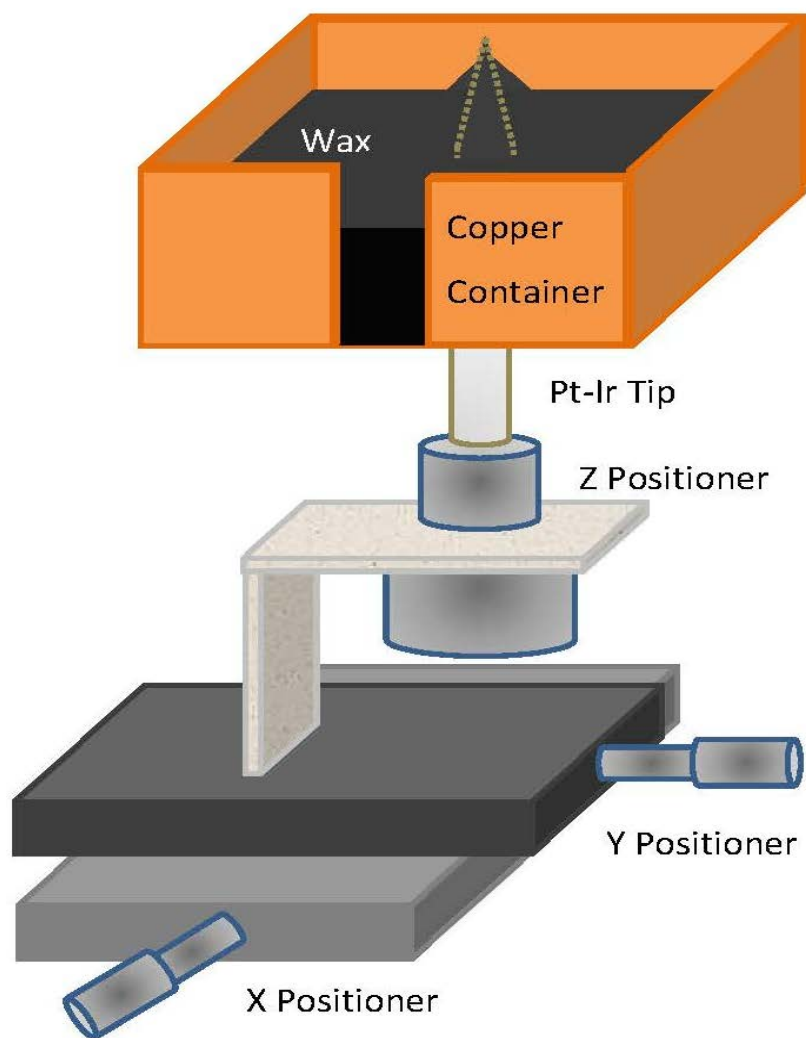


Figure 42. Schematic for EC-STM tip coating.

Solid Apiezon wax is placed in a copper container with a front and bottom opening in the centre of the container. The container is resistively heated with tungsten wires and its temperature controlled by adjusting the voltage of a power supply connected to the tungsten wires. The tip is centred below the bottom opening using X and Y positioners and then lifted through the wax when it is melted so that the tip is just exposed. Finally, the X positioner is used to bring the tip out from the front opening and the coated tip is kept in a closed container until use.

The quality of tip coating was found to be a critical parameter in the performance of the EC-STM. When a tip is correctly coated with Apiezon wax, the 5 to 10 mm top portion of the tip wire is well insulated except for a very tiny spot on the tip which protrudes from the wax coating. This portion remains uncoated because of the surface tension of the wax, and serves as the region where the tunneling current passes to the sample during the *in situ* EC-STM experiment. The resulting performance depends on the tip coating quality and the leakage current of the tip in the electrolyte being measured. If the leakage current is too large, the tip is not qualified for ES-STM experiments because the background leakage currents will far outweigh the contributions from tunneling, i.e. the signal. Too much wax coating will effectively suppress the background leakage current but also prevent adequate tunneling current for imaging. In the experiments described here, the leakage current of the tip was typically maintained at 0.1 to 1 nA under a potential of 1 V.

4.3.3. Cell Construction

The *in situ* EC-STM cell is homemade and constructed as shown in Figure 43.

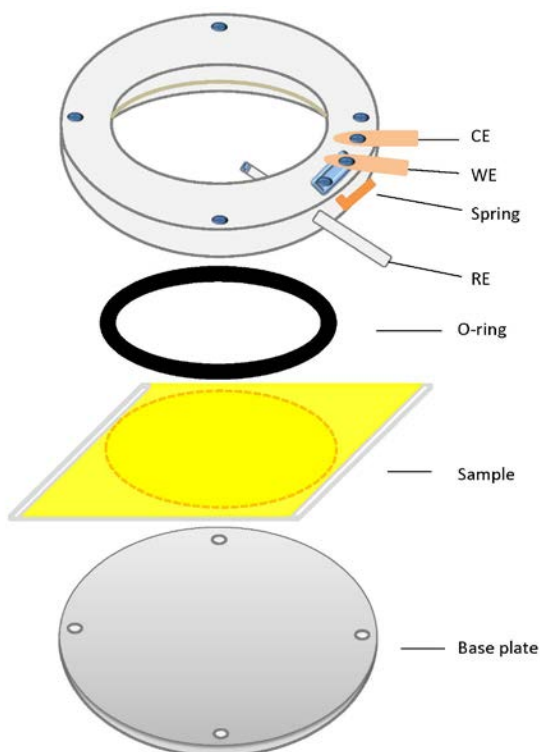


Figure 43. Diagram of components and construction of the EC-STM cell.

The cell body is a Teflon container which is screwed to a metal base and holds the sample in between. The sample, which serves as the working electrode (WE), is a piece of Au(111) single crystal, a Au film on mica or HOPG. The counter electrode (CE) is a Pt wire ring that is placed against the inside wall of the cell. The reference electrode (RE) is a Pt pseudo-reference electrode or a micro Ag|AgCl ([NaCl] = 3.5 M) electrode. The metal spring is used for connecting the WE, and O-

ring for sealing. The electrolytes investigated were 0.050 M CuSO₄ with and without the additives 1-propanol and malachite green.

4.3.4. *In Situ EC-STM Measurements*

During the *in situ* EC-STM, the tunneling current was typically set at 1~5 nA, with a the tip bias of 100~200 mV. The scan rate was 5~20 Hz (lines/s) for regular resolution but 120 Hz for atomic resolution. Scan areas were set to be 200 to 1000 nm² for imaging Cu growth processes, and approximately 5 nm² for atomic resolution trials. To keep the imaging system working stably, the WE potential for Cu electrodeposition was selected to be between 100 mV and -200 mV based on the conditions of the electrolyte system.

In general, there are two ways to perform *in situ* STM. One is to withdraw the tip before electrodepositing and re-approach after depositing to image the area of interest. The other is to maintain the tip in close proximity while depositing, and to image immediately after deposition. The advantage of the first method is that there is no influence of the tip on the deposition process. The disadvantage of this method is the difficulty of relocating the area of interest that can be lost following withdrawal and re-approach of the tip, due to instrumental or thermal drift effects. The second method offers the ease of identification and location of the scan area of interest, but with the drawback of tip influences on the deposition process. During scanning operation, the tip is typically ~1 Å away from the sample, and can impede the diffusion of ions through the electrolyte and also partially shield the area which is being investigated. The resulting growth rate is generally slower than

when the tip is withdrawn. Calculations of the magnitude of these effects from line scan analyses indicate that it takes approximately 10 minutes for copper to grow to similar size features with the tip in close proximity to the surface, as that in 3 minutes with the tip withdrawn.

For the experiments described in this thesis, EC-STM was carried out with the STM tip kept in proximity to the surface, so that imaging of the same scan area was possible without losing registry with the surface. The influences of thermal drift effects were minimized by long warm up times to achieve thermal equilibrium. The topographic and internal sensor STM images were obtained at different stages of copper nucleation and growth.

Prior to investigation by *in situ* EC-STM, the CV's were measured to determine the characteristic potentials of the system, such as the nucleation potential E_n , the cathodic peak potential E_p^c , the crossover potential E_x and anodic potential E_p^a , to which the depositing potential of the sample was referred (See to Chapter 2, similar CV curves are not shown again). To obtain high quality STM images, the parameters that influence the image quality need to be optimized. These include the set point, tunneling current I_t , and tip bias E_t , which control the distance between tip and sample; as well as the proportional gain, integral gain, and derivative gain (PID) which are determined by the sample roughness and local morphology. The deposition potential E_d is referenced to the Pt wire pseudo reference electrode. Pt pseudo reference electrodes are widely used in EC-STM studies because their potential is stable and resistant to possible surface

contamination from electrolytes [6, 104, 108]. However, one drawback of using Pt pseudo reference electrodes is that deposition potentials determined with their use are electrolyte dependent. Where possible, it is preferable to use a well-defined and accepted reference electrode system such as Ag|AgCl.

4.4. Initial Stages of Cu Electrodeposition Imaged by *in Situ* EC-STM

4.4.1. *Cu Electrodeposition On Au(111)*

In this section, we describe the nucleation, or initial stages of copper electrodeposition on Au(111) surfaces in additive-free CuSO₄ solution and in solutions than contain 1-propanol or malachite green solutions, monitored with *in situ* EC-STM.

Figure 44 shows an image of Au(111) after flaming annealing obtained in 0.050 M CuSO₄ electrolyte solution. This image reveals that the electrode surface contains atomically flat terraces. The step edge height of 0.21 nm corresponds to the distance between two Au atomic layers. On these electrodes, *in situ* EC-STM of copper electrodeposition were monitored.

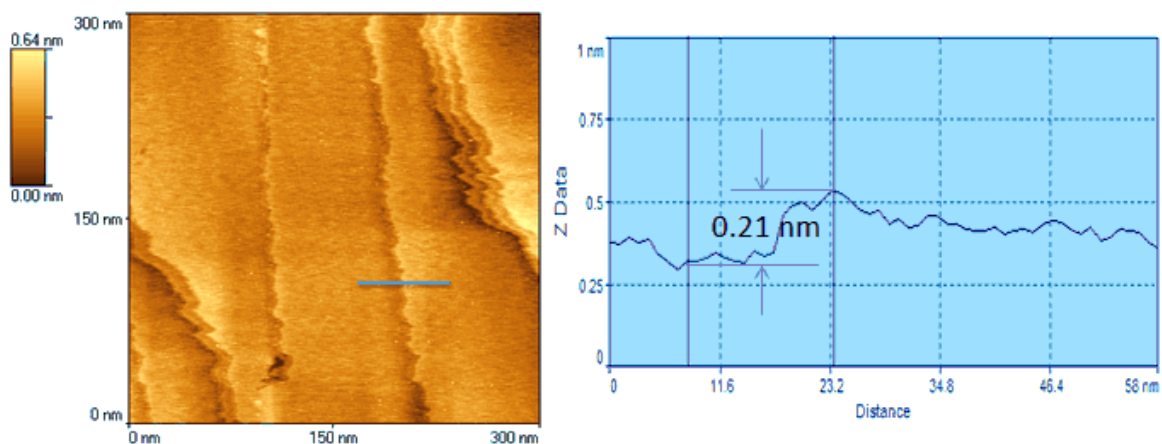


Figure 44. STM of flaming annealed Au(111) surface with terraces and linear analysis. The step height 0.21 nm indicates mono atomic layer.

Figure 45 shows the images of copper nucleation and initial growth from 0.050 M CuSO₄ solutions. Figure 45-**a** is an image of a portion of the clean Au(111) surface before electrodeposition. It is also a typical STM image of an annealed Au(111) surface in liquid, showing the characteristic terraces and atomic scale steps of the single crystal electrode. The spot scanned should be smooth on a sub-nanometer scale and contain identifiable terraces so that the deposition process can be easily monitored. The images **b**, **c**, and **d** are a series of consecutive images obtained at the initial nucleation and growth stages of deposition obtained at different electrodeposition time t_d . The circles give an example showing the changes. The images clearly reveal the change of surface morphology during copper deposition on Au(111). It is clear from these images that copper nucleation begins everywhere, both on terraces and step edges, followed by growth into larger domains.

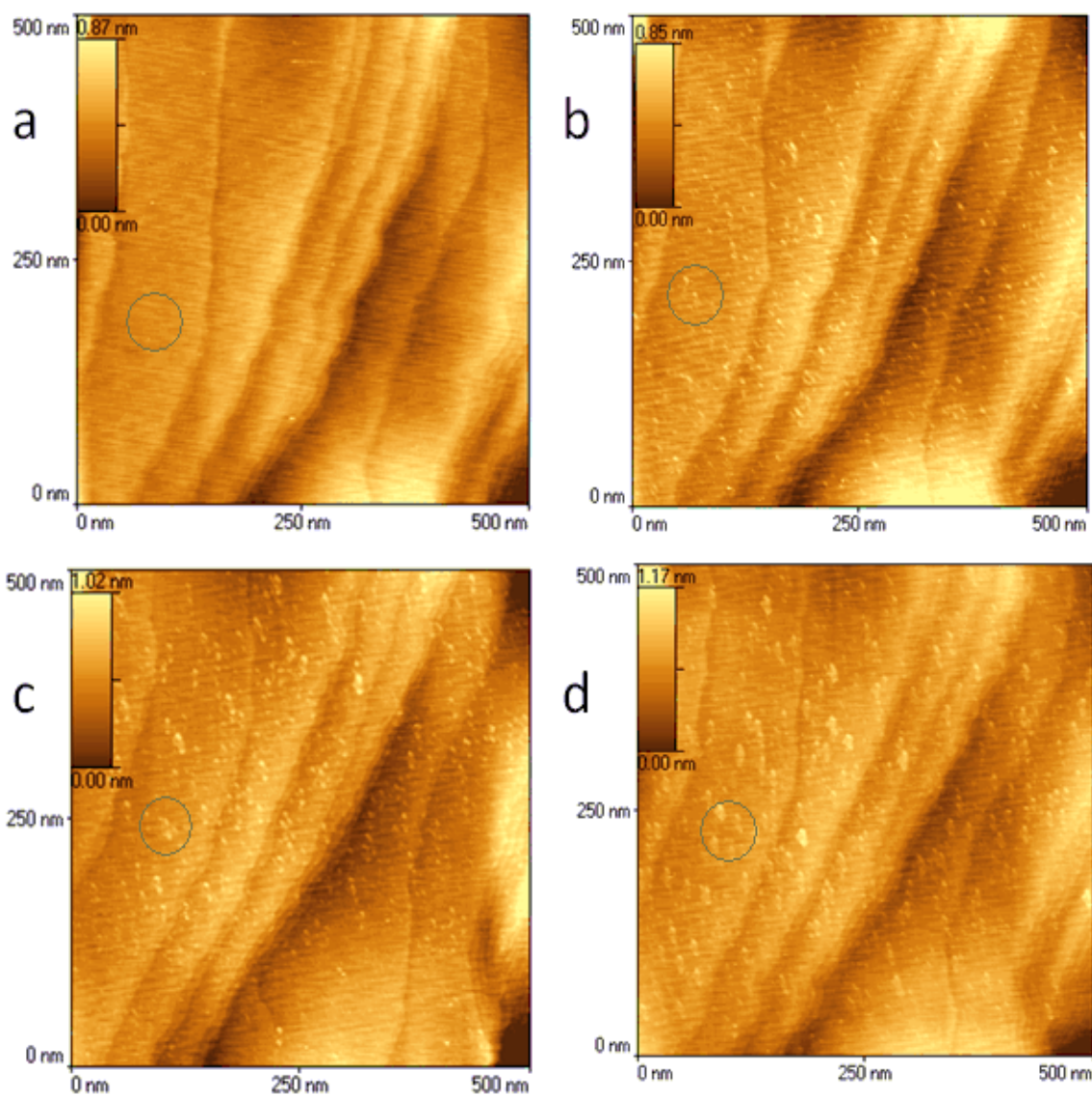


Figure 45. *In situ EC-STM images of Cu electrodeposition at -200 mV (vs. Pt) on Au(111) surface from 0.050 M CuSO₄ solution. Scan setting: PID = (2.0, 1.0, 1.0); scan rate 10 Hz, $I_t = 1$ nA and $E_t = 100$ mV. a. before electrodeposition, $z = 0.87$ nm. b. $t_d = 11$ min, $z = 0.85$ nm. c. $t_d = 34$ min, $z = 1.02$ nm. d. $t_d = 100$ min, $z = 1.17$ nm.*

After 100 minutes of deposition under these conditions, analysis of the images in Figure 45 indicate that resulting Cu islands are approximately 16 nm wide and 0.30

nm high. As the equilibrium potential of Cu^{2+}/Cu deposition is -300 mV vs. the Pt pseudo reference, these Cu crystallites (deposited at -200 mV) were formed at under-potential deposition (UPD) conditions.

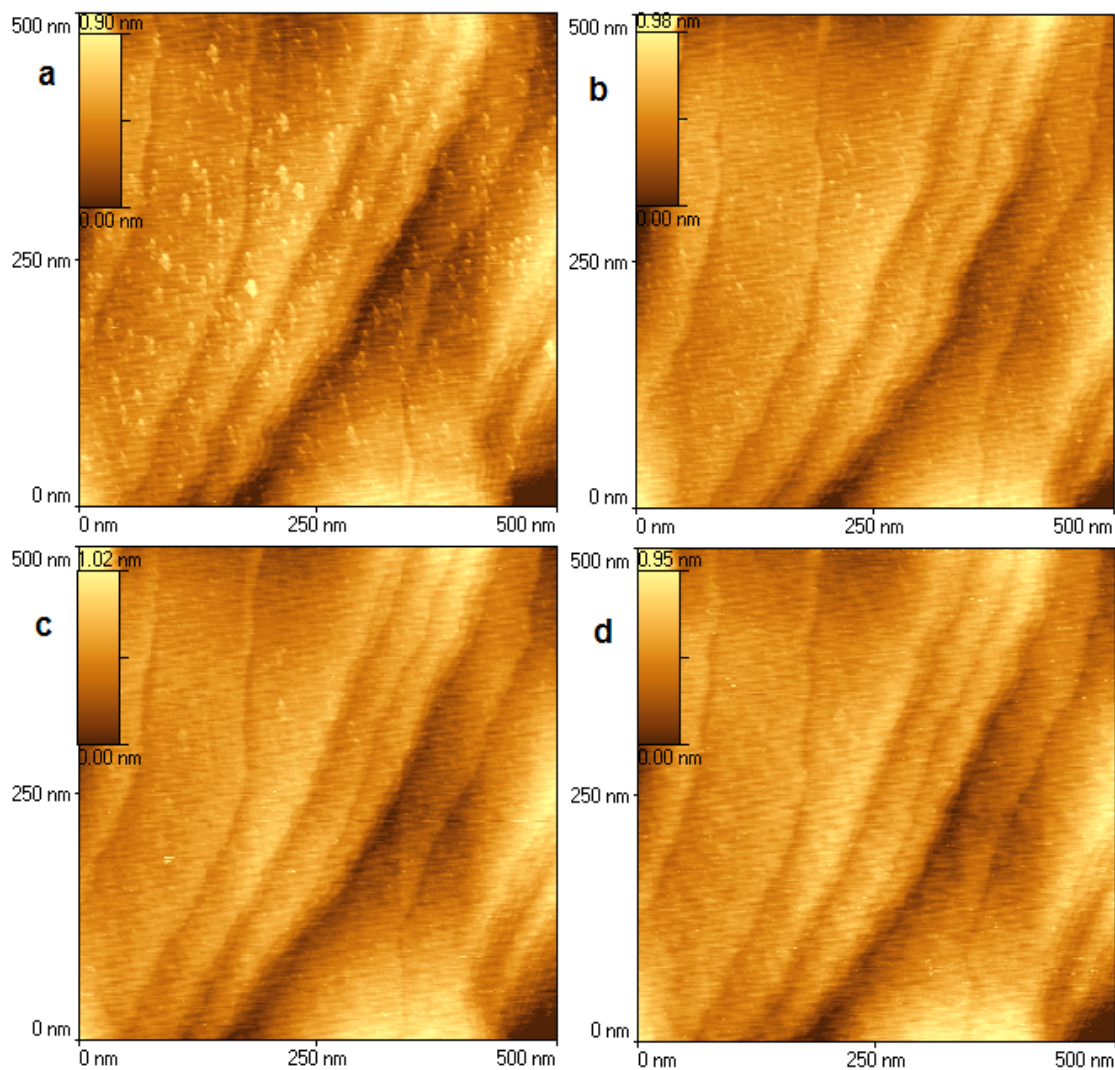


Figure 46. *In situ EC-STM images of Cu dissolving at 0 mV (vs. Pt) on Au(111) surface in 0.050 M CuSO_4 solution. Scan settings: PID = (2.0, 1.0, 1.0); scan rate 10 Hz, $I_t = 1$ nA and $E_t = 100$ mV. a. newly deposited Cu grains. b. $t_s = 2$ min. c. $t_s = 4$ min. d. $t_s = 6$ min.*

In addition to examining the nucleation and growth of copper electrodeposits, *in situ* EC-STM allows one to examine the reverse process, in which freshly deposited copper undergoes dissolution at dissolving potential E_s . Figure 46 shows the process.

Copper deposited under -200 mV (vs. Pt) for 100 minutes (Figure 46 image **a**) dissolves at a potential of $E_s = 0$ mv (vs. Pt) in 6 minutes. Images **b** to **d**, illustrate that as the dissolving time t_s increases, the nanoscale copper deposits become smaller in size and fewer in number, and finally disappear. Image **d** shows that the area after deposition and dissolution is recovered and is the same as the surface quality shown in Figure 45 image **a**. The electrodeposition process is completely reversible.

Figure 47 presents a 3-dimensional view of *in situ* EC-STM images of Cu electrodeposition at -300 mV (vs. Pt) on Au(111) surface from 0.050 M CuSO₄ solution. The line profile measurements show that the Cu island has grown to a height of 10 Cu-atomic layers and a width of 15 Cu-atomic distances. During these EC-STM studies, the experimental system was modified to include a standard and well accepted reference electrode, rather than the Pt pseudo reference electrode. As discussed, use of a true reference electrode allows one to quantify the potentials measured in an absolute way, independent of the particular electrolyte conditions employed. The measured potentials with respect to the common reference electrode (Ag|AgCl in 3.5 M NaCl) in our case can then be directly compared to the potential of a normal hydrogen electrode (NHE) and tabulated

standard reduction potentials of many redox couples. The Pt pseudo reference electrode was found to have a potential of 380 mV vs. Ag|AgCl (3.5 M NaCl) by direct determination. The potentials reported for all further EC-STM experiments described in this thesis are reported with respect to the Ag|AgCl (3.5 NaCl) reference electrode.

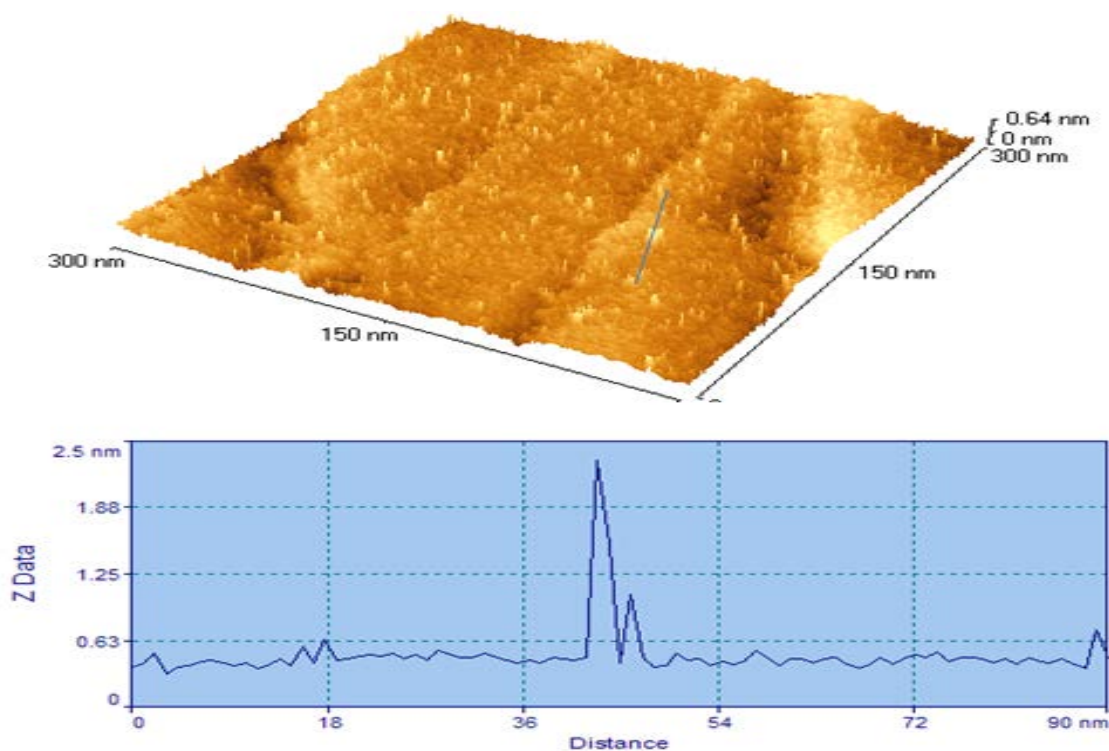


Figure 47. A 3-dimensional view of in situ EC-STM images of Cu electrodeposition at -300 mV (vs. Pt) on Au(111) surface from 0.050 M CuSO₄ solution. Scan settings: PID = (2.0, 1.0, 1.0); scan rate 10 Hz, I_t = 1 nA and E_t = 100 mV, t_d = 3 min. The linear analysis shows the deposited Cu islands are up to 2.0 nm high and 3.0 nm wide.

Figure 48 presents the *in situ* EC-STM images obtained in 0.050 M CuSO₄ solution with the Ag|AgCl reference electrode. Figure 48-a shows the clean Au(111) surface onto which the nucleation of Cu is examined.

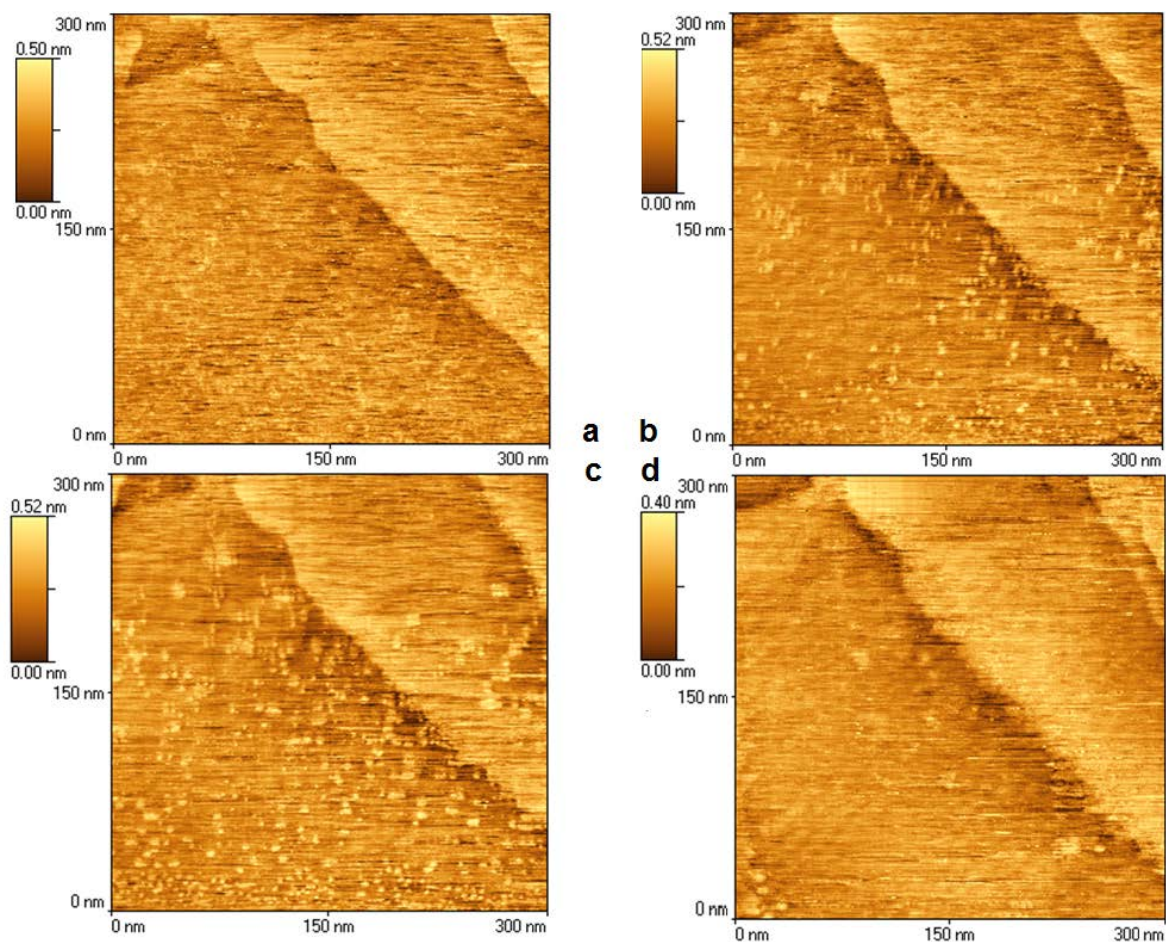


Figure 48. *In situ* EC-STM images of Cu deposition at 100 mV (vs. Ag|AgCl) and dissolution at 500 mV, on the Au(111) surface in 0.050 M CuSO₄ solution. Scan settings: PID = (2.0, 1.0, 0.0); scan rate 7 Hz, $I_t = 1$ nA and $E_t = 100$ mV. a. Initial image before deposition. b. $t_d = 4$ min. c. $t_d = 8$ min. d. $E_s = 500$ mV, $t_s = 1$ min.

The deposits formed at a potential of 100 mV (vs. Ag|AgCl) grow everywhere, both on the terraces and step edges without preference (images **b** and **c**). Figure 48-d shows the image of the area of interest following oxidation of the surface at 500 mV. Under these conditions, the previously deposited copper is removed from the substrate, and the clean Au(111) electrode is recovered. Comparison of Figure 47 and Figure 48 indicate that, as expected, the nature of the reference electrode does not affect the way copper nucleates and grows on Au(111).

Figure 49 shows a portion of the gold electrode after 10 minutes of deposition at the 100 mV deposition potential.

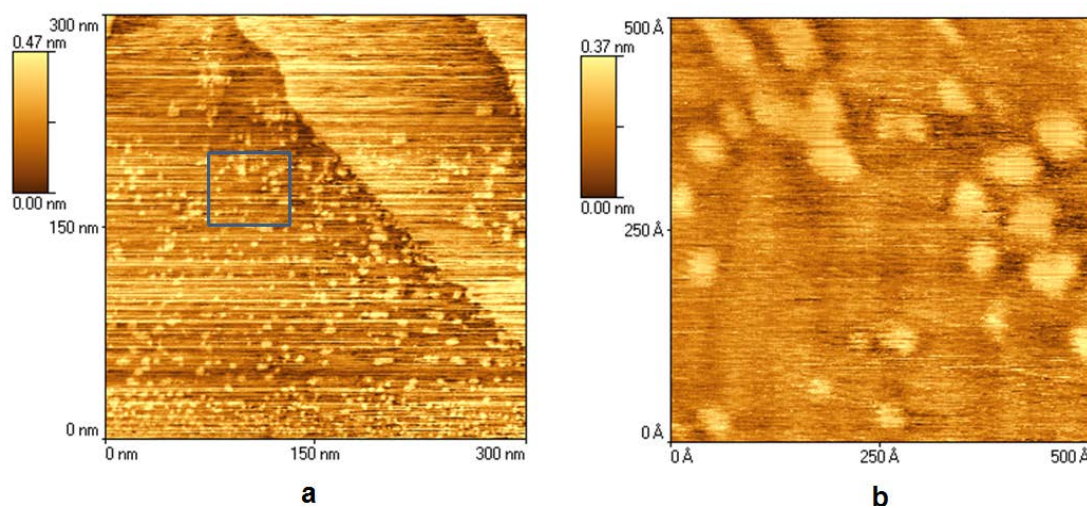


Figure 49. *In situ EC-STM images of Cu deposition at 100 mV (vs. Ag|AgCl) on the Au(111) surface in 0.050 M CuSO₄ solution. Scan settings: PID = (2.0, 1.0, 0.0); scan rate 7 Hz, I_t = 1 nA and E_t = 100 mV. a. t_d = 10 min. b. a close look at the selected area.*

Image **a** shows a 300 nm x 300 nm region and image **b** shows an expanded image of the marked region in image **a**, showing more clearly the features of the growing copper crystallites on the Au(111) surface. Measurements from image **b** show that the deposited copper grew in numerous domains up to 5.3 nm in width and 0.33 nm in height. As the equilibrium potential of 0.050 M Cu²⁺/Cu was 96 mV vs. the Ag|AgCl (3.5 M NaCl) electrode and the nucleation potential was 100 mV, i.e. anodic with respect to the equilibrium potential for bulk deposition, this deposition process was carried out at underpotential conditions [106].

4.4.1.1. Effect of Additives

The initial stages of copper nucleation on the Au(111) surface from 0.050 M CuSO₄ with 1.0 M 1-propanol were monitored with *in situ* EC-STM. Figure 50 shows the morphology changes of the surface while the sample potential was controlled by potential step negatively. After the cell was connected, the STM tip was approached to the surface of the sample. If the sample potential is anodic enough, there will be no copper deposited onto the surface of electrode. Image **a** was obtained at 300 mV and this morphology could be maintained by fixing the initial potential E_i at this value, There was no current flow at this potential and the image shows the features of a clean gold surface. When the potential is gradually lowered to $E_d = 150$ mV the onset of copper growth is observed as a formation of copper nuclei (image **b**). A series of consecutive images were obtained at 150 mV to find out that there was no significant change of the morphology of the surface,

which indicated that there was a balance between deposition and dissolution of copper at this potential.

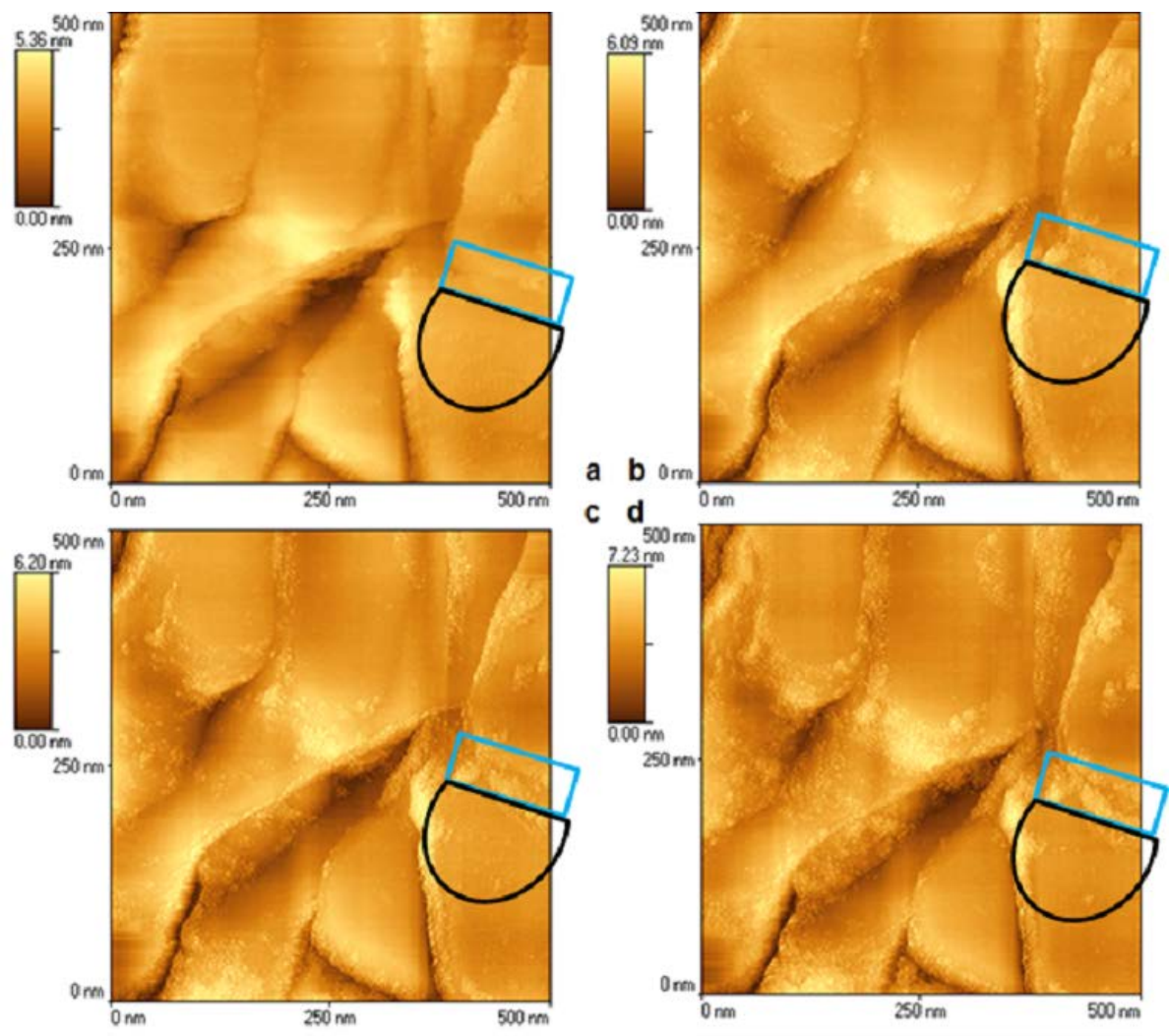


Figure 50. *In situ EC-STM images of Cu depositing on Au(111) surface in 0.050 M CuSO₄ + 1.0 M 1-propanol solution, by potential step. Scan settings: PID = (2.0, 1.0, 0.0); scan rate 6 Hz, I_t = 2 nA and E_t = 100 mV. a. E_i = 300 mV (vs. Ag/AgCl, the same for following), no deposition. b. E_d = 150 mV, t_d = 4 min. c. E_d = 140 mV, t_d = 4 min. d. E_d = 130 mV, t_d = 4 min.*

If E_d was stepped lower to 140 mV and 130 mV, there were more copper deposits and the surface morphology changed (images **c** and **d**, respectively). On the basis of CV measurements, the equilibrium deposition potential of 0.050 M Cu^{2+}/Cu in the presence of 1-propanol is 20 mV vs. Ag|AgCl (3.5 M NaCl). The lowest potential in the last step was 130 mV which was more anodic than the equilibrium potential. Deposition under this potential is a UPD process. Closer examination of Figure 50 **b-d** shows that the deposition occurs primarily at the step edges with deposition on the terraces occurring to a lesser extent. An example of step edge (in rectangle) and partial terrace (in hemisphere) is given in the images to show the nucleation and growth of copper crystallites. The step edge is the favorite site for Cu deposition.

Comparison of Figure 50 with Figure 48 provides direct evidence that 1-propanol has an effect on the nucleation and growth of copper on Au(111). Underpotential deposition from additive-free CuSO_4 solution, showed that nucleation occurred everywhere, without preference, on both the Au(111) terraces as well as their step edges. When 1-propanol was added into the electrolyte, the copper crystallites predominately formed along the step edges, the degree of nucleation was significantly smaller on the terraces. 1-propanol has changed the mechanism of copper nucleation.

Figure 51 shows the record of morphological changes of the Au(111) surface during copper nucleation from CuSO_4 solution with addition of MG. When the sample potential was lowered from the initial potential E_i of 200 mV, at which

the clean Au(111) surface features were imaged (image **a**), no copper nuclei or small crystallites were observed to form and grow on the terraces or edges.

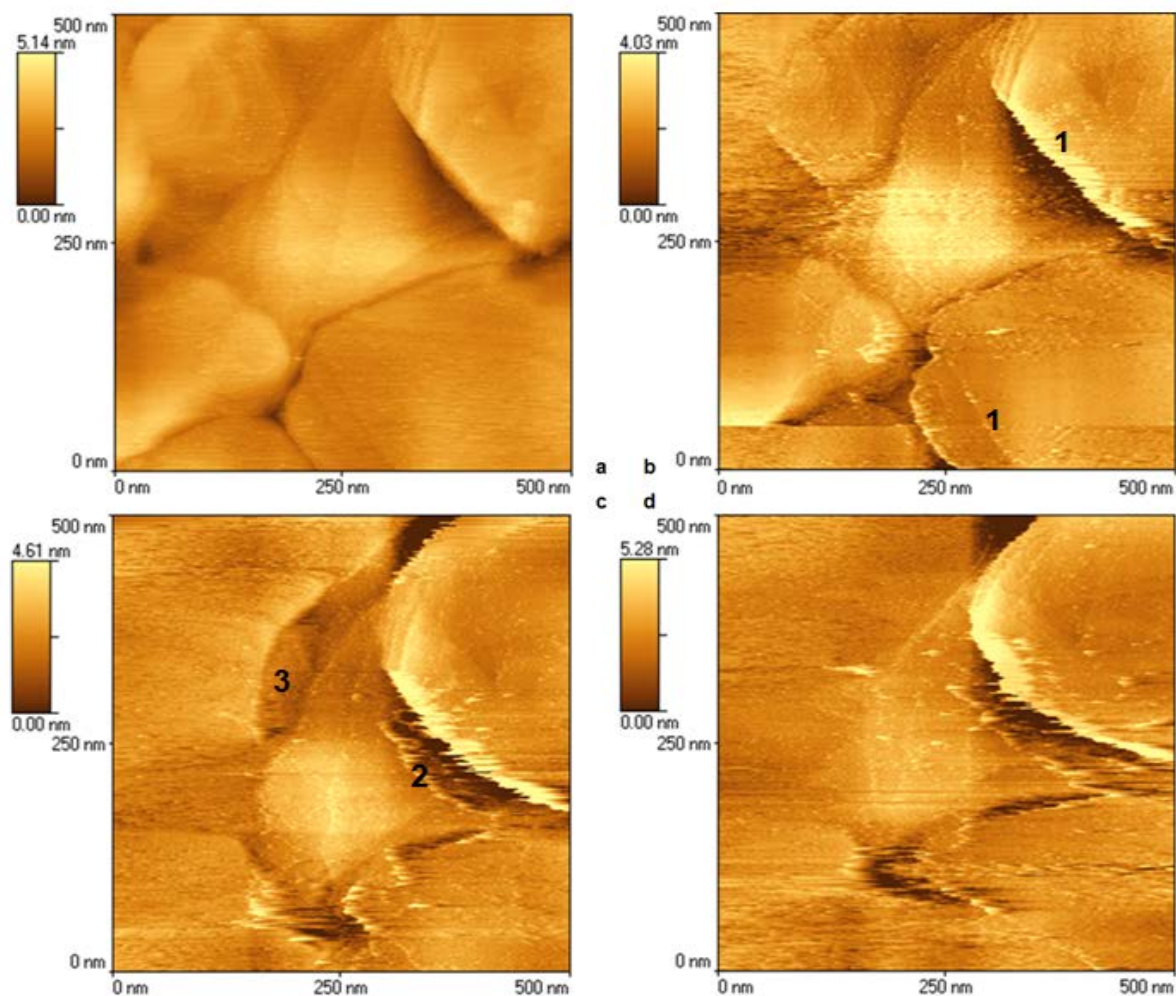


Figure 51. *In situ EC-STM images of Cu deposition on the Au(111) surface in 0.050 M CuSO₄ + 0.0050 M MG solution, by potential step. Scan settings: PID = (1.0, 1.0, 0.0); scan rate 8 Hz, I_t = 1 nA and E_t = 200 mV. a. E_i = 200 mV (vs. Ag/AgCl), no deposition. b. E_d = 90 mV, t_d = 4 min. c. E_d = 70 mV, t_d = 4 min. d. E_d = 50 mV, t_d = 4 min.*

Rather the edges of the Au(111) terraces, were themselves observed to grow. At a sample potential of 90 mV (image **b**), the number “1” in the image indicates regions where the edges were growing. The line feature analysis shows that not only do the terraces grow laterally, but in height as well. The height of the selected terrace was 0.20 nm in image **a**, but 0.48 nm in image **b**. These terrace heights did not increase obviously in the later images **c** and **d**. The number “2” gives an example where a new terrace appears. While terraces grow and new terraces occur, some terraces disappear, covered by others or merge into each other. Number “3” indicates a terrace in image **c** that disappears in image **d**. After Cu deposition, the potential was increased to 300 mV. Within a few minutes, a clean Au(111) surface was recovered (image not shown). The equilibrium potential of 0.050 M CuSO₄ and 0.0050 M MG was observed to be 8 mV vs. Ag|AgCl from CV. The reported changes of morphology described in Figure 51 were also under UPD.

Compared to the electrodeposition processes with additive-free and with 1-propanol containing electrolytes, addition of MG restricted copper nucleation to occur along Au(111) step edges, and growth was dominantly 2-dimensional. This may suggest that MG has preferentially adsorbed onto the (111) terraces leaving more opportunity for Cu deposition at the step edges [109].

4.4.2. Cu Electrodeposition on HOPG

Highly ordered pyrolytic graphite (HOPG) is a widely used substrate for scanning probe microscopy (SPM) and electrochemical processes [110-114]. To make a comparison of the effects of additives on copper electrodeposition on

different substrates, HOPG was used as the working electrode for *in situ* EC-STM investigation.

4.4.2.1. STM of HOPG

Figure 52 shows an STM image of HOPG from electrodeposition solution. HOPG is characterized by the highest degree of three-dimensional ordering.

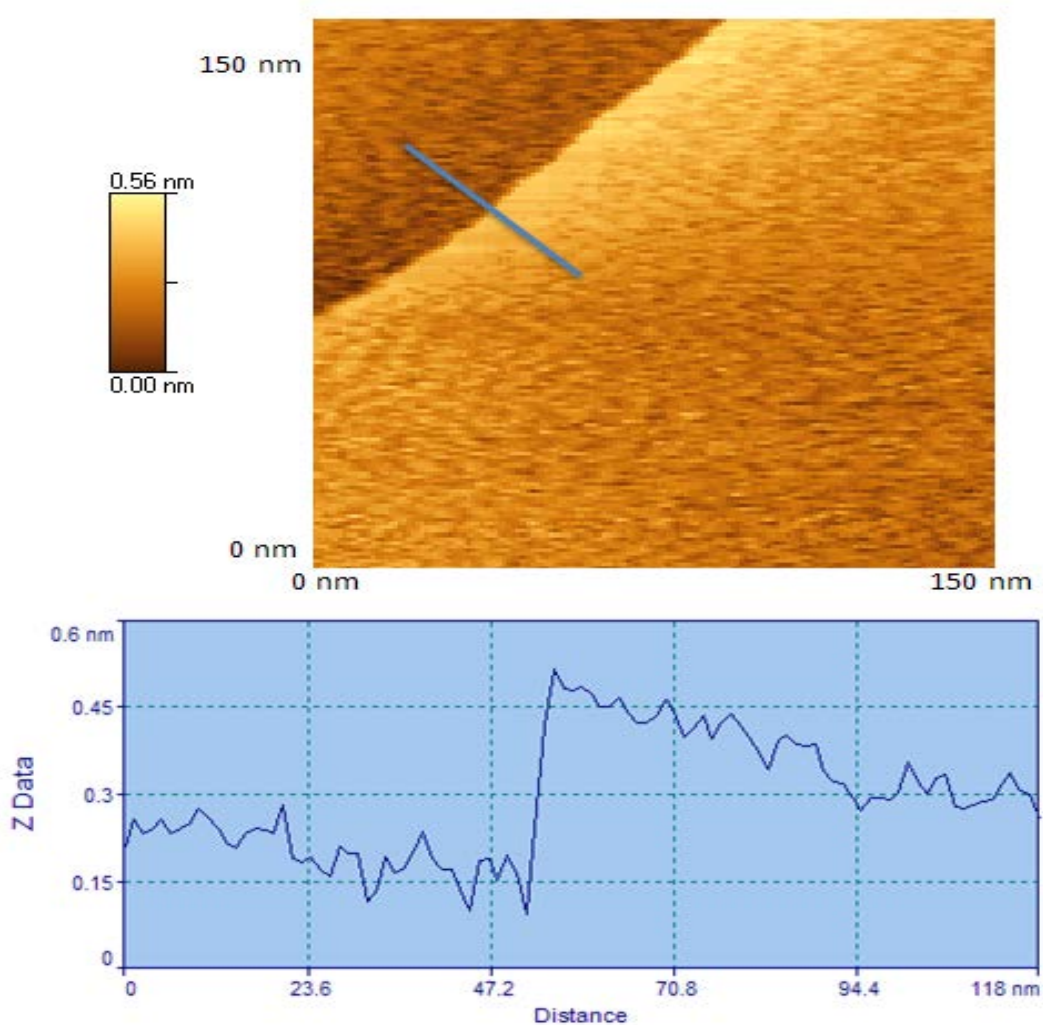


Figure 52. STM images of HOPG obtained in 0.050 M CuSO₄ solution. The bottom line profile shows that the step height is 0.35 nm.

The refreshed surface of HOPG is atomically smooth with large terraces. The surface lattice is a (111) plane with lattice parameter of 0.25 nm, which is similar to the Au(111) surface. The step height 0.35 nm equals to the height of a single layer of graphene, 0.34 nm.

4.4.2.2. Effect of Additives on Cu Electrodeposition on HOPG

HOPG is an ideally smooth and renewable substrate for SPM. Many *in situ* EC-STM studies of copper deposition have been performed on the surface of HOPG [115-119]. Cu nanoparticles on HOPG have been deposited at overpotentials and imaged with STM, but none of them has investigated the effect of additives on the electrodeposition of Cu on HOPG electrode. Figure 53 shows the change of the HOPG surface morphology with Cu deposition at -100 mV vs. Ag|AgCl from additive-free 0.050 M CuSO₄ electrolyte solution. Image **a** is a clean surface of HOPG before electrodeposition. Images **b**, **c**, and **d** show that copper nucleation and growth occur anywhere on the surface without selectivity and that the deposits grow 3-dimensionally. Line profile analysis of the resulting surfaces shows that within a few minutes of electrodeposition, some of the Cu islands have grown to hundreds of square nanometers in area and 4 nm in height.

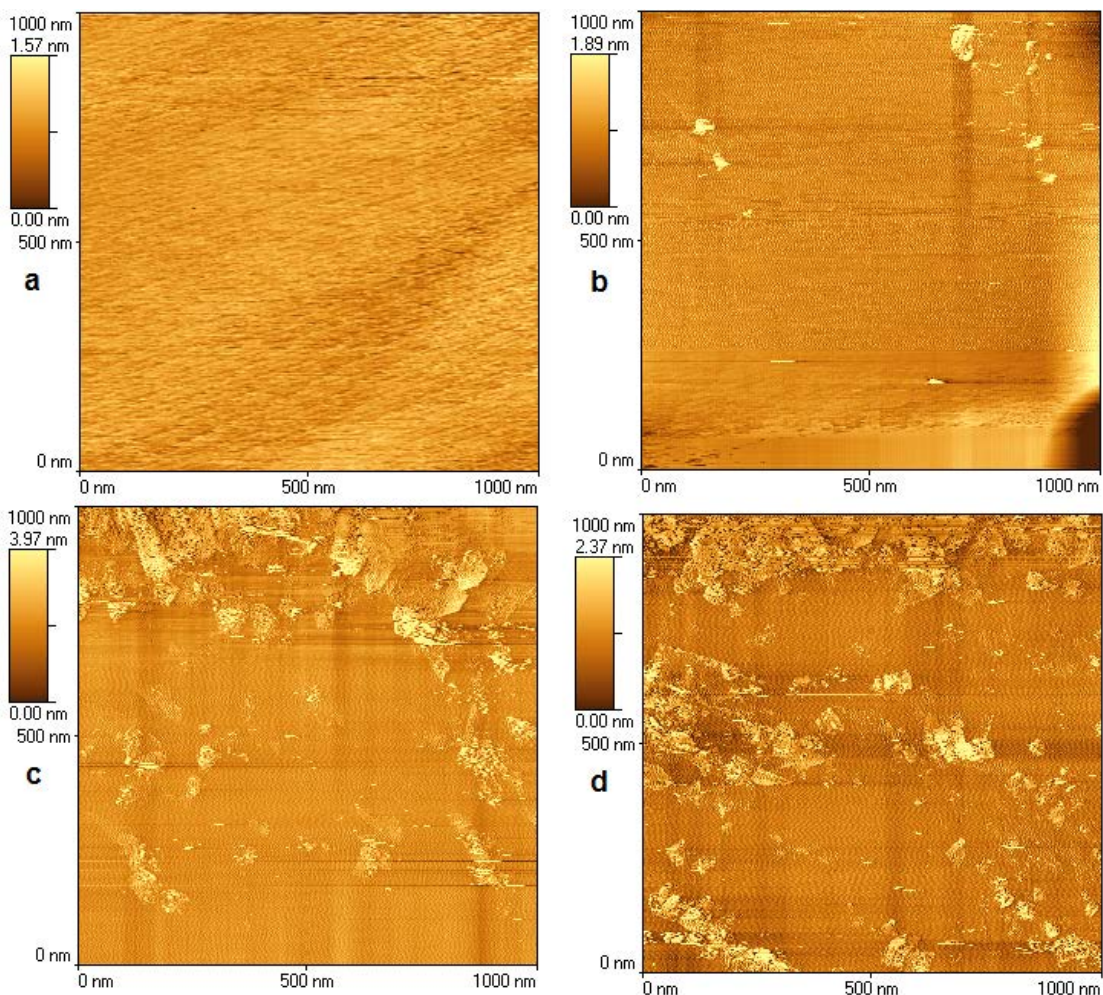


Figure 53. *In situ EC-STM topographic images of Cu electrodeposition on HOPG at -100 mV from 0.050 M CuSO₄ solution. Scan settings: PID = (2.0, 1.0, 0.0), E_t = 200 mV, and scan rate is 6 Hz. a. I_t = 6 nA, t_d = 0 min. b. I_t = 6 nA, t_d = 2 min. c. I_t = 9 nA, t_d = 4 min. d. I_t = 9 nA, t_d = 6 min.*

Figure 54 shows the process of Cu electrodeposition onto the surface of HOPG from CuSO₄ with 1-propanol added to the electrolyte solution. With an initial potential at 300 mV, the HOPG surface could be kept clean (image **a**). Copper nucleation begins when the potential was stepped down to 200 mV, as shown in

image **b**. As the potential was decreased further to 100 mV (image **c**), more Cu deposits formed on the terraces of HOPG.

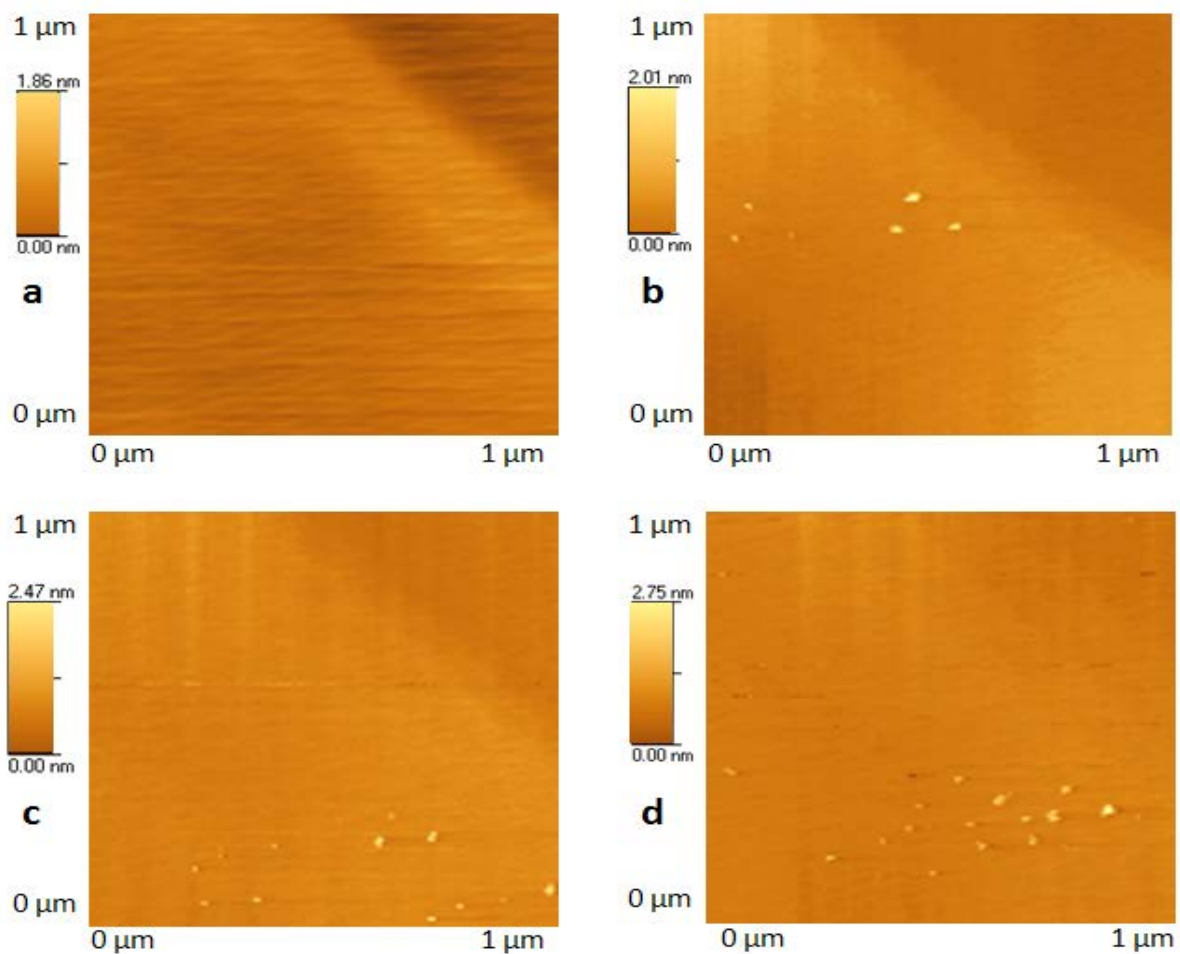


Figure 54. *In situ EC-STM topographic images of Cu electrodeposition on HOPG from 0.050 M CuSO₄ + 1.0 M 1-propanol solution by potential step. Scan settings: PID = (2.0, 1.0, 0.0), I_t = 2 nA, E_t = 100 mV, scan rate is 6 Hz, and area is 1000 x 1000 nm. a. E_d = 300 mV. b. E_d = 200 mV, t_d = 2 min. c. E_d = 100 mV, t_d = 2 min. d. E_d = 0 mV, t_d = 2 min.*

At this point, the Cu deposition was still under potential because the equilibrium potential of 0.050 M Cu^{2+}/Cu is 96 mV vs. Ag|AgCl. The under potential deposition of copper ions to HOPG has been seen with electrolyte containing propanol, which was not seen in an acidified CuSO_4 solution reported by L. Huang et al [119]. Image **d** shows further growth of Cu deposits at potential 0 mV.

Figure 55 reveals the change of HOPG surface features during electrochemical deposition of copper from 0.050 M CuSO_4 with 0.0050 M malachite green. As discussed in Chapter 2, addition of MG to the electrolyte shifts the reduction potential of copper negatively. The result is that at an initial potential of 100 mV, the surface features are unchanged and no deposition occurs (image **a**). When the potential is stepped down to -240 mV, image **a** is observed to change. Electrodeposition of copper results in the nucleation of copper at the HOPG step edges and the two-dimensional growth of Cu (111) terraces. Rather than nucleation of copper islands on the HOPG terraces, as observed in the absence of additives, the presence of the MG additive appears to induce an alternative mechanism of film growth. Image **b** illustrates this growth. As the terraces grow, the step edges are observed to move and in some cases merge. The step edge labeled “**1**” in image **a** is seen to move to the right (image **b**) while step edge “**3**” in image **a** is seen to catch up and merge with step edge “**1**” forming a single, larger step edge in image **b**. Throughout this growth process, there is no evidence of copper island formation on the terraces. When the deposition

potential is stepped to -250 mV, new terraces were generated and grew larger, as illustrated by the number “2” in images **c** and **d**.

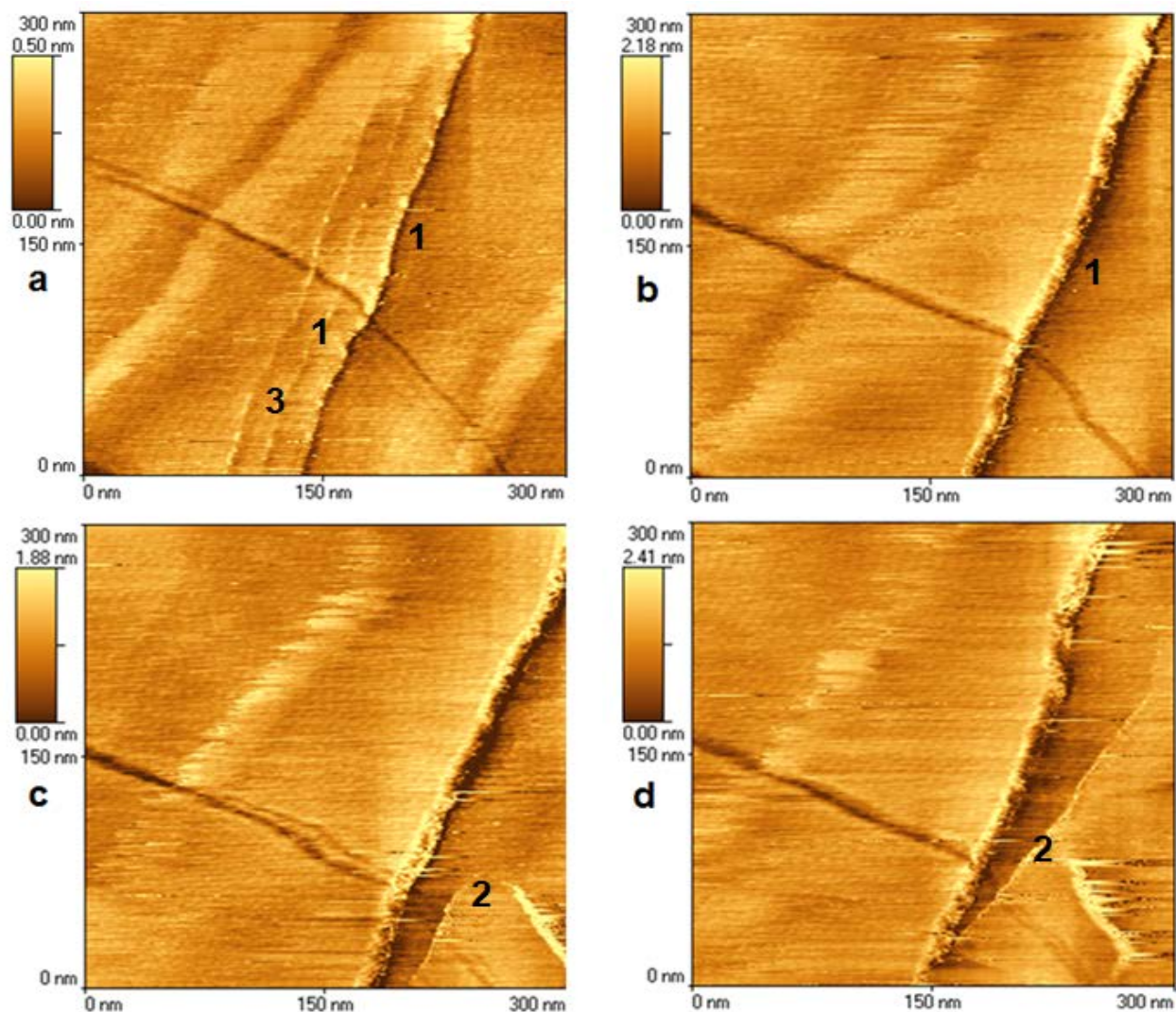


Figure 55. *In situ EC-STM topographic images of Cu electrodeposition on HOPG from 0.050 M CuSO₄ + 0.0050 M MG solution by potential step. Scan settings: PID = (2.0, 1.0, 0.0), and scan rate is 10 Hz. a. $I_t = 1$ nA, $E_t = 100$ mV, $E_i = 100$ mV. b. $I_t = 6$ nA, $E_t = 500$ mV, $E_d = -240$ mV, $t_d = 2$ min. c and d: $I_t = 6$ nA, $E_t = 600$ mV, $E_d = -250$ mV. c. $t_d = 2$ min. d. $t_d = 4$ min.*

The results of our *in situ* EC-STM experiments indicate that the effect of malachite green on Cu electrodeposition on HOPG is similar with that on Au(111) although the effect of 1-propanol on HOPG has some differences from that on Au(111).

4.5. Characteristics of (111) and (100) Surfaces and Effect of Additives on Cu Electrodeposition

In situ EC-STM demonstrated the effect of additive malachite green on the initial stages of copper electrodeposition on both Au thin film and HOPG electrodes. Electrodeposition of Cu in the presence of MG resulted in 2-dimensional growth of Cu under the experimental potentials employed. In previous chapters, MG has also been shown to affect the morphologies of electrodeposited Cu films. Square pyramids of copper were produced during electrodeposition in the presence of MG on Cu(111) surface. 1-propanol also showed to affect the nucleation and morphologies of copper. To understand these experimental results, the characteristics of the (111) and (100) orientations of Au and Cu are analyzed.

4.5.1. Packing of (111) and (100) Surface of Au and Cu

Gold and copper are all face centered cubic crystals. Their cleaved (111) and (100) surfaces have different lattice sizes and packing patterns. Figure 56 shows the structures of the Cu(111) and Cu(100) surfaces. It can be seen that (111) is close packed but (100) is more open. The surface coordinative atoms are 6 for (111) but 4 for (100) (Figure 56). The lattice sizes of Cu(111) and Cu(100)

surface are equal to 2.56 Å, but the unit cells take different shape and area. The hollow sites of (111) are 3-fold but 4-fold for (100). One can also find that the adsorption site density of (111) is higher than (100), hence the (111) surface provides more opportunity for adsorption.

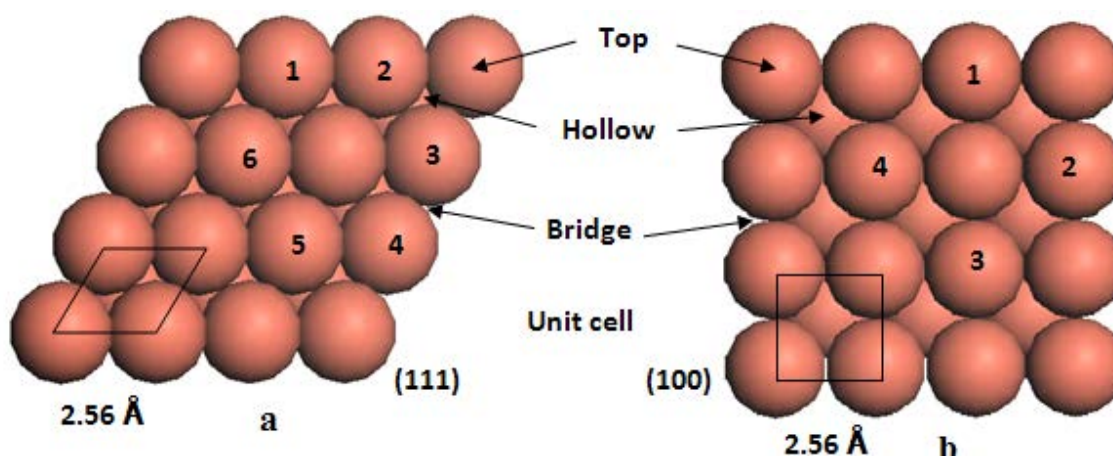


Figure 56. Schematic diagram of Cu(111) and Cu(100) surfaces with unit cell, lattice size, coordination and adsorption sites.

4.5.2. Electronic and Energetic Properties of (111) and (100) Surfaces of Cu and Au

The difference of atom arrangement on the (111) and (100) surfaces leads to a difference of electronic structure and corresponding surface energies [120-123]. The investigation of electronic densities indicates that the maximum Au(100) electronic density is higher than Au(111) surfaces by 0.02 electrons per cubic *bohr* and that the distribution of electronic density on the Au(100) surface extends further from the surface than that of Au(111) [124]. Therefore, the Au(100) surface

is expected to lose electrons more easily than the Au(111) surface. Using the Wannier parameters in thin-film calculations, D. G. Dempsey and Leonard Kleinman obtained surface-charge deficits of $-0.198e$ and $-0.269e$ for the (111) and (100) films, respectively, consistent with these arguments [125-127].

The electronic characteristics of the (111) and (100) surfaces determine their surface energies and work functions. Many research groups have investigated the surface properties experimentally and computationally [120, 126, 128]. Table 9 shows the work function and surface energy values for the (111) and the (100) facets of Au and Cu [124, 129].

Table 9. Work function and surface energy values for Au(111), Au(100), Cu(111) and Cu(100).

Surface	Work function (eV)		Surface energy (J/m^2)	
	Au	Cu	Au	Cu
(111)	5.56	4.86	0.790	1.17
(100)	5.48	4.61	0.918	1.28

The work function is the minimum energy needed to remove an electron from an uncharged solid to a point immediately outside the solid surface (or energy needed to move an electron from the Fermi level into vacuum). As (100) surfaces have lower work functions, the electrons are easier to be moved out of the surface, so that copper ions within an electrolyte can accept electrons and deposit on the (100) surface more easily than on the (111) surface. The less coordinated and looser packed (100) surface has a higher charge density than the more

coordinated and denser packed (111) surface, which makes it understandable that (100) has a higher surface energy than (111).

Thermodynamically, the greatest proportion of the most stable product will be produced. To approximately identify the most stable product, which is the most stable crystal facets while electrodeposition, one can consider of Wulff's theorem, which attempts to minimize the total interfacial free energy of a system within a given volume. The interfacial free energy, γ , can be defined as the energy required for creating a unit area of electrodeposited Cu. Because the copper crystal is an *fcc* structure with a lattice constant of a , the surface energies of the low-index crystallographic facets that typically encase nanocrystals can be estimated with these formula, $\gamma(110) = 4.24(\epsilon/a^2)$, $\gamma(100) = 4(\epsilon/a^2)$, and $\gamma(111) = 3.36(\epsilon/a^2)$ (ϵ is the bond strength), resulting in the energetic sequence of $\gamma(111) < \gamma(100) < \gamma(110)$ [130, 131]. This sequence implies that during copper electrodeposition, grains should take tetrahedral shape in order to maximize the area of (111) facets and minimize the total surface energy. However, Cu electrodeposition from additive-free electrolyte solutions did not appear to appreciably favour (111) over (100) facets from XRD results. This result implies that either the surface energy difference is too small to have an appreciable effect, or that kinetic factors (such as the rate of electron transfer, for example) obscure the expected thermodynamic difference.

Only when MG was added into the solution did the Cu electrodeposition show a clear preference for square pyramids and tetrahedral crystallites, indicating that MG molecules in the electrolyte play an important role in pyramid formation. One interpretation of this observation is that the presence of MG in the electrolyte amplifies the difference in surface energy. One mechanism to explain the formation of tetrahedral crystallites in the presence of MG is in terms of MG-surface interactions. Stronger interactions between MG and the (111) compared to the (100) surface would be expected to lead to preferential adsorption of MG on the (111) surface. Preferential adsorption of MG on the Cu(111) surface would lead to a preference for copper electrodeposition on the (100) surface, and faster rates of electrodeposition along the normal (100) surface.

This model is consistent with the *in situ* electrochemical STM observations of Cu electrodeposition on Au(111) and HOPG surfaces reported in Section 4.4. Electrodeposition of Cu in the absence of electrolyte additives led to 3-dimensional copper growth. In contrast, Cu electrodeposition on Au(111) and on HOPG in the presence of MG led to characteristically different growth. In the presence of MG, Cu electrodeposition resulted in preferential electrodeposition at step edges and the growth of the (111) terraces. The growth of step edges in preference to Cu electrodeposition on the (111) terraces of Au and on HOPG indicates differential growth kinetics and a preference for deposition on other crystal facets such as the (100) surface. These electrodeposition characteristics can be understood by a

preferential adsorption interaction between MG and the lower energy (111) surfaces.

4.6. Cu Nanoparticle Arrays

One of the goals of the research in our group is to control the morphology of surfaces and to be able to create well-defined patterned or nanostructured surfaces with inexpensive and fast methods. Nanotechnology includes a wide range of methods such as nanolithography, photolithography, electron beam lithography, soft lithography, nanoimprint lithography and scanning probe lithography [132-136]. Many of these methods are expensive, labor intensive and time consuming. In contrast, electrochemical deposition potentially presents an inexpensive and straightforward method to pattern nanoscale metal features. As an extension of the research described in this thesis and application of the effect of MG on copper electrodeposition, copper nanoparticle arrays were produced electrochemically. The effects of MG on deposited copper morphologies show a preference for the formation of square pyramids on the electrode surfaces. In this section, preliminary experiments to fabricate an array of nanometer-sized square pyramids are described.

Figure 57 illustrates the proposed colloidal patterning and deposition scheme. The colloidal patterning is achieved by casting (spin- or drop-casting) colloidal beads onto a metal substrate. Under appropriate conditions, the beads will close pack into a hexagonal array. Deposition of an insulator or large band

gap semiconductor onto the bead-covered metal substrate results in deposition on and around the beads. Bead removal (“lift off”) results in a hexagonally patterned substrate in which the bead-shadowed regions produce wells containing a small metal exposed region. This region is surrounded by insulating material and can then act as an isolated nanoscale electrode. Electrodeposition onto the electrode array should result in a patterned array of electrodeposited material. Choice of insulator and electrolyte then provides flexibility in material deposition properties.

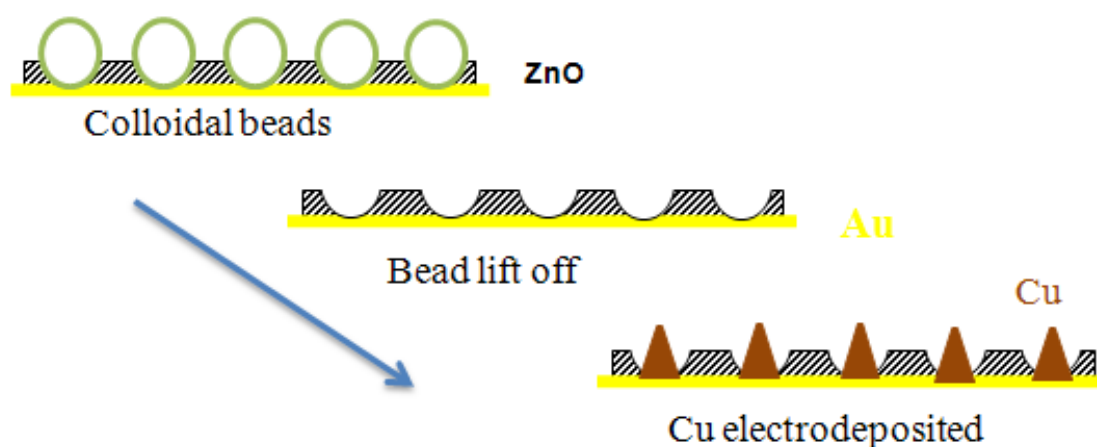


Figure 57. Designed experiment of Cu nanometer square pyramidal array formed by electrodeposition on Au microelectrode from CuSO_4 electrolyte solution with MG.

4.6.1. Making Cu Nanoparticle Arrays

The Au microelectrode arrays were fabricated in the clean room of 4D LABS at SFU by Claire McCague. The base material was a glass wafer on which a 200 nm Au film was evaporated to act as a conductor. The latex beads were then spin cast and dry etched to 250 nm in diameter. ZnO was then evaporated onto the

surface to form a layer of 166 nm thickness and to act as an insulating layer. Finally, the beads were removed by sonication to leave an array of ZnO bowls with exposed Au at the bottom of each bowl. This sample was used as the WE in an electrochemical cell containing 0.050 M CuSO_4 and 0.0050 M MG solution with Ag|AgCl as RE and Pt plate as CE. The deposition potential was controlled at -500 mV. Deposition was carried out for different time intervals and the resulting structures were monitored with AFM.

Figure 58 shows an AFM image of the resulting surface morphologies after seven minutes of Cu electrodeposition from 0.050 M CuSO_4 + 0.005 M MG solution while potential was controlled at -500 mV.

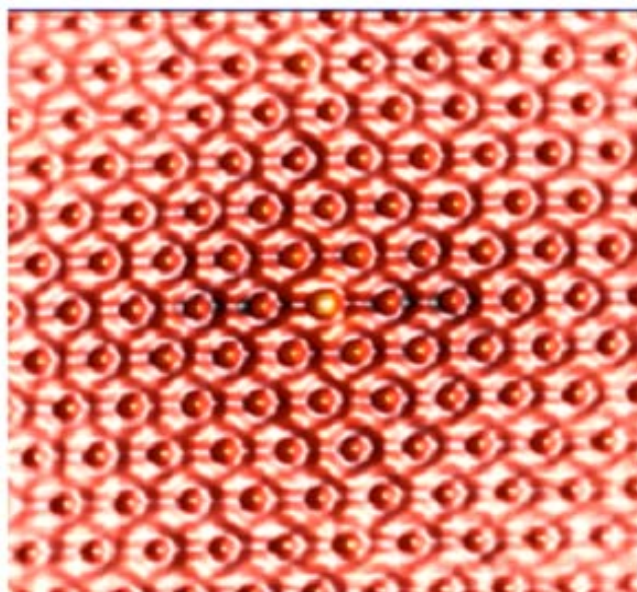


Figure 58. *AFM image of electrodeposition produced copper nanoparticle arrays. 5x5 μm .*

The image demonstrates that we have been able to produce pre-designed nanostructured arrays, the shape of which may need further confirmation though.

4.6.2. AFM images of Cu Nanoparticle Arrays

Figure 59 shows the topographic images and line cut of the nano-electrode arrays analysis before and at different stages of electrodeposition. The AFM images reveal the process of Cu nanostructure formation and growth from the point of initial nucleation (image a) at the bottom of the bowl and grow gradually higher than the ZnO layer(c). The images indicate that the resulting structures are approximately 100 nm in cross section, but with the current level of analysis, it is impossible to determine whether the nanostructures adopt the tetrahedral structure expected from macroscopic Cu crystallites under the same electrodeposition conditions. The linear features on the right of each image describe the change in dimensions of the particles with electrodeposition time. After seven minutes, a Cu nanoparticle array was formed. The average width of the nanoparticles was 100 nm and the height 3 nm. The array had a hexagonal structure with separation of 500 nm between nanoparticles, which is consistent with the separation of bowls before electrodeposition. Further optimization of the electrodeposition conditions is expected to result in more well defined structures. Analysis of the nanostructures for their crystallinity and detailed shape will require electron microscopy analysis.

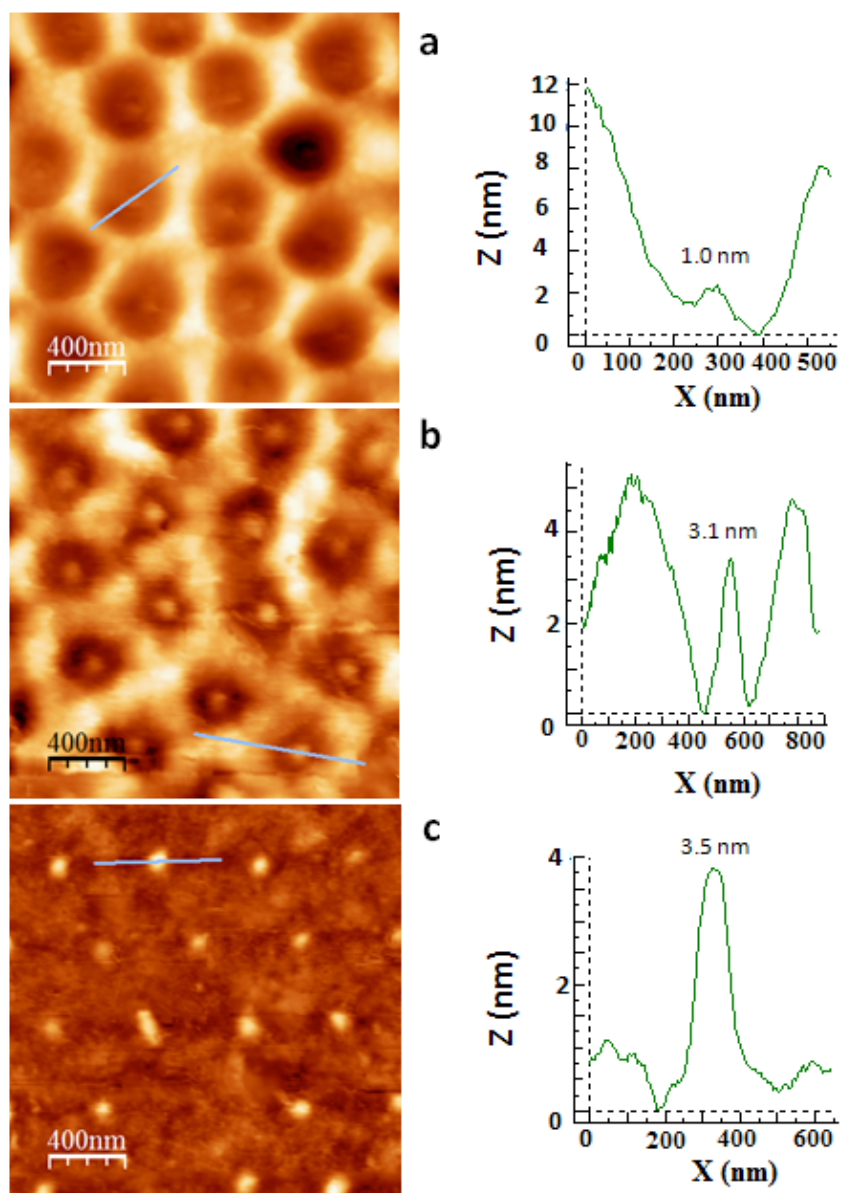


Figure 59. AFM images showing formation of copper nanoparticle arrays. *a.* before electrodeposition, *b.* electrodeposition 280 s at -500 mV and *c.* 420 s.

4.6.3. Applications of nanoscale electrode arrays

A “microelectrode” is any electrode whose characteristic dimension is, under the given experimental conditions, comparable to or smaller than the diffusion layer thickness. Under these conditions, a steady state is attained. The size of a 2D microelectrode can range from hundreds of nanometers to tens of micrometers. The 2D geometry can vary from disc, ring to rectangle; and the 3D from sphere, hemisphere, and cylinder to needle [137, 138]. The application of microelectrode arrays can be used for electrochemical reaction mechanisms and kinetics, trace electrochemical analysis, In vivo measurements on biological objects, et al [138-140].

One particularly interesting application of nanoelectrode arrays is for plasmonic applications. Plasmons are electron density waves created when light hits the surface of a metal under precise circumstances [141, 142]. The study of the interaction of light and metal is called plasmonics. Surface plasmons exist at the interface between two materials where the real part of the dielectric function changes sign across the interface such as a metal sheet in air. The most common use of plasmonics is in statics of localized surface plasmon resonances, such as enhancement of the performance of solar cells [143, 144]. Because electron density waves in plasmons are generated at optical frequencies, and are very small and fast, they can theoretically encode a lot of information, more than what's possible for conventional electronics. Plasmonics is thought to embody the strongest points of both optical and electronic data transfer, allowing the fast

transmission of information over very small wires. But before all-plasmonic chips are developed, the main limitation to plasmonics should be overcome. That is plasmons tend to dissipate after only a few micrometers which makes them too short-lived to serve as a basis for computer chips that are a few centimeters across [142].

Plasmonic nanoparticles can be fabricated either by e-beam lithography and a lift-off technique, evaporation of a deposited thin film, or as described here by deposition of a colloidal solution and electrodeposition [145, 146]. Figure 59 presents an AFM image of the nanoparticle array fabricated here. The image shows a relatively highly ordered hexagonal array of ZnO wells with small copper deposits at the base of each well. The image indicates that this method is a viable route to patterned metallic nanoscale structures at relatively low cost.

4.7. Conclusions

The *in situ* EC-STM method was developed for investigating the effect of additives (MG and 1-propanol) on Cu electrodeposition on Au and HOPG surfaces. The change of surface features were monitored as a function of electrodeposition time to help understand the nucleation and growth kinetics of electrodeposited copper. The results revealed that the nucleation of Cu from additive-free 0.050 M CuSO₄ solution on Au(111) and HOPG surfaces could occur everywhere on the surface and the resulting crystallites grew 3-dimensionally. In the case of electrodeposition with the additive 1-propanol in the electrolyte solution, copper

crystallites could be found all over the surface, with the nucleation and growth of Cu showing some preference on the step edges of the Au terraces. The most effective additive was malachite green. A concentration of 0.0050 M MG in the electrolyte was demonstrated to cause dramatically different nucleation and growth characteristics, including nucleation of Cu along the edges of terraces and growth of these terraces through Cu deposition.

Copper nanostructure arrays were obtained by electrodeposition on template gold .nanoelectrode fabricated through colloidal lithography methods. Further experiments are required to determine whether the effects of additives on electrodeposition can be used for fabricating customized nanoparticle arrays and plasmonic structures.

Chapter 5. Second Harmonic Generation Investigation of MG adsorption at Cu(111)/H₂O and Cu(100)/H₂O Interfaces

In order to further understand the effects of malachite green on the electrodeposition of Cu, non-linear optical SHG (second harmonic generation) measurements were performed. SHG experiments were conducted to investigate differences between the Cu(111) and Cu(100) surfaces, and the interfaces of Cu(111)/MG(*aq*) and Cu(100)/MG(*aq*).

5.1. Optical Second Harmonic Generation

Optical second harmonic generation (SHG) is a nonlinear optical process, in which photons interacting with a nonlinear material are effectively combined to form new photons with twice the energy, and therefore twice the frequency of the initial photons. It is a special case of sum frequency generation (SFG) in which two electric fields with different frequencies are mixed in a nonlinear medium to generate light at their sum frequency. SHG was first demonstrated by Peter Franken in 1961, and different types of SHG have been developed since then [147]. Surface second harmonic generation has been demonstrated as an effective and versatile method for probing interfaces and surfaces [148-151].

Optical SHG can be used as a tool to investigate surface and interface structure, providing information regarding adsorbate orientation [152-156]. This technique takes advantage of the inherently asymmetric environment of the interface formed between two bulk phases of matter. When the two bulk phases are both centrosymmetric, the noncentrosymmetric interface between them possesses a second-order surface nonlinearity and surface SHG arises out of the second-order susceptibility $\chi_s^{(2)}$:

$$\vec{P}^{(2)} = \chi_s^{(2)} \vec{E} \vec{E} \quad (29)$$

where $\vec{P}^{(2)}$ refers to polarization or dipole moment per unit volume which responds nonlinearly to the electric field components of the incident light \vec{E} . The polarization can give rise to the interface-specific SHG effect. These $\chi_s^{(2)}$ effects are only possible in media that lack a center of inversion symmetry. Figure 60 shows the schematic of SHG from the Cu/air interface. The $\chi^{(2)}$ of the bulk media is zero, but the surface $\chi_s^{(2)}$ is nonzero due to the lack of a center of inversion symmetry at the Cu/air interface.

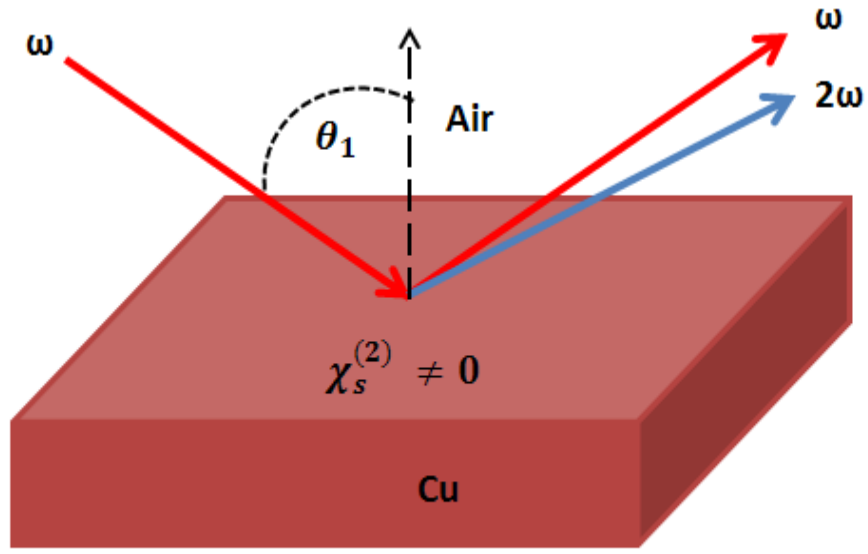


Figure 60. Schematic diagram of surface SHG from Cu/air interface.

Consider two optical plane waves of frequencies ω_1 and ω_2 that propagates through a medium with nonzero second order susceptibility $\chi_s^{(2)}$. The electric fields are

$$\vec{E}_1 = \vec{E}_1^0 \cdot \cos(\omega_1 t + \vec{k}_1 \vec{r}) \quad (30)$$

$$\vec{E}_2 = \vec{E}_2^0 \cdot \cos(\omega_2 t + \vec{k}_2 \vec{r}) \quad (31)$$

where \vec{k}_1, \vec{k}_2 are wave vectors, and \vec{r} is the direction of wave propagation.

Interference of these fields at the interface induces nonlinear polarization effects:

$$\vec{P}^{(2)} = \chi_s^{(2)} : \vec{E}_1 \vec{E}_2 = \vec{P}_{2\omega_1} + \vec{P}_{2\omega_2} + \vec{P}_{\omega_1+\omega_2} + \vec{P}_{\omega_1-\omega_2} + \vec{P}_0 \quad (32)$$

where \vec{P}_0 is a constant polarization of the medium induced by high electric fields. $\vec{P}_{2\omega_1}$ and $\vec{P}_{2\omega_2}$ are polarizations at double the frequencies, $\vec{P}_{\omega_1+\omega_2}$ is the polarization component at the sum frequency and $\vec{P}_{\omega_1-\omega_2}$ the polarization component at the difference frequency. These polarization components lead to re-radiation at each of their frequencies.

When the frequencies of the two waves are equal, they induce a third wave at double the frequency 2ω . This three wave mixing process is called second harmonic generation (SHG). In SHG the incident light is converted to its second harmonic. This means, for example, that two photons at 800 nm can combine and produce one 400 nm photon. The frequency of the incident light has been doubled, but the energy is conserved (Figure 60).

When a laser of frequency ω is incident on the Cu/air interface from *medium 1*, at an angle θ_1 with respect to the surface normal, the Cu/air interface (and molecules adsorbed at it) generates SHG signal. The reflected SHG 2ω output is spectrally separated from the simply reflected incident light and detected. The SHG signal intensity is given by:

$$I_{2\omega} = k \left| \chi_{eff}^{(2)} \right|^2 I_{\omega}^2 \quad (33)$$

where k is a constant determined by the laser pulse and spot size, the properties of *medium 1* and the incident angle. I_ω is the intensity of the incident light. $\chi_{eff}^{(2)}$ is the effective nonlinear susceptibility [62, 155, 157].

5.2. SHG Experiment

Figure 61 is a schematic of the apparatus used for SHG measurements.

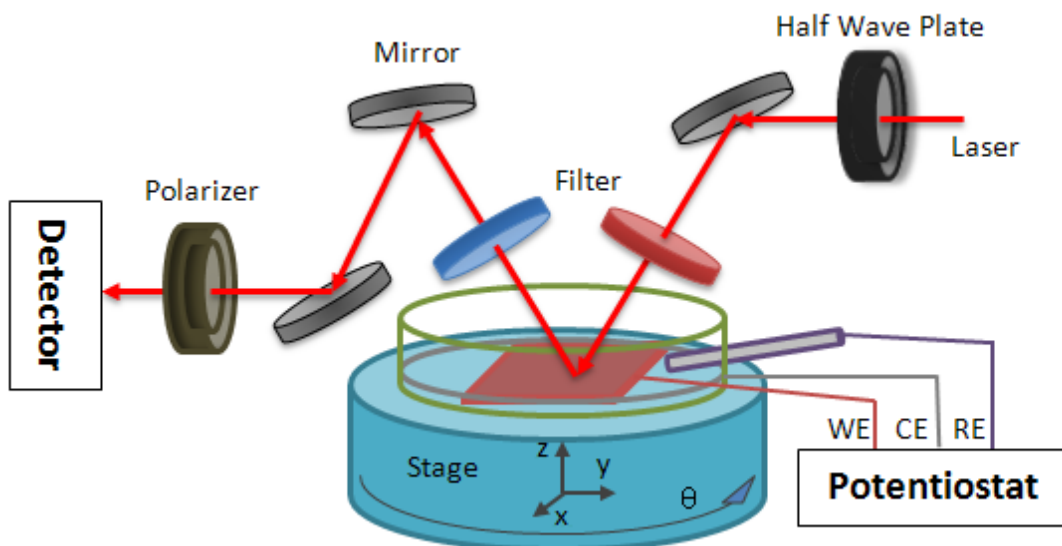


Figure 61. Schematic setup for SHG measurement with potential control system.

The sample is mounted at the bottom of a container, in which water or a MG solution is placed. In this set up, the sample potential can be controlled with a potentiostat to investigate the effect of potential on the SHG signal. The sample

position could be adjusted with translation and rotation stages which also permitted measurements of SHG rotational anisotropy of the copper single crystal Cu(111) and Cu(100). The mode-locked incident light at 800 nm with 100 fs pulse duration was supplied with a Ti-sapphire (Spectra Physics) laser system (Appendix B). The incident beam polarization could be varied with a half wave plate (HWP) and the incident power was controlled with neutral density filters. A spectral filter was used to remove 400 nm light that could be generated from previous interfaces and the noncentrosymmetric bulk media of other optics in the beam path, but allowed 800 nm light pass and to generate SHG at the interface of interest. The reflection filter removes the reflected incident 800 nm light but passes the resultant 400 nm SHG light. The polarization of the incident 800 nm beam is controlled by a zero-order $\lambda/2$ wave plate. The polarization of the SHG signal was selected with quartz, Glan Thompson polarizer placed between the sample and detector.

5.3. Results and Discussion

5.3.1. SHG Rotational Anisotropy of Cu(111) and Cu(100)

As shown in Figure 56, Cu(111) and Cu(100) have different atomic packing and surface symmetry, which have been confirmed by previous surface-sensitive SHG rotational spectroscopy studies [158-161]. The examined copper single crystals can be viewed as a collection of free electrons and core electrons associated with the Cu nuclei. When an electromagnetic wave passes through this medium, both the free and core electron density can be polarized by the wave's

oscillating electric field. A component of the resulting polarization will respond nonlinearly, giving rise to second harmonic generation. Because copper single crystal is a centrosymmetric medium, SHG is forbidden under the electric dipole approximation in the bulk, but allowed at the metal surface where inversion symmetry is broken, so the surface dipole susceptibility elements are particularly sensitive to the surface and it's associated electronic properties.

D. A. Koos etc. have studied surface-dipole contributions to anisotropic second-harmonic generation from noble-metal surfaces. Based on the crystal surface symmetry, the expressions for the SHG response from the crystal surface orientation as a function of azimuthal angle have been codified as follows [161]

$$I_{PP,2\omega} = \left| a_{PP}^{(0)} + a_{PP}^{(m)} \cos(m\varphi) \right|^2 \quad (34)$$

$$I_{PS,2\omega} = \left| a_{PS}^{(m)} \sin(m\varphi) \right|^2 \quad (35)$$

$$I_{SP,2\omega} = \left| a_{SP}^{(0)} + a_{SP}^{(m)} \cos(m\varphi) \right|^2 \quad (36)$$

$$I_{SS,2\omega} = \left| a_{SS}^{(m)} \sin(m\varphi) \right|^2 \quad (37)$$

where the azimuthal angle φ describes the rotation of the crystal sample about its surface normal; a is constant defined by Fresnel coefficients of the fundamental and SHG fields; m is 4 and 3 for the (100) and (111) crystal face respectively. The

subscripts refer to the input fundamental and output SHG beam polarizations, either in the plane of the incident beam (P polarized) or perpendicular (S polarized) to it.

As the surface SHG response of copper varies with incident wavelength and temperature [162, 163], all of the SHG data were obtained with a fundamental wavelength of 800 nm, a second harmonic wavelength of 400 nm and were collected at 295 K. The SHG rotational anisotropic experiments were performed in air under PP, PS, SS and SP conditions, and the results showed the sensitivity of the SH intensity to the surface symmetry (Figure 62). Image **a** reflects the C_{3v} symmetry of this surface Cu(111) and is in good agreement with equation (35). Image **b** however reflects the C_{4v} symmetry of the Cu(100) surface and is in agreement with equation (36). The intensity of SH signal generated from Cu(111) and Cu(100) surfaces in air was compared by obtaining SHG spectroscopies with incident polarization angle at selected peak rotational angles. From the P_{out} and S_{out} spectroscopies presented in Figure 63, we can see that, for both P- and S-polarized second harmonic beam, the Cu(111) surface generated larger SHG signals than the more-open Cu(100) surface.

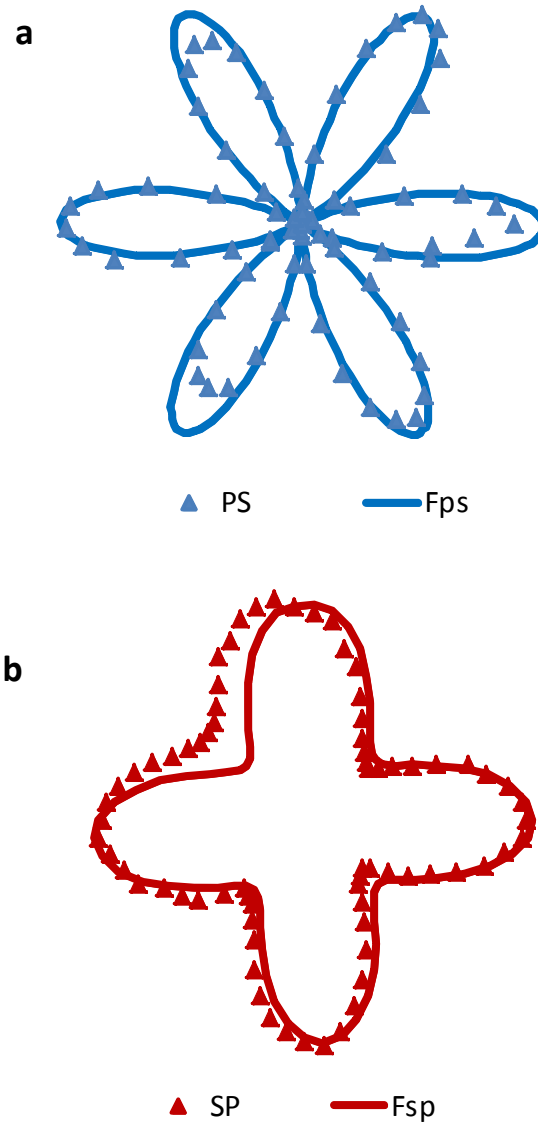


Figure 62. SHG rotational anisotropy of copper single crystal. a. Cu(111)/air interface, PS (P_{in} - S_{out}) polarization. b. Cu(100)/air interface, SP (S_{in} - P_{out}) polarization. The points indicate the experimental data and the solid lines the fitted data.

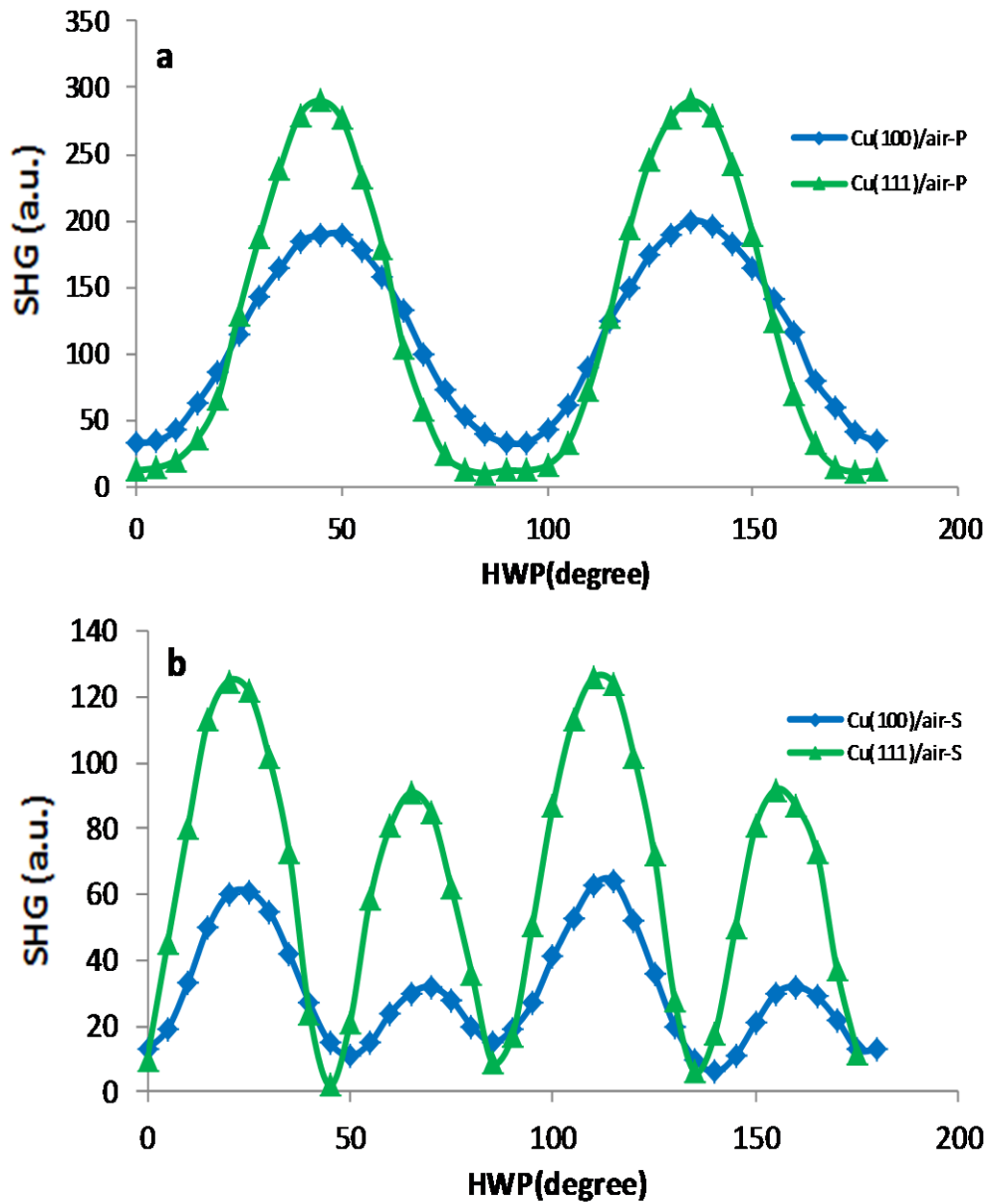


Figure 63. Comparison of SHG polarization spectroscopy of copper single crystal. a. $Cu(111)/air$ interface, P_{out} polarization to incident HWP. b. $Cu(100)/air$ interface, S_{out} polarization to incident HWP. The points indicate the experimental data and the solid lines are for eye guide.

Since the second harmonic response is the result of the interaction of the incidence laser's electric field with the polarizable electron density at the surface, the higher intensity SHG response from the (111) surface is consistent with the larger density of atoms in the (111) surface. Note that the polarizable electron density includes both the density of free electrons at the surface, as well as those bound to the core copper ions of the lattice. Petrocelli *et al* have previously investigated the wavelength dependence of the second harmonic generation efficiency from copper surfaces and observed a strong enhancement of the SHG response at the onset of interband (d-band to conduction band) transitions[162]. In our experimental configuration, the incident laser frequency lies below the onset of interband transitions, but our second harmonic frequency corresponds to an energy in excess. Under these circumstances, it is reasonable to expect that in two photon resonance with electronic transitions above the absorption edge, the second-order polarization may be strongly influenced by the nonlinear response of bound electrons of the copper lattice and the higher density of atoms on the Cu(111) surface. This result is consistent with the SHG rotational anisotropy experiments which yield SHG responses that reflect the symmetry of the lattice core.

5.3.2. SHG of Cu(100) and Cu(111) in MG Solution

One of the goals of this research was to understand the ways in which additives can alter the characteristics of electrodeposition. The choice of malachite green as one of these additives was made based on the desire to probe the electrochemical interface using nonlinear optical spectroscopy as a surface sensitive probe, and our extensive experience with this organic molecule and its surface second harmonic generation response. Our research group has previously examined the adsorption, orientation and order of MG molecules at the fused silica/air interface. The magnitude of the nonlinear response from Cu/MG is extremely large compared to that from Cu/H₂O and for this reason provides for sub-monolayer sensitivity. We have previously used the polarized SHG response to determine that ultrathin solution cast films of MG result in adsorption of MG molecules with a relatively narrow and upright averaged orientation distribution on the silica surface [150]. Here, we investigate the adsorption properties of MG additive molecules from solution at the Cu/H₂O interface as a first step to investigating the more complex Cu/electrolyte electrochemical interface. Figure 64 and Figure 65 show the polarized SHG response from the Cu(111)/MG(aq) and Cu(100)/MG(aq) solution interfaces. In order to investigate the sensitivity of the method to MG molecules without the further complexities of the Cu/electrolyte electrochemical interface, the SHG response of the uncharged copper surface in contact with different concentrations of 10⁻⁶ M to 10⁻² M MG solutions were examined.

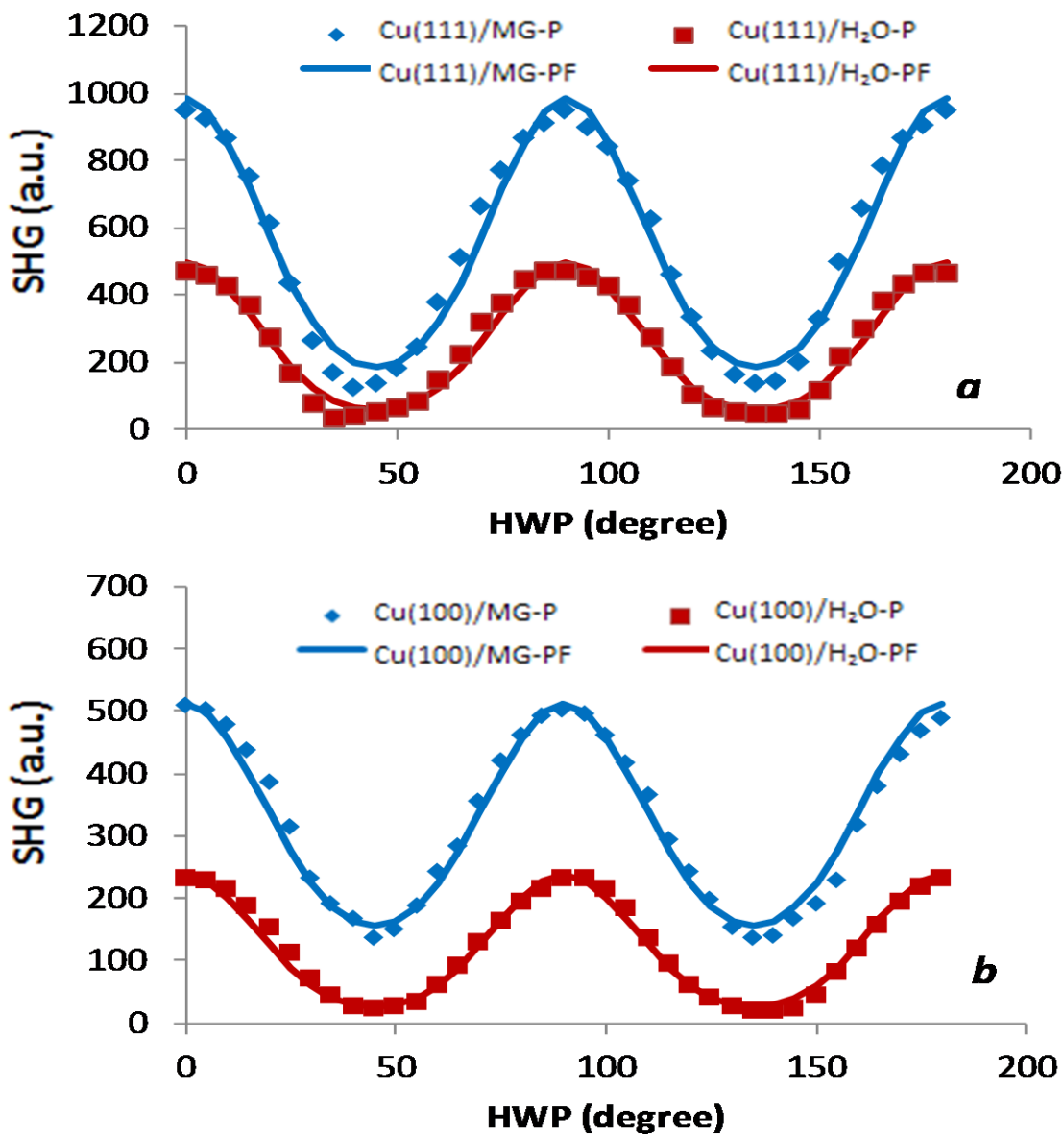


Figure 64. Comparison of SHG polarization spectroscopy of Cu(111) and Cu(100) in water and in 10^{-4} M MG solution. *a.* Cu(111), P_{out} polarization to incident HWP. *b.* Cu(100), P_{out} polarization to incident HWP angle. The points indicate the experimental data and the solid lines the fitted data.

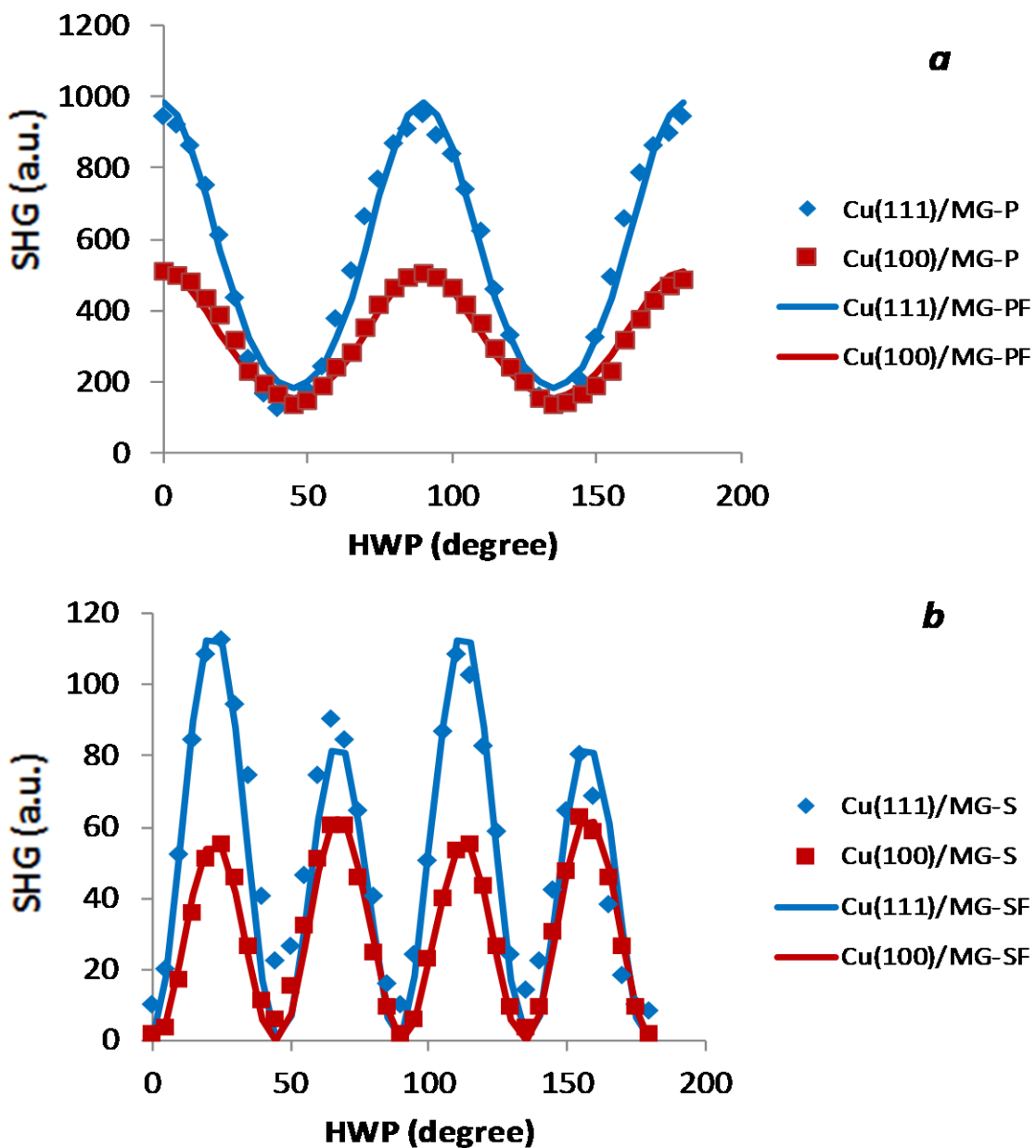


Figure 65. Comparison of SHG polarization spectroscopy of Cu(111) and Cu(100) in 10^{-4} M MG solution. *a.* P_{out} polarization to incident HWP angle. *b.* S_{out} polarization to incident HWP. The points indicate the experimental data and the solid lines the fitted data.

The SHG signals from the interfaces of Cu(111)/MG(aq) and Cu(100)/MG(aq) at different MG concentrations were measured at selected peak azimuthal angles. The S-polarized and P-polarized SHG signals were measured as a function of the incident polarization (HWP) angle. As illustrated in Figure 64, the SHG P polarized output intensity is observed to increase substantially by addition of MG into water, even at very low concentrations, indicating a significant change in the nonlinearity of the Cu/H₂O interface by addition of the additive MG.

The P-polarized response of the Cu/MG(aq) interface shows large intensities at all incident polarization angles, especially the maximum input polarization angles for Cu/liquid interfaces. The observed P-polarized response from the Cu/H₂O interface is similar in nature to that from the Cu/air interface (Figure 63-a), indicating that the source of nonlinearity from the Cu/H₂O interface is primarily dictated by the polarizable electron density of the copper surface, as discussed previously. In contrast, the increased intensity of the SH response from the Cu/MG(aq) interface suggests that the surface nonlinearity has been significantly raised. These observations are consistent with the adsorption of MG molecules at the Cu/H₂O interface, and a source of nonlinear polarization dominated by the nonlinear polarizability of the MG adsorbate molecules. Strictly speaking, since SHG is a coherent nonlinear spectroscopy, the observed response should reflect the interfering nonlinear contributions from all sources of nonlinear polarization. Although the nonlinearity from the Cu/H₂O and Cu/MG(aq) interfaces cannot be experimentally separated, our observations indicate that these two

sources of nonlinear response have the same phases, meaning that their contributions constructively interfere. The net second harmonic response after background correction therefore reflects a contribution from MG (refer to Figure 64). This observation indicates that the MG SHG response is very large even at 10^{-4} M MG concentration. When the concentration is 10^{-3} M, the SHG signal from MG completely dominates the response from the Cu/H₂O interface. Such a large nonlinear response from the adsorbed MG molecules is in keeping with our previous observations of the magnitude of nonlinear response from MG, and likely results from a near two photon resonance enhancement of the nonlinear signal at these wavelengths.

A comparison of the SHG response from Cu(111)/MG(aq) and Cu(100)/MG(aq) with the same concentration of MG is made in Figure 65. For both the S- and P-polarized SHG response, the data indicates that the response from the Cu(111)/MG solution interface is significantly larger than from the Cu(100)/MG solution interface. Given the surface selectivity of SHG, the observations in Figure 65 provide direct evidence that either a larger fraction of the MG molecules in solution partition to the Cu(111)/H₂O interface than to the Cu(100)/H₂O interface, or that MG molecules adopt different orientations at the two interfaces, or both [150].

To examine the differences between MG, as an additive, interacting with the (111) and (100) surfaces, we have obtained the polarized SHG signal from these aqueous interfaces at MG concentrations from 10^{-6} M to 10^{-2} M. By plotting the

square root of SH response at fixed polarization angles as a function of MG bulk solution concentration, an adsorption isotherm for MG can be obtained. As the solution of MG possesses a weak but important absorption at 400 nm (the wavelength of the measured SHG signal), the adsorption isotherm has been normalized according to Lambert-Beer Law to account for this absorption. The isotherms display the square root of the net SHG intensity (\sqrt{SHG}) versus MG concentration and are shown in Figure 66. (The (\sqrt{SHG}) is proportional to the surface concentration). The isotherms show that the SHG intensity increases at low MG concentrations due to MG's strong nonlinear response. The isotherms display characteristic behavior of monolayer coverage for bulk MG solution concentrations of $\sim 3-5 \times 10^{-4}$ M. The insets show the enormous increase of \sqrt{SHG} when the concentration of MG is increased further. This behavior can be attributed to MG multilayer adsorption on both the Cu(111) and Cu(100) surfaces. At these higher concentrations the SHG signal is effectively dominated by MG, making the nonlinear contribution from the underlying Cu substrates insignificant. This result enables us to extract molecular information of MG on substrates by data fitting. Comparing $P_{in}-P_{out}$ polarized SHG values in image (a) and (b), one can find that the SHG intensity generated from the Cu(111)/MG(aq) was larger than from the Cu(100)/MG(aq) interface at the same MG bulk solution concentration. This indicates a higher nonlinear susceptibility from the Cu(111)/MG(aq) interface than from the Cu(100)/MG(aq) interface, consistent with a higher concentration and/or different orientation of MG at the aqueous metal interface, as previously suggested.

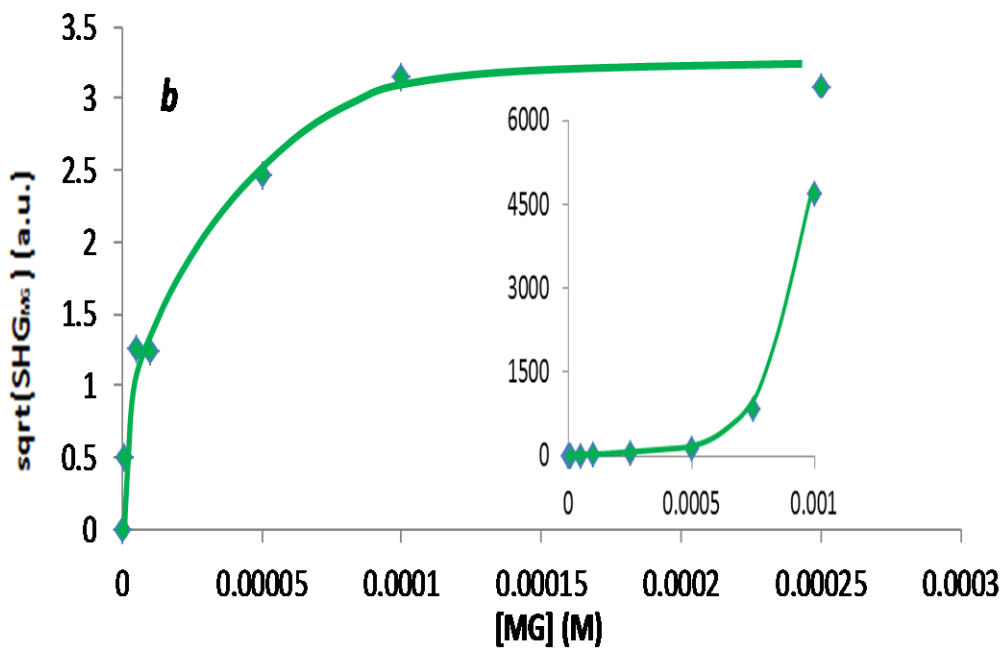
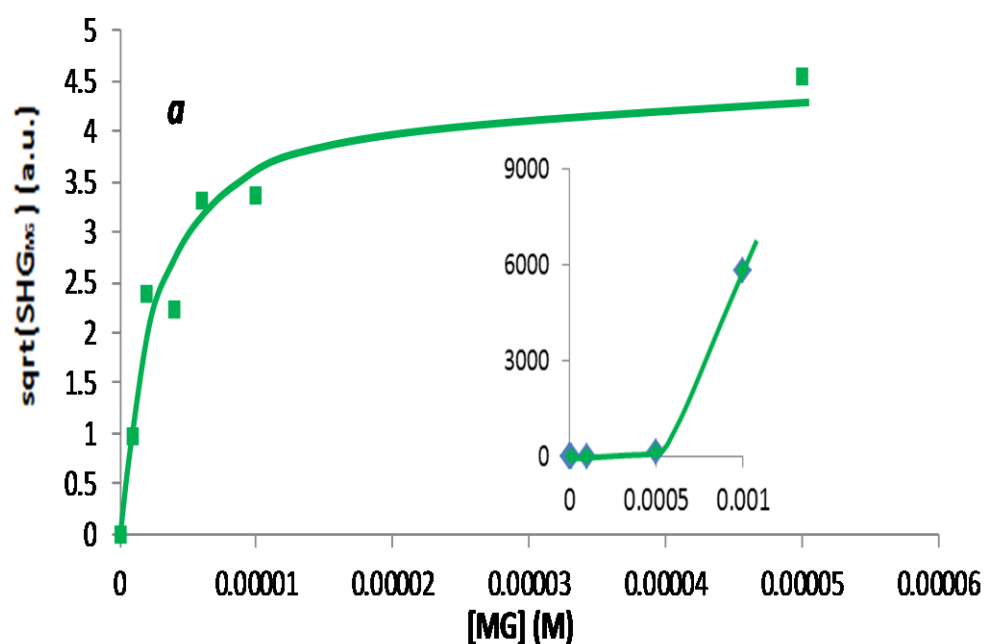


Figure 66. Isotherms of Pin-Pout polarized square root SHG of (a) Cu(111)/MG(aq) and (b) Cu(100)/MG(aq) versus MG concentration. Insets present the enormous increase with 10^{-3} M MG.

5.3.3. Potential Effect on SHG of Cu/MG(aq) Interface

To investigate the effects of potential on the behavior of the additive MG, the change of SHG intensity on the Cu(111)/MG(aq) and on Cu(100)/MG(aq) interfaces were measured when a cathodic potential was applied to the electrodes. Figure 67 shows the comparison of the polarized SHG studies obtained on the Cu(111)/MG(aq) and on Cu(100)/MG(aq) interface in 10^{-4} M MG solutions while the copper potential was controlled at 0 mV and -800 mV versus a Ag|AgCl (3.5 M NaCl) electrode. The results indicate that as the cathodic potentials were changed, so did the SHG response, indicating sensitivity to the applied potential. The effect was more pronounced at certain polarization angles. For P_{in} - P_{out} polarizations, the SHG response was observed to increase, while for S_{in} - P_{out} polarizations, the SHG response decreased in magnitude. The increase in response from Cu(111)/MG(aq) was larger than from the Cu(100)/MG(aq) electrode. This larger increase in response from the Cu(111)/MG(aq) interface, may indicate that the effect of the applied potential was to increase adsorbate coverage and/or change the orientation of the adsorbed MG additive molecules.

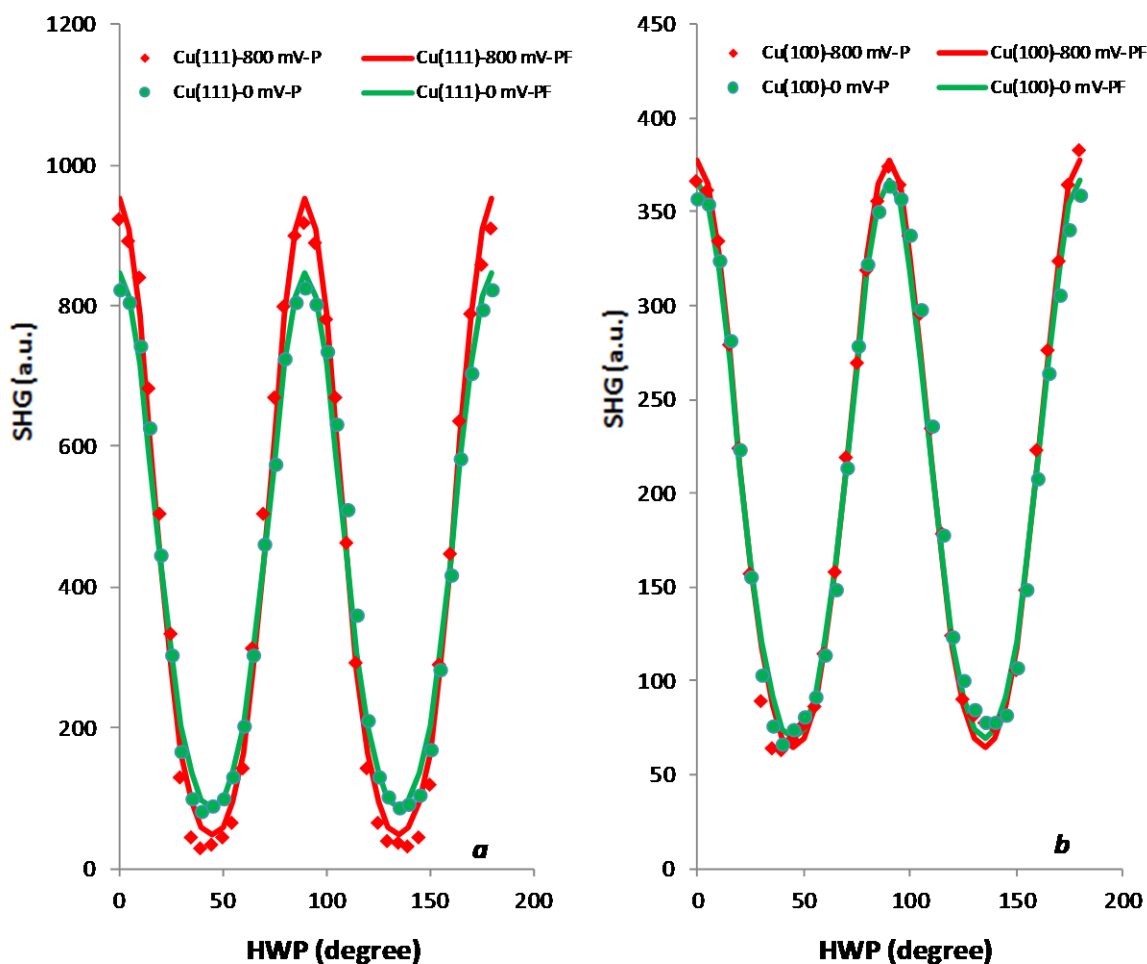


Figure 67. Potential effect on SHG response from Cu in 10^{-4} M MG solution. *a.* Cu(111)/MG(aq). *b.* Cu(100)/MG(aq).

5.4. Orientation of MG on Cu

5.4.1.1. SHG Data Fitting

SHG measurements can be used to determine the relative molecular orientation within an adsorbate layer [164-167]. The obtained polarization dependence of the surface SHG response can be used to extract the elements of

the second-order nonlinear susceptibility tensor $\chi_s^{(2)}$, and to obtain orientational information about the adsorbed molecules. For a monolayer of molecules distributed randomly in the plane of the substrate surface, which is defined to be the XY plane, the susceptibility tensor possesses only three independent elements χ_{XZX} , χ_{ZXX} , and χ_{ZZZ} . The values of these three components can be obtained by monitoring the polarization-selected SHG intensity as a function of the polarization angle of the incident light. The dependence of the polarization-selected SHG signal intensity and the incident polarization is given by [150]:

$$\begin{aligned}
 I_{2\omega} = k & |(c_1 \chi_{XZX} \cos 2\gamma \sin 2\gamma) \sin \psi \\
 & + [(c_2 \chi_{XZX} + c_3 \chi_{ZXX} + c_4 \chi_{ZZZ}) \cos^2 2\gamma \\
 & + c_5 \chi_{ZXX} \sin^2 2\gamma] \cos \psi|^2 I_{\omega}^2
 \end{aligned} \tag{38}$$

where ψ is the polarization detection angle. When $\psi = 0^\circ$ and 90° , the selected polarization is S-polarized and P-polarized SHG intensity respectively. γ is half wave plate angle and 2γ is the polarization angle of the incident beam.

Figure 68 shows the definition of the MG adsorption coordinate system. Z is the normal of the substrate surface XY . The molecular axis is defined as Z' and its orientation in XYZ coordinate system is defined by the three angles: θ , δ and φ . According to equation (38), the SHG data measured in 10^{-4} M MG and copper interfaces have been fitted; susceptibility components extracted from the fits are

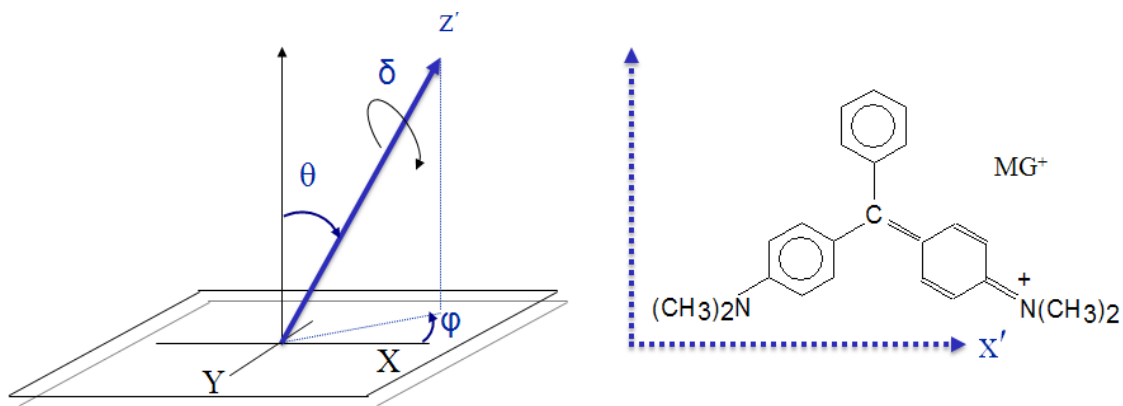


Figure 68. Schematic of the definitions of the orientation angles θ , δ and φ , defining the molecular orientation with respect to the surface. The molecular coordinate system $X'Y'Z'$ describing MG^+ orientation was also shown.

listed in Table 10. By relating the elements of the macroscopic nonlinear surface susceptibility tensor to the components of the molecular nonlinear polarizability, the molecular orientation distribution can be derived as a function of angles θ , δ and φ . φ is azimuthal angle to which the surface frame is symmetric so that the function can be simplified by integration over all φ . This implies a random orientation of molecules about the surface normal. δ cannot be calculated through data fitting, but θ can be obtained from the susceptibility components. Also ξ defines an angle that the molecular axis x' makes with the surface normal and can be expressed as a linear combination of the experimentally determined susceptibility components too.

Table 10. SHG data fitting results of copper in 10^{-4} M MG solution. Susceptibility components unit: 10^{-8} a.u.

Interfaces	χ_{xz}	χ_{zx}	χ_{zz}	θ ($^{\circ}$)	ξ ($^{\circ}$)
Cu(100)/MG ⁺	2.27	2.4	5.42	59 ± 5	76 ± 6
Cu(111)/MG ⁺	2.9	2.6	8.25	57 ± 5	62 ± 5
Cu(100) ^{-800mV} /MG ⁺	1.55	1.54	5.21	56 ± 5	60 ± 5
Cu(111) ^{-800mV} /MG ⁺	1.32	1.32	9.45	51 ± 4	41 ± 3

$$\cos^2 \xi = \frac{\chi_{zzz}}{2(\chi_{zzz} + \chi_{zxx} + \chi_{xzx})} \quad (39)$$

$$\cos^2 \theta = \frac{2\chi_{zxx} - \chi_{zzz}}{2\chi_{zxx} + \chi_{zzz}} \quad (40)$$

While data fitting it was assumed that all molecules possess the same averaged orientation angle. From the fitted data, one can see the orientation angles (θ , ξ) of MG⁺ on Cu(100) and Cu(111) surfaces. The effects of potential on orientation angles are different. The smaller the ξ , the more perpendicular the molecular axis x' is to the substrate frame.

The fitted angles from Table 10 show that in all cases, the MG ions tend to adopt orientation angles such that the molecule lies relatively flat to the Cu surface (large θ and ξ). Within error, the values of θ are similar for both of the Cu/MG⁺ interfaces, while ξ appears somewhat smaller for the Cu(111)/MG⁺ interface, indicating a slightly more upright orientation. Table 10 also indicates that on the electrified interfaces, the averaged orientations are modified relative to the non-

electrified interfaces, with MG adopting a slightly more upright orientation on the electrified Cu surfaces. The limited precision of these results and the limits of applicability of an oversimplified orientation analysis make it difficult to distinguish to what extent the larger SHG signals from the Cu(111) surface represent *significantly* different orientations on the different Cu surfaces, or a higher surface density of adsorbed MG. It should be noted that, as previously discussed, the differences in lattice packing between the Cu(111) and Cu(100) lattices represent a different geometry and higher density of adsorption sites on Cu(111) than on Cu(100). A more upright averaged orientation of MG on the Cu(111) surface may also represent a smaller area per adsorbed MG species, and the opportunity for increased surface density on the Cu(111) lattice.

5.5. Conclusion

In this Chapter, the nonlinear optical, surface sensitive spectroscopy, second harmonic generation has been used to investigate the electronic response of Cu (111) and Cu(100) in air, and in aqueous solutions containing the organic additive MG. SHG experiments in which the rotational anisotropy of the surface SHG signal is monitored as a function of azimuthal rotational angle demonstrated that the nonlinear response was sensitive to the symmetry of the Cu lattice and showed four-fold symmetry in the case of Cu(100) and 3- and 6-fold symmetry in the case of Cu(111), reflecting the surface atomic packing symmetry. SHG experiments on the Cu/H₂O interface demonstrated that addition of the additive

MG altered the nonlinear response of the interface significantly, even at low concentrations. At concentrations employed for the electrodeposition experiments described in previous chapters, the nonlinear response of the interface is dominated by MG.

At selected rotational orientations, the SHG response to incident polarization (HWP) angle in air, water and MG solutions revealed that the more close-packed Cu(111) surface generated more intense SHG signals than the more open Cu(100) surface in all tested media. The higher SHG intensity from Cu(111)/MG(aq) than from Cu(100)/MG(aq) indicates different behavior of MG molecules on Cu(111) and Cu(100). While the SHG orientation analysis showed that on all surfaces, MG additive molecules tended to adopt relatively flat orientations, adsorbed MG stood slightly more upright at the Cu(111)/MG(aq) interface. The larger signal associated with Cu(111) interfaces may also reflect a higher packing density of MG resulting from a higher density of adsorbed MG on the Cu(111) lattice. The results help to understand, at the molecular level, the effects of MG as an additive for Cu electrodeposition. The differences in orientation and packing density of MG at the Cu(100) and Cu(111) facets demonstrated here, are sufficient to account for the dramatic differences in electrodeposited Cu crystallite morphology in the presence of MG. The preference of MG for the Cu(111) facet, as reflected in higher packing density and somewhat more upright averaged orientation, is consistent with the growth mechanisms and kinetics revealed by the *in situ* electrochemical STM results, in which Cu electrodeposition

proceeds preferentially in 2–dimensions due to a lack of availability of adsorption sites on the Cu(111) facet.

Chapter 6. Computational Analysis of Effect of Additives on Cu Electrodeposition

Although the electronic characteristics of the (111) and (100) facets of the copper surface were discussed and analyzed in Chapter 4, further understanding of the effects of additives on copper electrodeposition were approached by computational simulation of adsorbates on copper substrates.

6.1. Molecular Dynamic Simulations

The Accelrys Materials Studio (MS) 4.3 was employed to perform the computation of adsorption energy and configuration. This software is widely used by scientists for simulating and modeling materials, especially for computational chemistry, bioinformatics, cheminformatics, molecular simulation, and quantum mechanics [168-171]. The adsorption mechanism of MG on Au and Cu single crystal (111) and (100) surfaces has been investigated with consistent valence forcefield (CVFF), polymer consistent forcefield (PCFF) and condensed-phase optimized molecular potentials for atomistic simulation studies (COMPASS) of the Adsorption Locator module of the program [169, 172]. To demonstrate the reliability of the results obtained with Materials Studio, a comparison of the adsorption energy was performed and compared with that reported through other methods. For example, the adsorption energy of hydrogen on the Pt (100) surface

was calculated as 43 kJ/mol by Adsorption Locator of Materials Studio, which is in good agreement with the microcalorimetric experimental value of 45 kJ/mol for hydrogen adsorption on Pt powders, and also is close to the value of 41 kJ/mol on the top sites of Pt (100) calculated using density functional theory (DFT) within the generalized gradient approximation (GGA) as implemented in the Vienna ab initio simulation package (VASP) [173].

Materials Studio has different modules that can perform adsorption computation. These modules are CASTEP (Cambridge serial total energy package), DMol (a unique DFT quantum mechanical method) and Adsorption Locator. These modules were compared by examining the output adsorption energies of cyclopropane on a Cu(111) surface. These energies were: 80.7 kJ/mol by CASTEP, 4.6 kJ/mol by DMol [171] and 47.8 kJ/mol by Adsorption Locator. Comparing these values with the experimental value of 37.8 kJ/mol [174], one can find Adsorption Locator gave the closest adsorption energy to the experimental value.

Adsorption Locator enables one to simulate a substrate loaded with an adsorbate and allows one to find low energy adsorption sites on both periodic and nonperiodic substrates. It can automatically optimize the configuration of adsorbate molecules on the surface of the substrate to minimize the total energy of the system or maximize the amount of adsorption energy. There are different options of forcefield to optimize elements and structure types, like CVFF, PCFF and COMPASS. Although the three forcefields gave different adsorption energies, the

trends for MG on Cu(111) and CU(100) were the same for each of the forcefields. Only the results obtained with the CVFF forcefield are reported here.

The analytic form of the energy expression used in CVFF can be summarized as:

$$E_{ad} = E_{ba} + E_{vib} + E_{vdW} + E_q \quad (41)$$

The adsorption energy E_{ad} has four contributing components. E_{ba} is the energy of deformation of bond lengths, bond angles, torsion angles, and out-of-plane interactions; E_{vib} is the energy of couplings between deformations of internal coordinates; E_{vdW} is the energy of van der Waals interactions with a Lennard-Jones function; E_q is the energy of electrostatic interactions. The computational reference condition was set to standard condition [169]. For more details about Adsorption Locator, please see Appendix C.

6.2. Optimal Geometry of Additives

The adsorbates, 1-propanol, malachite green neutral molecule and its cation were constructed and optimized both geometrically and energetically. Figure 69 and Figure 70 show the optimal structure of malachite green cation (MG^+) and 1-propanol, respectively, generated by Material Studio using the same forcefield and parameters with adsorption simulation. The total energy of MG and MG^+ were minimized to 754.5 kJ/mol and 824.3 kJ/mol, respectively, while the optimized energy of 1-propanol was found to be 23.9 kJ/mol.

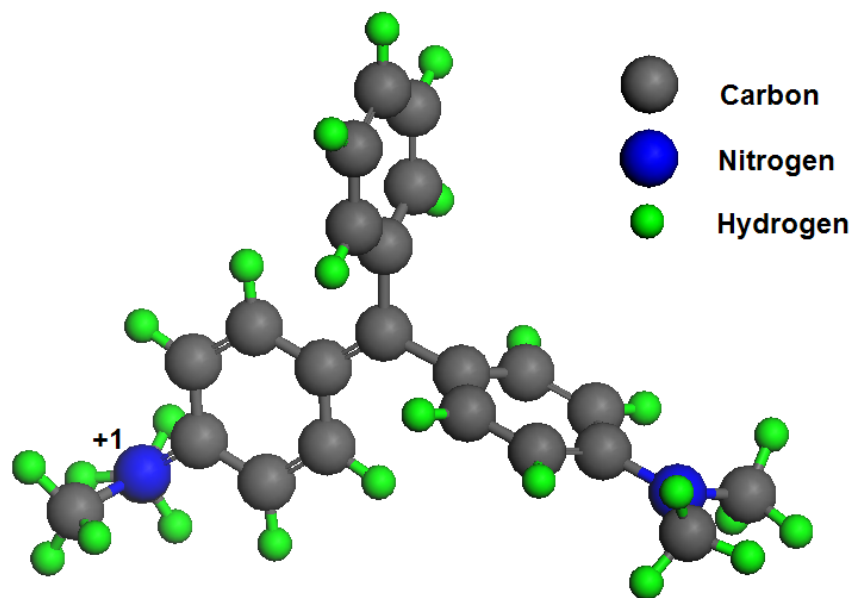


Figure 69. Geometric structure of ionized malachite green.

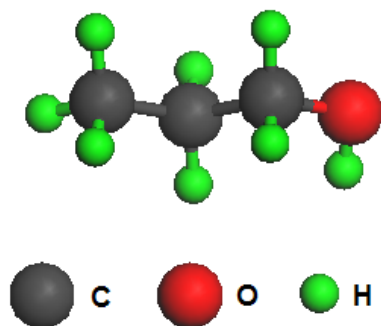


Figure 70. Geometric structure of 1-propanol.

6.3. Adsorption of Additives on Au, Cu and HOPG

To investigate the adsorption mechanism of additives on the Au, Cu and HOPG surfaces, the adsorption of MG, MG^+ and 1-propanol on neutral and negatively charged substrates was simulated with the Adsorption Locator module. The methods used are Monte Carlo methods which are a class of computational algorithms that rely on repeated random sampling to compute their results [175, 176]. The negatively charged substrate imitates the situation when a cathodic potential is applied. The surface charge density was assigned based on the measured capacitance of electrical double layers of the electrodes in the electrodeposition solution. The capacitance of a double layer varies usually from 0.2 to $50 \mu\text{F}/\text{cm}^2$ for different electrode materials and composition of electrolytes [177-179]. The first approximation was made by giving a medium value of $10 \mu\text{F}/\text{cm}^2$ and calculating the surface charge density, -0.05 electron charges per atom (electron/atom). The other assigned charges were calculated with measured double layer capacitances according to the following equation [180].

$$\frac{I_a - I_c}{2} = C_{dl} \frac{dE}{dt} \quad (42)$$

where I_a and I_c are the anodic and cathodic currents from the CV curve, corresponding to the potential of open circuit, E_{OC} . C_{dl} is the double layer capacitance and dE/dt the scan rate (40 mV/s). The scan range was set from $E_{OC} - 15$ mV to $E_{OC} + 15$ mV. The measured capacitance in 0.050 M CuSO_4 electrolyte

with 0.0050 M MG for Cu was $1 \mu F/cm^2$, Au $6 \mu F/cm^2$ and HOPG $60 \mu F/cm^2$, and the calculated surface charge densities were Cu -0.005, Au -0.03 and HOPG -0.3 electron/atom, respectively.

The effect of slab's thickness on adsorption energy and configuration of MG, MG^+ and 1-propanol on substrates was also investigated. The program gives ten configurations with the biggest adsorption energy or lowest total energy. A typical output of energy by Adsorption Locator is shown in Table 11.

Table 11. A typical energy output: adsorption of MG^+ on two-layer Au(111) with surface charge density of -0.03 electron/atom. Energy unit is kJ/mol.

Structures	Total energy	Adsorption energy	Rigid adsorption energy	Deformation energy	dEad/dNi
Substrate	0				
MG^+	824.3				
Au (111) - 1	-486.5	-1310.9	-1418.5	107.6	-1310.9
Au (111) - 2	-484.3	-1308.7	-1415.8	107.2	-1308.7
Au (111) - 3	-482.9	-1307.2	-1414.7	107.5	-1307.2
Au (111) - 4	-479.2	-1303.5	-1402.8	99.4	-1303.5
Au (111) - 5	-478.1	-1302.4	-1408.9	106.5	-1302.4
Au (111) - 6	-477.2	-1301.5	-1403.5	102.0	-1301.5
Au (111) - 7	-474.9	-1299.2	-1396.4	97.2	-1299.2
Au (111) - 8	-472.5	-1296.8	-1399.3	102.5	-1296.8
Au (111) - 9	-471.1	-1295.4	-1387.7	92.3	-1295.4
Au (111)-10	-468.3	-1292.6	-1393.1	100.5	-1292.6

The program outputting table lists the initial energy of adsorbate and substrate, and a series (usually 10) of optimized configurations and related energies in kcal/mol (which is converted into kJ/mol in Table 11). Configuration number 1 contains the lowest total energy (or releases the highest adsorption

energy), which is taken for comparison with different simulations. The deformation energy reports the energy released when the adsorbed adsorbate components are relaxed on the substrate surface. The value of dE_{ad}/dN_i reports the energy of substrate–adsorbate configurations where one of the adsorbate components has been removed. The most suitable configuration is defined as the one with the highest adsorption energy [181].

6.3.1. Adsorption of MG on Au

The adsorption of MG molecules and MG^+ cations on Au(111) and Au(100) surfaces were simulated at charge densities of 0, -0.03 and -0.05 electron/atom. To investigate the effect of the number of atomic layers of the substrate on the adsorption energy, up to four layers of Au slabs were used as substrates to simulate the adsorption of MG and MG^+ on Au. Table 12 lists the highest adsorption energies of MG and MG^+ on Au(111) and Au(100) with different charges and thickness.

Table 12. Adsorption energies of MG and MG^+ on Au(111) and Au(100) surfaces. Energy unit is kJ/mol and surface charge density electron/atom.

Substrate	Surfaces	(111)			(100)		
		Charges	0	-0.03	-0.05	0	-0.03
Layers	Adsorbates	MG	MG^+	MG^+	MG	MG^+	MG^+
1		-573.5	-1207.7	-1644.9	-497.5	-1124.7	-1554.5
2		-679.4	-1310.9	-1748.7	-615.8	-1238.7	-1667.4
3		-699.9	-1336.3	-1764.8	-645.4	-1250.8	-1696.7
4		-680.5	-1332.2	-1755.6	-649.3	-1275.7	-1706.7

For an example of the most suitable geometric configurations, Figure 71 gives a structural illustration of the adsorption of MG^+ on negatively charged two-layer Au(111) with surface charge density of -0.03 electron/atom.

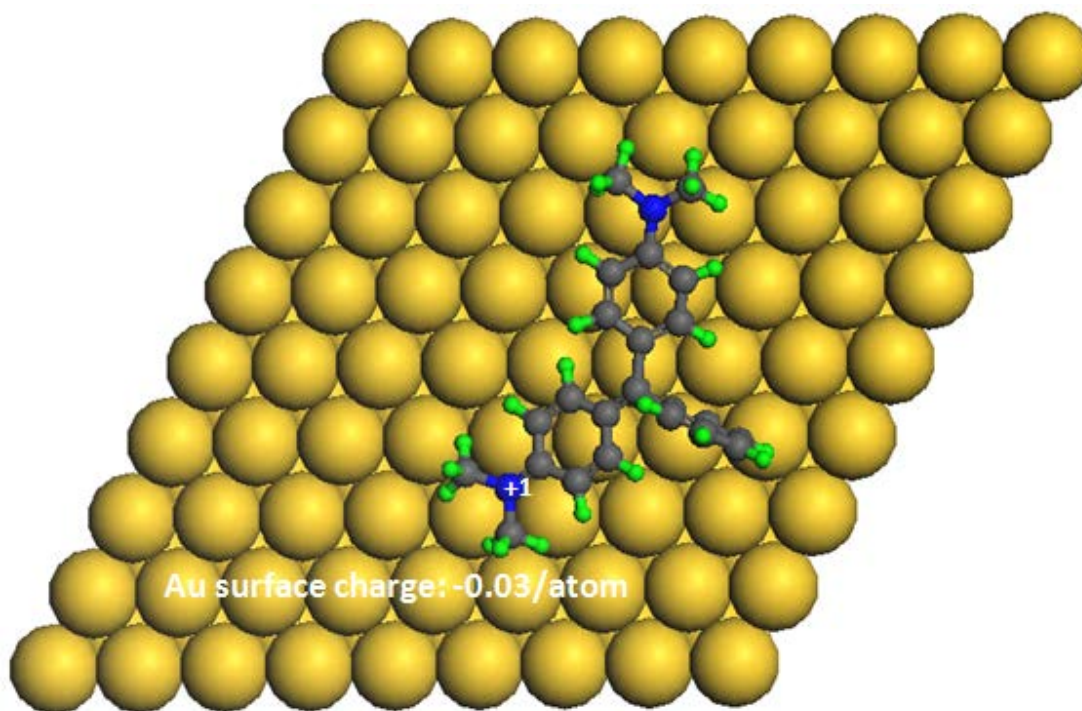


Figure 71. *The most suitable configuration for adsorption of MG^+ on two-layer negatively charged Au (111) substrate obtained by Adsorption Locator module.*

As can be seen from the above table, at the same surface charge density, when the number of atomic layers (thickness) of the slab increases, the adsorption energy had a large change of about 100 kJ/mol from 1 layer to 2 layers; but the

increments become much smaller from 2 layers to 3 layers. The change of adsorption energy from 3 to 4 layers is even less significant. When the electronic charge of the adsorbate and the substrate increases, the adsorption energy increases too. For the same surface charge density, the adsorption energy on Au(111) is generally larger than on Au(100), from which it is concluded that MG and MG^+ have a stronger interaction with Au(111) surface than with Au(100) surface. Comparison of the results in Table 12 indicate that the adsorption energies on the Cu(111) surface are ~5-10% greater than on the Cu(100) surface.

These results are consistent with our previous experimental observations which indicate preferential adsorption of MG on the Au(111) surface over the Au(100) surface. The adsorption mechanism reflects a dynamic equilibrium between MG in the electrolyte and in the adsorbed state. These simulations indicate that adsorption energies that differ by as little as 5-10% are sufficient to greatly modify the resulting nucleation and growth rates for Cu electrodeposition on Au. The stronger interaction with Au(111) provides fewer opportunities for copper ions to be reduced and deposit on the (111) facet and help to explain the observations of the *in situ* EC-STM experiments described previously (Figure 51). Copper nucleation and growth on the Au surface in the presence of MG proceeded at the Au(111) step edges, consistent with idea that the Au(111) terraces were effectively blocked by the additive MG and driving growth on other crystal facets (e.g. (100)).

6.3.2. Adsorption Energies of MG on Cu

The adsorption energies of MG and MG^+ on Cu(111) and Cu(100) surfaces are similar to that of Au surfaces. Table 13 shows the simulation results of adsorption energies of malachite green on Cu using the Adsorption Locator module, and the most suitable configuration of MG^+ on two-layer cathodic Cu(111) with surface charge density of -0.005 electron/atom is presented in Figure 72. The effect of thickness and surface charge density of the slab on the adsorption energies of MG and MG^+ on Cu surfaces is the same as that of MG and MG^+ on Au. The higher adsorption energy of MG and MG^+ on Cu(111) than on Cu(100) rationalized the experimental results. The stronger interaction between MG or MG^+ and Cu(111) provided fewer opportunities for Cu deposition on the Cu(111) facets. Under UPD conditions in the *in situ* EC-STM experiment, Cu deposited along Au(111) terraces, and once Cu(111) ad layers were formed, new terraces appeared and grew along the edges (Figure 51). Under over-potential circumstances, Cu displayed bulk 3-dimensional deposition. The lower adsorption energy on Cu(100) surface indicates weaker interaction between MG or MG^+ and Cu(100) surface, and provide more opportunities for copper ions to be reduced and deposited on Cu(100), resulting in copper crystals growing along the Cu(100) (Cu(200)) direction to form square pyramidal structures (Figure 37).

Table 13. Adsorption energies of MG and MG⁺ on Cu(111) and Cu(100) surfaces. Energy unit is kJ/mol and surface charge density electron/atom.

Substrate	Surfaces	(111)			(100)		
		Charges	0	-0.005	-0.05	0	-0.005
Layers	Adsorbates	MG	MG ⁺	MG ⁺	MG	MG ⁺	MG ⁺
1		-617.5	-726.5	-1817.5	-533.2	-638.7	-1709.1
2		-722.4	-856.6	-2013.5	-669.5	-786.0	-1845.1
3		-727.2	-864.8	-1946.6	-704.6	-810.9	-1843.4
4		-766.9	-879.1	-1952.1	-722.2	-834.7	-1873.1

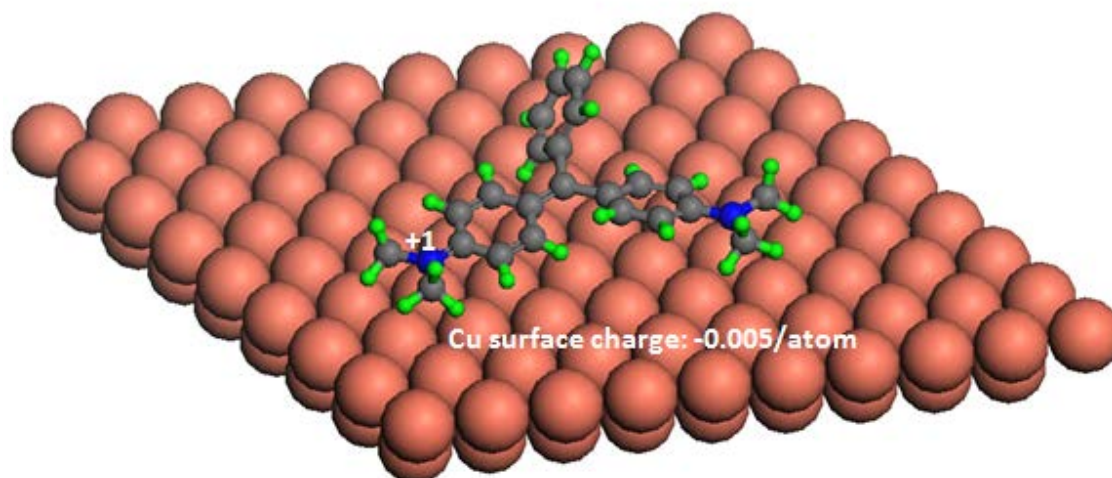


Figure 72. The most suitable configuration for adsorption of MG⁺ on two-layer negatively charged Cu (111) substrate obtained using Adsorption Locator module.

Relating the computational results to the experimental observations, we proposed the models for the effect of MG on Cu electrodeposition. Figure 73 shows the Cu nucleation along edges of existing terraces which were mostly covered by MG⁺. This phenomenon was observed in *in situ* EC-STM experiments. Figure 74 shows the bulk growth of Cu deposits along the normal of (200) surface

as MG^+ has a stronger interaction with Cu(111) surface which decreases the opportunities for Cu growing on the Cu(111) surface leaving copper ions reduced on the Cu(200) surfaces. Cu grows faster along the normal of the Cu(200). The behaviour of MG leads to the formation of square pyramids which were the observed morphologies on Cu film images obtained with AFM and SEM.

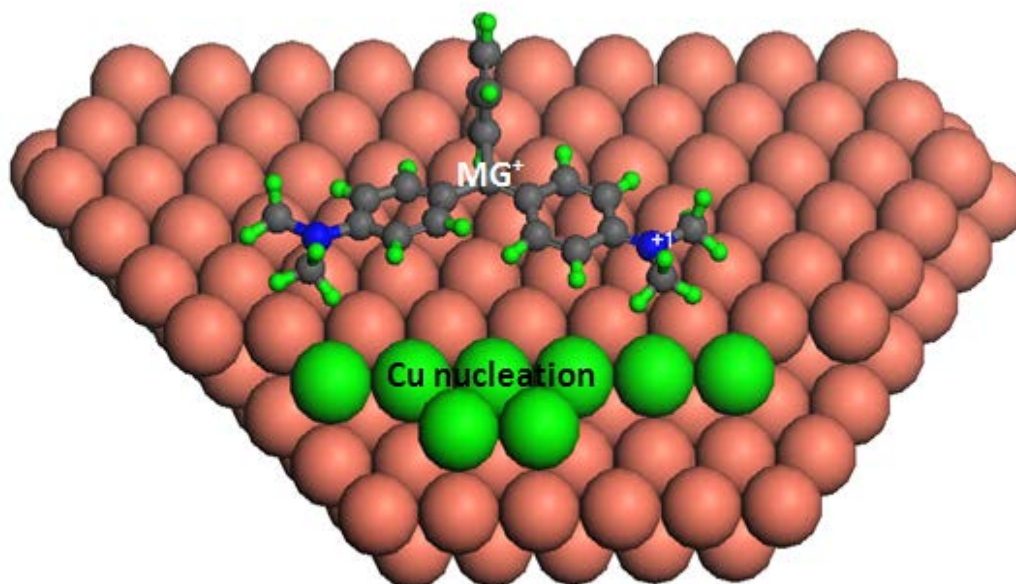


Figure 73. Model of Cu nucleation along existing terraces in the presence of additive MG in electrolyte solution.

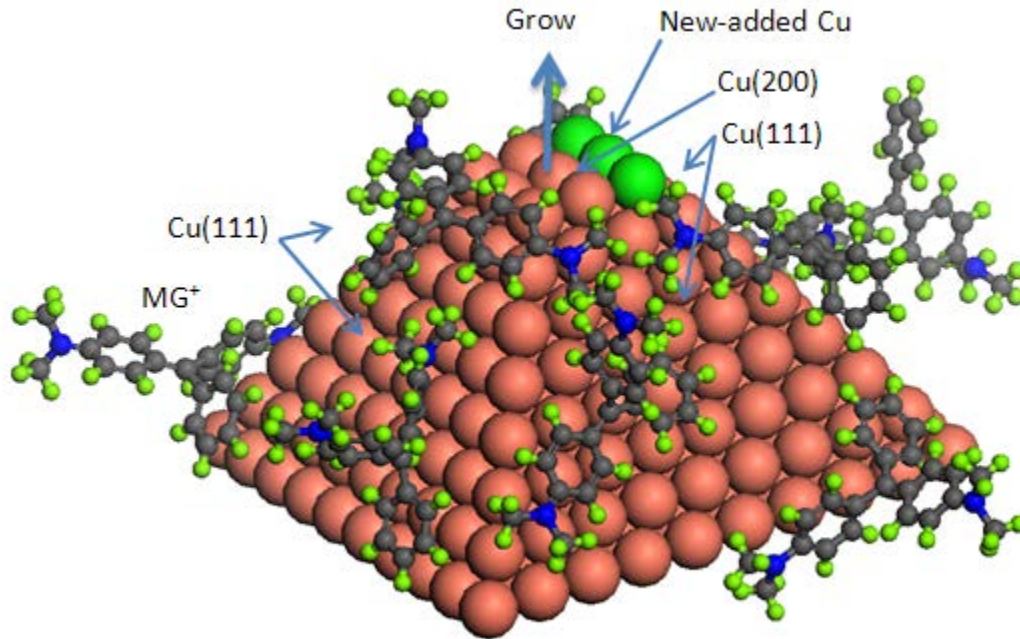


Figure 74. Model of the formation of a Cu square pyramid from the electrolyte with additive MG.

These models were generated through simulating the adsorption of malachite green cations on the cathodic substrate surfaces using the Adsorption Locator module, Materials Studio. They provided reasonable mechanisms of the effect of MG on the copper electrodeposition.

6.3.3. Adsorption of MG on HOPG

Table 14 shows the adsorption energies of MG and MG^+ on HOPG (111) and (100) surfaces simulated by MS. Figure 75 presents the most suitable molecular dynamic configuration for adsorption of MG^+ on one-layer negatively charged HOPG (111) surface.

Table 14. Adsorption energies of MG and MG⁺ on HOPG(111) and HOPG(100) surfaces. Energy unit is kJ/mol and surface charge density electron/atom.

Substrate	Surfaces	(111)			(100)			
		Charges	0	-0.05	-0.3	0	-0.05	-0.3
Layers	Adsorbates	MG	MG ⁺	MG ⁺	MG	MG ⁺	MG ⁺	
1		-89.6	-1273.2	-7503.1	0.0	-72.1	-1211.4	-7269.0
2		-112.9	-1298.3	-7532.4	0.0	-97.3	-1252.7	-7294.1

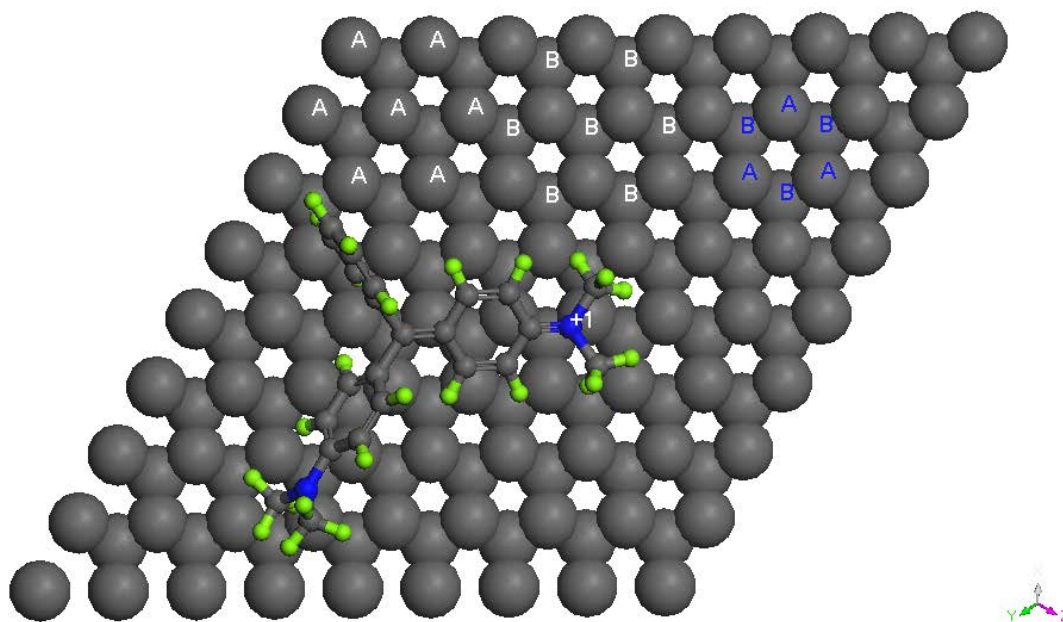


Figure 75. The most suitable configuration for adsorption of MG⁺ on negatively charged one-layer HOPG (111) substrate obtained using Adsorption Locator module. A and B refer to different types of carbon atoms on the surface.

In the table, only two layer substrates were presented because more layers were observed to make a negligible effect, which may be caused by the characteristic structure of HOPG. The packing of carbon atoms on a “one-layer”

HOPG layer consist of two “sub-layers” or two types of atoms. Type *A* is a little bit higher than type *B* as shown in Figure 75. All *A* or *B* atoms form (111) surfaces, which is indicated by white letters; but *A* and *B* atoms together form hexagonal rings on the surface, which is indicated by blue letters, which were consistent with our atomic STM images of HOPG (not shown). The usual atomic resolution displayed only *A* or *B* type of atoms and the ideal atomic resolution displayed both *A* and *B* atoms.

Analysis of the dimensions demonstrated that the distances from *A* to *A* or from *B* to *B* apparent atoms are 2.5 Å which matches the lattice size of Cu(111), 2.56 Å. The simulation demonstrated that adsorption energies of MG and MG⁺ on the HOPG surfaces showed the same trends as on Au and Cu surfaces. Increasing number of slab layers can increase adsorption energy by a small amount, but the increasing surface charge densities can dramatically increase adsorption energies. It is important to notice that the adsorption energy of MG and MG⁺ on HOPG(111) surface is larger than on HOPG(100) surface for the same surface charge density and adsorbate. The stronger interaction of MG and MG⁺ with HOPG(111) surface provided less opportunities for copper to deposit on (111) surface. So during the *in situ* EC-STM experiments, the phenomenon was observed that copper nucleation from CuSO₄ electrolyte with addition of MG formed and grew along existing edges of HOPG(111) terraces, or produced new terraces (Figure 55).

The simulation of adsorption of malachite green on Au, Cu and HOPG indicated that the more close-packed (111) surface has a higher adsorption energy than more open (100) surface. This result helps explain the experimentally observed effect of MG on Cu electrodeposition. The trends of adsorption energy obtained in the simulation are consistent with the investigation of hydrogen adsorption on Cu reported by P. Kratzer *et al.* They found that the more open (100) surface exhibits a minimum energy barrier which is 0.1 eV larger than the minimum energy barrier of the more closed (111) surface [182].

6.3.4. Adsorption of 1-Propanol on Substrates

The same adsorption simulations for 1-propanol on Au, Cu and HOPG crystal surfaces as MG on them have also been performed, but the number of slab layers used are one and two because of the small size of 1-propanol molecule, which may be adsorbed onto the sides of thicker slabs. Table 15 presents the simulated adsorption energies with different surface charge densities, and Figure 76 shows the most suitable configuration of 1-propanol on two-layer Au(111) with surface charge density of -0.03 electron/atom.

Table 15. Adsorption energies of 1-propanol on Au(111) and Au(100) surfaces. Energy unit is kJ/mol and surface charge density electron/atom.

slab Layers	Surfaces Charges	Au(111)			Au(100)		
		0	-0.03	-0.05	0	-0.03	-0.05
1		-114.2	-127.2	-133.9	-102.2	-115.5	-121.3
2		-133.6	-144.0	-150.1	-122.4	-135.1	-141.1

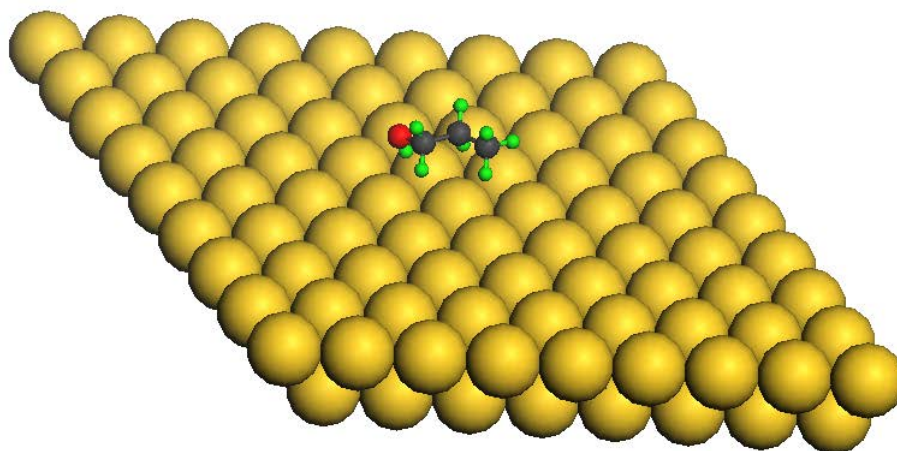


Figure 76. *The most suitable configuration for adsorption of 1-propanol on two-layer Au (111) with surface charge density -0.03 electron/atom, obtained by Adsorption Locator of Materials Studio.*

From the above simulation, it is found that the adsorption energy trends for 1-propanol on Au substrate are the same as for malachite green on Au. That is larger number of slab layers and surface charge density produce larger adsorption energy. Also, the adsorption energy on Au(111) is higher than on Au(100) surface for the same layer slab and surface charge density. These trends have also been seen for the adsorption of 1-propanol on Cu and HOPG substrates (results are not shown here). Comparing the adsorption energies listed in Table 12 and Table 15, one can find that the adsorption energy of malachite green on Au is about 7 times of that of 1-propanol on Au. The analysis of simulating total energy diagrams

demonstrated that the stronger interaction between MG^+ and substrates not only came from higher van de Waals force, but also from much higher electrostatic force than that between 1-propanol and substrates. Very low concentrations of MG exerted a remarkable effect on copper electrodeposition, but 1-propanol needed high concentrations. Because the size of 1-propanol molecule is much smaller than MG, it can diffuse much faster than MG in solution. The diffusion coefficient of 1-propanol is 26 times of that of MG [183, 184]. The weakly adsorbed small 1-propanol molecules provided more opportunities for copper to deposit on. This behavior of 1-propanol was different from that of MG and MG^+ on the surfaces of electrodes, which produced the different effects of 1-propanol and MG on copper electrodeposition as observed in previous chapters.

6.4. MG Molecular Orientation Simulation

Further investigation of MG and MG^+ molecular orientation adsorbed on Cu(111) and Cu(100) surface was performed by molecular dynamics simulation with Materials Studio. Neutral and charged adsorbates and substrates were simulated to determine the orientation of MG and MG^+ . Figure 77 shows the simulated configuration of MG^+ on a negatively charged Cu(100) bilayer slab. The XY defines the surface of Cu slab; θ is the orientation angle of the molecular axis Z' to the normal of the substrate surface Z, which is consistent with the definitions in SHG data fitting the in previous chapter. The angle α is defined between the normal of the bare benzene ring (without dimethylamino group) plane z'' .

Table 16. Molecular dynamic simulation of MG orientation on copper substrate. "-" stands for negatively charged substrate.

Simulation	$\bar{r}(\text{\AA})$	$\theta(^{\circ})$	$\alpha(^{\circ})$
Cu(111)/MG	3.20	78.43	55.69
Cu(111)/MG ⁺	3.10	71.91	67.50
Cu(111) ⁻ /MG ⁺	3.04	69.56	80.31
Cu(100)/MG	3.23	74.45	81.59
Cu(100)/MG ⁺	3.26	73.61	76.31
Cu(100) ⁻ /MG ⁺	3.18	73.34	76.18

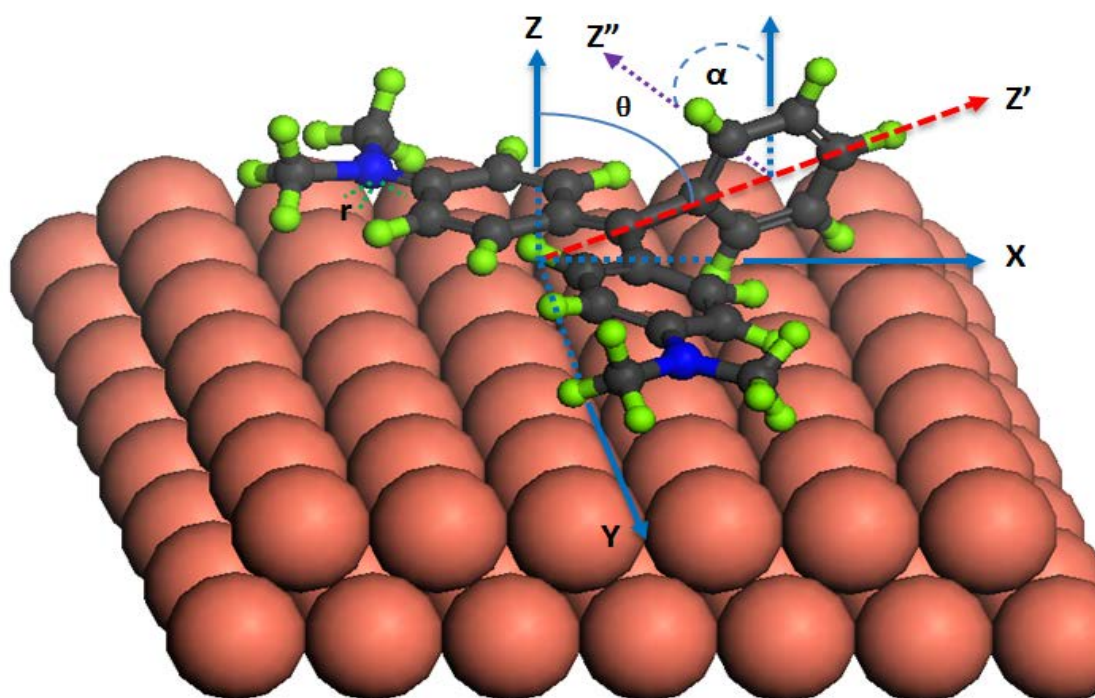


Figure 77. Simulating result of MG⁺ orientation on cathodic Cu(100) substrate.

The distance from positively charged nitrogen atom to the nearest Cu atom is r . In Table 16, \bar{r} refers to the average value of the three minimum r measurements, which depicts how close the adsorbed MG or MG^+ is to the substrate surface.

From the simulated data list in Table 16, it can be seen that the adsorption distance \bar{r} of MG and MG^+ to Cu(111) is shorter than to Cu(100). These distances indicate that MG and MG^+ have a stronger interaction with Cu(111) surface, which is consistent with previous adsorption energy calculation. The charges on either adsorbate or substrate can decrease the distance because of strengthened interaction with each other. The smaller the θ , the more perpendicular the molecular axis z' is to the slab surface; the larger the α , the more perpendicular the bare ring to the slab. These simulation results indicate that the MG adsorbates adopt relatively flat orientations on the surface, consistent with our previous SHG determined averaged orientations. The values of θ decrease slightly when the slab is negatively charged, which indicates the MG^+ molecular axis becomes slightly more perpendicular to the slab surface. This result is also consistent with that of the SHG data fitting. The simulation results indicate that the charges have a different effect on the angle of α for the two surfaces. The bare benzene ring becomes more perpendicular to Cu(111) but less to Cu(100) when the charges increase. The stronger interaction, higher density of adsorption sites, and somewhat more perpendicular orientations to the cathodic Cu(111) surface predicted by these simulations are consistent with our previously described

experimental SHG results and reinforce the model for MG and its effects on electrodeposition.

6.5. Conclusion

The effects of the additives, MG and 1-propanol, on Cu electrodeposition were simulated using the molecular dynamics methods available in the Adsorption Locator module of the Materials Studio software suite. Both neutral MG molecules and their positive ions prefer to adsorb on the more close packed (111) surface than on the more open (100) surface. These results were consistent with those yielded by VASP. The adsorption mechanism of MG^+ on a cathodic substrate was discussed and the most suitable configurations of MG^+ on Au, Cu and HOPG were given. The adsorption distance and orientation angles of malachite green on the copper, gold, and HOPG surfaces were obtained, and in all cases, MG was found to adopt a relatively flat orientation, which optimized the attractive van der Waals interactions between the adsorbate and surface. The simulations also predicted stronger interactions between malachite green and (111) surfaces, consistent with the observations of the *in situ* EC-STM, AFM and SEM studies described previously. Models of Cu nucleation on (111) terrace edges and bulk deposition to form square pyramids were also generated by the Materials Studio software. The molecular and adsorption differences between 1-propanol and MG were also investigated. The interaction strengths between 1-propanol and the gold, copper, and HOPG surfaces were found to be significantly lower than those between MG

and these surfaces. While 1-propanol was found to interact more strongly with the (111) facets than the (100) facets, similar to the behaviour observed for MG, the significantly smaller interaction strengths for 1-propanol with all surfaces yielded very different additive effects on the electrodeposition of Cu, presumably due to the ready availability of adsorption sites on both (111) and other crystal surface facets.

Chapter 7. Summary, Conclusions and Future Work

7.1. Summary and Conclusions

This thesis describes the investigation of the effect of additives on copper electrodeposition through electrochemical and nanoimaging techniques. The deposition mechanism was modified by either of the additives 1-propanol or MG, such that the surface features of the electrodeposited copper films were significantly altered. A series of cyclic voltammograms of CuSO_4 on Au electrodes were measured at concentrations from 0.010 to 0.090 M and scan rates from 2 to 500 mV/s in order to determine the electrochemical properties of the Cu ion's reduction on the Au electrode. The reaction was observed to be not a reversible process. The cathodic and anodic peak potentials were found at -215 and 347 mV for 0.050 M CuSO_4 at 20 mV/s. When additives were added to the electrolyte, the peak potentials and currents of the CVs and linear potential sweep voltammograms had been changed because of the blocking effects of additive adsorption on the electrode surface. The additive 1-propanol produced pronounced decreases in the cathodic peak current, without shifting the peak potential significantly. However, these effects required the presence of relatively high concentrations of 1-propanol (~1.0 M) in order to observe substantial effects. In the

case of MG addition in solution, concentrations as low as 0.0050 M can reduce the cathodic peak potential by 200 mV without changing peak current. The different effects of 1-propanol and MG on the copper electrochemical process implied different mechanisms for the two additives. Since 1-propanol reduced the plateau limiting current in the CV and there was no evidence for formation of complexes of $[\text{Cu}(\text{C}_3\text{H}_8\text{O})_n(\text{H}_2\text{O})_{6-n}]^{2+}$, a model of hydrogen bonding between 1-propanol and water solvated copper ions $[\text{Cu}(\text{H}_2\text{O})_6]^{2+}$ was suggested. MG did not change the cathodic plateau current, suggesting that there is no complex formation between the Cu and MG ions in the electrolyte solution.

Cu films were electrodeposited onto Au-TFE electrodes from additive-free 0.050 M CuSO_4 solution with 1.0 M 1-propanol and with 0.0050 M MG, respectively. The characteristics of the resulting Cu films were analyzed with AFM, SEM and XRD techniques. The morphology measurements and grain analysis from AFM and SEM images of the copper films found that the area roughness and grain size of Cu are decreased by addition of 1-propanol and MG. The architectures of Cu grains from additive-free solution took non-regular shapes. The Cu grains from electrolytes with 1.0 M 1-propanol contained many trigonal pyramids and Cu grains obtained from electrolyte solutions containing 0.0050 M MG took the shape of square pyramids. These shapes of electrodeposited Cu grains were likely due to the different interactions of the additive molecules with the available crystalline facets of the growing metal film. XRD patterns from these films illustrate that the electrodeposited Cu films are polycrystalline, but the Cu(111)

orientation is preferred over other planes. The XRD pattern suggested that additives (especially MG) could increase this preference, One way to explain this preference is that the additive MG molecules/cations occupy electrodeposition sites on the Cu(111) surface more effectively than on the Cu(100) facet, resulting in a greater electrodeposition rate of Cu in the (200) direction. Although single crystal Cu is not electrochemically grown on the Au surface, the use of additives in electrolyte solution may provide a means of approaching it. This remarkable effect of additives on the morphology of electrodeposited copper films may stimulate more interest in controlling the mechanisms that affect the growth of copper films on Au.

The morphology modifications of the electrode surface during copper electrodeposition were monitored through *in situ* EC-STM experiments. STM images of copper nucleation and growth on Au(111) and HOPG from electrolytes with and without additives were obtained. The results revealed that the nucleation of Cu from additive-free 0.050 M CuSO₄ solution occurred everywhere on the surface and grew 3-dimensionally, which led to a rough-deposited film. When 1.0 M 1-propanol was added into the electrolyte, the nucleation and growth of Cu showed a small preference for sites on the step edges of the Au(111) terraces, though copper crystallites could also be found over the planar area of the Au(111) terraces on the surface. The most effective of the additives examined was Malachite Green. A very low concentration of 0.0050 M MG in electrolyte could cause the nucleation and expansion of Cu exclusively along the step edges of the

(111) terraces. These observations support the idea that MG adsorbs and interacts strongly with the (111) facets occupying potential Cu electrodeposition sites and driving the electrodeposition kinetics toward growth in the (100) direction.

The surface sensitive nonlinear optical spectroscopy, second harmonic generation (SHG), was used to investigate the Cu (100) and Cu(111) single crystal surfaces and the adsorption of MG from aqueous solutions to these interfaces. The SHG rotational anisotropic response from Cu(111) and Cu(100) surface in air was determined. The SHG results reflected the surface atomic packing symmetry. The SHG response to incident polarization angle in air, water and MG solutions revealed that the more closed Cu(111) surface can generate larger SHG signals than the more open Cu(100) surface, consistent with the higher density of atoms and adsorption sites on these facets. The higher SHG signal intensity from Cu(111)/MG(aq) than Cu(100)/MG(aq) also reflected the difference in behavior of MG molecules adsorbed on Cu(111) and Cu(100). Fitting the polarized SHG data provided averaged orientation information regarding the MG adsorbate. The SHG data suggested that on all surfaces, the averaged orientation of the MG adsorbate molecules is relatively flat, however, MG molecules adsorbed on the (111) surface of copper showed slightly more upright orientations than on the (100) copper surface. The SHG results indicate a higher surface concentration of MG molecules on the (111) surface, consistent with preferential adsorption of MG to this crystal face. The slightly more upright averaged orientation may result from a tighter packing of adsorbate molecules on the (111) facet and repulsive interactions

between them, or may result directly from the difference in atomic packing of Cu atoms on the two crystal facets.

The effect of MG on Cu deposition has also been simulated by molecular dynamics methods using the Adsorption Locator module of Materials Studio. The calculated adsorption energies of malachite green on the (111) surfaces of Cu, Au, and HOPG were approximately 10% greater than on their (100) facets. Both neutral MG molecules and their positive ions prefer to occupy sites on the more close packed (111) surface than on the more open (100) surface. The adsorption mechanisms of MG^+ on these cathodic substrates were discussed and the most suitable configurations of MG^+ on Au, Cu and HOPG were proposed. Models for Cu nucleation at the (111) facet step edges and bulk deposition to form square pyramids were generated by Materials Studio.

Taken together, our results provide a detailed understanding of the effects of the additives 1-propanol and malachite green on copper electrodeposition. They offer a new perspective on additive effects and suggest that with further optimization, control of electrodeposition can result in tailored nanostructured surfaces. Preliminary experiments to control the shapes of Cu crystallites and to produce customized nanoparticle arrays appear promising. Copper nanoparticle arrays were electrodeposited from 0.050 M CuSO_4 with 0.0050 M MG in solution on predesigned gold aperture electrodes, demonstrating the viability of the approach. However, additional and higher quality imaging methods are required to

identify the specific structures produced and to determine their degree of crystallinity.

7.2. Future Work

Further studies of the mechanisms of electrodeposition and the effects of additives on electrodeposition require more electrochemical experiments, including techniques such as, but not limited to, AC impedance and chronoamperometry. The effect of other experimental conditions such as the pH value of the electrolyte solution, combined additives, supporting electrolyte and temperature, on the electrochemical process of copper ion reduction should also be investigated. *In situ* EC-STM experimental techniques need to be improved in order to obtain atomic resolution images at particular potentials along the CV curve of the electrochemical system. Ideally, these images should provide the arrangement of deposited adatoms to the existing lattice and the growth of atom layers. Some additives and electrode materials that have strong bonding should be found for monitoring the behavior of additive molecules on the electrode surface. Optical experiments, especially *in situ* EC-spectroscopy, for behavior of additive molecules in solution and on electrode surfaces will be developed. For example, EC-second harmonic generation and EC-sum frequency generation will provide information regarding how many additive molecules adsorb on the electrode during electrodeposition, where they are adsorbed and how they are oriented.

As additives can help to customize the shape of electrodeposited nanostructures, future work to optimize this process and to control the shape of the nanoparticles is extremely desirable. Development of new micro- and nanoelectrode arrays and plasmonic structures that can be made from simple, fast and cost effective alternatives to current nanoscale patterning methods, are potentially extremely valuable in the development and implementation of new and emerging technologies.

References

1. Stanczak, M., *A Brief History of Copper*. CSA-Discovery Guides, 2005: p. 1-4.
2. Dresher, W.H., *Copper and Nanotechnology*. PH.D Thesis, 2006: p. 1-7.
3. Vereecken, P.M.; Binstead, R.A.; Deligianni, H. and Andricacos, P.C., *The chemistry of additives in damascene copper plating*. IBM J. RES. & DEV., 2005. **49** (1).
4. Jovic, V.D. and Jovic, B.M., *Copper electrodeposition from a copper acid baths in the presence of PEG and NaCl*. J.Serb.Chem.Soc., 2001. **66**(11-12): p. 935-952.
5. Zhou, X.J.; Harmer, A.J.; Heinig, N.F. and Leung, K.T., *Parametric Study on Electrochemical Deposition of Copper Nanoparticles on an Ultrathin Polypyrrole Film Deposited on a Gold Film Electrode*. Langmuir 2004. **20**: p. 5109-5113.
6. Andersen, J.E.T.; Bech-Nielsen, G. and Moller, P., *Bulk copper electrodeposition on gold imaged by in situ STM: morphology and influence of tip potential*. Journal of Applied Electrochemistry 1996. **26** p. 161-170.
7. Gilbert, S.E.; Cavalleri, O. and Kern, K., *Electrodeposition of Cu Nanoparticles on Decanethiol-Covered Au(111) Surfaces: An in Situ STM Investigation*. The Journal of Physical Chemistry, 1996. **100**(30): p. 12123-12130.
8. Dietterle, M.; Will, T. and Kolb, D.M., *The initial stages of Cu electrodeposition on Ag(100): an in situ STM study*. Surface Science 1998. **396** p. 189-197.
9. Breuer, N.; Stimming, U. and Vogel, R., *FORMATION, STABILITY, AND DISSOLUTION OF CLUSTERS ON ELECTRODES MONITORED BY IN-SITU STM*. Electrochimica Acta, 1995. **40**(10): p. 1401-1469.
10. Andersen, J.E.T. and Moller, P., *Influence of the tip on electrode processes and on morphologies studied by in situ STM: Cu/Au*. Surface and Coatings Technology, 1997. **89** p. 1-9.
11. Randler, R.J.; Kolb, D.M.; Ocko, B.M. and Robinson, I.K., *Electrochemical copper deposition on Au(100): a combined in situ STM and in situ surface X-ray diffraction study*. Surface Science, 2000. **447** p. 187-200.
12. Thouvenel-Romans, S.; Agladze, K. and Steinbock, O., *Traveling Fronts of Copper Deposition*. J. AM. CHEM. SOC. , 2002. **124**: p. 10292-10293.
13. Eyraud, M.; Kologo, S.; Bonou, L. and Massiani, Y., *Effect of additives on Cu electrodeposits: electrochemical study coupled with EQCM measurements*. Journal of Electroceramics, 2006. **16**(1): p. 55-63.
14. Kapoius, V.; Karpaviiien, V. and Steponaviius, A., *Electrochemical Processes at a Platinum Electrode in CuSO₄ Solutions in the UPD Region and at Initial Electrocrystallization Stages: Effect of Polyethylene Glycol*. Russian Journal of Electrochemistry, 2002. **38**(3): p. 6.
15. Riemer, I.T.a.S., *Roughness development in electrodeposited soft magnetic CoNiFe films in the presence of organic additives*. J.Serb.Chem.Soc. , 2003. **68**(4-5): p. 13.

16. Franklin, T.C., *Some mechanisms of action of additives in electrodeposition processes. Surface and Coatings Technology*, 1987. **30**(4): p. 14.
17. Peter, L.; Kupay, Z.; Cziraki, A.; Padar, J.; Toth, J. and Bakonyi, I., *Additive Effects in Multilayer Electrodeposition: Properties of Co-Cu/Cu Multilayers Deposited with NaCl Additive. J. Phys. Chem. B*, 2001. **105**: p. 7.
18. Pricer, T.J.; Kushner, M.J. and Alkire, R.C., *Monte Carlo Simulation of the Electrodeposition of Copper. Journal of The Electrochemical Society*, 2002. **149**(8): p. C406.
19. Danilov, A.I.; Andersen, J.E.T.; Molodkina, E.B.; Polukarov, Y.M.; Meller, P. and Ulstrup, J., *The influence of intermediate particles on the nucleation of copper on polycrystalline platinum. Electrochimica Acta*, 1997. **43**(7): p. 733-741.
20. Adolf, J.D., *Function of Additives in Copper Electrodeposition for Semiconductor Device Metallization. Thesis*, 2008: p. 1-77.
21. Hasegawa, M.; Negishi, Y.; Nakanishi, T. and Osaka, T., *Effects of Additives on Copper Electrodeposition in Submicrometer Trenches. Journal of The Electrochemical Society*, 2005. **152**(4): p. C221.
22. Hebert, K.R., *Analysis of Current-Potential Hysteresis during Electrodeposition of Copper with Additives. Journal of The Electrochemical Society*, 2001. **148**(11): p. C726.
23. Kim, J.-W.; Lee, J.-Y. and Park, S.-M., *Effects of Organic Additives on Zinc Electrodeposition at Iron Electrodes Studied by EQCM and in Situ STM. Langmuir*, 2004. **20**: p. 459-466.
24. Cetnarowski, G. and Leach, G.W., *Optical second-harmonic generation study of exfoliated MoS₂-malachite green inclusion materials. Langmuir : the ACS journal of surfaces and colloids*, 2006. **22**(21): p. 8995-9001.
25. Kikteva, T.; Star, D. and Leach, G.W., *Optical Second Harmonic Generation Study of Malachite Green Orientation and Order at the Fused-Silica/Air Interface. J. Phys. Chem. B*, 2000. **104**: p. 2860-2867.
26. Ritchie, I.M.; Bailey, S. and Woods, R., *The Metal-Solution Interface. Advances in Colloid and Interface Science*, 1999. **80** p. 183-231.
27. *Basic Geochemical Research Supports Energy Industries. ORNL Review*, 2001. **34**(2).
28. *Electrical Double-Layer Formation Part 1. September 13, 2011. <http://what-when-how.com/nanoscience-and-nanotechnology/electrical-double-layer-formation-part-1-nanotechnology/>: p. 1-13.*
29. Inam-UI-Haque; Sadiq, I. and Khan, A., *Chrome Electrodeposition Additives. Jour. Chem. Soc. Pak.*, 2002. **24**(4): p. 308-314.
30. U.S. Mohanty, B.C.T., S.C. Das and V.N. Misra, *Effect of Thiourea during Nickel Electrodeposition from Acidic Sulfate Solutions. Metallurgical and Materials Transactions B*, 2005. **36B**: p. 5.
31. Imanishi, A.; Yokoyama, T.; Kitajima, Y. and Ohta, T., *Structural and Electronic Properties of Adsorbed Thiophene on Cu(111) Studied by S K-Edge X-Ray Absorption Spectroscopy. Bull. Chem. Soc. Jpn.*, 1998. **71**(4): p. 831-835.
32. Ciszewski, A., *Effects of saccharin and quaternary ammonium chlorides on the electrodeposition of nickel from a Watts-type electrolyte. Surface and Coatings Technology*, 2004. **183**(2-3): p. 127-133.

33. Selvakumari, T.M.; Emerson, R.N. and Ganesan, S., *Effect of Organic Additives on the Magnetic Properties of Nano Crystalline Hard Magnetic Films*. *Digest Journal of Nanomaterials and Biostructures*, 2011. **6**(1): p. 9-12.
34. De Leon, P.; Albano, E.; Salvarezza, R. and Solari, H., *Interface dynamics for copper electrodeposition: The role of organic additives in the growth mode*. *Physical Review E*, 2002. **66**(4).
35. Tabakovic, I. and Riemer, S., *Role of Organic Additives on Electrodeposition of Soft Magnetic Alloys*. <http://www.electrochem.org/dl/ma/203/pdfs/0636.pdf>, September 15, 2011.
36. Vasko, V., *Effect of organic additives on structure, resistivity, and room-temperature recrystallization of electrodeposited copper*. *Microelectronic Engineering*, 2004. **75**(1): p. 71-77.
37. Dolati, A.; Imanieh, I.; Salehi, F. and Farahani, M., *The effect of cysteine on electrodeposition of gold nanoparticle*. *Materials Science and Engineering: B*, 2011. **176**(16): p. 1307-1312.
38. Oniciu, L. and Mureşan, L., *Some fundamental aspects of levelling and brightening in metal electrodeposition*. *Journal of Applied Electrochemistry*, 1991. **21**(7): p. 565-574.
39. Dini, J.W., *Electrodeposition: the materials science of coatings and substrates 1ed1993*, New Jersey: Noys Publications. 371.
40. Kawaminami, M.; Sugimoto, R.; Yokoshima, T.; Asa, F.; Momma, T.; Osaka, T. and Honma, H., *Effect of Organic Alcohol Additives on the Shape for Electrodeposited Ni Microprobes*. <http://www.electrochem.org/dl/ma/200/pdfs/0781.pdf>, September 15, 2011.
41. Varvara, S.; Muresan, L.; Nicoara, A.; Maurin, G. and Popescu, I.C., *inetic and morphological investigation of copper electrodeposition from sulfate electrolytes in the presence of an additive based on ethoxyacetic alcohol and triethyl-benzyl-ammonium chloride*. *Materials Chemistry and Physics*, 2001. **72** p. 332-336.
42. Fabricius, G. and Sundholm, G., *The effect of additives on the electrodeposition of copper studied by the impedance technique*. *Journal of Applied Electrochemistry*, 1985. **15** p. 797-801.
43. Leung, T.Y.B.; Kang, M.; Corry, B.F. and Gewirth, A.A., *Benzotriazole as an Additive for Copper Electrodeposition Influence of Triazole Ring Substitution*. *Journal of The Electrochemical Society*, , 2000. **147** (9): p. 3326-3337.
44. V.A. Vas'ko , I.T., S.C. Riemer and M.T. Kief, *Effect of organic additives on structure, resistivity, and room-temperature recrystallization of electrodeposited copper*. *Microelectronic Engineering*, 2004. **75**: p. 7.
45. Ewing, W. and Evans, J.W.D., Fiona M. , *The Effect of Plating Additives on the Recovery of Copper from Dilute Aqueous Solutions Using the Chelating Resin Dowex M4195*. *5th International Symposium on Hydrometallurgy, TMS (The Minerals, Metals & Materials Society)*, 2003: p. 1-10.
46. Kelly, J.J.; Tian, C. and Westb, A.C., *Leveling and Microstructural Effects of Additives for Copper Electrodeposition*. *Journal of The Electrochemical Society*, , 1999. **146** (7): p. 2540-2545.
47. Soliman, H.M.A., *Formalin solution and acetone as organic additives in electrodeposition of copper*. *Digest Journal of Nanomaterials and Biostructures*, 2011. **6**(1): p. 9-12.
48. Pratt, A., *Overview of the Use of Copper Interconnects in the Semiconductor Industry*. *Advanced Energy*, 2004: p. 1-20.

49. Lin, T.-H.; Lin, C.-W.; Liu, H.-H.; Sheu, J.-T. and Hung, W.-H., Potential-controlled electrodeposition of gold dendrites in the presence of cysteine. *Supplementary Material (ESI) for Chemical Communications*, 2011: p. 1-12.
50. Li, N.-F.; Lei, T.; Liu, Y.; He, Y.-H. and Zhang, Y.-D., Electrochemical preparation and characterization of gold-polyaniline core-shell nanocomposites on highly oriented pyrolytic graphite. *Transactions of Nonferrous Metals Society of China*, 2010. **20**(12): p. 2314-2319.
51. Henderson, A.L.; Schmitt, T.C.; Heinze, T.M. and Cerniglia, C.E., Reduction of Malachite Green to Leucomalachite Green by Intestinal Bacteria. *Applied and Environmental Microbiology*, 1997. **97**: p. 4099-4101.
52. Cho, B.P.; Yang, T.; Blankenship, L.R.; Moody, J.D.; Churchwell, M.; Beland, F.A. and Culp, S.J., Synthesis and Characterization of N-Demethylated Metabolites of Malachite Green and Leucomalachite Green. *Chem. Res. Toxicol.*, 2003. **16**: p. 285-294.
53. Apel, E.L., Investigating Complex Ions of Copper(II). <http://www.chemtopics.com/aplab/complexions.pdf>, October 1, 2011: p. 198-204.
54. What does CuSo4+H2O become when mixed together? <http://answers.yahoo.com/question/index?qid=20091129114127AALI4>, October 1, 2011: p. 1.
55. Crichton, T., Different colors of CuSO4. <http://www.finishing.com/173/41.shtml>, October 1, 2011: p. 1.
56. Gafurov, M.M.; Ataev, M.B.; Aliev, A.R. and Larin, S.V., Visible and Ultra-Violet Absorption Spectra of Aqueous Solutions of Transition Metal Salts Affected by a High-Voltage Pulse Electric Discharge. *Journal of Structural Chemistry* 2007. **48**(1): p. 104-107.
57. Kemp, D.D. and Gordon, M.S., An Interpretation of the Enhancement of the Water Dipole Moment Due to the Presence of Other Water Molecules. *J. Phys. Chem. A*, 2008. **112**: p. 4885-4894.
58. Roney, A.B. and Space, B., A Molecular Dynamics Study of Aggregation Phenomena in Aqueous n-Propanol. *J. Phys. Chem. B* 2004. **108**: p. 7389-7401.
59. D. Grujicic, B.P., Electrodeposition of copper: the nucleation mechanisms. *Electrochimica Acta*, 2002. **47**: p. 12.
60. Drewe, R. Malachite Green. *The Krib Chemistry [Text]* 1997 29 October 1998 Available from: <http://www.thekrib.com/Chemistry/malachite-green.html>.
61. Sirtori, V.; Cavallotti, P.L.; Rognoni, R.; Xu, X.; Zangari, G.; Fratesi, G.; Trioni, M.I. and Bernasconi, M., Unusually large magnetic anisotropy in electrochemically deposited Co-rich Co-Pt films. *ACS applied materials & interfaces*, 2011. **3**(6): p. 1800-3.
62. Song, J. and Kim, M.W., Second Harmonic Generation Study of Malachite Green Adsorption at the Interface between Air and an Electrolyte Solution: Observing the Effect of Excess Electrical Charge Density at the Interface. *J. Phys. Chem. B* 2010. **114**: p. 3236-3241.
63. Pettinger, B.; Ren, B.; Picardi, G.; Schuster, R. and Ertl, G., Tip-enhanced Raman spectroscopy (TERS) of malachite green isothiocyanate at Au(111): bleaching behavior under the influence of high electromagnetic fields. *Journal of Raman Spectroscopy*, 2005. **36**(6-7): p. 541-550.
64. Dedeloudis, C. and Fransaer, J., AFM study of the behavior of polystyrene and glass particles during the electrodeposition of copper. *Langmuir : the ACS journal of surfaces and colloids*, 2004. **20**(25): p. 11030-8.

65. Dorobantu, L.S.; Bhattacharjee, S.; Foght, J.M. and Gray, M.R., Analysis of force interactions between AFM tips and hydrophobic bacteria using DLVO theory. *Langmuir : the ACS journal of surfaces and colloids*, 2009. **25**(12): p. 6968-76.
66. Dvir, H.; Jopp, J. and Gottlieb, M., Estimation of polymer-surface interfacial interaction strength by a contact AFM technique. *Journal of colloid and interface science*, 2006. **304**(1): p. 58-66.
67. Hyde, M.E.; Jacobs, R. and Compton, R.G., *In Situ AFM Studies of Metal Deposition*. *The Journal of Physical Chemistry*, 2002. **106**(43): p. 11075-11080.
68. Munoz, E.C.; Schreiber, R.S.; Cury, P.K.; Suarez, C.A.; Cordova, R.A.; Gomez, C.H.; Marotti, R.E. and Dalchiele, E.A., The influence of poly(ethylene oxide) and illumination on the copper electrodeposition process onto n-Si(100). *The journal of physical chemistry. B*, 2006. **110**(42): p. 21109-17.
69. Wu, A.; Li, Z.; Yu, L.; Wang, H. and Wang, E., A relocated technique of atomic force microscopy (AFM) samples and its application in molecular biology. *Ultramicroscopy*, 2002. **92**(3-4): p. 201-7.
70. Mai, W., *Fundamental Theory of Atomic Force Microscopy*. <http://www.nanoscience.gatech.edu/zlwang/research/afm.html>, October 9, 2011: p. 1.
71. Li, H.-Q., *General Ideas About AFM*. <http://www.chembio.uoguelph.ca/educmat/chm729/afm/introdn.htm>, October 9, 2011.
72. AppNano. <http://www.appnano.com/products/applications/contact-mode>, December 12, 2012.
73. Wilson, R.A. and Bullen, H.A., *Introduction to Scanning Probe Microscopy (SPM)*. http://asdlib.org/onlineArticles/ecourseware/Bullen/SPMModule_BasicTheoryAFM.pdf, October 9, 2011: p. 1-8.
74. Lennard-Jones_potential.pdf. http://en.wikipedia.org/wiki/Lennard-Jones_potential, October 10, 2011: p. 1-4.
75. Galloway, *Atomic Force Microscopy: A Guide to Understanding and Using the AFM*. 2004: p. 1-18.
76. Voutou, B. and Stefanaki, E.-C., *Electron Microscopy: The Basics*. <http://www.mansic.eu/documents/PAM1/Giannakopoulos1.pdf>, October 25, 2011: p. 1-11.
77. Swapp, S., *Scanning Electron Microscopy (SEM)*. http://serc.carleton.edu/research_education/geochemsheets/techn, October 25, 2011: p. 1-5.
78. CRAIN'S PETROPHYSICAL HANDBOOK <http://www.spec2000.net/09-xrd.htm>, December 12, 2012.
79. He, B.B.; Preckwinkel, U. and Smith, K.L., *Fundamentals of Two-Dimensional X-Ray Diffraction*. JCPDS-International Centre for Diffraction Data 2000, *Advances in X-ray Analysis*, 2000. **43** p. 273-280.
80. Holton, J., *Glossary of X-ray terms*. <http://ucxray.berkeley.edu/~jamesh/elves/manual/basics.html>, November 1, 2011.
81. Jmf8h, *X-ray Diffraction*. <http://web.pdx.edu/~pmoeck/phy381/Topic5a-XRD.pdf>, November 1, 2011: p. 1-47.
82. *X-ray diffraction primer*. <http://pubs.usgs.gov/of/2001/of01-041/htmldocs/xrpd.htm>, November 1, 2011.

83. Kang, M. and Gewirth, A.A., Influence of Additives on Copper Electrodeposition on Physical Vapor Deposited (PVD) Copper Substrates. *Journal of The Electrochemical Society*, 2003. **150**(6): p. C426.
84. Vopsaroiu, M.; Fernandez, G.V.; Thwaites, M.J.; Anguita, J.; Grundy, P.J. and O'grady, K., Deposition of polycrystalline thin films with controlled grain size. *Journal of Physics D: Applied Physics*, 2005. **38**(3): p. 490-496.
85. Vopsaroiu, M.; Thwaitesa, M.J.; Fernandez, G.V.; Lepadatu, S. and O'grady, K., Grain Size Effects in Metallic Thin Films Prepared Using a New Sputtering Technology. *Journal of Optoelectronics and Advanced Materials*, 2005. **7**(5): p. 2713 - 2720.
86. Duka, E., Mechanical characterisation of very thin films. *Physics of Advanced Materials Winter School 2008*: p. 1-11.
87. A.K. Sikder, A.K., P. Shukla, P.B. Zantye and M. Sanganaria, Effect of Multistep Annealing on Mechanical and Surface Properties of Electroplated Cu Thin Films. *Journal of Electronic Materials*, 2003. **32**(10): p. 6.
88. Valic, A.M.a.a.D., A study of copper electrowinning parameters using a statistically designed methodology. *Journal of Applied Electrochemistry*, 2003. **33**: p. 9.
89. Kirk, N.B. and Wood, J.V., The effect of the calcination process on the crystallite shape of sol-gel cerium oxide used for glass polishing. *Journal of materials science* 1995. **30**: p. 2171-2175.
90. Pickel, M., Scanning Tunneling Microscope. <http://www.fkf.mpg.de/ga/research/stmtutor/stmconc.html>, 2000: p. 1-15.
91. Scanning tunneling microscope. http://en.wikipedia.org/wiki/Scanning_tunneling_microscope, November 22, 2011.
92. Melmed, A.J., The art and science and other aspects of making sharp tips. *J. Vac. Sci. Technol. B*, 1991. **9** (2): p. 601-607.
93. Albonetti, C.; Bergenti, I.; Cavallini, M.; Dediu, V.; Massi, M.; Moulin, J.-F.O. and Biscarini, F., Electrochemical preparation of cobalt tips for scanning tunneling microscopy. *Review of Scientific Instruments*, 2002. **73**(12): p. 4254.
94. Oliva, A.I.; G., A.R. and Pen˜a, J.L., Electrochemical preparation of tungsten tips for a scanning tunneling microscope. *Rev. Sci. Instrum.*, 1996. **67**(5): p. 1917-1921.
95. Klein, M. and Schwitzgebel, G., An improved lamellae drop-off technique for sharp tip preparation in scanning tunneling microscopy. *Rev. Sci. Instrum.*, 1997. **68** (8): p. 3099-3103.
96. Rogers, B.L. and Shapter, J.G., A method for production of cheap, reliable Pt-Ir tips. *REVIEW OF SCIENTIFIC INSTRUMENTS*, 2000. **71**(4).
97. Zhang, R. and Ivey, D.G., Preparation of sharp polycrystalline tungsten tips for scanning tunneling microscopy imaging. *J. Vac. Sci. Technol. B*, 1996. **14**(1).
98. Iwami, M.; Uehara, Y. and Ushioda, S., Preparation of silver tips for scanning tunneling microscopy imaging. *REVIEW OF SCIENTIFIC INSTRUMENTS VOLUME , NUMBER 11 NOVEMBER 1998*. **69**: p. 4010-4011.
99. Schulte, A., STM tips for in-situ scanning tunneling microscopy in aqueous solutions prepared using electrophoretic deposition of paint. *SPIE Conference on Materials and Device Characterization in Micromachinjpg*, 1998: p. 353-357.
100. Z, TEM Pictures of STM Tips.

101. Libioulle, L., Very sharp platinum tips for scanning tunneling microscopy. *Ftev. Sci. Instrum.*, 1995. **66** (1): p. 97-100.
102. Alessandrini, A. and Facci, P., The New Frontiers of Organic and Composite Nanotechnology. *Electrochemically assisted scanning probe microscopy: A powerful tool in nano(bio)science*, ed. V. Erokhin, M.K. Ram, and O. Yavuz2008, Oxford: Elsevier. 435.
103. Smith, J.P., *Mixing electrochemistry with microscopy*. *Anal. Chem.*, 2001: p. 39 A-42 A.
104. Bae, S.E. and Gewirth, A.A., *In situ EC-STM studies of MPS, SPS, and chloride on Cu100: structural studies of accelerators for dual damascene electrodeposition*. *Langmuir : the ACS journal of surfaces and colloids*, 2006. **22**(25): p. 10315-21.
105. An, S.; Lim, T.; Kim, Y.; Bae, S.; Yoon, J. and Lee, C., *EC-STM studies on copper electrodeposition at n-Si(111):H electrodes*. *Colloids and Surfaces A: Physicochemical and Engineering Aspects*, 2008. **313-314**: p. 339-342.
106. Shingaya, Y.; Matsumoto, H.; Ogasawara, H. and Ito, M., *In situ and ex situ IRAS, LEED and EC-STM studies of underpotentially deposited copper on a Pt(III)electrode in sulfuric acid solution: coadsorption of sulfate ion with copper*. *Surface Science* 1995. **335** p. 23-31.
107. Matsuoka, O.; Ono, S.S.; Nozoye, H. and Yamamoto, S., *Structure and dynamics of oxy-overlayer on Cu(111) electrode surfaces in alkaline aqueous solution revealed by electrochemical STM and quartz crystal microbalance measurement*. *Surface Science*, 2003. **545**(1-2): p. 8-18.
108. V. Kapo Cius; V. Karpavi Den and Dus, A.S., *Electrochemical Processes at a Platinum Electrode in CuSO4 Solutions in the UPD Region and at Initial Electrocrystallization Stages: Effect of Polyethylene Glycol*. *Russian Journal of Electrochemistry*, 2002. **38**(3): p. 274-279.
109. An, S.-H.; Lim, T.-H.; Kim, Y.-H.; Bae, S.-E.; Yoon, J.-H. and Lee, C.-W.J., *EC-STM studies on copper electrodeposition at n-Si(111):H electrodes*. *Colloids and Surfaces A: Physicochemical and Engineering Aspects*, 2008. **313-314**: p. 339-342.
110. Lopez-Salido, I.; Lim, D.C.; Dietsche, R.; Bertram, N. and Kim, Y.D., *Electronic and geometric properties of Au nanoparticles on Highly Ordered Pyrolytic Graphite (HOPG) studied using X-ray Photoelectron Spectroscopy (XPS) and Scanning Tunneling Microscopy (STM)*. *The journal of physical chemistry. B*, 2006. **110**(3): p. 1128-36.
111. Higashi, T.; Shigemitsu, Y. and Sagara, T., *Faradaic phase transition of dibenzyl viologen on an HOPG electrode surface studied by in situ electrochemical STM and electroreflectance spectroscopy*. *Langmuir : the ACS journal of surfaces and colloids*, 2011. **27**(22): p. 13910-7.
112. Chen, T.; Chen, Q.; Pan, G.B.; Wan, L.J.; Zhou, Q.L. and Zhang, R.B., *Linear dislocation tunes chirality: STM study of chiral transition and amplification in a molecular assembly on an HOPG surface*. *Chemical communications*, 2009(19): p. 2649-51.
113. Suzuki, Y.; Enoki, H. and Akiba, E., *Observation of HOPG by STM and contact AFM in various gas atmospheres under pressures up to 1.1 MPa*. *Ultramicroscopy*, 2005. **104**(3-4): p. 226-32.
114. Lackinger, M.; Griessl, S.; Heckl, W.M. and Hietschold, M., *STM and STS of coronene on HOPG 0001 in UHV - adsorption of the smallest possible graphite flakes on graphite*. *Analytical and bioanalytical chemistry*, 2002. **374**(4): p. 685-7.
115. Brown, G.M.; Allison, D.P.; Warmack, R.J.; Jacobson, K.B.; Larimer, F.W.; Woychik, R.P. and Carrier, W.L., *Electrochemically induced adsorption of radio-labeled DNA on gold and HOPG substrates for STM investigations*. *Ultramicroscopy*, 1991. **38**(3-4): p. 253-64.

116. Tong, X.Q.; Aindow, M. and Farr, J.P., Instrumental effects on in situ electrochemical STM studies: an investigation of a current surge induced Pd deposit on HOPG. *Microscopy research and technique*, 1996. **34**(1): p. 87-95.
117. Xie, Z.; Mao, B.; Zhuo, X.; Mu, J. and Tian, Z., In Situ Studies of Copper Electrodeposition on HOPG by Using ECSTM. *Journal of Electrochemistry*, 1996. **2**(2): p. 164-169.
118. Daphna R. Yaniv and McCormick, L.D., Novel STM-EC center for in situ imaging under potentiostatic/galvanostatic control: Electrodeposition of copper and cadmium on carbon substrates. *Electroanalysis*, 1991. **3**(2): p. 103-110.
119. Huang, L.; Lee, E.-S. and Kim, K.-B., Electrodeposition of monodisperse copper nanoparticles on highly oriented pyrolytic graphite electrode with modulation potential method. *Colloids and Surfaces A: Physicochemical and Engineering Aspects*, 2005. **262**(1-3): p. 125-131.
120. Appelbaum, J., Electronic structure of the Cu(111) surface. *Solid State Communications*, 1978. **27**(9): p. 881-883.
121. Eberhardt, W., Interaction of CO and N₂ with the Cu(111) surface. *PHYSICAL REVIEW B*, 1983. **28**(6): p. 3605-3607.
122. Gay, J.G.; Smith, J.R. and Arlinghaus, F.J., Large Surface-State/Surface-Resonance Density on Copper (100). *PHYSICAL REVIEW LETTERS*, 1979. **42**(5).
123. Olsson, F.; Persson, M.; Borisov, A.; Gauyacq, J.P.; Lagoute, J. and Fölsch, S., Localization of the Cu(111) Surface State by Single Cu Adatoms. *Physical Review Letters*, 2004. **93**(20).
124. Sa'Nchez, C. and Leiva, E.P.M., Cu underpotential deposition on Au(111) and Au(100). Can this be explained in terms of the energetics of the Cu/Au system? *Electrochimica Acta*, 1999. **45** p. 691-697.
125. Kaden, C.; Ruggerone, P.; Toennies, J.; Zhang, G. and Benedek, G., Electronic pseudocharge model for the Cu(111) longitudinal-surface-phonon anomaly observed by helium-atom scattering. *Physical Review B*, 1992. **46**(20): p. 13509-13525.
126. Smith, J.R.; Gay, J.G. and Arlinghaus, F.J., Self-consistent local-orbital method for calculating surface electronic structure: Application to Cu (100). *PHYSICAL REVIEW B VOLUME*, 1980. **21**(6): p. 2201-2221.
127. Dempsey, D. and Kleinman, L., Extended-Hückel study of the (111), (100), and (110) surfaces of copper. *Physical Review B*, 1977. **16**(12): p. 5356-5366.
128. Wang, X.F.; Li, W.; Lin, J.G. and Xiao, Y., Electronic work function of the Cu (100) surface under different strain states. *EPL (Europhysics Letters)*, 2010. **89**(6): p. 66004.
129. Foiles, S.M.; Baskes, M.I. and Daw, M.S., Embedded-atom-method functions for the fcc metals Cu, Ag, Au, Ni, Pd, Pt, and their alloys. *Physical Review B*, 1986. **33**(12): p. 7983-7991.
130. Xia, Y.; Xiong, Y.; Lim, B. and Skrabalak, S.E., Shape-controlled synthesis of metal nanocrystals: simple chemistry meets complex physics? *Angewandte Chemie*, 2009. **48**(1): p. 60-103.
131. Zhang, J.-M.; Ma, F. and Xu, K.-W., Calculation of the surface energy of FCC metals with modified embedded-atom method. *Applied Surface Science*, 2004. **229**(1-4): p. 34-42.
132. Hassani, S.S. and Sobat, Z., Studying of various nanolithography methods by using Scanning Probe Microscope. *Int.J.Nano.Dim* 1(3), 2011: p. 159-175.

133. Guo, L.J., *Nanoimprint Lithography: Methods and Material Requirements*. *Advanced materials*, 2007. **19**(4): p. 495-513.
134. Pimpin, A. and Srituravanich, W., *Review on Micro- and Nanolithography Techniques and their Applications*. *Engineering Journal*, 2012. **16**(1): p. 37-56.
135. Xie, X.N.; Chung, H.J.; Sow, C.H. and Wee, A.T.S., *Nanoscale materials patterning and engineering by atomic force microscopy nanolithography*. *Materials Science and Engineering: R: Reports*, 2006. **54**(1-2): p. 1-48.
136. Xie, Z.; Yu, W.; Wang, T.; Zhang, H.; Fu, Y.; Liu, H.; Li, F.; Lu, Z. and Sun, Q., *Plasmonic Nanolithography: A Review*. *Plasmonics*, 2011. **6**(3): p. 565-580.
137. *Multielectrode array*. http://en.wikipedia.org/wiki/Multielectrode_array, March 25, 2012: p. 1-7.
138. Štulík, K.; Amatore, C.; Holub, K.; Marecek, V. and Kutner, W., *Microelectrodes: Definitions, Characterization, and Applications*. *Pure Appl. Chem.*, 2000. **72**(8): p. 1483-1492.
139. Halliwell, J.; Whitaker, M. and Ogden, D., *Using microelectrodes*. *Microelectrode Application in Biology*: p. 1-15.
140. Gross, G.W.; Rieske, E.; Kreuzberg, G.W. and Meyer, A., *A new fixed-array multi-microelectrode system designed for long-term monitoring of extracellular single unit neuronal activity in vitro*. *Neuroscience Letters*, 1977. **6**(2-3): p. 101-105.
141. *Surface plasmon-plasmonics*. <http://en.wikipedia.org/wiki/Plasmonics>, March 25, 2012: p. 1-6.
142. *What is Plasmonics*. <http://www.wisegeek.com/what-is-plasmonics.htm>, March 25, 2012.
143. Dag, G., *Plasmonics with coated nanodomains for thin and affordable solar cells*. <http://www.robaid.com/tech/plasmonics-with-coated-nanodomains-for>, 2011: p. 1-2.
144. *Plasmonic Enhancement of Silicon Solar Cells*. Temple and Bagnall Poster at 3rd Conf Surface Plasmon Photonics.
145. Chen, W.-H.; Chen, Y.-S.; Fu, S.-J.; Ko, W.-Y. and Lin, K.-J., *Large-sized Fabrication of Tunable Plasmonic Electrodes via Electrodeposition*. *Journal of the Chinese Chemical Society*, 2010. **57**: p. 162-166.
146. *Plasmonics*. <http://users.ecs.soton.ac.uk/dmb/plasmonics.php>, March 25, 2012: p. 1.
147. *Second Harmonic Generation*. http://en.wikipedia.org/wiki/Second-harmonic_generation, March 6, 2012.
148. *Surface second harmonic generation*. http://en.wikipedia.org/wiki/Surface_second_harmonic_generation#Interface_structure, March 6, 2012.
149. Shen, Y.R., *Optical Second Harmonic Generation at Interfaces*. *Annual Review of Physical Chemistry*, 1989. **40**: p. 327-350.
150. Kikteva, T.; Star, D.; Lee, A.M.; Leach, G.W. and Papanikolas, J.M., *Five wave mixing: surface-specific transient grating spectroscopy as a probe of low frequency intermolecular adsorbate motion*. *Physical Review Letters*, 2000. **85**(9): p. 1906-9.
151. Johansson, T.P. and Leach, G.W., *Sum frequency generation study of Langmuir Blodgett film architecture*. *The journal of physical chemistry. B*, 2006. **110**(33): p. 16567-74.
152. Corn, R.M. and Higgins, D.A., *Molecular Orientation in Thin Films as Probed by Optical Second Harmonic Generation: In Characterization of Organic Thin Films* Butterworth-Heinemann, Ed. Boston, 1995.

153. Shen, Y.R., *Surface Properties Probed by Second-Harmonic and Sum Frequency Generation*. *Nature* 1989. **337**: p. 519-525.
154. Eisenthal, K.B., *Equilibrium and Dynamic Processes at Interfaces by 2nd Harmonic and Sum Frequency Generation*. *Annual Review of Physical Chemistry Letters*, 1992. **43**: p. 627-661.
155. Heinz, T.F.; Tom, H.W.K. and Shen, Y.R., *Determination of molecular orientation of monolayer adsorbates by optical second-harmonic generation*. *PHYSICAL REVIEW A*, 1983. **28**(3): p. 1883-1885.
156. Guyot-Sionnest, P.; Chen, W. and Shen, Y., *General considerations on optical second-harmonic generation from surfaces and interfaces*. *Physical Review B*, 1986. **33**(12): p. 8254-8263.
157. Feller, M.B.; Chen, W. and Shen, Y.R., *Investigation of Surface-Induced Alignment of Liquid-Crystal Molecules by Optical 2nd-Harmonic Generation*. *Physical Review A*, 1991. **43**(12): p. 6778-6792.
158. Cheikh-Rouhou, W.; Sampaio, L.C.; Bartenlian, B.; Beauvillain, P.; A. Brunc; Ferré, J. and Georges, P., *SHG anisotropy in Au/Co/Au/Cu/vicinal Si(1 1 1)*. *Journal of Magnetism and Magnetic Materials* () 2002. **240** p. 532-535.
159. Hoffbauer, M.A., *Rotationally anisotropic second-harmonic generation studies of the structure and thermal stability of Cu(110)*. *Journal of Vacuum Science & Technology B: Microelectronics and Nanometer Structures*, 1992. **10**(1): p. 268.
160. Richmond, G.L. and Bradley, R.A., *Surface Second Harmonic Generation Studies of Single Crystal Metal Surfaces*. *Laser Spectroscopy and Photochemistry on Metal Surfaces*, 1995: p. 132-183.
161. Koos, D.; Shannon, V. and Richmond, G., *Surface-dipole and electric-quadrupole contributions to anisotropic second-harmonic generation from noble-metal surfaces*. *Physical Review B*, 1993. **47**(8): p. 4730-4734.
162. Petrocelli, G.; Marteuucci, S. and Francini, R., *Wavelength dependence of second-harmonic generation at the copper surface*. *Appl. Phys. A*, 1993. **56**: p. 263-266.
163. Janz, S.; Lüpke, G. and Van Driel, H., *Phase diagram of vicinal Cu(111) surfaces as determined by second-harmonic generation*. *Physical Review B*, 1993. **47**(12): p. 7494-7500.
164. Zhang, L. and Cui, D., *Investigation of Second-Harmonic Generation and Molecular Orientation in Electrostatically Self-Assembled Thin Films*. *Polymers*, 2011. **3**(3): p. 1297-1309.
165. Eisert, F.; Dannenberger, O. and Buck, M., *Molecular orientation determined by second-harmonic generation: Self-assembled monolayers*. *PHYSICAL REVIEW B*, 1998. **58**(16): p. 10860-10870.
166. De Beer, A.G. and Roke, S., *Obtaining molecular orientation from second harmonic and sum frequency scattering experiments in water: angular distribution and polarization dependence*. *The Journal of chemical physics*, 2010. **132**(23): p. 234702.
167. Higgins, D.A.; Naujok, R.R. and Corn, R.M., *Second harmonic generation measurements of molecular orientation and coadsorption at the interface between two immiscible electrolyte solutions*. *CHEMICAL PHYSICS LETTERS* 1993. **213**(5,6): p. 485-490.
168. Chen, W.-K.; Liu, S.-H.; Cao, M.-J.; Lu, C.-H.; Xu, Y. and Li, J.-Q., *Adsorption of Methanol and Methoxy on Cu(111) Surface: A First-principles Periodic Density Functional Theory Study*. *Chinese Journal of Chemistry*, 2006. **24**: p. 872-876.

169. Heinz, H.; R.A.Vaia; B.L.Farmer and R.R.Naik, *Accurate Simulation of Surfaces and Interfaces of Face-Centered Cubic Metals Using 12-6 and 9-6 Lennard-Jones Potentials. J.Phys.Chem., 2008. 112: p. 17281-17290.*
170. Feng, J.; Pandey, R.B.; Berry, R.J.; Farmer, B.L.; Naik, R.R. and Heinz, H., *Adsorption mechanism of single amino acid and surfactant molecules to Au {111} surfaces in aqueous solution: design rules for metal-binding molecules. Soft Matter, 2011. 7(5): p. 2113.*
171. Wang, X.; Selvam, P.; Lv, C.; Kubo, M. and Miyamoto, A., *A theoretical study on the cyclopropane adsorption onto the copper surfaces by density functional theory and quantum chemical molecular dynamics methods. Journal of Molecular Catalysis A: Chemical, 2004. 220(2): p. 189-198.*
172. Sun, H., *COMPASS: An ab Initio Force-Field Optimized for Condensed-Phase Applications Overview with Details on Alkane and Benzene Compounds. J. Phys. Chem. B, 1998. 102: p. 7338-7364.*
173. Aryanpour, M.; Venkatasubramanian, V. and Pitsch, H., *Ab-Initio Study of Hydrogen Adsorption and Evolution on Pt(100) Surface. 2008: p. 1-14.*
174. Martel, R.; Rochefort, A. and Mcbreen, P.H., *Metallacyclobutane and Cyclopropyl Species on Cu(111) and Cu(110). J. Am. Chem. Soc., 1998. 120: p. 2421-2427.*
175. Monte Carlo method. http://en.wikipedia.org/wiki/Monte_Carlo_method, February 24, 2012: p. 1-12.
176. Harinipriya, S. and Subramanian, V., *Monte Carlo simulation of electrodeposition of copper: a multistep free energy calculation. J Phys Chem B. Apr 3(;);, 2008 112(13): p. 4036-4047.*
177. Http://Web.Nmsu.Edu/~Snm/Classes/Chem435/Lab14/Double_Layer.Ht, *Electric Double Layer. Electric Double Layer, September 2012: p. 1-3.*
178. Lockett, V.; Sedev, R. and Ralston, J., *Differential Capacitance of the Electrical Double Layer in Imidazolium-Based Ionic Liquids: Influence of Potential, Cation Size, and Temperature. J. Phys. Chem. C, 2007: p. 1-10.*
179. Oldham, K.B., *A Gouy–Chapman–Stern model of the double layer at a (metal)/(ionic liquid) interface. Journal of Electroanalytical Chemistry, 2008. 613(2): p. 131-138.*
180. *Measurements of the double layer capacitance. Bio-Logic Science Instruments, 2012: p. 1-4.*
181. K.F.Khaled and Abdel-Shafi, N.S., *Quantitative Structure and Activity Relationship Modeling Study of Corrosion Inhibitors: Genetic Function Approximation and Molecular Dynamics Simulation Methods. Int. J. Electrochem. Sci., 2011. 6: p. 4077 - 4094.*
182. Kratzer, P.; Hammer, B. and Norskov, J.K., *Geometric and electronic factors determining the differences in reactivity of H₂ on Cu(100) and Cu(111). Surface Science, 1996. 359 p. 45-53.*
183. Ke, E.; Chen, Z.; Ye, J. and Xiao, F., *2D Diffusion-ordered Nuclear Magnetic Resonance Spectroscopy for Structure Analysis of Mixtures. Journal of Xiamen University (Natural Science), 199. 38(3): p. 4.*
184. Liu, L.; Zhao, F.; Xiao, F. and Zeng, B., *Improved Voltammetric Response of Malachite Green at a Multi-Walled Carbon Nanotubes Coated Glassy Carbon Electrode in the Presence of Surfactant. Int. J. Electrochem. Sci., 2009. 4.*
185. *SPMLab Version 5.01 Software Reference Manual. 2000.*
186. Horcas, I.; R.Fernandez; Gomez-Rodriguez, J.M.; Colchero, J.; Gomez-Herrero, J. and Baro, A.M., *Review of Scientific Instruments, 2007. 78.*

187. *Materials Studio*. <http://computationalmaterials.blogspot.ca/2010/05/materials-studio.html>, 20120505: p. 1.
188. *Frenkel, D. and Smit, B., Understanding Molecular Simulation: From Algorithms to Applications. 2nd Edition ed2002, San Diego: Academic Press.*
189. *Metropolis, N.; Rosenbluth, A.W.; Rosenbluth, M.N. and Teller, A.H.T., E., Equation of State Calculations by Fast Computing Machines. J. Chem. Phys., 1953. 21.*

Appendices

Appendix A.

Refining SPM Images

In order to display SPM images clearly and cleanly, all SPM softwares provide ways of processing or refining such as leveling or flattening, filter, and correlation [185, 186].

Leveling

Leveling or flattening is the process by which one can automatically or manually define a level plane for the display of ones data. Because most modes of scanning probe microscopy describe topography on a scale which is the absolute Z height from some “zero” point, the relative Z value assigned to surface measurement points are directly affected by how level the sample is. To actually mount a sample perfectly level is usually not a realistic goal because of the extremely small scale involved in SPM (1 μm or less). But, with the leveling process, one can use the software to compensate for sample tilt, allowing accurate measurement of Z height across a sample without adding any erroneous tilt information to the data.

Filter

The smoothing filter or matrix filter eliminates the high frequency components of the image. To do this, each point of the image is replaced with the average of its first neighboring points. Thus, every given matrix element f_{ij} , will be replaced by a new value, d_{ij} given by:

$$\begin{pmatrix} f_{j+1,i+1} & f_{j+1,i} & f_{j+1,i-1} \\ f_{j,i+1} & f_{j,i} & f_{j,i-1} \\ f_{j-1,i+1} & f_{j-1,i} & f_{j-1,i-1} \end{pmatrix}, \quad d_{ij} = \frac{1}{9} \left(\sum_{n=j-1}^{j+1} \sum_{m=i-1}^{i+1} f_{nm} \right)$$

Further smoothing can be obtained by repeated application of the filter.

Self-Correlation

Self-correlation is defined as:

$$G(k_1, k_2) = \sum f(x, y) f(x + k_1, y + k_2),$$

where $f(x,y)$ is the image matrix. This equation takes the image and the same image shifted a distance k_1 and k_2 in the X and Y axis with respect to the center of the image.

The resulting image, $G(k_1, k_2)$, is a measure of how different the two images are. The more similar the image and the shifted image are, the higher the value of the self-correlation. In self-correlation, the highest value is obtained at the center of the image (where k_1 and k_2 are zero). Any periodicity in the original image will be shown as a periodic pattern in the self-correlation.

Appendix B.

Laser System for SHG Experiment

The SHG measurements were performed using the regeneratively amplified output of a mode-locked Ti-sapphire (Spectra Physics) laser. A 6 W cw Nd:YVO₄ laser (Verdi, coherent) is used to pump a mode-locked Ti: Sapphire oscillator (Spectra Physics, Tsunami 3960) which produces a pulse train at frequency of 82 MHz, with a nominal wavelength 800 nm and pulse duration of 80 fs. This pulse train is directed to a Ti: Sapphire chirped pulse regenerative amplifier (Positive Light, Spitfire) for amplification. The amplifier is pumped by a pulsed intracavity frequency-doubled, Q-switched Nd:YLF laser (Positive Light, Merlin), which operates at a repetition rate of 1 kHz. The amplifier produces pulsed radiation with the pulse duration of 100 fs, pulse energy 1 mJ, and nominal wavelength of 800 nm. To avoid possible sample damage by the laser irradiation, 75 mW was used to conduct SHG in this experiment.

Appendix C.

Adsorption Locator, Material Studio

Materials Studio software is used for simulation and modelling of materials developed and distributed by Accelrys. This software is used in advanced research of various materials--polymers, nanotubes, catalysts, metals, ceramics, and so on--by universities, research centers and hi-tech companies [187].

***Adsorption Locator** enables one to simulate a substrate loaded with an adsorbate or an adsorbate mixture of a fixed composition. Adsorption Locator is designed for the study of individual systems, allowing one to find low energy adsorption sites on both periodic and nonperiodic substrates or to investigate the preferential adsorption of mixtures of adsorbate components, for example. Adsorption Locator identifies possible adsorption configurations and low energy adsorption sites by carrying out Monte Carlo searches of the configurational space of the substrate-adsorbate system as the temperature is slowly decreased. This process is repeated to identify further local energy minima.*

The following topics provide specific details about the theory behind Adsorption Locator:

Generation of substrate-adsorbate configurations

In an Adsorption Locator simulation, the candidate substrate-adsorbate configurations are sampled from a canonical ensemble. In the canonical ensemble, the loading of all adsorbate components on the substrate, as well as the temperature, are fixed.

The probability of a configuration, m , in the canonical ensemble is given by [188]:

$$\rho_m = C \exp[-\beta E_m]$$

where C is an arbitrary normalization constant, β is the reciprocal temperature, and E_m is the total energy of configuration m . The reciprocal temperature is given by:

$$\beta = 1/(k_B T)$$

where k_B is the Boltzmann constant and T is the absolute temperature. The total energy of configuration m is calculated according to the following sum:

$$E_m = E_m^{AA} + E_m^{AS} + U_m^A$$

where E_m^{AA} is the intermolecular energy between the adsorbate molecules, E_m^{AS} is the interaction energy between the adsorbate molecules and the substrate, and U_m^A is the total intramolecular energy of the sorbate molecules. The intramolecular energy of the substrate is not included as its structure is fixed throughout the simulation; thus, this energy contribution is fixed and vanishes, since only energy differences play a role in Adsorption Locator calculations.

The total intramolecular energy, U^A , is the sum of the intramolecular energy of all adsorbates of all components:

$$U^A = \sum_{N_m} u_{intra}$$

where N_m denotes the set of adsorbate loadings of all components in configuration m .

An Adsorption Locator simulation always starts with a clean substrate. The first stage is to adsorb the specified number of adsorbate molecules of each component. This is accomplished by a random series of insertion steps and equilibration moves (only moves that do not change the loading are permitted) until the specified loading has been reached. During this stage, only insertion steps that do not create structures with intermolecular close contacts and that pass all adsorbate location constraints are accepted.

Note. The loading stage in Adsorption Locator has a maximum of 100000 insertion steps. If the specified mixture could not be loaded within this number of insertion steps, the simulation stops and a loading failure is reported. In this case, one should decrease the number of adsorbate molecules specified for the simulation.

The starting configuration will take several steps to adjust to the current temperature. A simulation is, therefore, separated into an equilibration and a production stage. The properties returned at the end of the run are based on the production stage only.

In the equilibration and production stages of an Adsorption Locator simulation, each step starts with the selection of a step type using the weights set at the start of the run. The step type can be either a translation or a rotation. After a step type is selected, a random component is chosen and the step type is applied to a random adsorbate of that component. The Metropolis Monte Carlo method is then used to decide whether to accept or reject the change.

Metropolis Monte Carlo method

Experimentally, a molecular system is described by a small number of parameters, such as volume and temperature. The collection of molecular configurations that satisfy this partial knowledge is called an ensemble of configurations. An ensemble is described by a distribution function, ρ_m , which represents the probability of each configuration, m , in the ensemble. The Metropolis Monte Carlo method used in Adsorption Locator samples the configurations in an ensemble by generating a chain of configurations, m, n, \dots , where the probability of transition from m to n is π_{mn} . Thus, if configuration m is sampled with a frequency ρ_m , then, on average, $\rho_m \pi_{mn}$ of them are transformed to n . Likewise, $\rho_n \pi_{nm}$ of configurations n are transformed to m . Clearly, these fluxes must be the same to preserve the density, ρ , otherwise, there would be a net flow from m to n (or vice versa) and this would increase ρ_n (or ρ_m) and a different ensemble would be sampled. Thus, the following detailed balance condition for equilibrium is obtained:

$$\rho_m \pi_{mn} = \rho_n \pi_{nm}$$

In the Metropolis Monte Carlo method, the step that transforms configuration m to n is a two-stage process. First, a trial configuration is generated with probability α_{mn} . Then, either the proposed configuration, n , is accepted with a probability P_{mn} or the original configuration, m , is retained with a probability $(1 - P_{mn})$. The overall transition probability, π_{mn} , is thus obtained from:

$$\pi_{mn} = \alpha_{mn} P_{mn}$$

It is easy to verify by substitution that the following choice for the acceptance probability satisfies the above equation.

$$P_{mn} = \min \left[1, \frac{\alpha_{nm} \rho_n}{\alpha_{mn} \rho_m} \right]$$

This expression can be simplified further. In the traditional Metropolis Monte Carlo method [189], trial configurations are generated without bias, i.e., $\alpha_{mn} = \alpha_{nm}$. As such, the corresponding acceptance probability becomes:

$$P_{mn} = \min \left[1, \frac{\rho_n}{\rho_m} \right]$$

Thus, transitions of a configuration m to a more likely one ($\rho_n > \rho_m$) are always accepted, but transitions to configurations with a lower probability ($\rho_n < \rho_m$) are less likely to be accepted.

Canonical ensemble

The canonical ensemble is described in the Generation of substrate-adsorbate configurations topic. The probability of a configuration in this ensemble is given by ρ_m . Substitution into P_{mn} leads to the acceptance probability:

$$P_{mn} = \min[1, \exp[-\beta(E_n - E_m)]]$$

Transitions to a configuration of lower energy ($E_n < E_m$) are always accepted, but transitions to high energy configurations ($E_n > E_m$) are only accepted with a probability which decreases exponentially with the difference in energy to zero. As such, high energy configurations are unlikely to be sampled, precisely what the probability density of the canonical ensemble ρ_m dictates.

The Metropolis Monte Carlo method in Adsorption Locator provides four step types for a canonical ensemble: conformer, rotation, translation, and regrowth.

CVFF forcefield

The consistent-valence forcefield (CVFF), the original forcefield provided with the Discover program, is a generalized valence. The augmented CVFF was developed for materials science applications and is provided with Discover in Materials Studio. CVFF also has the ability to use automatic parameters (Automatic assignment of values for missing parameters) when no explicit parameters are present. These are noted in the output file from the calculation. CVFF has been used extensively for many years. It is primarily intended for studies of structures and binding energies, although it predicts vibrational frequencies and conformational energies reasonably well. The analytic form of the energy expression used in CVFF is shown below:

$$\begin{aligned}
 E_{pot} = & \sum_b D_b [1 - e^{-\alpha(b-b_0)}] + \sum_{\theta} H_{\theta} (\theta - \theta_0)^2 + \sum_{\phi} H_{\phi} [1 + s \cos(n\phi)] + \sum_{\chi} H_{\chi} \chi^2 \\
 & + \sum_b \sum_{b'} F_{bb'} (b - b_0)(b' - b'_0) + \sum_{\theta} \sum_{\theta'} F_{\theta\theta'} (\theta - \theta_0)(\theta' - \theta'_0) \\
 & + \sum_b \sum_{\theta} F_{b\theta} (b - b_0)(\theta - \theta_0) + \sum_{\phi} F_{\phi\theta\theta'} \cos(\theta - \theta_0)(\theta' - \theta'_0) \\
 & + \sum_{\chi} \sum_{\chi'} F_{\chi\chi'} + \sum \varepsilon [(r^*/r)^{12} - 2[(r^*/r)^6]] + \sum q_i q_j / \varepsilon r_{ij}
 \end{aligned}$$

Terms 1-4 are commonly referred to as the diagonal terms of the valence forcefield and represent the energy of deformation of bond lengths, bond angles, torsion angles, and out-of-plane interactions, respectively.

Terms 5-9 are off-diagonal (or cross) terms and represent couplings between deformations of internal coordinates. For example, Term 5 describes the coupling between stretching of adjacent bonds. These terms are required to accurately reproduce experimental vibrational frequencies and, therefore, the dynamic properties of molecules. In some cases, research has also shown them to be important in accounting for structural deformations. However, cross terms can become unstable when the structure is far from a minimum.

Terms 10-11 describe the non-bond interactions. Term 10 represents the van der Waals interactions with a Lennard-Jones function. Term 11 is the Coulombic representation of electrostatic interactions. The dielectric constant, ϵ , can be made distance dependent (that is, a function of r_{ij}).

In the CVFF forcefield, hydrogen bonds are a natural consequence of the standard van der Waals and electrostatic parameters.